

**Structures and Charge Distributions of Cluster Anions
Studied by Infrared Photodissociation Spectroscopy**

by

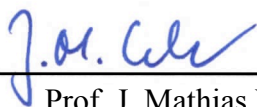
B. J. Knurr

B.A., Macalester College, 2009

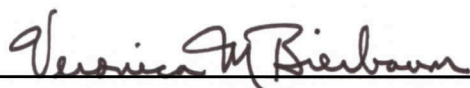
A thesis submitted to the
Faculty of the Graduate School of the
University of Colorado in partial fulfillment
of the requirements for the degree of
Doctor of Philosophy
Department of Chemistry and Biochemistry

2015

This thesis entitled:
Structures and Charge Distributions of Cluster Anions Studied by Infrared Photodissociation
Spectroscopy
written by B. J. Knurr
has been approved for the Department of Chemistry and Biochemistry



Prof. J. Mathias Weber



Prof. Veronica M. Bierbaum

Date 11/21/2014

The final copy of this thesis has been examined by the signatories, and we find that both the content and the form meet acceptable presentation standards of scholarly work in the above mentioned discipline.

Knurr, B. J. (Ph.D., Chemical Physics)

Structures and Charge Distributions of Cluster Anions Studied by Infrared Photodissociation Spectroscopy

Thesis directed by Prof. Prof. J. Mathias Weber

Anions are relevant in many different facets of chemistry. The study of anions, their interaction with other atoms and molecules and the effect of solvation on those interactions are of interest to further the understanding of chemical processes. Studies on cluster ions *in vacuo* allow for the generation of and excellent control over chemically interesting species. Experiments of this nature are ideal for studying the fundamental interactions of molecular partners by eliminating many of the complications of obtaining spectroscopic data on an individual species in the condensed phase. The clusters studied can also be viewed as model systems for more complex chemical processes that are otherwise difficult to understand at a molecular level.

In one part of this work, infrared spectra were obtained for $[M(\text{CO}_2)_n]^-$ ($M = \text{Au}, \text{Ag}, \text{Co}, \text{Ni}$ and Cu) clusters. These studies were performed in an effort to understand the interactions resulting in the reduction of CO_2 . These cluster systems are viewed as model single atom catalysts for the purpose of CO_2 reduction. Au, Ag and Cu were all found to form η^1 (monodentate) $[\text{MCO}_2]^-$ complexes of the metal and one CO_2 molecule with a structure akin to the formate anion. Study of the solvation environment of these η^1 complexes reveals that the excess charge on the core can be polarized onto the CO_2 moiety with increasing efficiency from Au to Cu . Co, Ni and Cu all exhibit core ions of the form $[\text{CO}_2\text{MCO}_2]^-$ where the CO_2 ligands are bound in a bidentate (η^2) fashion. The polarizability of the core species increases from Co to Cu . Cu is a member of both the first row transition metals and the coinage metals, and it shows interaction motifs characteristic of both groups of metals. Additionally, two studies were performed on $[\text{CoO}(\text{CO}_2)_n]^-$ and $[\text{NiO}(\text{CO}_2)_n]^-$ clusters. It is shown that similar core structures are present in both CoO and NiO clusters and that the general behavior of the clusters is comparable to the analogous non-oxide clusters.

Two studies were performed on non-metal containing systems. A charge transfer reaction between a nitromethane anion and iodomethane was vibrationally induced. It is found that vibrational excitation of C-H stretches on either of the species in the complex leads to charge transfer from the nitromethane to the iodomethane and results in the formation of I^- product anions. Arrhenius tagging is used to study the energetics of the reaction and achieve quenching of the reactive channel. The reaction is discussed in the framework of a vibrationally induced S_N2 reaction.

The infrared spectra of a naphthalene anion clustered with one to six water molecules were measured. The π -system of the naphthalene accommodates the excess electron with a network of water molecules evolving on one side of the naphthalene. It was found that water-water H-bonds are generally more favorable than water-ion π -H-bonds. With three or more water molecules present, the spectra indicate that there is more than one conformation of the water network present.

Dedication

To my parents and my teachers for always pushing me to be a good scientist and an even better person.

Acknowledgements

There have been many people who have helped me on my journey through graduate school. I *must* begin by acknowledging my advisor, Professor J. Mathias Weber for not only thinking I would be a good fit in the graduate program but also in his group. Without his support, teaching and awful puns (at which I have not only laughed but also contributed) I don't think I would have been nearly as productive or enjoyed my graduate experience as much as I have. Mathias has been not only an excellent mentor but also a good friend and there is no way I can thank him enough for all he has done for me.

I must also thank my group members both former and present. Jesse Marcum, Chris Adams and Sydney Kaufman were all present when I joined the lab and were instrumental in making me feel welcome as a group member and as a scientist. They were all patient and helpful while I was learning the ropes of being a graduate student. I learned some of my best lab problem solving and critical thinking skills from them. I must also acknowledge Chris specifically for teaching me how to turn the instrument on and what everything does with respect to "making and shooting ions". Without his guidance and patience with me, even while writing his own thesis, I would not have been as productive as I have been. I have to thank Casey Christopher for his unwavering friendship and willingness to discuss just about everything. It was a pleasure to be his lab mate for three years and friend for longer. I must thank the four undergraduate researchers, Eric Pozzi, Grant Gogul, Caitlin Majlinger and Luke Long, letting me vicariously participate in their research. I wish them all well in their current studies and endeavors. In the last two years I have gotten to know the two newest members of the group, Shuang "Xavier" Xu and Michael Thompson, and in the past year I

have handed over the reins of “my” experiment to Michael. Michael is already proficient with the instrument and, with likely little luck, will easily be more productive than I was. I wish them both the best in their graduate careers and know that there is much success in their futures.

I was fortunate enough to work in within the JILA community. The resources and, in particular, the people I have had the pleasure of meeting and learning from are many and are all appreciated. From learning about electronics to machining techniques to how the purchasing system works and all the time they took to talk to me about various (and potentially off topic) subjects, I am grateful. I also received a lot of support from the Ion Super Group. Professors Veronica Bierbaum, Barney Ellision and Carl Lineberger and their respective groups have given me so much valuable feedback on my research and professional growth. It has been a pleasure meeting and engaging with such a strong group of scientists.

I gratefully acknowledge the grants that have funded this research and my education. All of this research has been funded by grants from the National Science Foundation through either the Career Foundation (CHE-0845618) or the JILA AMO Physics Frontier Center (PHY-1125844 and PHY-0551010). I was further supported by the University of Colorado Department of Chemistry and Biochemistry through Teaching Assistantships.

Lastly I must acknowledge my family and friends. My gratitude for the support and encouragement everyone has given me during my time as a graduate student can not be put into words. In particular all the time my parents spent listening to me rant about research and teaching. Most importantly I have to thank my wife, Anne, for her support and encouragement through this process and for sticking with me through everything.

Contents

Chapter	
1 Introduction and Motivation	1
2 The Experiment	3
2.1 Overview of Experiment	3
2.2 Experimental Details	3
2.2.1 Cluster Generation	3
2.2.2 Time of Flight Mass Spectrometer	7
2.2.3 Laser System	11
2.2.4 Data Collection and Analysis	13
3 Infrared Studies of Metal-(CO ₂) _n Anion Clusters	16
3.1 Introduction	17
3.2 [Au(CO ₂) _n] ⁻ and [Ag(CO ₂) _n] ⁻ Clusters	20
3.2.1 Computational Methods	22
3.2.2 Infrared Spectra of [Au(CO ₂) _n] ⁻ Clusters	23
3.2.3 Infrared Spectra of [Ag(CO ₂) _n] ⁻ Clusters	30
3.3 [Co(CO ₂) _n] ⁻ and [Ni(CO ₂) _n] ⁻ Clusters	41
3.3.1 Computational Methods	43
3.3.2 Infrared Spectra of [Co(CO ₂) _n] ⁻ Clusters	43
3.3.3 Infrared Spectra of [Ni(CO ₂) _n] ⁻ Clusters	55

3.4	Infrared Studies of $[\text{Cu}(\text{CO}_2)_n]^-$ Clusters	65
3.4.1	Computational Methods	65
3.4.2	Infrared Spectra of $[\text{Cu}(\text{CO}_2)_n]^-$ Clusters	66
3.5	Comparison of all Metal- $(\text{CO}_2)_n$ Anion Clusters	74
4	Infrared Studies of $[\text{CoO}(\text{CO}_2)_n]^-$ and $[\text{NiO}(\text{CO}_2)_n]^-$ Clusters	79
4.1	Introduction	79
4.2	Computational Methods	80
4.3	Spectra and Analysis	80
4.3.1	Infrared Spectra of $[\text{CoO}(\text{CO}_2)_n]^-$ Clusters	80
4.3.2	Infrared Spectra of $[\text{NiO}(\text{CO}_2)_n]^-$ Clusters	89
4.4	Conclusions	95
5	Observation of a Vibrationally Induced Electron Transfer Reaction in a Binary Molecular Complex	97
5.1	Introduction	97
5.2	Computational Methods	100
5.3	Results and Discussion	101
5.4	Conclusion	111
6	Infrared Spectra of Naphthalene Water Clusters	112
6.1	Introduction	112
6.2	Computational Methods	114
6.3	Results and Discussion	115
6.3.1	OH Stretching Vibrations	115
6.3.2	CH Stretching Vibrations	130
6.4	Conclusion	131

Bibliography	132
---------------------	-----

Appendix

A Supplementary Material for Chapter 3.2.2	147
--	-----

B Supplementary Material for Chapter 3.3.3	150
--	-----

C Supplementary Material for Chapter 6	154
--	-----

C.1 $[\text{C}_{10}\text{H}_8\cdot\text{H}_2\text{O}]^-$	154
--	-----

C.2 $[\text{C}_{10}\text{H}_8\cdot(\text{H}_2\text{O})_2]^-$	157
--	-----

C.3 $[\text{C}_{10}\text{H}_8\cdot(\text{H}_2\text{O})_3]^-$	160
--	-----

C.4 $[\text{C}_{10}\text{H}_8\cdot(\text{H}_2\text{O})_4]^-$	163
--	-----

C.5 $[\text{C}_{10}\text{H}_8\cdot(\text{H}_2\text{O})_5]^-$	167
--	-----

C.6 $[\text{C}_{10}\text{H}_8\cdot(\text{H}_2\text{O})_6]^-$	173
--	-----

Tables

Table

3.1	Calculated partial charges for the solvation isomers of $[\text{Co}(\text{CO}_2)_4]^-$ presented in Figure 3.19. Isomers 1 - 4 refer to the top to bottom structures presented in Figure 3.19. The column labeled Solvent indicates the amount of partial charge delocalized into the solvent environment. The partial charges are reported in units of e	49
3.2	Calculated partial charges of the core isomers for $[\text{Ni}(\text{CO}_2)_n]^-$. See Figure 3.23 and discussion in the text for additional information on the core structures. The column labeled Solvent indicates the amount of partial charge delocalized into the solvent environment. The partial charges are reported in units of e	63
4.1	Calculated partial charges for the predicted core structures of $[\text{CoO}(\text{CO}_2)_n]^-$ presented in Figures 4.2 and 4.4. The partial charges are reported in units of e	87
4.2	Calculated partial charges for the predicted core structures of $[\text{NiO}(\text{CO}_2)_n]^-$ presented in Figure 4.7. The partial charges are reported in units of e	95
5.1	Experimentally determined and calculated peak positions in cm^{-1} for the dominant vibrational features observed in Figure 5.2. The experimental frequencies are reported for $\text{CH}_3\text{NO}_2^- \cdot \text{CH}_3\text{I}$ with values for $\text{CH}_3\text{NO}_2^- \cdot \text{CD}_3\text{I}$ given in parentheses where observed. Calculated frequencies (see above for discussion) are given for the non-deuterated complex only and are reported in $\text{km} \cdot \text{mol}^{-1}$. The vibrational assignments given are based on structure I in Figure 5.3.	103

Figures

Figure

2.1	Schematic for the entrainment setup. X and Y represent different molecular species and are pulsed into the entrainment region using series 9 General Valves.	6
2.2	Schematic diagram of the laser vaporization setup used to generate metal containing clusters	8
2.3	Schematic of the experimental apparatus including the vaporization source with the electron gun shown for completeness.	9
2.4	Mass spectrum observed using the vaporization source with a cobalt disc and CO ₂ as the carrier gas.	10
2.5	Schematic diagram of the Laservision optical parametric converter setup used for the generation of tunable infrared radiation in these experiments.	13
2.6	Schematic diagram of the multi-pass cell ring reflector used to increase the number of passes of IR light on the mass selected ion packet.	14
3.1	The Walsh diagram for CO ₂	19
3.2	The observed redshift of the antisymmetric CO stretch in CO ₂ when interacting with Au ⁻ and various halides. As is indicated on the graph, the redshift of the antisymmetric stretching frequency of CO ₂ interacting with Au ⁻ is calculated while the other redshifts have been experimentally measured. The redshifts are all with respect to 2349 cm ⁻¹	21

3.3	Experimental spectra of $[\text{Au}(\text{CO}_2)_n]^-$ clusters. The numbers denote the number of CO_2 molecules in the cluster. The right and left panes are individually normalized so they are on different scales. The arrow indicates the predicted frequency of the AuCO_2^- binary complex from the calculations of Boese <i>et al.</i> All spectra were obtained monitoring the loss of a single solvent CO_2	24
3.4	Comparison of the three calculated lowest energy structures for $[\text{Au}(\text{CO}_2)_2]^-$ clusters to the experimental spectrum for $[\text{Au}(\text{CO}_2)_2]^-$. Relative energies are given in meV.	26
3.5	Comparison of the lowest energy structures for $[\text{Au}(\text{CO}_2)_n]^-$ clusters ($n = 3, 4$). Relative energies are given in meV and are with respect to the lowest energy conformer of a given cluster size. Since these structures are all within 60 meV of each other, they are considered to be isoenergetic.	28
3.6	Experimental spectra of $[\text{Ag}(\text{CO}_2)_n]^-$ clusters. The numbers denote the number of CO_2 molecules in the cluster (n). The right and left panes are individually normalized so they are on different scales. All of these spectra were obtained monitoring the loss of a single solvent CO_2 . The dashed lines are meant to guide the eye.	31
3.7	Comparison of the lowest energy structures for $[\text{Ag}(\text{CO}_2)_n]^-$ clusters ($n = 2 - 4$). All reported structures are within 60 meV relative energy of each other for a given cluster size and are considered to be isoenergetic.	33
3.8	Peak positions in the lower energy region (left panel in Figure 3.6) plotted against cluster size. Solid squares represent structures where the terminal solvation position is filled. The open squares represent structures where the terminal solvation position is vacant. Solid circles indicate when the charge carrier is CO_2^-	34
3.9	Comparison of structures exhibiting symmetric solvation around a Ag^- anion for $n = 2 - 4$. The green dotted line is meant to show the red shift trend observed and predicted. The magenta dot-dash line shows the nearly unshifted solvent CO_2 peak corresponding to the existence of a formate type core.	36

- 3.10 Comparison of Ag loss channels for $[\text{Ag}(\text{CO}_2)_4]^-$ (D) and $[\text{Ag}(\text{CO}_2)_5]^-$ (C) to $(\text{CO}_2)_n^-$ clusters exhibiting different core structures (A and B). The feature at 1660 cm^{-1} corresponds to a CO_2^- core while the set of peaks between 1800 cm^{-1} and 2000 cm^{-1} indicates a C_2O_4^- core. 37
- 3.11 Potential energy curve for $[\text{Ag}(\text{CO}_2)_4]^-$ generated by varying the OCO bond angle of the partially reduced CO_2 moiety. The red curve represents the structures as shown. The black curve contains a dielectric continuum corresponding to CO_2 around the shown structures to approximate the effect of increased solvation (see Section 3.2.1 for additional information). A robust second minimum is recovered with the formation of a C_2O_4 species, which is additionally stabilized by the dielectric continuum. The relative energies presented here are not zero-point corrected. 38
- 3.12 Potential energy curve for $[\text{Au}(\text{CO}_2)_4]^-$ generated by varying the OCO bond angle of the partially reduced CO_2 moiety. No second minimum is recovered corresponding to a C_2O_4^- core unlike in $[\text{Ag}(\text{CO}_2)_4]^-$ (see Figure 3.11). The relative energies presented here are not zero-point corrected. 40
- 3.13 Plot of the antisymmetric CO stretching frequency in a formate core against the calculated partial charge localized on the activated CO_2 moiety for an assigned structure (see text). The blue triangles represent $[\text{Ag}(\text{CO}_2)_n]^-$ clusters while the orange squares represent $[\text{Au}(\text{CO}_2)_n]^-$ clusters. The black circle is the antisymmetric stretching frequency of a CO_2^- in a Ne matrix. The solid line is a linear fit of all the points in the plot. The dashed lines represent the maximum charge transfer based on the most red shifted frequency observed. 41
- 3.14 Experimental spectra of $[\text{Co}(\text{CO}_2)_n]^-$ clusters monitoring the loss of one CO_2 . The two regions (1000 cm^{-1} to 2150 cm^{-1} and 2270 cm^{-1} to 2400 cm^{-1}) are individually normalized and are therefore on different scales. Data was not acquired down to 1000 cm^{-1} for larger clusters due to low parent cluster intensity and correspondingly poor daughter anion signal intensity. 44

- 3.15 Comparison of the peak positions for $[\text{Au}(\text{CO}_2)_n]^-$ (top), $[\text{Ag}(\text{CO}_2)_n]^-$ (middle) and $[\text{Co}(\text{CO}_2)_n]^-$ (bottom) clusters. Note that fragmentation is first observed for Au and Ag at $n = 2$ while it not observed until $n = 3$ for Co. 45
- 3.16 Structures of CoCO_2^- for singlet and triplet occupations. The capital letter denotes the core isomer while the subscript indicates a singlet or triplet conformation. Relative energies are given in units of meV. 46
- 3.17 Lowest energy calculated structures for $[\text{Co}(\text{CO}_2)_2]^-$. The letter denotes the core structure while the number in parentheses indicates the number of solvent molecules and the superscript denotes singlet or triplet configuration. Relative energies are given in meV. 48
- 3.18 Comparison of the calculated lowest energy structures for $[\text{Co}(\text{CO}_2)_2]^-$ to the experimental spectrum. The letter denotes the core structure while the number in parentheses indicates the number of solvent molecules and the superscript denotes singlet or triplet configuration. Relative energies are given in meV. 50
- 3.19 Comparison of calculated different solvation isomers around structure ^1E to the experimental spectrum for $[\text{Co}(\text{CO}_2)_4]^-$. Relative energies are given in meV. 51
- 3.20 Comparison of calculated likely minor isomers to the experimental spectrum for $[\text{Co}(\text{CO}_2)_4]^-$. Relative energies are given in meV. 53
- 3.21 Orbitals in the d-block of the $[\text{CO}_2\text{CoCO}_2]$ core ion expected for a “butterfly” ML_4 configuration (left) and a bent ML_2 configuration (center), compared to the calculated molecular orbitals for the singlet core ion structure ^1E (right). Note that the HOMO-3 orbital is not part of the d-block but is shown for completeness. The occupied orbitals are shown as bold horizontal lines for each configuration. Calculated orbital energies are given in eV. The dotted lines show how the d_{z^2} orbital changes from ML_4 to ML_2 and correlation between calculations and ligand field theory. Note that the definition of the z -axis is not along the symmetry axis of the complex but rather is defined by the d_{z^2} character of the HOMO. 54

3.22	Experimental spectra of $[\text{Ni}(\text{CO}_2)_n]^-$ clusters. The numbers indicate the number of CO_2 molecules (n) present in each cluster. The traces on the left and right are individually normalized and are on different scales.	56
3.23	Calculated lowest energy structures for $[\text{Ni}(\text{CO}_2)_n]^-$ clusters. The capital letter indicates the core structure and the number denotes the number of solvent molecules present. Plain text indicates $n = 2$ structures while bold text denotes $n = 3$ structures. Relative energies are reported in meV and are given with respect to the lowest energy structure for a given cluster size. Relative energies for isomers B and G are not reported as there are no structures to compare them with and are shown in <i>italic</i> text.	57
3.24	Comparison of calculated structures for $[\text{Ni}(\text{CO}_2)_3]^-$ to the experimental spectrum for $n = 3$. See Figure 3.23 and text for discussion on the structures. Relative energies are given in meV.	59
3.25	Comparison of various solvation positions around the core isomer E. Note that the predicted spectrum shifts only slightly with varying solvation position. The calculated spectrum of isomer E* is shown on the bottom for completeness.	60
3.26	Calculated vibrational frequencies as a function of cluster size for assigned core structures compared to the experimental peak positions as a function of cluster size (see text for discussion). The letters indicate the core structure giving rise to each set of peaks (see Figures 3.23). The experimental spectrum for $[\text{Ni}(\text{CO}_2)_5]^-$ is shown on top for reference.	62
3.27	A comparison of the combined calculated spectra for isomers E and F to the experimental spectrum of $[\text{Ni}(\text{CO}_2)_2]^-$. Note that while the fit is not ideal, it is reasonable that a multiphoton process could recover the observed experimental spectrum. . . .	64
3.28	Experimental spectra of $[\text{Cu}(\text{CO}_2)_n]^-$. The numbers denote the number of CO_2 molecules in the cluster. All spectra are individually normalized so that the left and right traces are on different scales.	67

- 3.29 Experimental spectra of $[\text{Cu}(\text{CO}_2)_n]^-$ with the three groups of spectral features highlighted (see text for discussion). Numbers denote the number of CO_2 molecules in the cluster. All spectra are individually normalized so that the left and right traces are on different scales. 68
- 3.30 Calculated lowest energy structures for $[\text{Cu}(\text{CO}_2)_n]^-$ ($n = 1$ to 4). The notation is chosen to be consistent with that for $[\text{Co}(\text{CO}_2)_n]^-$ and $[\text{Ni}(\text{CO}_2)_n]^-$ clusters. The letter denotes the core structure and the number/letter combination in parentheses indicates the number of solvent molecules and their positions. The purple box indicates $n = 1$ species, the blue boxes indicate $n = 2$ species, the green boxes indicate $n = 3$ species and the orange box indicates $n = 4$ species. Bare core structures are shown on the top row while solvation isomers are shown in the descending columns. Relative energies are given in meV and are with respect to the lowest energy isomer for a given cluster size. 69
- 3.31 Comparison of calculated structures B(1a), B(1b) and A(1) to the experimental spectrum of $[\text{Cu}(\text{CO}_2)_2]^-$. See Figure 3.30 for relative energies. 70
- 3.32 Plot of the antisymmetric CO stretching frequency in a formate core against the calculated partial charge localized on the activated CO_2 moiety for an assigned structure (see text). The blue triangles represent $[\text{Ag}(\text{CO}_2)_n]^-$ clusters while the orange squares represent $[\text{Au}(\text{CO}_2)_4]^-$ clusters and the red squares represent $[\text{Cu}(\text{CO}_2)_n]^-$. The black circle is the antisymmetric stretching frequency of a CO_2^- in a Ne matrix. The solid line is a linear fit of all the points in the plot. The dashed lines represent the maximum charge transfer observed based on the most red shifted frequency observed. 71
- 3.33 Comparison of calculated structures with a $[\text{Cu}(\text{CO}_2)_2]^-$ core to the experimental spectrum for $n = 3$. See Figure 3.30 for description and relative energies of the structures presented. 73

- 3.34 Comparison of the calculated spectra for different solvation positions around isomers E and G to the experimental spectrum for $[\text{Cu}(\text{CO}_2)_6]^-$. Note that since isomer G is a minor contributor to the experimental spectrum, the features around 1700 cm^{-1} will likely be obscured by the formate signature. See Figure 3.30 for additional information on the structures presented here and text for additional discussion on symmetric and antisymmetric solvation. 75
- 3.35 Spectral shifts of the experimental and simulated features for $[\text{Ni}(\text{CO}_2)_n]^-$ ($n = 3$ to 6). The top trace show the spectrum for $n = 6$ for comparison. The lines are meant to guide the eye and are not a fit of any of the data, the letters indicate the assignments of the core isomers as shown in Figure 3.30. 76
- 4.1 Experimental spectra of $[\text{CoO}(\text{CO}_2)_n]^-$ for ($n = 3 - 8$). The numbers denote the number of CO_2 molecules present in the cluster. The exploratory experimental data for $n = 8$ was truncated after determining that the spectrum was not appreciably evolving as a function of cluster size. The left and right traces are individually normalized and are not on the same scale. 81
- 4.2 Calculated lowest energy structures for $[\text{CoO}(\text{CO}_2)_n]^-$. The capital letter denotes the core structure and superscripts 1 and 3 denote singlet and triplet, respectively. Relative energies are given in meV and are all with respect to isomer ^3A 83
- 4.3 Comparison of calculated core isomers for $[\text{CoO}(\text{CO}_2)_2]^-$ to the experimental spectrum of $[\text{CoO}(\text{CO}_2)_3]^-$. Isomer labels and relative energies are given for each structure. See text for discussion. 85
- 4.4 Calculated lowest energy structures for $[\text{CoO}(\text{CO}_2)_3]^-$. The capital letter denotes the core structure, the superscript 1 and 3 indicate singlet and triplet configurations, and the number/letter combination denote the number and configuration of the solvent molecules. Relative energies are reported in meV. 86

4.5	Comparison of the calculated singlet structures in Figure 4.4 to the experimental spectrum for $[\text{CoO}(\text{CO}_2)_3]^-$. Isomer labels and relative energies are given to the right.	88
4.6	Experimental spectra of $[\text{NiO}(\text{CO}_2)_n]^-$. The numbers indicate the number of CO_2 molecules present. The left and right traces are individually normalized and are on different scales.	90
4.7	Calculated lowest energy structures for $[\text{NiO}(\text{CO}_2)_n]^-$. Structures in the leftmost column are bare core structures while the structures to the right are solvation isomer(s) of the core structures. The letters denote the core structure while the letter/number combination indicate the number of solvent molecules and their orientation around the core. Relative energies for $[\text{NiO}(\text{CO}_2)]^-$ structures are shown in <i>italics</i> , $[\text{NiO}(\text{CO}_2)_2]^-$ are shown in plain text and $[\text{NiO}(\text{CO}_2)_3]^-$ are shown in bold . No relative energy is presented for F(1) since there is no other structure of the form $[\text{NiO}(\text{CO}_2)_4]^-$ to compare it with. All relative energies are reported in meV.	91
4.8	Comparison of calculated structures G(1), H(1) and A to the experimental spectrum of $[\text{NiO}(\text{CO}_2)_2]^-$. See Figure 4.7 for relative energies and text for discussion.	92
4.9	Comparison of calculated structures for $[\text{NiO}(\text{CO}_2)_3]^-$ to the experimental spectrum of $[\text{NiO}(\text{CO}_2)_3]^-$. See Figure 4.7 for relative energies and text for discussion.	94
5.1	Schematic representations of the potential results of vibrational excitation of the bare binary complex (top) and the Ar solvated complex (bottom). R1 refers to Equation 5.1 while R2 refers to Equation 5.2.	100
5.2	Photodissociation action spectra of $\text{CH}_3\text{NO}_2^- \cdot \text{CH}_3\text{I}$ (top trace) and $\text{CH}_3\text{NO}_2^- \cdot \text{CD}_3\text{I}$ (bottom trace) acquired by monitoring the formation of I^- photoproducts. The dashed lines indicate the CH stretching modes attributed to the CH_3I molecule within the complex.	102
5.3	Calculated lowest energy structures for $[\text{CH}_3\text{NO}_2, \text{CH}_3, \text{I}]^-$ complexes. The relative energy for conformation II is with respect to conformation I.	104

- 5.4 Comparison of the experimental spectrum of $\text{CH}_3\text{NO}_2^- \cdot \text{CH}_3\text{I} \cdot \text{Ar}$ to the simulated spectra of calculated conformers I (middle panel) and II (bottom panel). The spectrum of the argon tagged ion is used because it is better resolved compared to the spectrum of the bare ion. Note that the peak at $\sim 2950 \text{ cm}^{-1}$ for conformer I contains two close lying transitions (see Table 5.1) which account for the splitting observed in the experimental spectrum. 105
- 5.5 Experimental spectra of $\text{CH}_3\text{NO}_2^- \cdot \text{CH}_3\text{I} \cdot \text{Ar}_n$ ($n = 0 - 3$). The different colors of the spectra indicate a change in the photofragmentation channel. The red curves are monitoring charge transfer and the subsequent formation of I^- photoproducts (see R1 in Figure 5.1) while the blue curves are monitoring Ar evaporation (see R2 in Figure 5.1). Note that both channels are observed for $n = 2$ 107
- 5.6 Schematic representation of the potential energy surface along the reaction coordinate of dissociative electron transfer from CH_3NO_2^- to CH_3I (energies are to scale). (a) Adiabatic electron affinity of CH_3NO_2 (172 meV). (b) Binding energy of the $\text{CH}_3\text{NO}_2^- \cdot \text{CH}_3\text{I}$ entrance channel complex (490 meV, calculated for conformation I). (c) Estimated lower limit of the barrier height for the electron transfer reaction (230 meV, experimentally determined from Ar solvation). (d) Relative energy of the exit channel complex for structure III (500 meV, solid curve) and structure IV (~ 1150 meV, dashed curve). The dashed line represents the $\text{S}_{\text{N}}2$ product. (e) Exit channel asymptote for the formation of I^- and neutral products based on the two possible exit channel complexes. The solid curve is based on the heat of reaction for dissociative electron attachment to CH_3I (620 meV). The dashed curve represents the $\text{I}^- + \text{CH}_3\text{NO}_2\text{CH}_3$ asymptote (~ 1550 meV). 108

- 5.7 Calculated potential energy curve (top) and charge on the iodine atom (bottom) as a function of the CI bond distance. The full squares in the top trace are calculated with only the CI bond distance fixed, letting all other molecular coordinates relax. The open diamonds represent calculations where the out-of-plane angle of the methyl group of the CH₃I molecule (θ_{oop}) was fixed at 10.0°, corresponding to the geometry at a CI bond distance of ~ 2.575 Å in the unrestricted calculation. The open squares are data points calculated with the same angle (θ_{oop}) fixed at 5.5°, corresponding to the geometry at 2.625 Å CI bond distance in the unrestricted calculation. We note that θ_{oop} changes very rapidly as the transition state is approached. The resulting approximated diabatic potential energy curves are shown as dashed lines in the inset of the top panel; the structures shown as insets from left to right represent the entrance channel, transition state, and exit channel geometries, respectively. 110
- 6.1 Experimental spectrum and calculated spectra of [Np·(H₂O)]⁻. Top trace is the experimental spectrum of [Np·(H₂O)]⁻·Ar₈ acquired by monitoring the loss of 6 Ar atoms. Bottom traces are calculated conformers and their predicted infrared spectra. The dashed lines are meant to show ionic π -H-bonds. 116
- 6.2 Observation of vibrational autodetachment in [Np·(H₂O)]⁻·Ar_{*m*} clusters. Top trace: *m* = 4, monitoring the loss of all 4 Ar atoms. Center trace: *m* = 5, monitoring the loss of all 5 Ar atoms. Bottom trace: *m* = 8, monitoring the loss of 5 Ar atoms. Note that the loss of 6 Ar atoms (shown in Figure 6.1) yields the same spectrum as the loss of 5 Ar atoms. 119
- 6.3 Experimental spectrum and calculated spectra of [Np·(H₂O)₂]⁻. Top trace is the experimental spectrum of [Np·(H₂O)₂]⁻·Ar₂ acquired by monitoring the loss of 2 Ar atoms. Bottom traces are calculated conformers and their predicted infrared spectra. The dashed lines show the hydrogen bonds. 121

- 6.4 Experimental spectrum and calculated spectra of $[\text{Np}(\text{H}_2\text{O})_3]^-$. Top trace is the experimental spectrum of $[\text{Np}(\text{H}_2\text{O})_3]^- \cdot \text{Ar}_8$ acquired by monitoring the loss of 5 Ar atoms. Bottom traces are calculated conformers and their predicted infrared spectra. The second trace from the top is a combination of conformers 3-1 and 3-2. The dashed lines show the hydrogen bonds. 123
- 6.5 Experimental spectrum and calculated spectra of $[\text{Np}(\text{H}_2\text{O})_4]^-$. Top trace is the experimental spectrum of $[\text{Np}(\text{H}_2\text{O})_4]^- \cdot \text{Ar}_2$ acquired by monitoring the loss of 2 Ar atoms. Bottom traces are calculated conformers and their predicted infrared spectra. The dashed lines show the hydrogen bonds. 126
- 6.6 Experimental spectrum and calculated spectra of $[\text{Np}(\text{H}_2\text{O})_5]^-$. Top trace is the experimental spectrum of $[\text{Np}(\text{H}_2\text{O})_5]^- \cdot \text{Ar}_2$ acquired by monitoring the loss of 2 Ar atoms. Bottom traces are calculated conformers and their predicted infrared spectra. The dashed lines show the hydrogen bonds. 127
- 6.7 Experimental spectrum and calculated spectra of $[\text{Np}(\text{H}_2\text{O})_6]^-$. Top trace is the experimental spectrum of $[\text{Np}(\text{H}_2\text{O})_6]^- \cdot \text{Ar}_2$ acquired by monitoring the loss of 2 Ar atoms. Bottom traces are calculated conformers and their predicted infrared spectra. The dashed lines show the hydrogen bonds. 129
- A.1 Calculated infrared spectra in the region of the partially reduced antisymmetric CO stretch of the formate core for $[\text{Au}(\text{CO}_2)_4]^-$ clusters. The experimental spectrum for $[\text{Au}(\text{CO}_2)_4]^-$ is shown in the top panel. The calculated spectra are shown in the lower panels with their corresponding structures and relative energies given to the right. Calculated OCO bond angles range from 139.3° to 142.6° for the bonded CO_2 moiety and 175.2° to 178.0° for the solvent CO_2 molecules. 148

- A.2 Calculated infrared spectra in the region of the partially reduced antisymmetric CO stretch of the formate core for $[\text{Au}(\text{CO}_2)_5]^-$ clusters. The experimental spectrum for $[\text{Au}(\text{CO}_2)_5]^-$ is shown in the top panel. The calculated spectra are shown in the lower panels with their corresponding structures and relative energies given to the right. Calculated OCO bond angles range from 139.3° to 142.6° for the bonded CO_2 moiety and 175.2° to 178.0° for the solvent CO_2 molecules. 149
- B.1 Calculated spectra of bare core isomers for $[\text{Ni}(\text{CO}_2)_2]^-$ clusters. All of the isomers presented here are discussed in Chapter 3.3.3. 151
- B.2 Additional calculated spectra of bare core isomers for $[\text{Ni}(\text{CO}_2)_n]^-$ clusters. Isomers B and F are discussed in Chapter 3.3.3. Isomers H and I were determined not to contribute to the experimental spectra and were not included in the discussion. . . . 152
- B.3 Estimated barrier height for the conversion of isomer E^* to D. Due to the barrier height, we do not expect this isomer conversion process to occur in our experiment. . . 153

Chapter 1

Introduction and Motivation

Ions are ubiquitous to chemistry. They are part of many chemical systems from crystalline lattices to interstellar species to chemical reaction intermediates. [1–3] Because of the charged nature of ions, they exhibit different behavior than their neutral analogs in many chemical settings. One area of chemistry where the differences between ions and neutrals is most noticeable is when studying solvation effects. Solvation is present in many chemical reactions where the products and the efficiency of the reaction can be dependent on the identity of the solvent species. Solvent can sometimes interact with ions in predictable ways like the δ^+ H atoms orienting toward the Cl^- anions and the δ^- O atoms to the Na^+ cations when NaCl is dissolved in water. Other times the solvent-ion interactions are less predictable. For example, when solvating SF_6^- with H_2O , the first water molecule makes a hydrogen bond to one of the F atoms localizing the excess charge on the interacting F atom. When a second water molecule is added, it hydrogen bonds to the same F atom rather than solvating any of the F atoms of the SF_6^- anion or forming a water-water hydrogen bond. [4] By studying the structure and charge distribution of gas phase anionic complexes, we can understand the molecular level interactions. By also investigating solvation effects on anionic complexes, understanding the role of solvent on a molecular level can be improved.

The study of molecular level properties of ionic systems *in situ* is difficult due to complications such as speciation, short lifetimes and low concentrations of chemically relevant transient species. These issues can be avoided by performing experiments on cluster anions *in vacuo* rather than in solution. There are a number of techniques that can be used for the generation of gas

phase clusters. These techniques allow for control over the composition of the cluster species and the solvation environment. These advantages grant the ability to generate and study spectroscopically model chemical systems. An attractive method of study is infrared spectroscopy. Within the molecular vibrations are encoded the structure and charge distribution of the species being probed. The effects of solvation on these properties are included within the evolution of the spectra as the solvent environment changes. If the solvation environment can be made large enough, measurements of or extrapolation to behavior in bulk solution is possible. [5, 6] Using computational chemistry to simulate the structures, vibrations and charge distributions of clusters can be a powerful complement to infrared spectroscopy. These two techniques used in tandem can identify structures and the effects of solvation on the core charged species.

This thesis focuses on the interactions of two different species in the presence of an excess electron and how solvation by various solvents affects those interactions. Chapter 2 details the experimental apparatus and techniques used to study gas phase anionic clusters. Due to the low concentrations of anions in mass selected ion beams, direct absorption infrared spectroscopy is not feasible. Instead infrared photodissociation spectroscopy is used to take spectra of the clusters. Chapter 3 presents the study of five different transition metal anions interacting with multiple CO_2 molecules. These results are generalized into trends of the observed charge carrier and the effects of solvation by CO_2 on the charged species. These clusters are treated as model systems for single atom catalysts for the reduction of CO_2 . Chapter 4 is an extension of Chapter 3 where the structural motifs of two different transition-metal oxide anions solvated by CO_2 are presented. The last two Chapters (5 and 6) deviate from metal containing clusters. Chapter 5 presents a vibrationally induced charge transfer reaction in a bimolecular system, while Chapter 6 looks at the interaction of 1 - 6 H_2O molecules with a naphthalene anion and can be viewed as a model system for the wetting of graphene.

All of the studies discussed in this thesis were accompanied by density functional theory calculations. However, since the parameters of the calculations are different for each study, the computational details will be presented and discussed in the corresponding Chapter or Section.

Chapter 2

The Experiment

2.1 Overview of Experiment

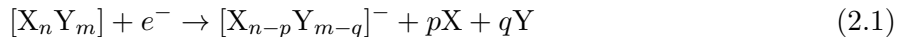
In general, the experimental setup generates gas phase cluster anions that are mass selected and probed with tunable infrared radiation. The setup is based on a design by Lineberger and coworkers. [7] Clusters are generated by entrainment of either laser vaporization or pulsed gaseous species into a supersonic expansion of a carrier gas (here either Ar or CO₂). The anionic clusters are then accelerated perpendicular to the propagation direction of the expansion into a Wiley McLaren time of flight mass spectrometer where they are mass selected based on their mass to charge ratio. A single cluster size is then irradiated by the tunable output of a optical parametric converter. The generation of daughter fragment ions is monitored as a function of photon wavelength resulting in an infrared photodissociation action spectrum. The experiment operates at a repetition rate of 20 Hz.

2.2 Experimental Details

2.2.1 Cluster Generation

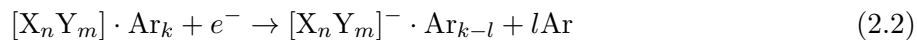
There are a number of ways to form gas phase molecular clusters. One of the most common ways is to use pulsed supersonic expansions of gas phase species to create cold molecular clusters *in vacuo*. Depending on the expansion gases used, their stagnation pressures and the mechanical shape of the nozzle as well as different expansion conditions, a variety of cluster species can be

formed. Electron bombardment of these clusters with high energy electrons ($E_{KE} \sim 800$ eV) can ionize molecules in the expansion creating slow secondary electrons. These slow secondary electrons can then attach themselves to a molecular cluster forming (through evaporative cooling) anionic molecular clusters (see eqn. 2.1).



Alternatively, the electrons could attach themselves to an individual molecule generating an anion that can then go on to collide with other molecular species in three-body collisions. These species can then bind to the anion creating clusters. A cluster such as $[X_n Y_m]^-$ can further be solvated in a noble gas such as Ar, Ne or Kr forming a species of the form $[X_n Y_m]^- \cdot Ar_k$. If a molecular cluster is formed prior to electron attachment, the electron binding energy must be dissipated upon electron attachment. This can occur in a number of ways. If the cluster constituents are bound by more than the binding energy of the electron, then the cluster will remain intact but will be considered a “hot” cluster. Here the energy released will be stored in vibrational or rotational motion or electronic excitation. Without a way for the energy to dissipate from the cluster, it is likely that the excess electron will be ejected again and the anion will not survive. If there are components bound to the cluster by less than the binding energy of the excess electron, they will likely be evaporated to dissipate the energy of attachment. This has been described before as an evaporative ensemble, [8] where the energy will dissipate through evaporative cooling until there is not enough internal energy remaining to “boil off” the most weakly bound remaining cluster constituent. The internal energy of the cluster can be approximated to be roughly of the order of the binding energy of the last molecule that was evaporated. Since the internal cluster temperature is proportional to the binding energy of the weakest bound constituent, solvation with noble gas atoms generally leads to colder clusters, as they have lower binding energies. In turn, colder clusters tend to exhibit more well resolved spectra, simplifying data analysis and potentially allowing for the detection of previously unobservable features. The process of electron attachment to an Ar

solvated molecular cluster is given in equation. 2.2.



The general experimental setup used in all of the experiments described here is based on a design by Lineberger and co-workers [7] and has been described extensively by Weber. [9] For these experiments two different source setups have been used to generate the clusters of interest.

2.2.1.1 Pulsed Valve Entrainment

In the first configuration of the ion source, two Series 9 General Valves are used to introduce a molecular species of interest into an entrainment block (see Figure 2.1). After the entrained gases are allowed to mix for 1 to 10 msec, a supersonic expansion of a carrier gas (Ar or CO₂) generated by an Even-Lavie pulsed valve [10] creates a supersonic expansion through the entrained gas mixture. During the entrainment process, the species X and Y are pulled (entrained) into the expansion of carrier gas (this is shown by the red arrows in Figure 2.1). [7,11] The expansion propagates out of the entrainment block and into the source chamber. As the expansion propagates, collisions of the species within the expansion result in collisional cooling and aggregation into molecular or ionic clusters. The propagation distance is approximately 5 cm and can be varied by a few millimeters. Changes to this distance affect the amount of time the expansion can propagate, which affects the composition of the clusters formed. The expansion is bombarded with a high energy (800 - 1000 eV) beam of electrons generated from a resistively heated tungsten filament. The beam of electrons is focused into the high density region of the expansion using an Einzel lens, electrostatic deflectors and a ring magnet. The resulting electron impact plasma contains slow secondary electrons which can attach to individual molecules or molecular clusters generated by the expansion. The timing of the gas pulses is controlled by a Quantum Composers delay pulse generator. Pressures in the source chamber are typically on the order of low 10⁻⁶ mbar to 1 × 10⁻⁴ mbar. This pressure range is measured by a nude Bayard Alpert ion gauge where the chamber is being evacuated by a 1000 L·s⁻¹ TURBOVAC 1000c turbomolecular pump and a ~2500 L·s⁻¹ Edwards diffusion pump.

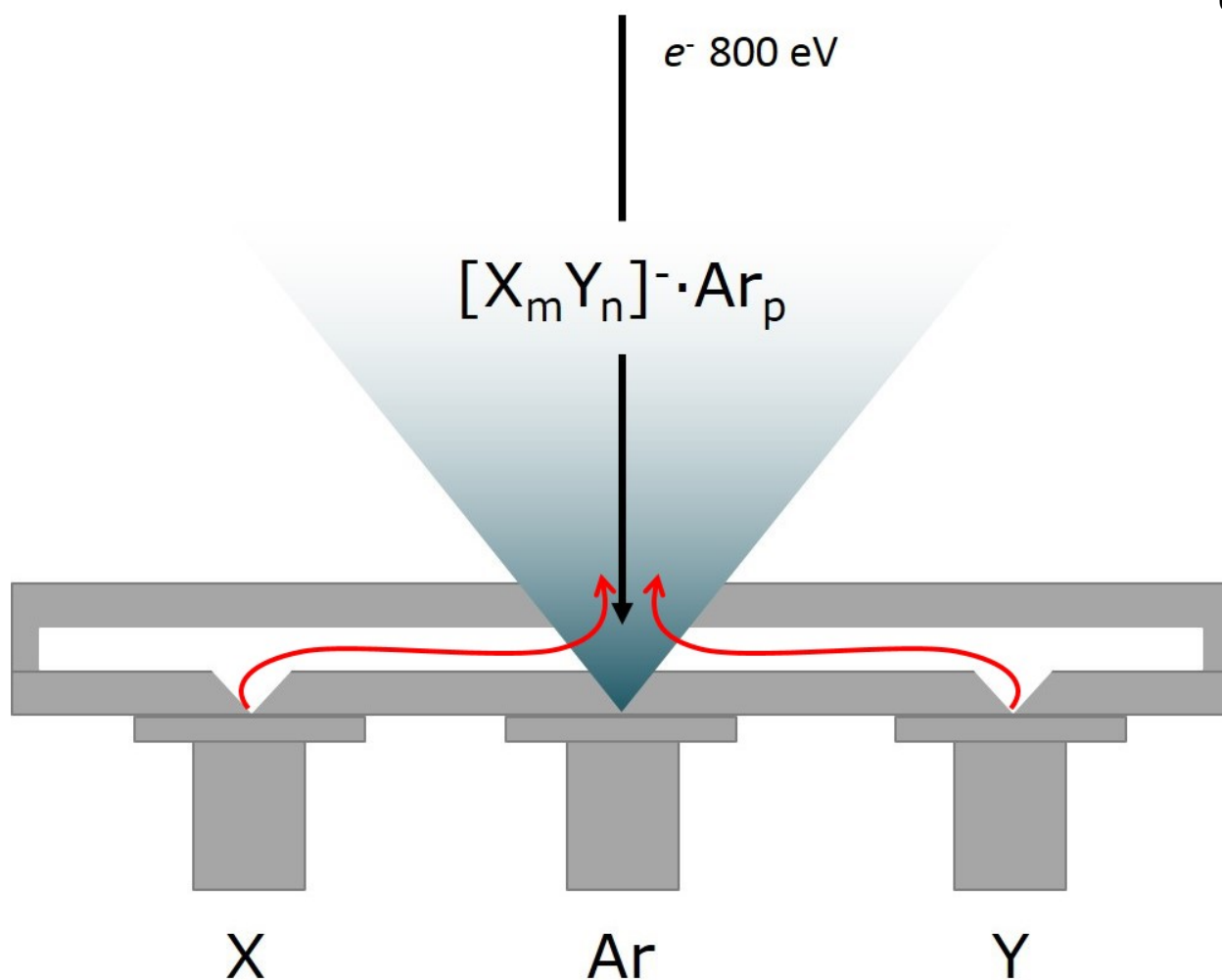


Figure 2.1: Schematic for the entrainment setup. X and Y represent different molecular species and are pulsed into the entrainment region using series 9 General Valves. The red arrows denote the general trajectories of the entrained species (here X and Y) into the carrier gas expansion. The carrier gas (argon) is pulsed out using an Even-Lavie pulsed valve. The black arrow represents the trajectory of the high energy electron beam.

This ion source setup was used to generate Ar-tagged nitromethane-iodomethane clusters $((\text{CH}_3\text{NO}_2)^- \cdot \text{CH}_3\text{I} \cdot \text{Ar}_n)$ and naphthalene-water clusters $([\text{Np}(\text{H}_2\text{O})_n]^- \cdot \text{Ar}_m)$ discussed in Chapters 5 and 6, respectively.

2.2.1.2 Laser Vaporization

The previously described entrainment setup is unable to easily generate molecular clusters containing metal atom(s) due to the exceptionally low vapor pressure of most metals. To circumvent this issue, laser vaporization is employed to create metal vapor. In this case, one of the General Valves present in the entrainment setup is replaced with a rotating metal rod driven by a DC motor. A metal disc is then mounted to the end of the rod as shown in Figure 2.2. The third harmonic of a nanosecond pulsed Nd:YAG laser (355 nm) is used to vaporize material from the edge of the rotating metal disc. By rotating the disc, generally even wear across the edge of the disc is achieved resulting in a more stable ion beam. The vaporization occurs about 1.5 cm off to the side of the Even-Lavie valve nozzle (see Figure 2.2). Within 300 to 500 μ seconds of the vaporization laser firing, a supersonic expansion of CO₂ is generated from the Even-Lavie valve (stagnation pressure typically 5.5 bar). In this source configuration, the vaporization process already creates a sufficient quantity of slow secondary electrons so the electron gun is not required for anion cluster formation. The vaporization setup typically results in the formation of metal-(CO₂)_n⁻ clusters as well as pure (CO₂)_n⁻ clusters, metaloxide-(CO₂)_n⁻ clusters and some dimetal-(CO₂)_n⁻ clusters for cobalt and nickel. The timing of the gas pulse and the vaporization laser pulse are controlled by synchronized Quantum Composer pulse delay generators.

2.2.2 Time of Flight Mass Spectrometer

In both laser vaporization and entrainment setups, clusters with anionic, cationic and neutral charges are produced. To separate out only the anionic species, the source chamber is set up to work in tandem with a time of flight mass spectrometer. After the molecular beam has propagated into the acceleration region of the time-of-flight mass spectrometer, it is accelerated perpendicular to the direction of propagation by two electrostatic reflectors operating in a Wiley-McLaren field configuration (see Figure 2.3). This is done by pulsing two plates to -4000 V (repeller) and -2800 V to -3300 V (extractor). This accelerates the anionic species into the flight tube with the same

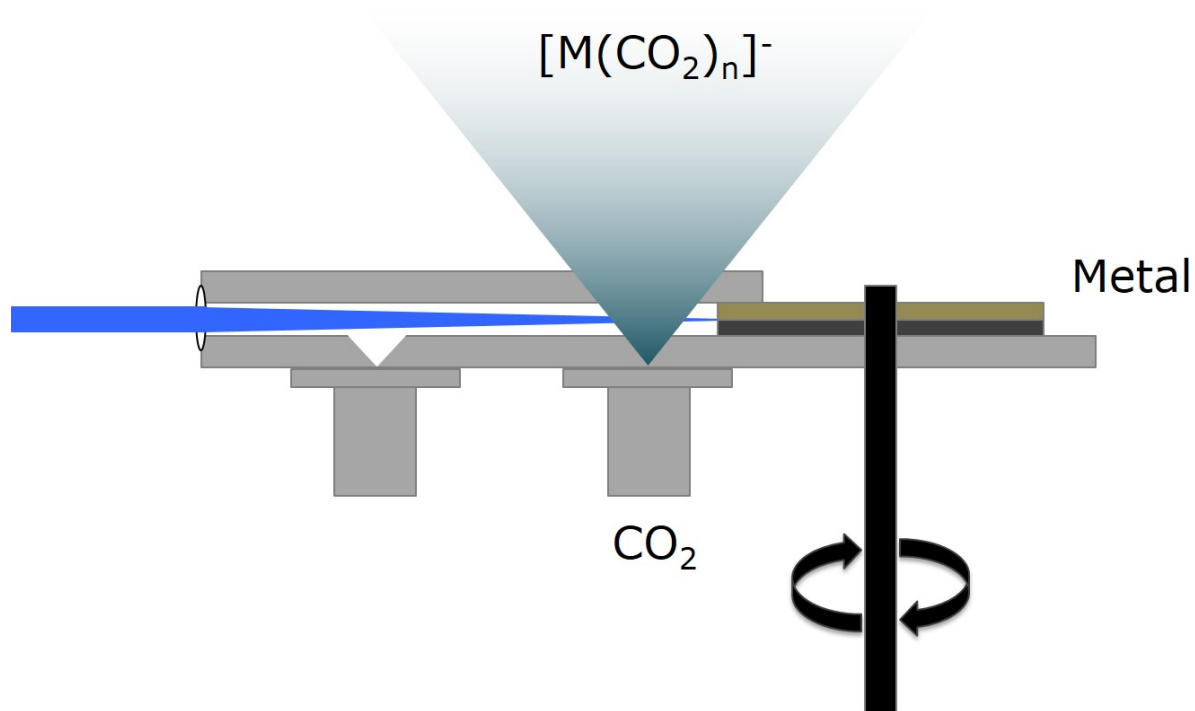


Figure 2.2: Schematic for the laser vaporization entrainment source. Here, one of the General Valves in Figure 2.1 is replaced with the rotating metal disc (see text). The laser enters on the left hand side of the setup and is focused onto the edge of the metal disc using a small lens. The metal vapor is expanded in a supersonic expansion of CO_2 . No electron beam was required in these experiments.

average kinetic energy and allows for the spatial focusing of ions with the same mass to charge ratio at the first space focus, whose position is controlled by the voltage on the extractor plate. The first spatial focus is at the laser interaction region (see Figure 2.3). The ion beam is steered through the flight tube by two sets of electrostatic reflectors and an Einzel lens. The ion beam is then reversed and refocused onto a multichannel plate (MCP) detector using a reflectron secondary mass analyzer. Typical pressures in the flight tube are on the order of 10^{-8} mbar yielding a mean free path on the order of 10^4 meters. The total ion trajectory length is approximately 3 meters.

Since all of the anionic species generated in the source are given the same kinetic energy in the same direction from nearly the same starting point and they all have the same distance to travel to the detector, their flight time and mass to charge ratio are related as follows (for species

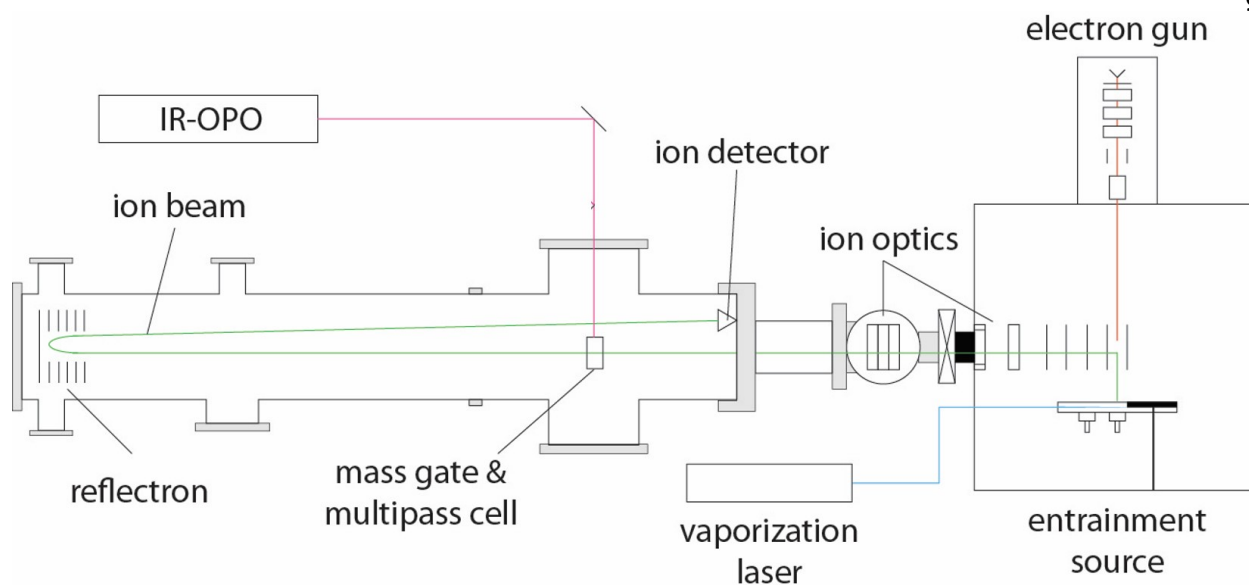


Figure 2.3: Schematic of the experimental apparatus including the vaporization source with the electron gun shown for completeness. The green line indicates the ion beam trajectory and all essential parts of the apparatus are labeled and discussed further in the text.

of the same charge):

$$\frac{t_1}{t_2} = \sqrt{\frac{m_1}{m_2}}. \quad (2.3)$$

Assuming that all ions are singly charged, the mass of all the constituents of the ion beam can be identified. With the masses known and the precursor species used in the expansion known, the chemical composition of the mass peaks can be determined. As an example, Figure 2.4 shows a portion of the mass spectrum acquired using a cobalt disc as a vaporization target. We are able to identify progressions owing to $(\text{CO}_2)_n^-$ clusters, $[\text{Co}(\text{CO}_2)_n]^-$ clusters and nearly overlapping $[\text{CoO}(\text{CO}_2)_n]^-$ and $[\text{Co}_2(\text{CO}_2)_{n-1}]^-$ clusters. Mass peaks corresponding to the formation of dianions were not observed in any of the studies presented. The mass resolution of the mass spectrometer ($\frac{m}{\Delta m}$) is on the order of 500.

Following identification of the mass peaks in the ion beam, a mass gate can be used to select a small mass window ($\frac{m}{\Delta m} \approx 15$) for spectroscopic interrogation. The mass gate operates

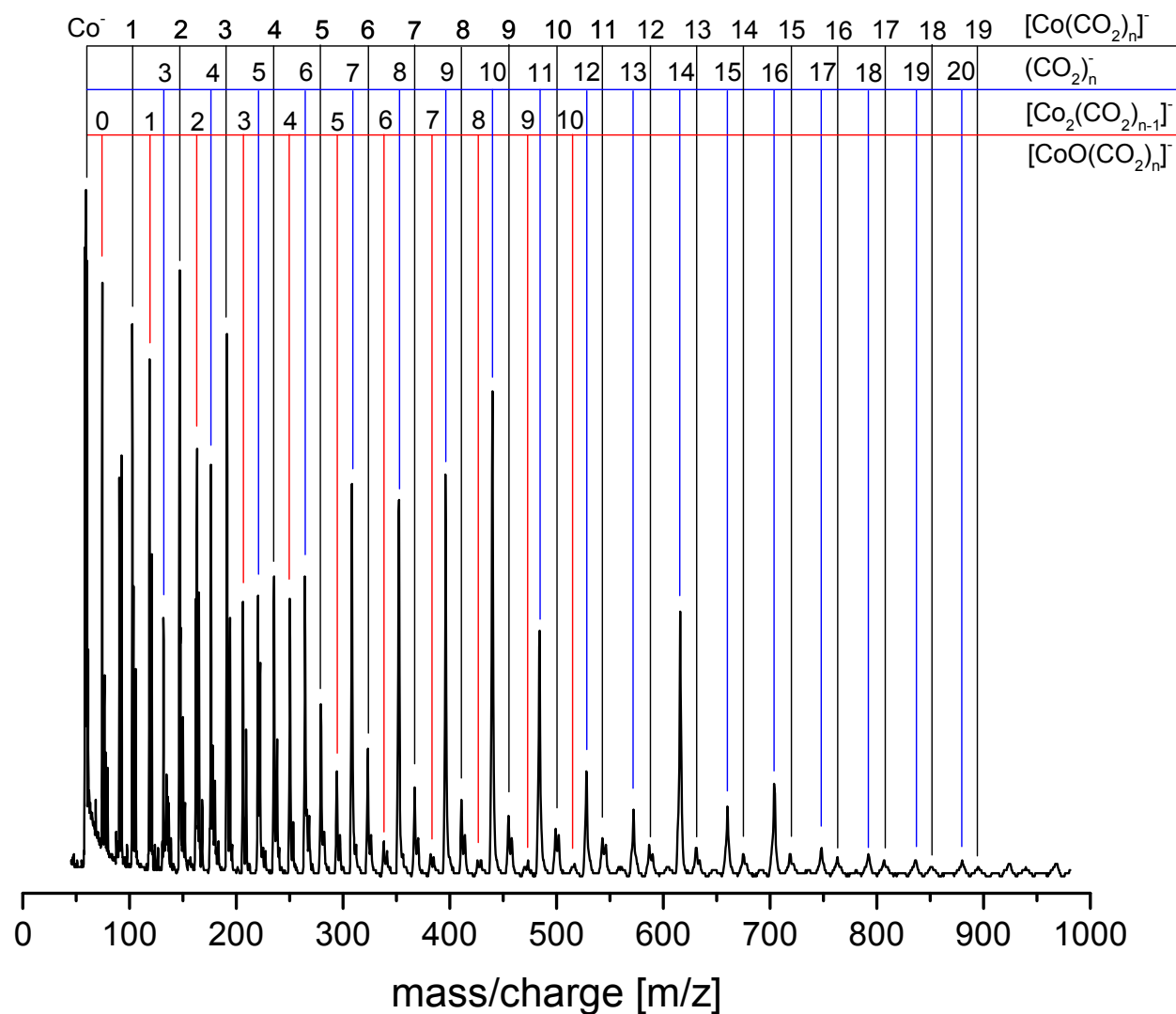
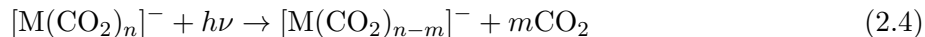


Figure 2.4: Mass spectrum observed using the vaporization source with a cobalt disc and CO₂ as the carrier gas.

by generating an electric field on a charged set of plates that disrupts the flight path of the ion beam. By switching the field to zero for an appropriate time window ($\sim 1 \mu\text{sec}$), a selected cluster size range is allowed to continue on the normal ion beam trajectory. The plates are then recharged and the remainder of the ion beam is deflected. The timing of the mass gate is controlled by a Quantum Composer delay pulse generator.

Absorption of an infrared photon results in excitation of a vibrational mode in the cluster.

Through anharmonic coupling and the resulting intramolecular vibrational relaxation, the energy of the initially excited vibrational state is redistributed over the cluster constituents. If enough energy is absorbed, a species possessing a lower binding energy than that of the absorbed photon can dissociate. If dissociation occurs prior to the ions reaching the reflectron, the lighter daughter ions will be turned around and impinge on the detector earlier than the undissociated parent ions. The reflectron voltage can then be scaled to the ratio of the daughter mass divided by the parent mass to allow unambiguous assignment of the daughter species. The generation of daughter ions can be detected as a function of the laser wavelength yielding an infrared photodissociation spectrum of the parent cluster (see equation 2.4 as an example of photodissociation of a metal-(CO₂)_n⁻ cluster ion).



In summary, the order of events for cluster generation followed by interrogation by tunable IR light is as follows: 1.) General Valves emit gas into the entrainment block/Vaporization laser fires creating metal vapor 2.) Carrier gas is expanded out of the Even-Lavie valve 3.) Anionic clusters are accelerated into the Time-of-Flight mass spectrometer 4.) A small mass range of ions is transmitted using a mass gate 5.) The selected anions are irradiated by tunable IR light 6.) Remaining parent and newly formed daughter anions are turned around by the Reflectron and impinge upon a MCP detector

2.2.3 Laser System

The mass selected ions are irradiated by the tunable output of a LaserVision OPO/OPA (optical parametric oscillator/optical parametric amplifier) system with an additional difference frequency mixing stage, operating in the range of 600 cm⁻¹ to 4400 cm⁻¹. The OPO/OPA system is pumped by approximately 500 mJ of 1064 nm light generated from an Innolas Spitlight 600 Nd:YAG laser operating at 20 Hz with a pulse duration of 7 ns. This laser system has two scanning regions, mid IR and far IR. The mid IR region is from 2260 cm⁻¹ to 4400 cm⁻¹. Light in this

wavenumber range is generated by doubling part of the 1064 nm pump radiation, generating 532 nm light. The 532 nm light is then converted into signal and idler waves by two KTP crystals in the oscillator part of the OPO (see Figure 2.5 and equation 2.5). Since signal and idler have orthogonal polarizations, the signal wave is rejected by a polarizer while the idler wave is allowed to oscillate. The idler wave then exits the OPO resonator, its beam profile rotated 90° by a dove prism, and overlapped with the rest of the 1064 nm light in the OPA, which consists of a chain of four KTA crystals. Difference frequency mixing of the idler wave and the 1064 nm pump light results in the generation of mid IR light in a wavenumber range of 2260 cm⁻¹ to 4400 cm⁻¹ (see equation 2.6).

$$2 \times \nu_{1064} = \nu_{\text{signal}} + \nu_{\text{idler}} \quad (2.5)$$

$$\nu_{1064} - \nu_{\text{idler}} = \nu_{\text{mid IR}} \quad (2.6)$$

$$\nu_{\text{idler}} - \nu_{\text{mid IR}} = \nu_{\text{far IR}} \quad (2.7)$$

The far IR tuning range is from 600 cm⁻¹ to 2150 cm⁻¹. Light in this range is generated by difference frequency mixing of the mid IR output with the amplified idler wave (see equation 2.7). The output power of the OPO/OPA is between 5 mJ and 20 mJ of mid IR light and 10 μJ to 100 μJ of far IR light depending on the wavelength of the photons being generated. The bandwidth of the laser system is 2 cm⁻¹.

Irradiation occurs in a multi-pass cell based on a design by Liu and coworkers (see Figure 2.6). [12] The multi-pass cell is made out of OFHC copper for high IR reflectivity and allows adjustment of the number of passes of the laser across the ion beam from 1 to 14 (estimated). The multi-pass cell can be rotated, which allows the user to choose the number of passes. Irradiating the ion packet with multiple passes of the IR light generates additional fragment ions compared to only one pass of the IR light and improves the signal to noise ratio of single scans by up to a factor of four. The ability of the cell to rotate provides a convenient way to test for multiphoton processes by reducing the number of passes such that the intensity of a peak attributed to a single

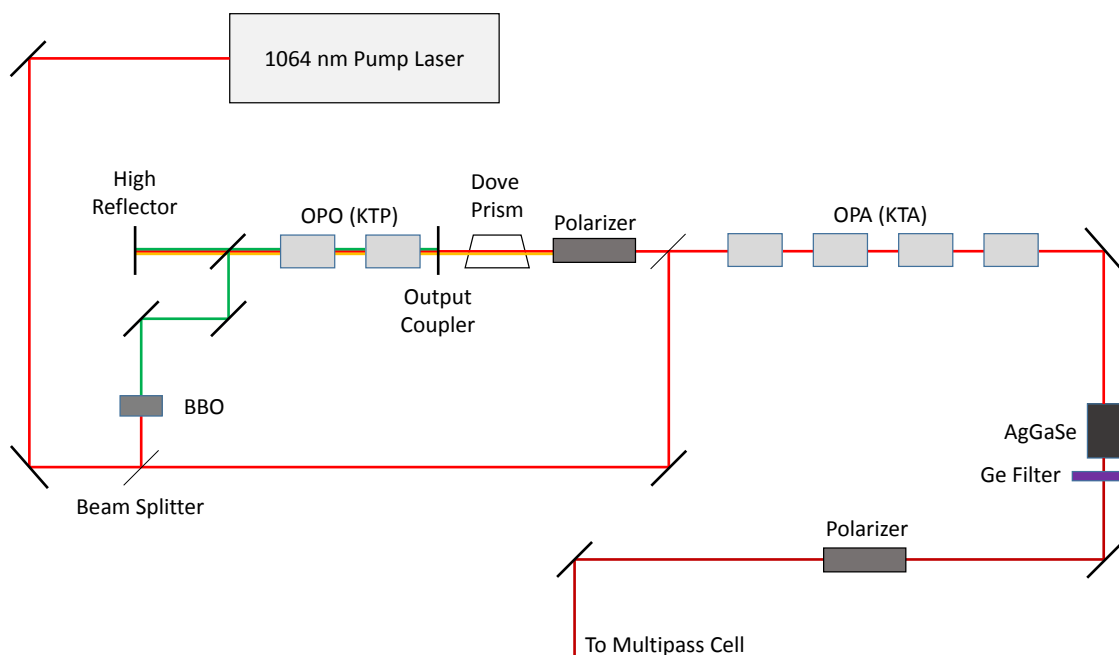


Figure 2.5: Schematic diagram of the Laservision optical parametric converter setup used for the generation of tunable infrared radiation in these experiments.

photon process is reduced by half. We can then monitor the intensities of all the other peaks in our spectra. All other single photon process will also reduce by half while any multiphoton process will reduce by $\frac{1}{N^2}$ where N is the number of photons in the process. This test was performed for all of the metal- $(\text{CO}_2)_n^-$ and metal-oxide- $(\text{CO}_2)_n^-$ cluster studies.

2.2.4 Data Collection and Analysis

Spectra are collected by centering a Tektronics TDS 2022 digital oscilloscope on a fragment peak. The time window of the oscilloscope is adjusted so that it is nearly the same width as the mass peak (~ 100 nsec). The average signal in the active window is recorded by the oscilloscope and averaged for a different number of laser shots depending on the scanning rate (discussed below). A LabVIEW program reads out the averaged signal and records it while the laser is scanned. There are on average between 100 and 1000 parent ions per shot for a given cluster species with

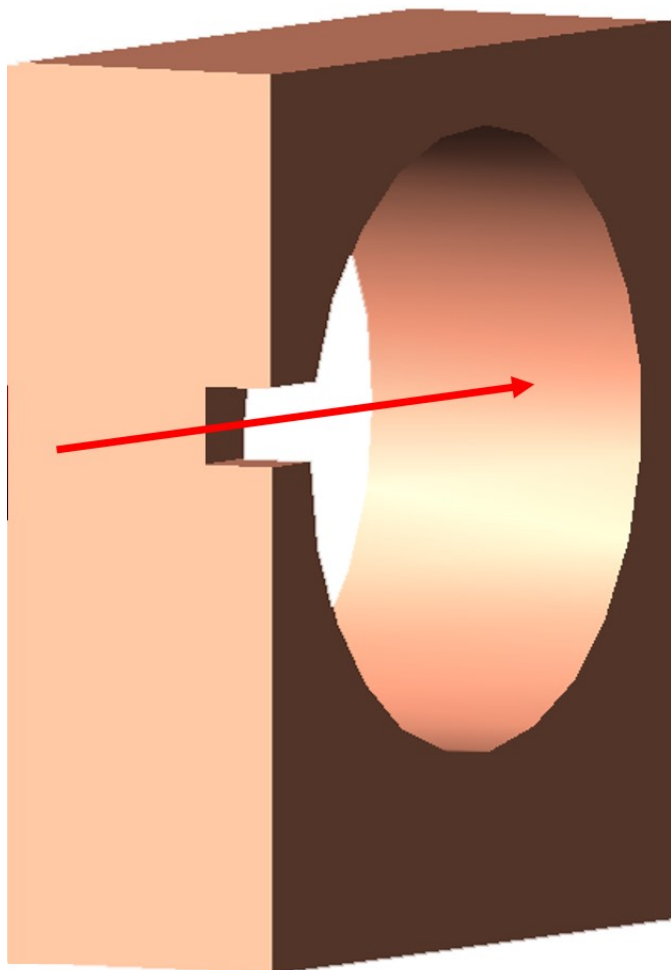


Figure 2.6: Schematic diagram of the multi-pass cell ring reflector used to increase the number of passes of IR light on the mass selected ion packet. See text for discussion.

larger clusters and metal containing clusters having lower parent ion intensities compared to other species. Photodissociation efficiency is around 5% meaning that there are at most ~ 50 daughter ions generated. Due to this low number of fragment anions, the individual spectra acquired can exhibit a poor signal to noise ratio. The spectra are collected in $\sim 1 \text{ cm}^{-1}$ steps averaging 16 shots (fast mode) or 64 shots (slow mode) of the experiment over a specified tuning range. The slow scanning rate yields a higher signal to noise ratio on individual scans but leads to data acquisition times that are four times longer compared to the fast scanning rate.

A number of spectra are taken for a given cluster species and fragmentation channel over

multiple days and averaged into one spectrum. This is done to improve the signal to noise ratio of the average spectrum and ensure reproducibility from day to day. On average, 10 to 20 individual spectra are averaged together. Each individual spectrum acquired by monitoring the generation of daughter ions is corrected for background signal. The final average spectrum is both corrected for laser fluence by measuring the output power of infrared light as a function of frequency and calibrated using an Ocean Optics HR2000+ spectrometer to measure the wavelength of the signal wave. All data analysis is carried out within the OriginLab program.

Chapter 3

Infrared Studies of Metal-(CO₂)_n Anion Clusters

This Chapter has been reproduced in part with permission from the following previously-published articles:

Knurr, B. J., Weber, J. M., “Solvent-Driven Reductive Activation of Carbon Dioxide by Gold Anions.” *Journal of the American Chemical Society*, 2012. 134: p. 18804 - 18808. DOI: 10.1021/ja308991a. Copyright 2014 American Chemical Society.

Knurr, B. J., Weber, J. M., “Solvent-Mediated Reduction of Carbon Dioxide in Anionic Complexes with Silver Atoms.” *Journal of Physical Chemistry A*, 2013. 117: p. 10764 - 10771. DOI: 10.1021/jp407646t. Copyright 2014 American Chemical Society.

Knurr, B. J., Weber, J. M., “Infrared Spectra and Structures of Anionic Complexes Cobalt with Carbon Dioxide Ligands.” *Journal of Physical Chemistry A*, 2014. 118: p. 4056 - 4062. DOI: 10.1021/jp503194v. Copyright 2014 American Chemical Society.

Knurr, B. J., Weber, J. M., “Interaction of Nickel with Carbon Dioxide in [Ni(CO₂)_n]⁻ Clusters Studied by Infrared Spectroscopy.” *Journal of Physical Chemistry A*, 2014. 118: p. 8753 - 8757. DOI: 10.1021/jp507149u. Copyright 2014 American Chemical Society.

Knurr, B. J., Weber, J. M., “Structural Diversity of Cu-CO₂ Complexes - Infrared Spectra and Structures of [Cu(CO₂)_n]⁻ Clusters.” *Journal of Physical Chemistry A*, 2014. 118: p. 10246 - 10251. DOI:10.1021/jp508219y. Copyright 2014 American Chemical Society

3.1 Introduction

The creation of sustainable energy sources has been one of the most pressing recent scientific endeavors. On the assumption that our fuel economy will depend on carbon-based fuels for the foreseeable future, development of carbon neutral fuel cycles are essential for the environmental and economic health of society. Carbon dioxide is a byproduct of many industrial processes as well as combustion reactions involving fossil fuels. CO₂ has also been shown to be a potent greenhouse gas with a number of negative environmental effects attributed to its increased emission. [13–15] It follows that research and the development of techniques aiding in the creation of carbon neutral processes are of importance to global sustainability.

One major avenue being explored is the sequestration and recycling of CO₂ generated in combustion reactions. Recovered CO₂ can be converted into chemically usable fuels or feedstock for the generation of fuels. Virtually any scheme for the conversion of CO₂ involves reduction of the CO₂, where the most simple case ends in the formation of formate (HCOO⁻). [16] This simple scheme requires the transfer of two electrons and one proton to a CO₂ molecule. A more recently developed and promising avenue toward CO₂ conversion involves a six-electron process whereby CO₂ is converted to methanol in the presence of pyridine based homogeneous catalysts. [17, 18]

A number of other approaches, typically involving metal based catalysts, have been used to mediate CO₂ reduction. [19–26] Of particular interest are systems where the catalyst is composed of a single metal atom or a small metal cluster. [27] In these cases, the catalysts are supported on surfaces [28–31] or embedded into supramolecular assemblies [32] or multiligand systems. [19, 20, 33] A number of these studies have shown conversion from CO₂ into CO or small organic species (i.e. CH₃OH, CH₄, etc.). However, the mechanistic, molecular level details of these processes are not well understood.

In the processes mentioned above, a CO₂ molecule will undergo reduction, where the simplest starting point is one-electron reduction. One-electron reduction of an isolated CO₂ molecule is energetically very expensive with a cost of ca. 0.6 eV. [34] In addition to the large energetic cost, a

free CO_2^- anion is only metastable where the longest observed lifetime is 90 μs . [34] However, the formation of a complex between the CO_2 molecule and a catalyst can aid in both charge transfer and stabilization of the activated species. In this case, a fractional amount of the excess charge would be transferred to the CO_2 and further interaction with reaction partners could complete the reduction process and subsequent chemical reactions.

Addition of an excess electron to CO_2 in a linear geometry leads to a population the $2\pi_u$ orbital (see Figure 3.1). However, by following the curves of the Walsh diagram [35] to minimize the energy of the system, it is clear that the anion will rearrange from a linear geometry with $(1\pi_g)^4(2\pi_u)^1$ occupation to a bent geometry with a $(1a_2)^2(4b_2)^2(6a_1)^1$ configuration. This weakens the π interactions present in the neutral CO_2 molecule, resulting in a lengthening of the CO bonds from 1.162 Å in the neutral species [36] to ~ 1.24 Å in the anion. In complexes containing CO_2 , the OCO bond angle depends on the amount of excess charge localized on the CO_2 unit and can vary from 180° for the neutral to $\sim 135^\circ$ for the anion. These changes in bond strength and geometry are reflected in the frequency of the antisymmetric CO stretching mode of CO_2 . In neutral CO_2 , the antisymmetric stretch is observed at 2349 cm^{-1} . [37] In a CO_2^- anion, the frequency of the same vibrational motion has been observed in a Ne matrix at 1658.3 cm^{-1} . [38] An antisymmetric stretch observed between these two extremes encodes the structure and charge distribution on the CO_2 and, as will be shown in this chapter, can be used as a spectroscopic probe of the reduction process.

Reduction of CO_2 to convert it into usable chemicals usually occurs in solution. The condensed phase environment complicates the interpretation of spectroscopic probes of reaction intermediates and short lived transient species that are characteristic of the reaction mechanisms. Due to speciation and the short lifetime of many reaction intermediates, it is difficult to definitively isolate the spectral signatures of relevant species *in situ*. Experiments *in vacuo* afford spectroscopic characterization of well defined molecular targets. This allows for the identification of potential reaction intermediates and can aid condensed phase research by elucidating the chemical processes underlying their reactions.

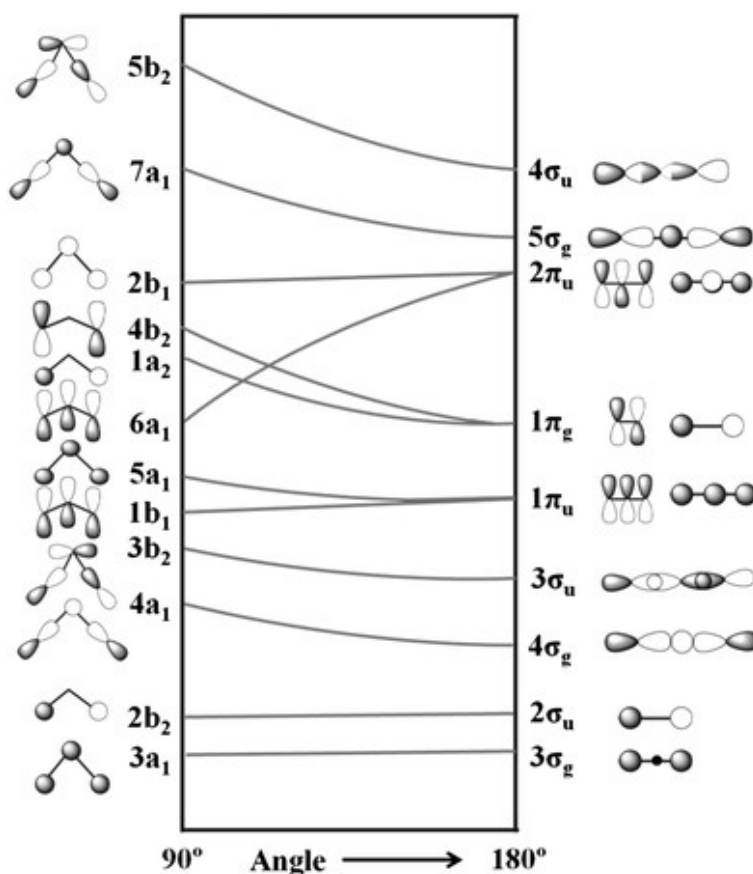


Figure 3.1: The Walsh diagram for CO₂. [35, 39] Reproduced from [40] with permission of The Royal Society of Chemistry. See text for discussion about the CO₂ anion and the CO₂ neutral.

While the presence of a complicated chemical environment makes spectroscopy *in situ* difficult, it is necessary for CO₂ reduction reactions and can have profound effects on the relevant species and chemistry. In the context of the present work we are interested in the nature of the charge carrier in metal-CO₂ of the form $[M(\text{CO}_2)_n]^-$ clusters (M = Au, Ag, Co, Ni, Cu), and in the effects of solvation (here the solvent is CO₂) on the structure and charge distribution of the ionic “core” species. We hope that this body of work will aid in rational catalyst design and a greater understanding of the chemical processes underlying CO₂ reduction using metal containing catalysts.

3.2 $[\text{Au}(\text{CO}_2)_n]^-$ and $[\text{Ag}(\text{CO}_2)_n]^-$ Clusters

There has been a substantial amount of interest in Au as a catalytic material. Gold clusters supported on surfaces have been shown to be catalytically active toward the oxidation of CO to CO_2 as well as the reduction of a single CO_2 molecule. [27,41–44] In modeling the binary Au-CO_2^- complex in the context of the oxidation of CO to CO_2 mediated by AuO, two types of interaction were predicted. [45] First, the two could interact as an ion-molecule pair where the CO_2 molecule solvates a Au^- anion due to the partial positive (δ^+) charge on the carbon atom being attracted to the Au^- . Additionally, the repulsive force of the partial negative (δ^-) charge on the oxygen atoms would push them away from the Au^- anion. These interactions would lead to relatively small deformation of the CO_2 molecule and the CO antisymmetric stretch would be only weakly perturbed. Alternatively, the carbon atom of the CO_2 molecule could form a covalent bond with the Au^- anion. This interaction would create a y-shaped complex reminiscent of a formate anion (HCOO^-) where the hydrogen has been replaced by the Au atom. This structure will be referred to as the formate motif. The formate motif is structurally similar to the proposed key intermediate for CO_2 reduction by a pyridine anion where a C-N bond is formed between the CO_2 and the N atom ($\text{C}_5\text{H}_5\text{N-CO}_2^-$). In this configuration, the geometry change of the CO_2 ligand towards that of the anion (see Figure 3.1) suggests that the formation of a Au-C bond would facilitate charge transfer to the CO_2 . As a consequence of this uptake of excess charge, there would be a substantial redshift of the CO antisymmetric stretching frequency providing a distinct spectroscopic signature to observe.

Spectroscopic studies have been performed on the binary $[\text{AuCO}_2]^-$ complex to characterize the type(s) of interaction present. [46] Even though the ion molecule complex had been predicted to be slightly lower in energy [45], only the covalent interaction was observed through multiphoton photodissociation spectroscopy. [46] This result contrasts with those obtained for the interactions of most halide anions with CO_2 (with the exception of F^- [47]) where the CO_2 was always found to solvate the halide anion with minimal charge delocalization onto the CO_2 molecules (see Figure 3.2).

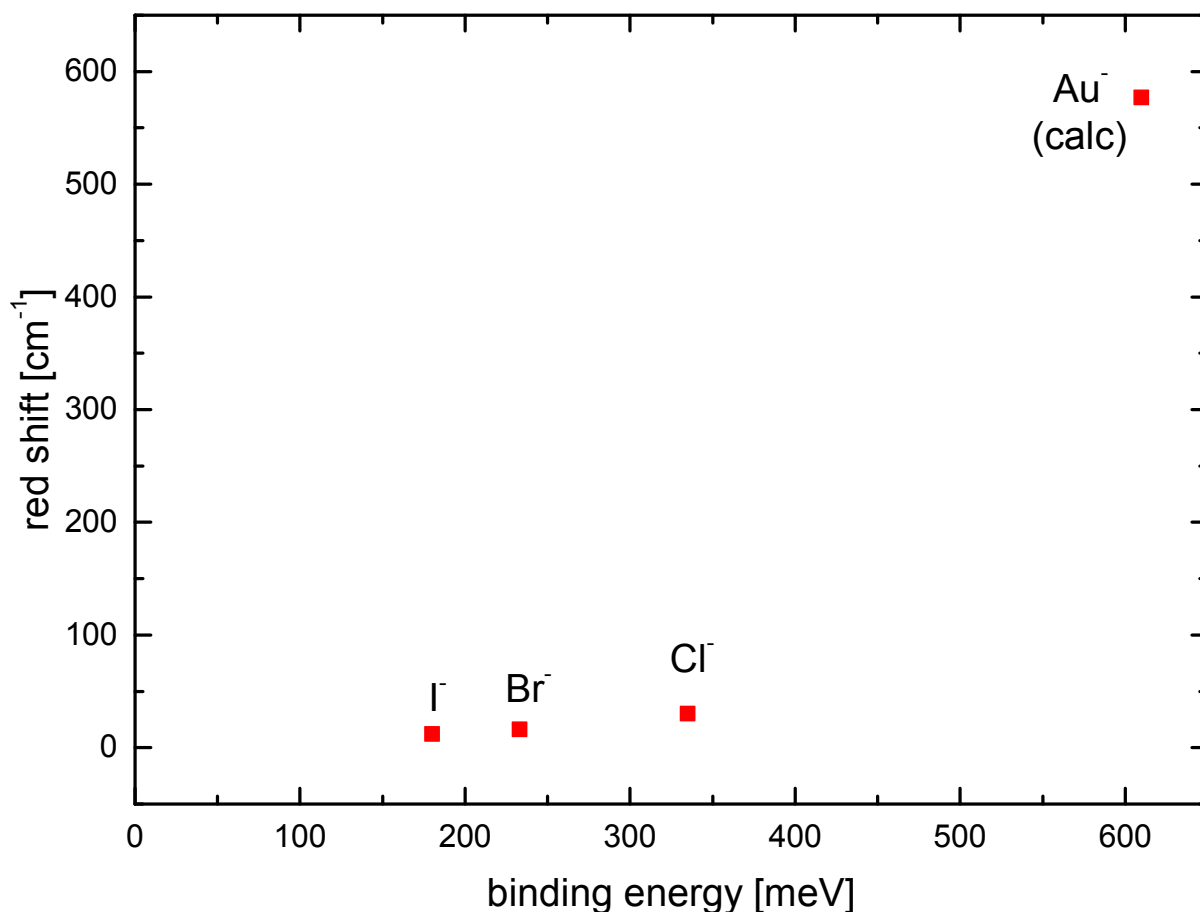


Figure 3.2: The observed redshift of the antisymmetric CO stretch in CO₂ when interacting with Au⁻ and various halides. [46, 48] As is indicated on the graph, the redshift of the antisymmetric stretching frequency of CO₂ interacting with Au⁻ is calculated while the other redshifts have been experimentally measured. The redshifts are all with respect to 2349 cm⁻¹. [37]

[48] Both Au⁻ and the halides possess a closed outer sub-shell with comparable electronegativities (specifically 2.54 for Au and 2.66 for I). [49] However, the interaction of Au⁻ with CO₂ shows a reactivity observed only in [F(CO₂)]⁻ clusters while the other halides remain closed sub-shell species solvated by CO₂ molecules.

While an understanding of the binary complex is useful, the addition of solvent molecules is a necessary next step since any industrial process is likely to be carried out in a solvent environment (e.g. supercritical CO₂, H₂O, alcohols, etc.). By building clusters one solvent molecule at a time, we can study the cumulative effect of solvation on the metal-CO₂ anion core.

Silver surfaces and nanoparticules have been tested as catalysts in the electrochemical reduction of CO_2 . [50–55] In these studies, a number of species, including CO , CH_3OH and HCOO^- , were formed. However, there is a lack of mechanistic understanding of the underlying chemical processes leading to formation of these species. There have been efforts to characterize the surface composition of Ag coated substrates [52] but in general there is a deficiency of spectroscopic studies on the catalytic processes that facilitate CO_2 reduction.

The electron configuration of Ag is $[\text{Kr}]4d^{10}5s^1$ which is very similar to that of Au which is $[\text{Xe}]4f^{14}5d^{10}6s^1$. However, many of the properties of these two atoms are quite different. For example, the electron affinity of Au is 2.309 eV [56] while the electron affinity of Ag is 1.303 eV. [57] Similarly, Au has a greater electronegativity and ionization energy than Ag but a similar atomic radius. This and other differences can be attributed to larger relativistic effects in Au compared to Ag. Superficially, one might expect that the interactions of CO_2 with Ag will be similar in nature to those of Au but, due to the differences in atomic properties, the charge distributions and effect of solvent on the core species are likely to differ.

3.2.1 Computational Methods

For $[\text{Au}(\text{CO}_2)_n]^-$ and $[\text{Ag}(\text{CO}_2)_n]^-$ clusters, a variety of levels of theory and basis sets were employed. The TURBOMOLE v. 5.9.1 and 6.2 suite of programs were used for all calculations. [58] For all calculations where vibrational spectra are reported, we employed density functional theory using the B3-LYP functional [59, 60] and the def2-TZVPP basis sets for all atoms. [61] We also performed exploratory calculations employing the PBE0 functional [62] and RI-MP2 level [63] of theory. Comparison of calculations performed with the def2-TZVPP basis sets [61] to def2-TZVP [64] and aug-cc-pVTZ basis sets [65] with different functionals or levels of theory yielded that the B3-LYP functional with def2-TZVPP basis sets for all atoms was the best compromise between computational cost and accuracy for this work. All vibrational frequencies were calculated using the AOFORCE program. [66, 67] The calculated vibrational frequencies corresponding to CO_2 molecules bonded to a metal atom were scaled by 0.9380 to account for anharmonicity. This

scaling factor as obtained by comparing the calculated value of the antisymmetric CO stretch in AuCO_2^- with the high level calculations of Boese *et al.* [46] Frequencies corresponding to weakly perturbed CO_2 molecules were scaled by 0.97537. This factor was generated by comparing the calculated frequency for a free CO_2 to the measured antisymmetric stretch of CO_2 reported by Shimaniouchi. [37] All partial charges were calculated using a natural population analysis. [68] All of the energies reported are zero-point corrected.

To model the effects of solvation beyond the first solvation shell in both $[\text{Au}(\text{CO}_2)_4]^-$ and $[\text{Ag}(\text{CO}_2)_n]^-$ ($n = 2$ and 4), we employed a conductor-like screening model (COSMO). [69–72] We used a dielectric constant of 1.6 (corresponding to saturated liquid CO_2 at 291 K) [73] and a molecular-shaped cavity generated using the default radii for carbon (2.0 Å), oxygen (1.72 Å) and silver (2.223 Å). The results from the COSMO simulation do not include zero-point corrections.

3.2.2 Infrared Spectra of $[\text{Au}(\text{CO}_2)_n]^-$ Clusters

To explore the effect of solvation on the binary AuCO_2^- complex, we probed $[\text{Au}(\text{CO}_2)_n]^-$ clusters by infrared photodissociation spectroscopy. Figure 3.3 shows the experimental spectra obtained for $[\text{Au}(\text{CO}_2)_n]^-$ clusters ($n = 2 - 13$) by observing the loss of one CO_2 molecule. The panel on the right side in the wavenumber range 2250 cm^{-1} to 2450 cm^{-1} contains signatures of solvent type CO_2 molecules. These CO_2 molecules mostly retain their identity as free CO_2 molecules and still exhibit an antisymmetric stretching frequency near 2349 cm^{-1} with only minor deviation due to the presence of the negative charge. On the other hand, the left panel of Figure 3.3 shows signatures of partially reduced CO_2 species. These CO_2 units have lost their identity as free CO_2 molecules and their vibrational frequencies encode information about their structure and role in the charge carrying species.

An initial inspection of the experimental spectra reveals three distinct trends. First, the signature of the partially reduced CO_2 shifts to the red with increasing cluster size from $n = 2 - 7, 9$. Second, the same partially reduced CO_2 signature shifts back to the blue as cluster size increases from $n = 10 - 13$. Third, the peaks corresponding to solvent CO_2 molecules show multiple

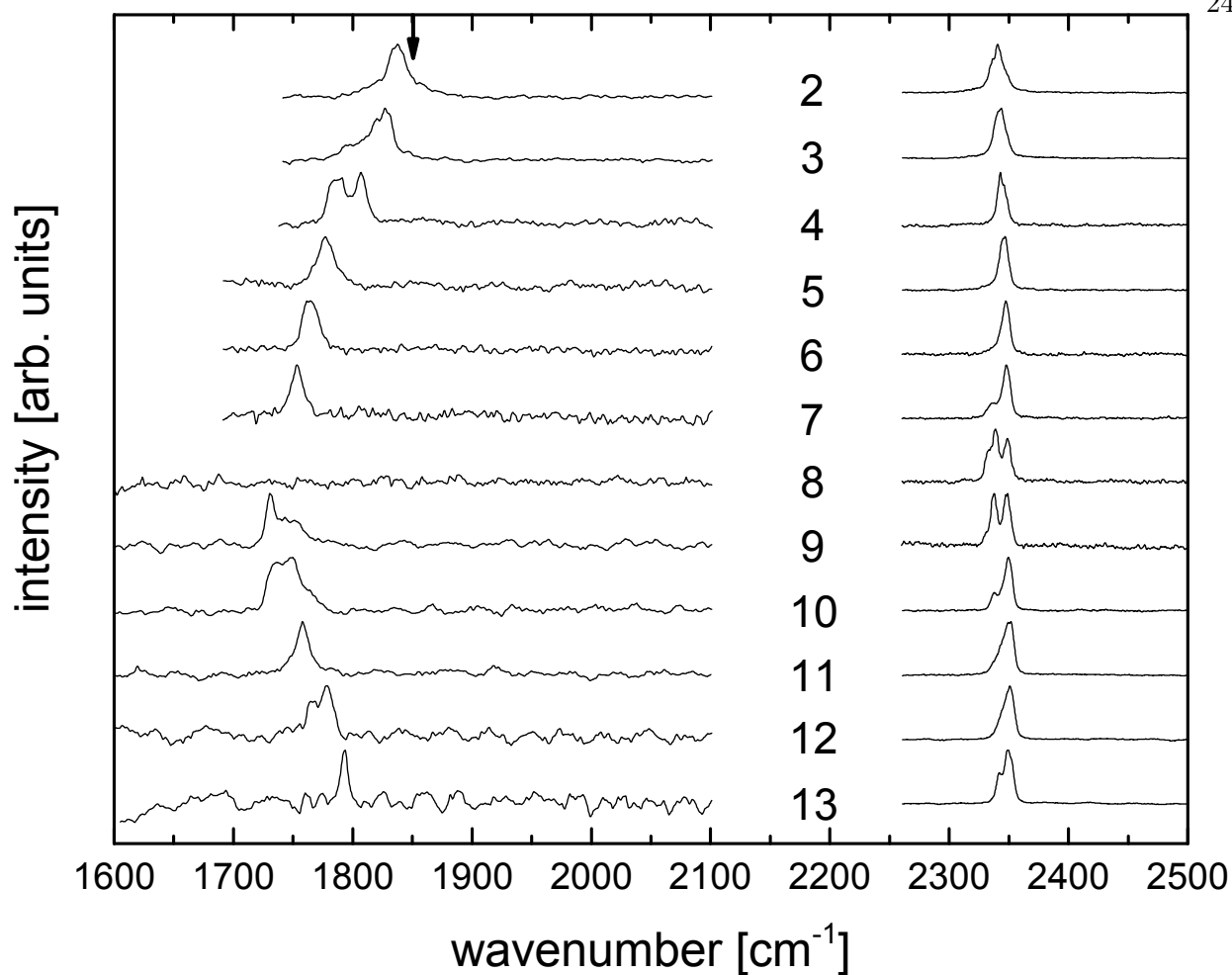


Figure 3.3: Experimental spectra of $[\text{Au}(\text{CO}_2)_n]^-$ clusters. The numbers denote the number of CO_2 molecules in the cluster. The right and left panes are individually normalized so they are on different scales. The arrow indicates the predicted frequency of the AuCO_2^- binary complex from the calculations of Boese *et al.* [46] All spectra were obtained monitoring the loss of a single solvent CO_2 .

components at cluster sizes $n \geq 7$. Additionally, $[\text{Au}(\text{CO}_2)_8]^-$ exhibits no signature of a partially reduced CO_2 molecule and a rather complicated solvent signature compared to other cluster sizes.

These trends will be discussed one at a time, beginning with the observed redshift from $n = 2 - 9$. As was discussed in the introduction to this chapter, strongly redshifted CO antisymmetric stretching frequencies indicate partial reduction of a CO_2 molecule. Assuming that the core structure is of the form $[\text{AuCO}_2]^-$ assigned by Boese *et al.* [46], the redshift observed in the left panel of

Figure 3.3 indicates that solvation is polarizing the excess charge density onto the partially reduced CO_2 molecule. Stated another way, initial solvation is increasing the degree of reduction of the partially reduced CO_2 unit.

To check the validity of this hypothesis we begin by considering the effect of CO_2 as a solvent species. It has been observed before in halide and $\text{O}_2^- \cdot \text{CO}_2$ cluster species that individual CO_2 molecules interacting closely with the charged species can result in a small amount of the excess charge becoming delocalized onto the solvent CO_2 molecules. [48, 74] In short, the CO_2 molecules polarize the excess charge towards themselves and can take up a small amount of the charge without forming covalent bonds. The analogy to this case would be that solvation around the CO_2 moiety of the formate complex should result in polarization of the excess charge onto the covalently bound CO_2 species and off of the metal atom.

To test this theory, we performed DFT calculations at a variety of different levels of theory (see Section 3.2.1 for details). From converged geometric structures, we generated vibrational frequencies and compared them to the experimental spectra. Figure 3.4 shows a comparison of the three lowest energy structures calculated for $[\text{Au}(\text{CO}_2)_2]^-$. The structure shown in the bottom panel of Figure 3.4 is termed symmetric solvation of the Au^- anion and is the result of solvation of the Au atom (opposite the bonded CO_2 ligand) of the binary core. Here the two CO_2 molecules are positioned on opposite sides of the Au atom and, as consequence, cancel the electron withdrawing capabilities of each other. This results in a small amount of charge transfer onto both CO_2 molecules resulting in a $\sim 20 \text{ cm}^{-1}$ estimated redshift of the antisymmetric stretching mode and no activated CO_2 species. However, it is clear that this solvation motif does not recover the experimental feature around 1810 cm^{-1} .

The other two structures presented in Figure 3.4 are examples of solvation around the $[\text{Au}-\text{CO}_2]^-$ formate motif. It is obvious that the top two structures both recover the experimental spectrum reasonably well but there are differences. For the rest of the chapter, we refer to the top structure as an example of a “side” solvation position while the structure shown in the middle panel shows occupation of the “terminal” solvation position. If only side solvation is present, a smaller

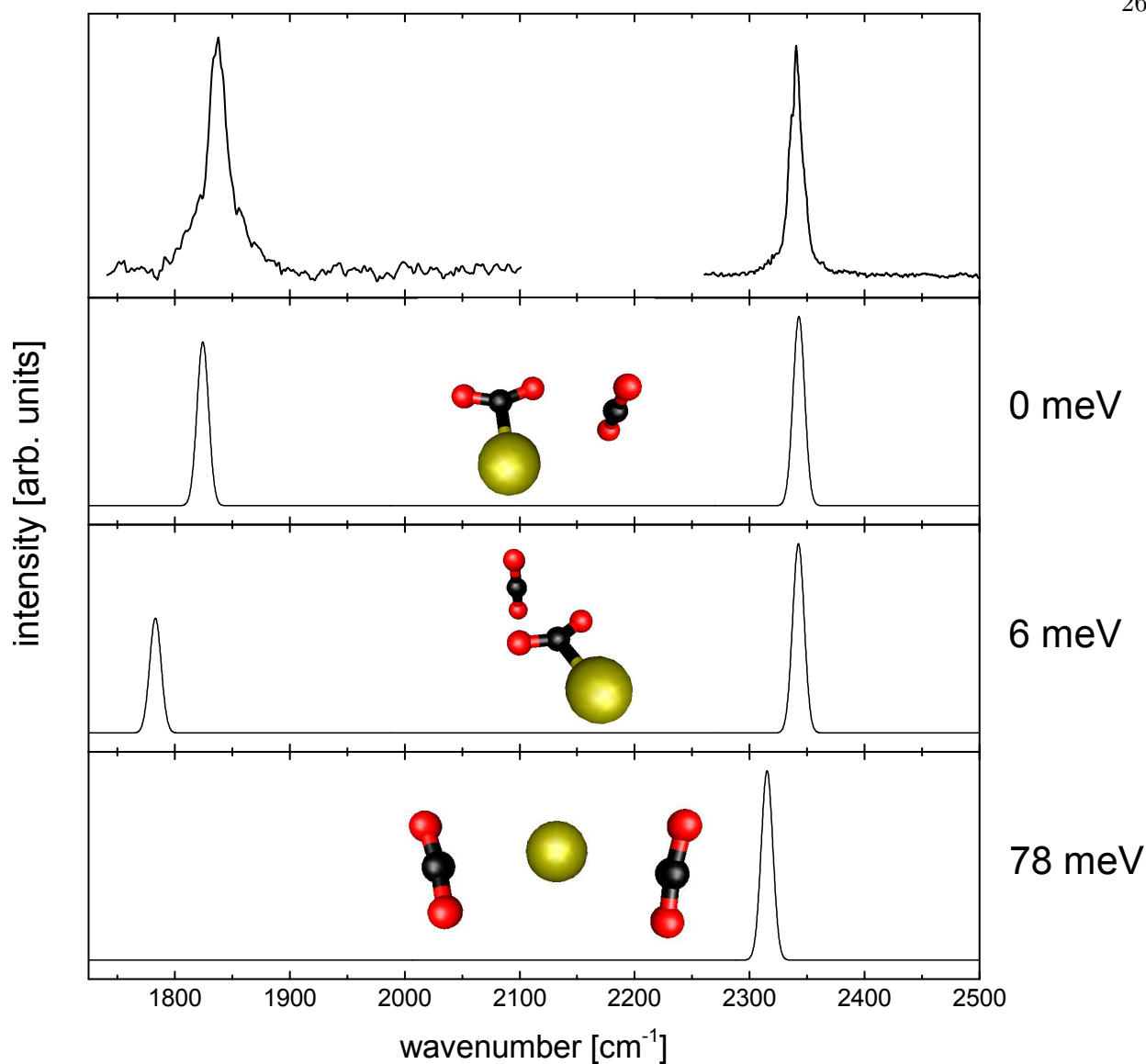


Figure 3.4: Comparison of the three calculated lowest energy structures for $[\text{Au}(\text{CO}_2)_2]^-$ clusters to the experimental spectrum for $[\text{Au}(\text{CO}_2)_2]^-$. Relative energies are given in meV.

redshift of the bonded CO_2 antisymmetric stretching frequency should be expected than when the terminal solvation position is occupied since the ability of the solvent CO_2 to polarize the charge will be greater when situated behind the bonded CO_2 and along the Au-C bond axis. Calculations corroborate this prediction and show that side solvation results in a lesser amount of the excess charge being localized on the activated CO_2 moiety than terminal solvation ($-0.48 e$ vs. $-0.55 e$).

This indicates, consistent with chemical intuition, that not only can CO₂ act as polarizing solvent, but its location in the cluster alters its effect on the solute. Here, we tentatively assign the side solvation isomer as the dominant solvation motif for [Au(CO₂)₂]⁻.

Based on our observations for [Au(CO₂)₂]⁻, solvation must be occurring around the CO₂ moiety for cluster sizes $n = 3 - 9$. Interestingly, there are two peaks that begin to appear at $n = 3$, both are very pronounced in $n = 4$ and only one peak is recovered at $n = 5$. The higher-energy feature in $n = 3$ and 4 follows a constant 10 cm⁻¹ shift with each additional CO₂ from $n = 2 - 4$. The lower-energy shoulder in $n = 3$ also shifts by 10 cm⁻¹ to the lower-energy peak for $n = 4$ and again by 10 cm⁻¹ to the single peak in $n = 5$. No peak is recovered in $n = 5$ corresponding to a 10 cm⁻¹ shift of the high-energy feature in $n = 4$. These observations suggest that there are unique solvation isomers populated at small cluster sizes that give rise to these different features.

Figure 3.5 shows a comparison of the calculated spectra for different solvation isomers of [Au(CO₂)_{*n*}]⁻ for ($n = 3, 4$). As can be seen, solvation in side positions (see middle panel on the left side of Figure 3.5) results in a smaller predicted redshift than solvation in the terminal position (see bottom panel on left side of Figure 3.5). Comparing the theoretical and experimental spectra, it becomes apparent that when the terminal solvation position is filled, the lower energy set of peaks are recovered. When the terminal solvation position is left vacant, the higher energy peaks in the spectra of $n = 3$ and 4 are predicted. At $n = 5$, the terminal position is always filled leaving only the lower-energy peak. For the remaining cluster sizes, the terminal position is already filled so another effect must give rise to the multiple features observed at large cluster size ($n \geq 7$ discussed below).

Calculations corroborate the idea that solvation around the CO₂ moiety causes charge polarization onto the activated CO₂ ligand and a concomitant redshift of the antisymmetric CO stretch. If a blue shift is observed with increased solvation, then the additional CO₂ molecules must be occupying positions that polarize charge density off of the CO₂ moiety. At $n = 9$, it is likely that all of the solvation positions around the bonded CO₂ are filled. Subsequent addition of CO₂ molecules would force them to solvate the Au atom as the solvation energy of occupying the first

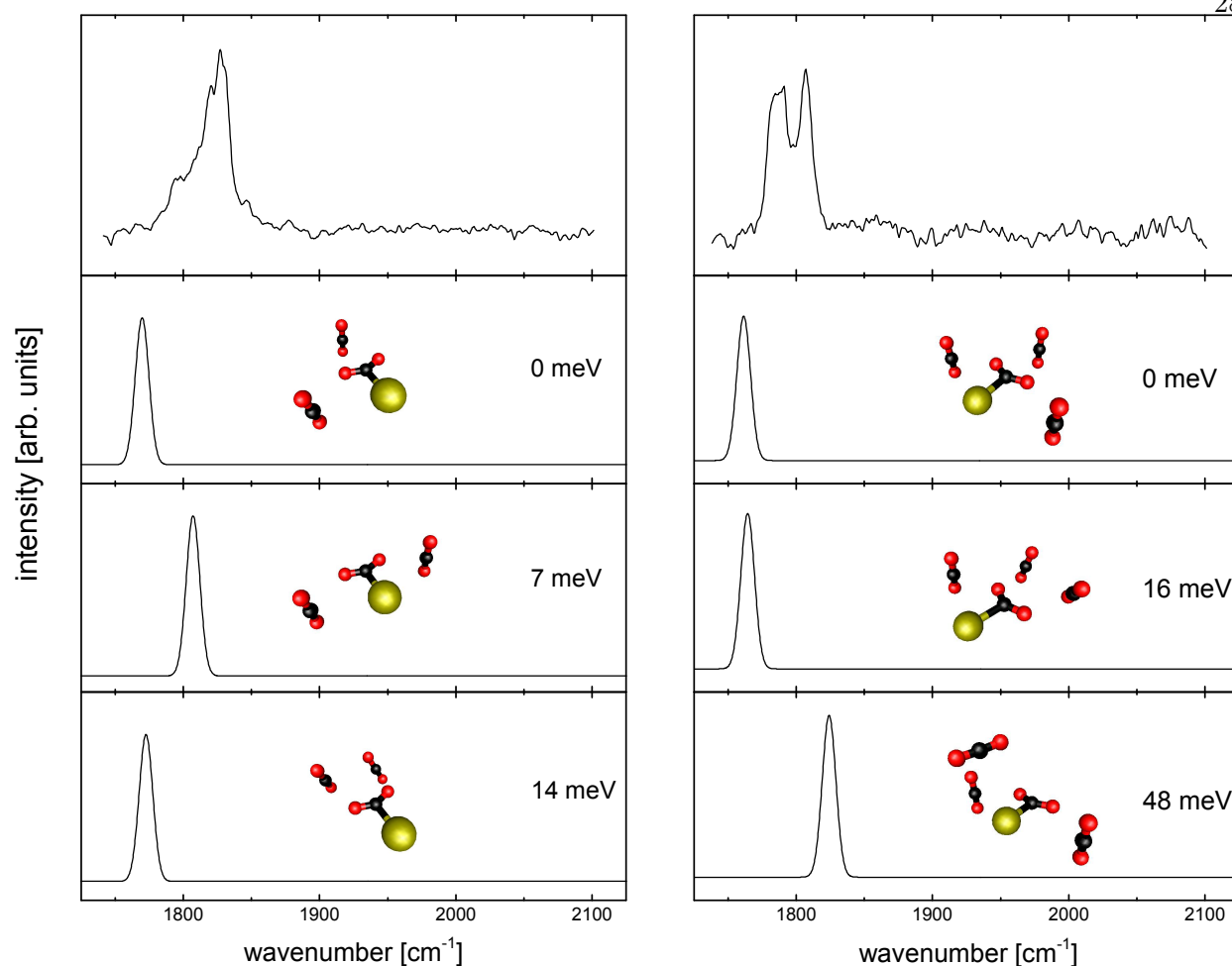


Figure 3.5: Comparison of the lowest energy structures for $[\text{Au}(\text{CO}_2)_n]^-$ clusters ($n = 3, 4$). Relative energies are given in meV and are with respect to the lowest energy conformer of a given cluster size. Since these structures are all within 60 meV of each other, they are considered to be isoenergetic.

solvation shell of the Au moiety will be more favorable than the solvation energy of opening a second solvation shell around the CO_2 moiety. It is reasonable to assume that solvation around the Au atom would polarize charge onto the Au and away from the CO_2 unit based on what has already been seen for solvation around the bonded CO_2 moiety. Additionally, calculations for higher energy conformers of smaller complexes have already predicted this behavior (see bottom panel of Figure 3.4) as solvation around the Au atom resulted in a deactivation of the bonded CO_2 . For $n \geq 10$, solvation is occurring around the Au moiety resulting in an observed blue shift as cluster

size increases because additional solvent can not be accommodated around the partially reduced CO_2 moiety. It is difficult to survey all of the possible solvation isomers for clusters larger than $n = 5$. Appendix A shows additional calculated structures for $n = 4$ and 5.

The next observation to discuss is the lack of a signature of a partially reduced CO_2 in $n = 8$ clusters. In a photoelectron study, it was observed that $\text{Br}^{\cdot-}(\text{CO}_2)_n$ clusters (Br^- is similar in size to Au^-) exhibit closure of the first solvation shell around Br^- at $n = 8$. [47] Additionally, $(\text{CO}_2)_n^-$ clusters exhibit an abrupt change in the charge carrier as a function of cluster size. [75] Due to the electronic instability of the CO_2^- anion, $(\text{CO}_2)_n^-$ clusters initially possess a C_2O_4^- core. At $n = 6$, the solvation energy gained by solvating a more compact CO_2^- core becomes greater than the electronic stability of the C_2O_4^- core and the charge carrier switches to CO_2^- . At $n = 14$ the first solvation shell of CO_2^- is filled and rather than expand into the second solvation shell, it is energetically more favorable to switch back to the C_2O_4^- core so that the solvation energy is maximized by the larger first solvation shell of C_2O_4^- compared to opening the second solvation shell of CO_2^- . In $[\text{Au}(\text{CO}_2)_n]^-$ clusters, a similar switch occurs but happens over only one cluster size. At $n = 8$ the solvation energy of solvating the Au^- is greater than the electronic stability of the formate core. For all other cluster sizes, the presence of the formate core is energetically more favorable than solvation of a compact charge carrier.

Lastly, at $n = 7$ we observed the first splitting of the solvent feature and we retain at least two solvent CO_2 peaks for all larger cluster sizes. This is likely due to the position of the solvent molecule with respect to the structure of the charge carrier. At $n = 7$, most of the space around the activated CO_2 moiety is probably filled since the blue shift is first observed two cluster sizes later. At this cluster size, additional solvent molecules may begin to position themselves closer to the Au atom. This could result in a different amount of charge uptake by various solvent molecules depending on their position around the core resulting in multiple solvent signatures. While it is difficult to definitively say, it is likely that for $n \geq 7$, the first major change as to which part of the formate core is being solvated is occurring resulting in the multiple solvent CO_2 peaks observed.

To briefly summarize, in $[\text{Au}(\text{CO}_2)_n]^-$ clusters solvation occurs around the CO_2 moiety at

$n = 2 - 7, 9$ with the terminal position(s) always being filled for $n \geq 5$. This causes a polarization of the excess charge onto the covalently bonded CO_2 moiety. From $n = 10 - 13$, additional solvation occurs around the Au atom resulting in a deactivation of the partially reduced CO_2 . At $n = 8$, it is more energetically favorable to solvate a Au^- anion rather than form the AuCO_2^- formate complex.

3.2.3 Infrared Spectra of $[\text{Ag}(\text{CO}_2)_n]^-$ Clusters

The experimental spectra of $[\text{Ag}(\text{CO}_2)_n]^-$ are shown in Figure 3.6 and were obtained by monitoring the loss of one CO_2 molecule. Again, there are two regions of the experimental spectra. The higher energy region ($2250 \text{ cm}^{-1} - 2400 \text{ cm}^{-1}$) shows signatures of weakly perturbed CO_2 molecules. These features, like in $[\text{Au}(\text{CO}_2)_n]^-$ clusters, are due to solvent CO_2 molecules that are not part of the charge carrier. The lower energy region (1600 cm^{-1} to 2150 cm^{-1}) contains signatures of the charge carrying species. There are three primary features in the spectra to consider. First, there is a set of peaks in Figure 3.6, highlighted by the red dashed line, that shift to the red with increasing number of CO_2 molecules. Second, within the first few cluster sizes probed the solvent feature changes shape and shifts to higher energy. Lastly, there is a relatively stationary peak highlighted by the dashed blue line at ca. 1660 cm^{-1} that was not observed in $[\text{Au}(\text{CO}_2)_n]^-$ clusters. Again, we will interpret these features one at a time.

We will first analyze the red shifting feature. Since fragmentation is first observed at $n = 2$, it is reasonable to assume that the core species is of the form $[\text{AgCO}_2]^-$ since the binding energy of a CO_2 bonded to the metal atom is calculated to be on the order of 0.5 eV. This is outside the photon energy range of the experiment and fragmentation would only be observable through multi-photon processes (like were observed by Boese *et al.* [46]). Since Ag is electronically very similar to Au, it is also likely that the structural motifs for both the charge carrier and solvation observed in $[\text{Au}(\text{CO}_2)_n]^-$ clusters are at play here.

We performed DFT calculations on $[\text{Ag}(\text{CO}_2)_n]^-$ ($n = 2 - 4$) clusters, employing the same formate core with the side/terminal solvation model discussed above in Section 3.2.2. If we compare the calculated vibrational frequencies for the predicted $[\text{Ag}(\text{CO}_2)_n]^-$ ($n = 2 - 4$) structures with

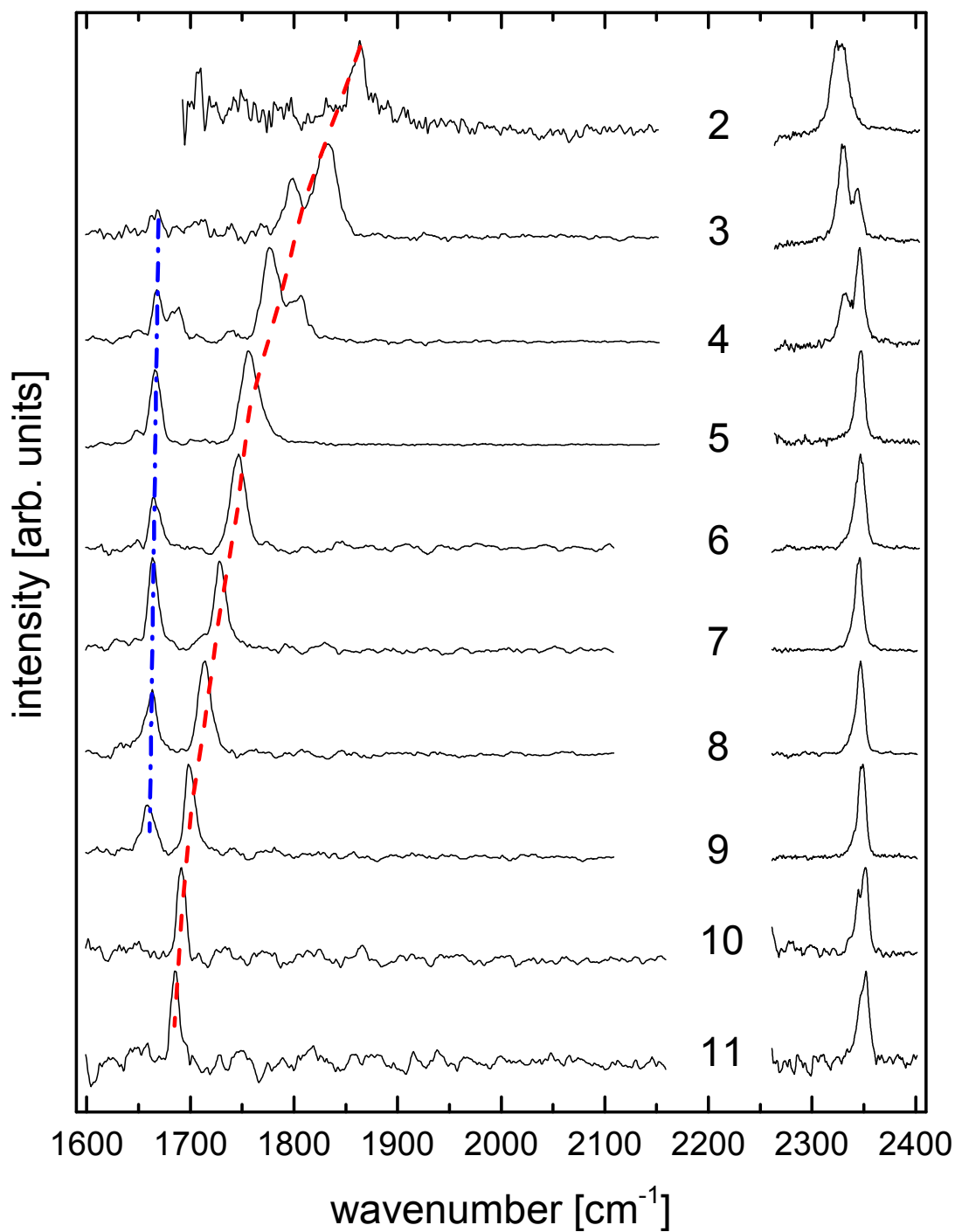


Figure 3.6: Experimental spectra of $[\text{Ag}(\text{CO}_2)_n]^-$ clusters. The numbers denote the number of CO_2 molecules in the cluster (n). The right and left panes are individually normalized so they are on different scales. All of these spectra were obtained monitoring the loss of a single solvent CO_2 . The dashed lines are meant to guide the eye.

their corresponding experimental spectra, we observe very good agreement (see Figure 3.7). The single peak in $n = 2$ is recovered by the side solvation isomer (see top trace in the left panel of Figure 3.7). The two peaks observed in $n = 3$ and 4 are predicted by different solvation isomers of the formate core. The higher energy feature is best reproduced by leaving the terminal position vacant while structures where the terminal position is occupied recover the lower energy peak. At $n = 5$, only a single peak remains in this region indicating that the terminal position is now filled for all larger clusters. This is identical behavior to that observed in similarly sized $[\text{Au}(\text{CO}_2)_n]^-$ clusters and is summarized in Figure 3.8. However, in contrast to the behavior of large $[\text{Au}(\text{CO}_2)_n]^-$ clusters (i.e. $n \geq 7$), no blue shift is observed in $[\text{Ag}(\text{CO}_2)_n]^-$ clusters as cluster size increases. The differential red shift decreases in magnitude as the number of CO_2 molecules increases but the peak corresponding to the activated CO_2 molecule continues to shift to lower energies. Additionally the peak position for this set of features appears to be asymptotically approaching the antisymmetric CO stretching frequency of CO_2^- at approximately 1660 cm^{-1} . This observation will receive additional consideration below.

We next consider the structure of the solvent peaks in small $[\text{Ag}(\text{CO}_2)_n]^-$ clusters (right side of Figure 3.6). In $[\text{Ag}(\text{CO}_2)_2]^-$, the solvent peak is centered at 2325 cm^{-1} rather than 2345 cm^{-1} as has been common in the spectra of $[\text{Au}(\text{CO}_2)_n]^-$. It also appears fairly broad compared to the solvent peaks for cluster sizes $n \geq 5$. In $[\text{Ag}(\text{CO}_2)_3]^-$, there are two distinct solvent signatures, a more intense peak at 2330 cm^{-1} and a smaller peak at 2345 cm^{-1} . In $[\text{Ag}(\text{CO}_2)_4]^-$, the intensity ratio of the two peaks is reversed and the lower energy peak continues to shift to the blue now centered at 2335 cm^{-1} . At $[\text{Ag}(\text{CO}_2)_5]^-$ only one solvent feature, at 2345 cm^{-1} , is observed. The shifts observed here are akin to what was seen before in halide CO_2 interactions for different halides. [48] Based on the interpretation offered for halide- CO_2 interactions, there is likely only a small amount of the excess charge transferred onto the CO_2 molecules. Of the starting geometries used, nearly all structures converged to a formate core where there is a significant amount of charge localized on one CO_2 molecule. The only family of structures that did not converge to the formate are those exhibiting symmetric solvation of a Ag^- anion. In these structures the CO_2 molecules

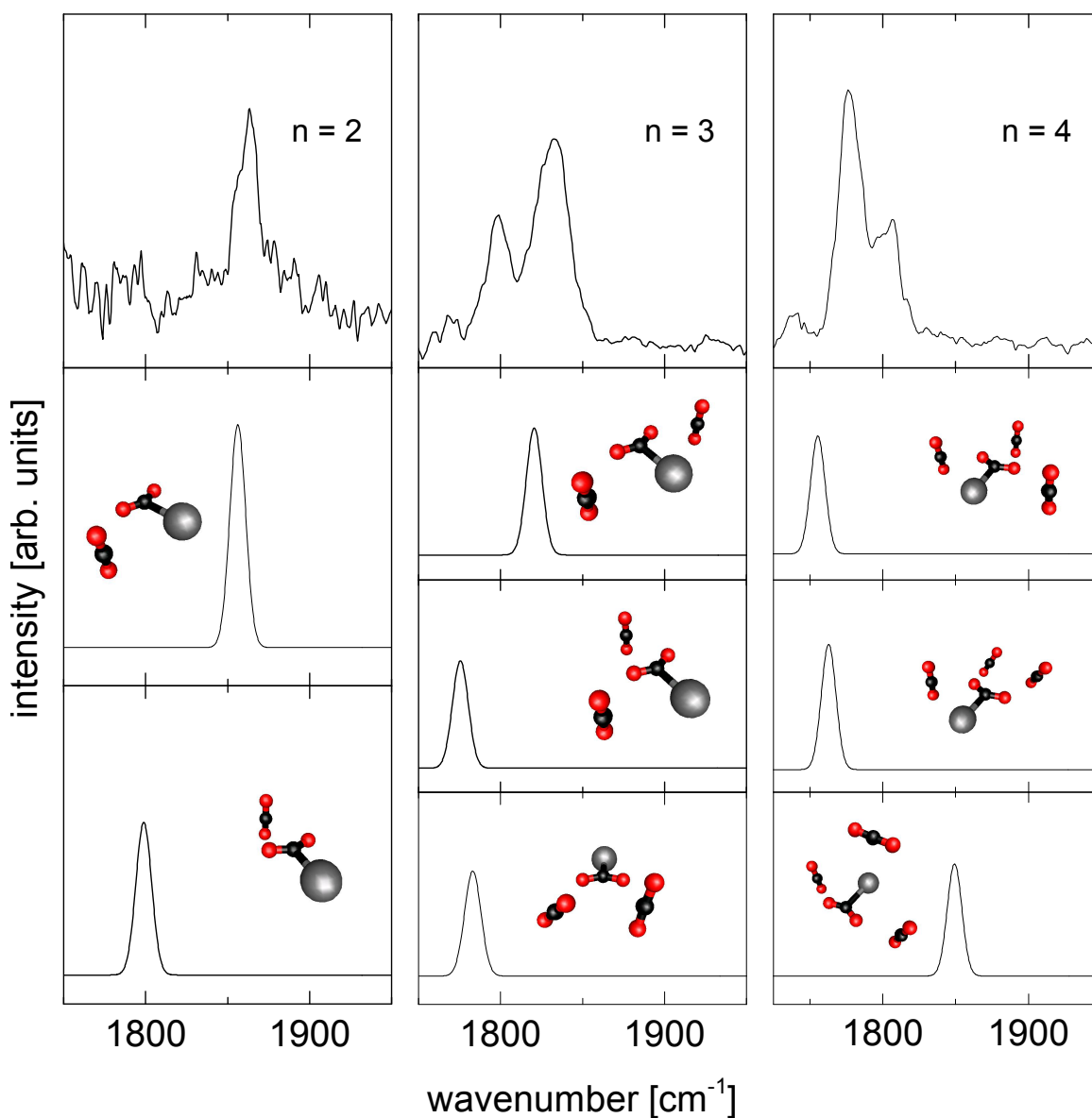


Figure 3.7: Comparison of the lowest energy structures for $[\text{Ag}(\text{CO}_2)_n]^-$ clusters ($n = 2 - 4$). All reported structures are within 60 meV relative energy of each other for a given cluster size and are considered to be isoenergetic.

solvate the Ag^- anion in such a way that they prevent any one CO_2 molecule from creating a covalent bond with the Ag atom.

Calculations of structures exhibiting symmetric solvation around a Ag^- anion are shown in Figure 3.9. As can be clearly seen, this family of structures recovers the position and red shift

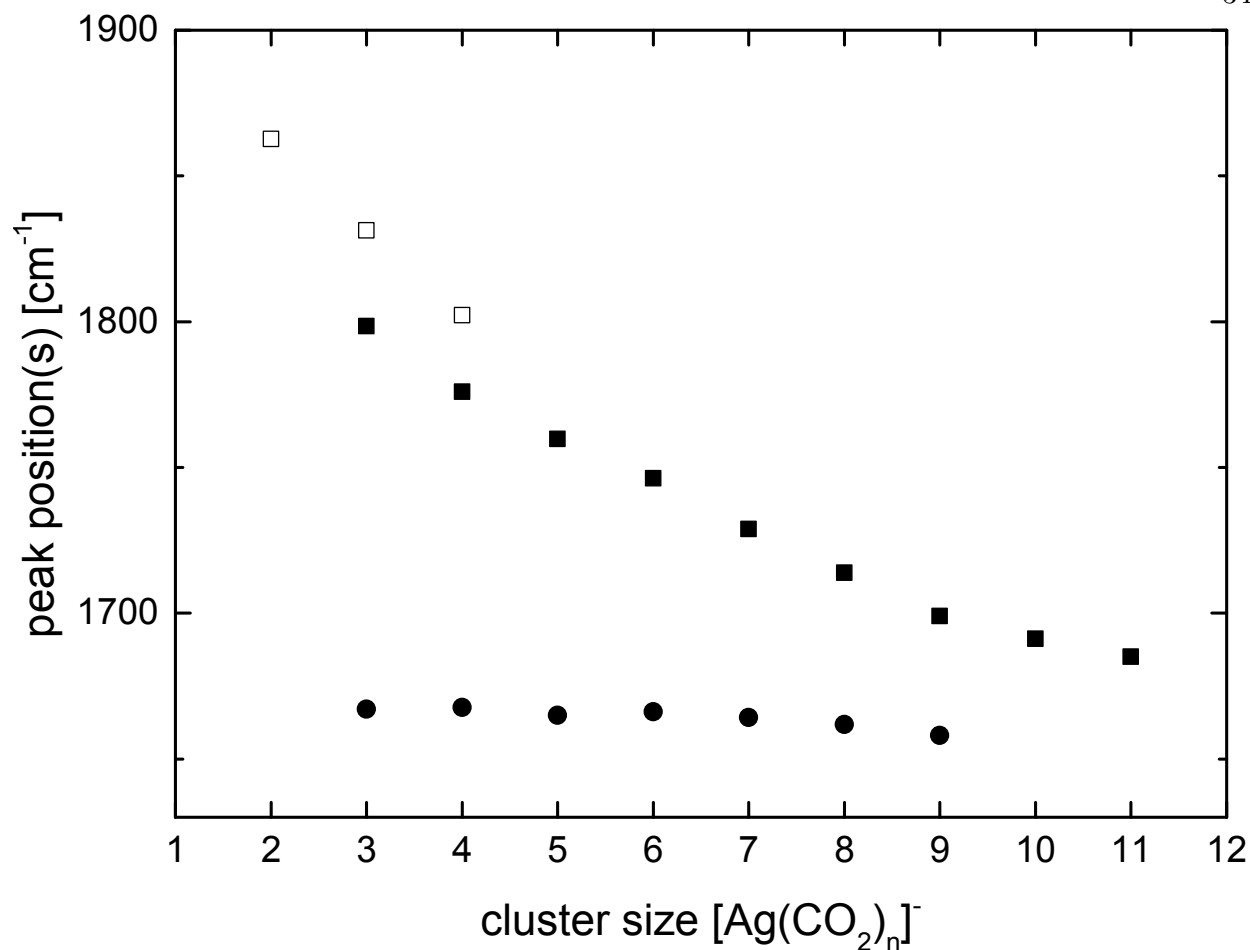


Figure 3.8: Peak positions in the lower energy region (left panel in Figure 3.6) plotted against cluster size. Solid squares represent structures where the terminal solvation position is filled. The open squares represent structures where the terminal solvation position is vacant. Solid circles indicate when the charge carrier is CO_2^- (see text).

of the solvent peak in all cases where it is observed. The reason symmetric solvation is no longer observed at clusters larger than $n = 4$ is likely due to a lack of available solvation positions that would not preferentially enable one of the CO_2 molecules to form a covalent bond with the Ag^- anion. Stated another way, solvation behind an already symmetrically solvating CO_2 molecule would polarize charge onto it and prompt it to form a covalent bond with the Ag^- anion. Based on the signal to noise of the far-IR region and lack of a peak at 2345 cm^{-1} in $[\text{Ag}(\text{CO}_2)_2]^-$ clusters, this cluster shows nearly exclusively symmetric solvation with only a small amount of the formate

complex being formed. There likely exists a peak at 2345 cm^{-1} for $n = 2$ but it is obscured by the broad feature centered at 2325 cm^{-1} . At $n = 3$, symmetric solvation is still preferred but there is more of the formate complex being formed. By $n = 4$, the argentoformate complex $[\text{AgCO}_2]^-$ is the dominant species.

The last trend to discuss is the feature that appears in $n = 3 - 9$ and is centered around 1660 cm^{-1} . This frequency is near to that of the antisymmetric stretch of CO_2^- at 1658.3 cm^{-1} [38] suggesting that the charge carrier is no longer the formate like complex but rather a CO_2^- anion. If this is true, then the Ag atom would no longer be part of the charge carrier, rather playing the role of a solvent and consequently should be a possible fragment species. We performed experiments monitoring the loss of a neutral Ag^0 atom and the resulting spectra are shown by traces C and D in Figure 3.10. Comparing the features observed in the loss of Ag channel to those in the loss of CO_2 channel, it is clear that the peak belonging to the formate core is not observed when monitoring the loss of Ag while the 1660 cm^{-1} feature is. Additionally, a set of three peaks is observed for $n = 4$ in the loss of Ag spectrum. This set of peaks is indicative of a C_2O_4^- charge carrier rather than a CO_2^- charge carrier, which is the expected core species for small $(\text{CO}_2)_n^-$ clusters ($n = 2 - 5$). [75] This observation indicates that the Ag atom can and does indeed act as a solvent species rather than part of the charge carrier. In addition to the formate core structure, the peak at 1660 cm^{-1} shows that signatures similar to those of neat $(\text{CO}_2)_n^-$ clusters are observed in $[\text{Ag}(\text{CO}_2)_n]^-$ clusters.

To further validate the observation that Ag can act as a “solvent” we performed calculations on $[\text{Ag}(\text{CO}_2)_4]^-$ clusters in an attempt to isolate a structure where the Ag is not part of the charge carrier. We varied the OCO bond angle of the covalently bonded CO_2 moiety in the lowest energy isomer of $[\text{Ag}(\text{CO}_2)_4]^-$ (see Figure 3.7 top structure right panel) to try and isolate a second minimum energy structure where Ag is not part of the charge carrier. A robust local minimum is recovered corresponding to the formation of a C_2O_4^- charge carrier rather than the formate-like species, consistent with spectroscopic observations.

We also tested the effects of a continuum dielectric corresponding to room temperature CO_2 around the calculated structures. The black curve in Figure 3.11 represents this scenario. It

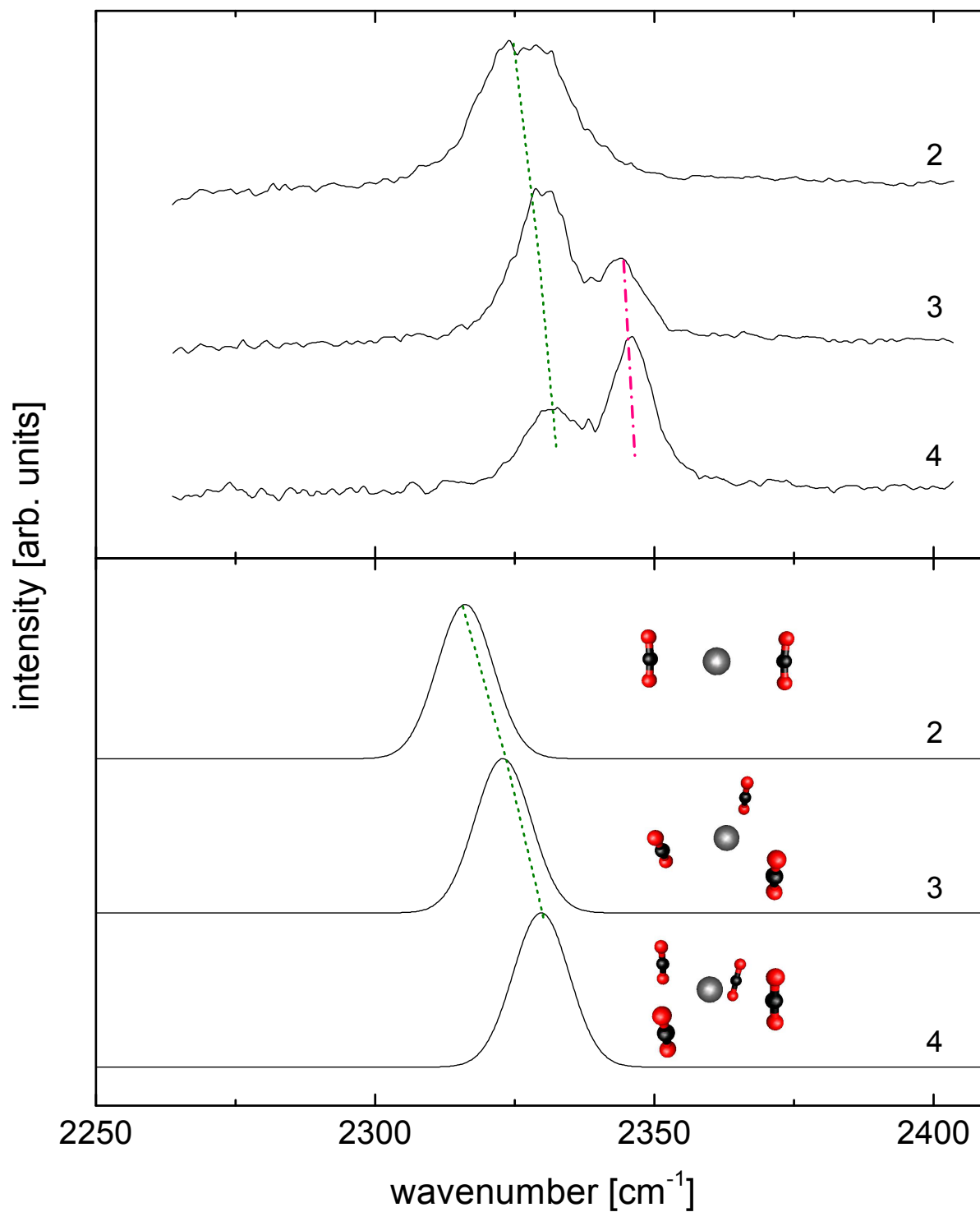


Figure 3.9: Comparison of structures exhibiting symmetric solvation around a Ag^- anion for $n = 2 - 4$. The green dotted line is meant to show the red shift trend observed and predicted. The magenta dot-dash line shows the nearly unshifted solvent CO_2 peak corresponding to the existence of a formate type core.

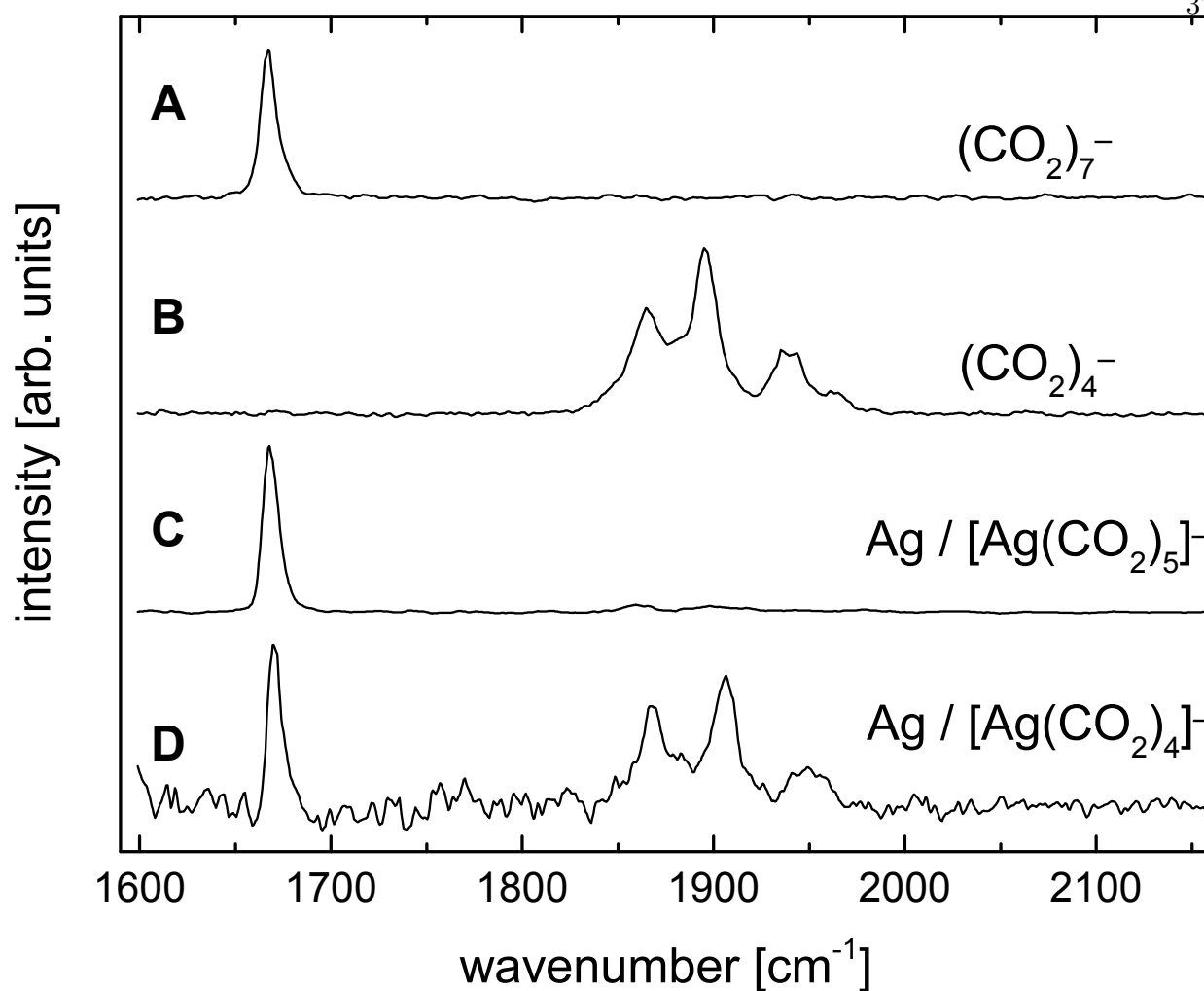


Figure 3.10: Comparison of Ag loss channels for $[\text{Ag}(\text{CO}_2)_4]^-$ (D) and $[\text{Ag}(\text{CO}_2)_5]^-$ (C) to $(\text{CO}_2)_n^-$ clusters exhibiting different core structures (A and B). The feature at 1660 cm^{-1} corresponds to a CO_2^- core while the set of peaks between 1800 cm^{-1} and 2000 cm^{-1} indicates a C_2O_4^- core. See text for discussion.

is apparent that, while an oversimplification of solvent effects, the addition of a CO_2 dielectric continuum is stabilizing to the C_2O_4^- core. However, we stress that solvent is not merely a dielectric as can be seen in Figure 3.7. At this point, it is clear that CO_2 -based charge carriers can exist in the presence of a Ag atom.

We return briefly to the comment made above concerning the red shift of the peak corresponding to the formate core. Since behavior akin to $(\text{CO}_2)_n^-$ clusters is observed, it is reasonable to

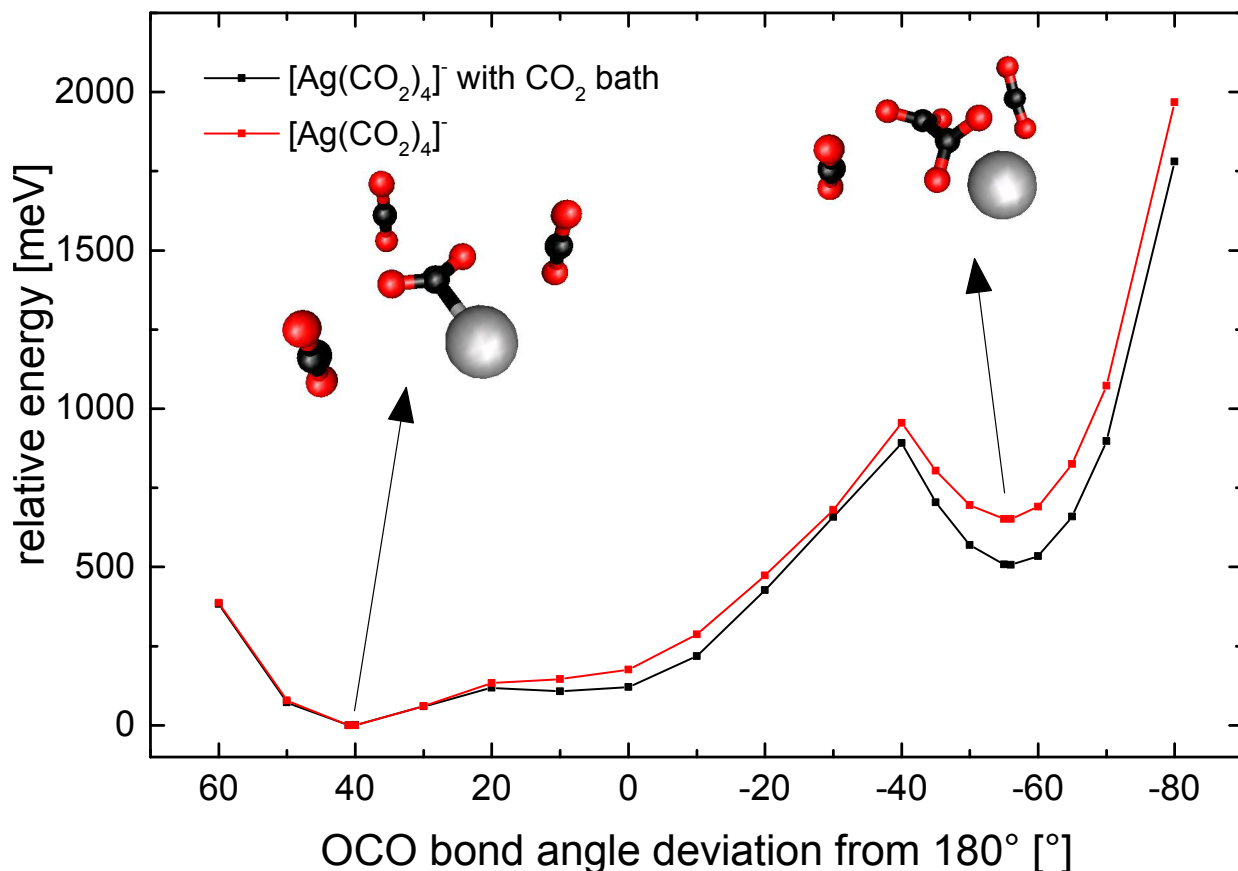


Figure 3.11: Potential energy curve for $[\text{Ag}(\text{CO}_2)_4]^-$ generated by varying the OCO bond angle of the partially reduced CO_2 moiety. The red curve represents the structures as shown. The black curve contains a dielectric continuum corresponding to CO_2 around the shown structures to approximate the effect of increased solvation (see Section 3.2.1 for additional information). A robust second minimum is recovered with the formation of a C_2O_4 species, which is additionally stabilized by the dielectric continuum. The relative energies presented here are not zero-point corrected.

hypothesize that the peak corresponding to the formate complex is indeed approaching a frequency similar to the antisymmetric stretch of a CO_2^- anion. However, without spectra of larger clusters (i.e. $n \geq 12$) it is impossible to say with certainty that this is true. Figure 3.8 summarizes this asymptotic behavior. This section will finish with a comparison of $[\text{Ag}(\text{CO}_2)_n]^-$ and $[\text{Au}(\text{CO}_2)_n]^-$ clusters.

The primary core structure formed in both $[\text{Au}(\text{CO}_2)_n]^-$ and $[\text{Ag}(\text{CO}_2)_n]^-$ clusters is a binary

complex of the metal and one CO_2 in a structure resembling the formate anion. The behavior of these cores in the presence of solvent CO_2 molecules is similar with preferential solvation around the covalently bound CO_2 resulting in increased reduction of that CO_2 ligand initially being observed. Solvation around the metal atom observed in $[\text{Au}(\text{CO}_2)_n]^-$ clusters ($n \geq 10$) resulted in a blue shift of the antisymmetric CO stretching frequency corresponding with deactivation of the bonded CO_2 ligand. No blue shift was observed in $[\text{Ag}(\text{CO}_2)_n]^-$ clusters. This can be attributed to the difference in electronegativity between Au and Ag (2.54 vs. 1.93, respectively). [49] This strong difference results in it being more energetically favorable for the Au atom to retain part of the excess charge and thus hamper charge transfer to the bonded CO_2 ligand. This is also consistent with the behavior observed when attempting to obtain a second minimum corresponding to a C_2O_4^- charge carrier in $[\text{Au}(\text{CO}_2)_4]^-$ clusters (see Figure 3.12). No second minimum is recovered due to the high electronegativity of Au.

Because the formate structure exists in both $[\text{Ag}(\text{CO}_2)_4]^-$ and $[\text{Au}(\text{CO}_2)_4]^-$ clusters it is informative to compare their results and draw a connection to the observed CO antisymmetric stretching frequency and the degree of reduction. Figure 3.13 shows the experimentally observed frequency of the partially reduced CO_2 ligand plotted against the calculated charge on that CO_2 based on the assigned structure for that frequency. Additionally, the frequency of a CO_2^- anion is also shown. [38] The data indicate an empirical linear correlation between the antisymmetric stretching frequency and the partial charge on the CO_2 moiety in this wavenumber region. We caution that this linear trend breaks down at higher vibrational frequencies and appears to be cubic in nature. [76, 77] Based on this relationship, we can extrapolate the amount of charge localized on the activated CO_2 ligand. For $[\text{Au}(\text{CO}_2)_4]^-$ clusters, a maximum of $-0.79 e^-$ is donated to the bonded CO_2 . For $[\text{Ag}(\text{CO}_2)_4]^-$ clusters, we observe $-0.92 e^-$ donated with no indication that the trend of increased charge donation with increasing solvation will reverse.

The results in this section indicate that Ag is better suited to reductive activation of CO_2 than Au. This is owing to the observation of lower antisymmetric stretching frequencies of the activated CO_2 ligand in $[\text{Ag}(\text{CO}_2)_n]^-$ corresponding to increased reductive activation compared

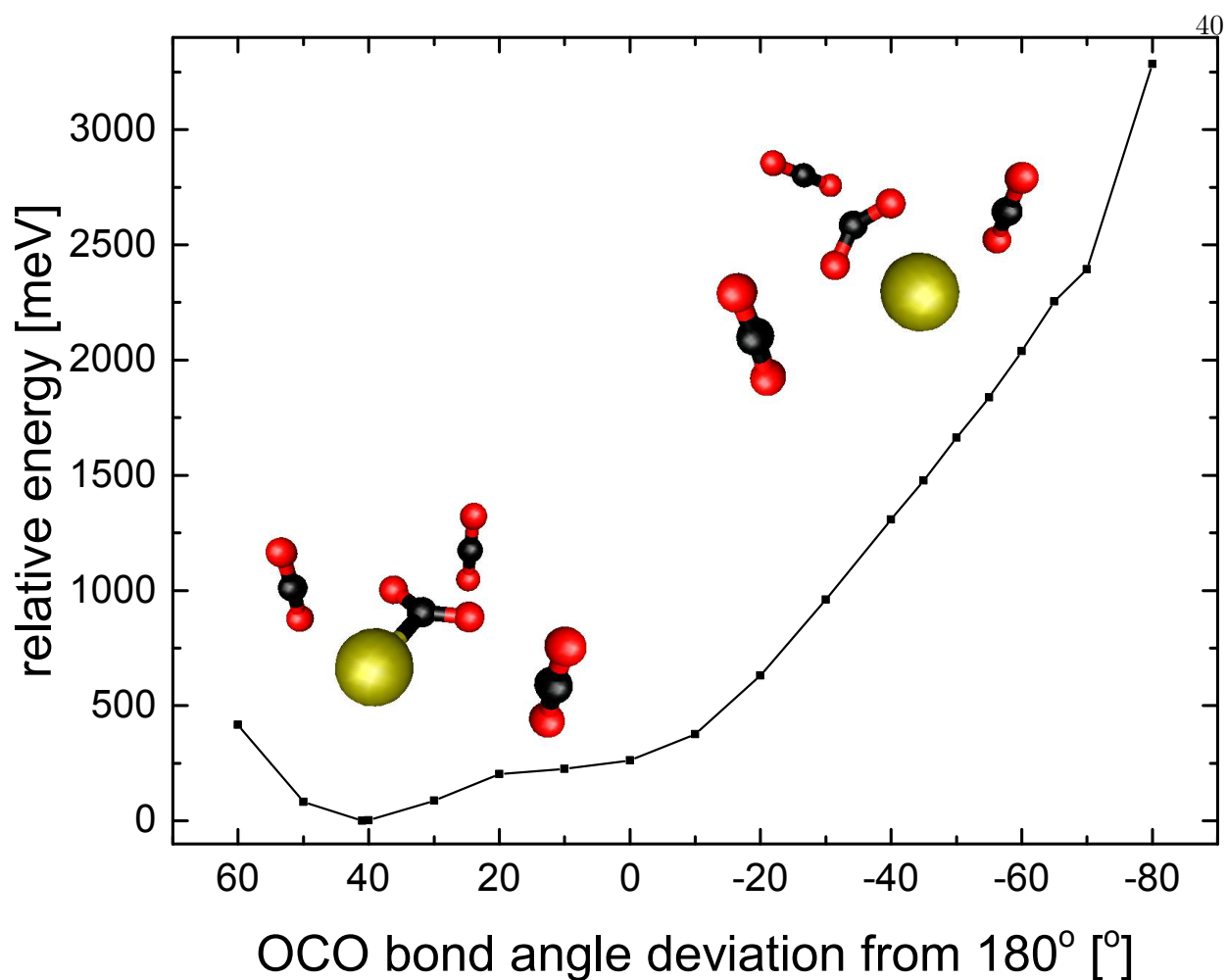


Figure 3.12: Potential energy curve for $[\text{Au}(\text{CO}_2)_4]^-$ generated by varying the OCO bond angle of the partially reduced CO_2 moiety. No second minimum is recovered corresponding to a C_2O_4^- core unlike in $[\text{Ag}(\text{CO}_2)_4]^-$ (see Figure 3.11). The relative energies presented here are not-zero point corrected.

to $[\text{Au}(\text{CO}_2)_n]^-$ clusters. Additionally, the ability of Ag to take the role of a solvent rather than part of the charge carrier indicates that it is likely easier to abstract reduced CO_2 from Ag rather than from Au. These results suggest an initial trend that lower electronegativity of a 9th column transition metal corresponds to an increased ability to reduce CO_2 .

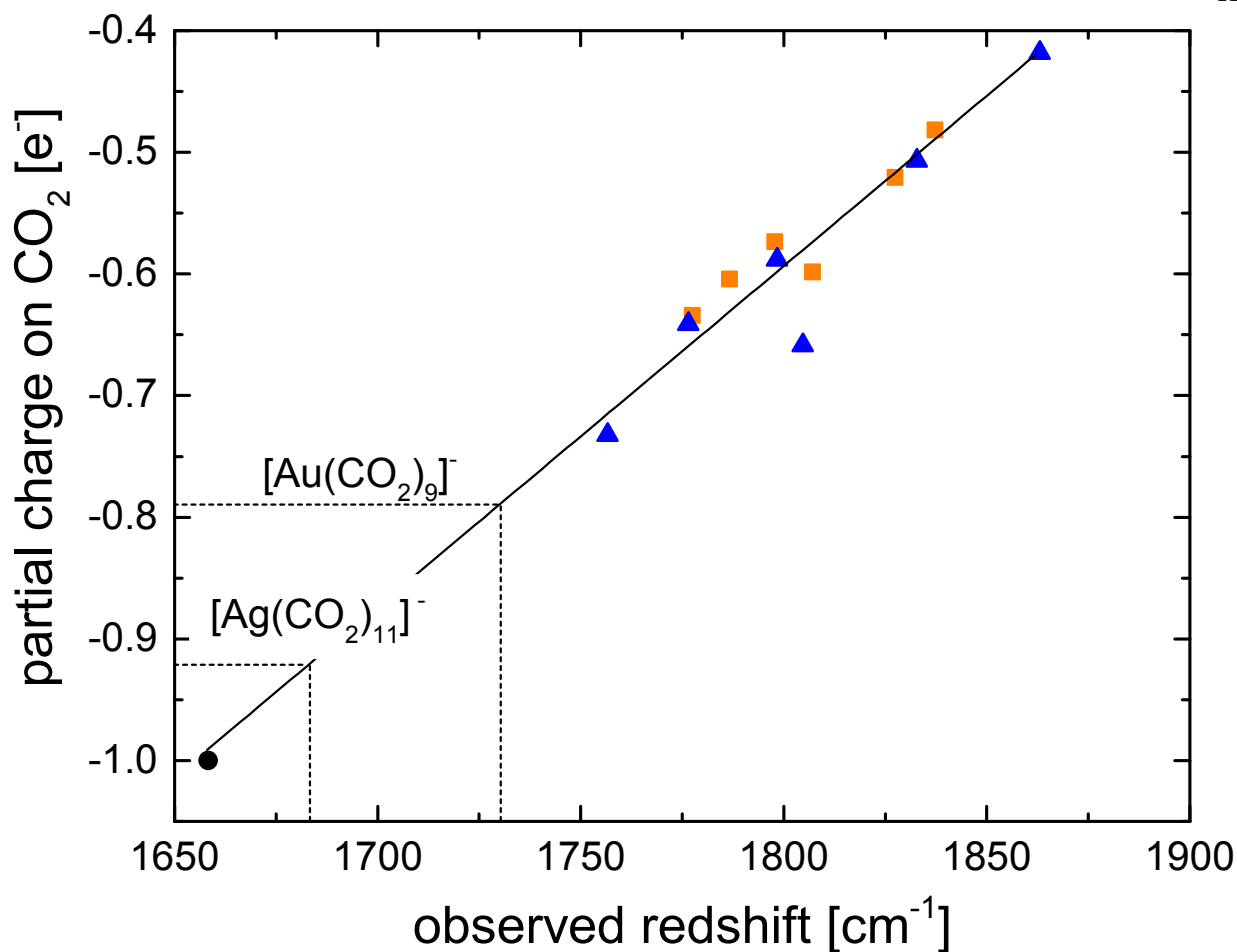


Figure 3.13: Plot of the antisymmetric CO stretching frequency in a formate core against the calculated partial charge localized on the activated CO₂ moiety for an assigned structure (see text). The blue triangles represent [Ag(CO₂)_n]⁻ clusters while the orange squares represent [Au(CO₂)_n]⁻ clusters. The black circle is the antisymmetric stretching frequency of a CO₂⁻ in a Ne matrix. [38] The solid line is a linear fit of all the points in the plot. The dashed lines represent the maximum charge transfer based on the most red shifted frequency observed.

3.3 [Co(CO₂)_n]⁻ and [Ni(CO₂)_n]⁻ Clusters

Organometallic complexes containing transition metals have found interest and application in many chemical contexts. In particular, transition metal complexes have been observed as important catalysts and support materials for catalysts. Unfortunately, there is little detailed information on the molecular level functionality of these catalytically relevant materials. In a deviation from the 9th column transition metals (or coinage metals Au and Ag), we shall consider the interactions

of CO₂ with cobalt and nickel anions. Since the electron configurations of these two metals are different from those of Au and Ag and from each other ([Ar]4s²3d⁷ for Co and [Ar]4s²3d⁸ for Ni), one would expect that different chemistry will likely be observed compared to what was reported in Section 3.2.

Cobalt has garnered interest as a catalyst in several prototypical reactions and in a number of metal-organic compounds. [78, 79] However, few spectroscopic studies have been performed *in vacuo* on cobalt containing species that involve a net negative charge. Some work has been carried out in the context of Fischer-Tropsch synthesis by Gerhards and coworkers, where the interaction of alcohols with atomic and cluster anions of Co was probed by IR spectroscopy. [78, 79] The Fischer-Tropsch process has received attention as a scheme by which alternative fuels can be generated by converting CO and H₂ to hydrocarbons. [80] This makes the conversion CO₂ to CO a process of potential industrial importance. Cobalt has in fact seen application in reduction schemes where CO₂ is converted to CO, a feedstock for Fischer-Tropsch processes. [81]

Nickel has also been utilized in a wide variety of catalytic applications. Some of these applications have involved being a direct component of the catalyst to being a part of the substrates and other support materials. [82–84] However, there are again few spectroscopic studies of mass selected species leaving the molecular level details of these materials and processes relatively uncharacterized. In the context of catalytically active materials, nickel has been shown to be a useful active component in dry reforming reactions between CH₄ and CO₂ where syngas (CO and H₂) is generated. [85] Additionally, nickel has also seen application in a number of electroplating processes utilizing supercritical CO₂. [86, 87] Kubiak and coworkers have shown that Ni ions embedded in an organic framework are active in the conversion of CO₂ to CO₃²⁻ and CO. [88] With the breadth of catalytic applications of Ni in processes involving CO₂, the properties of [Ni(CO₂)_n]⁻ clusters are of interest. In an effort to elucidate bonding trends, charge carrier structures, and solvation effects, this section will discuss the structures, charge distributions, and bonding trends of [Co(CO₂)_n]⁻ and [Ni(CO₂)_n]⁻ clusters.

3.3.1 Computational Methods

We employed density functional theory to aid in the interpretation of the experimental spectra. We used the TURBOMOLE v. 5.9.1 and 6.2 suite of programs [58] to perform calculations for $[\text{Co}(\text{CO}_2)_n]^-$ and $[\text{Ni}(\text{CO}_2)_n]^-$ clusters, respectively. The B3-LYP functional [59, 60] with a dispersion correction was used in both cases. For $[\text{Co}(\text{CO}_2)_n]^-$ clusters an older dispersion correction was used [89] while a more recent version was employed for $[\text{Ni}(\text{CO}_2)_n]^-$ clusters. [90] It has generally been found in this work that the form of the dispersion correction used does not change the outcome of the calculations appreciably when compared to each other. However, the use of a dispersion correction does lead to, on average, better results compared to calculations where the correction is not used. The def2-TZVPP basis sets were assigned to all atoms. [61] Vibrational frequencies were calculated using the AOFORCE program. [66, 67] The calculated vibrational frequencies were all scaled by 0.97537 to correct for anharmonicity. This factor was generated by comparing the calculated frequency for a free CO_2 to the measured antisymmetric stretch of CO_2 reported by Shimaniouchi. [37] All reported energies in this section are zero-point corrected and all partial charges were calculated using a natural population analysis. [68]

3.3.2 Infrared Spectra of $[\text{Co}(\text{CO}_2)_n]^-$ Clusters

Figure 3.14 shows the experimental spectra obtained monitoring the loss of one CO_2 molecule from $[\text{Co}(\text{CO}_2)_n]^-$ clusters. A number of stark differences are present when compared to the spectra observed for $[\text{Au}(\text{CO}_2)_n]^-$ and $[\text{Ag}(\text{CO}_2)_n]^-$ clusters. First, the onset of fragmentation is observed at $n = 3$ for Co rather than at $n = 2$ for Au and Ag. Second, there are two distinct and dominant spectral signatures present in the far IR region rather than only one for Au and Ag (not including the feature attributed to a CO_2^- charge carrier in $[\text{Ag}(\text{CO}_2)_n]^-$ clusters). Third, the frequencies of the peaks observed in $[\text{Co}(\text{CO}_2)_n]^-$ clusters are relatively invariant with respect to increasing solvation unlike in Au and Ag where $\sim 10 \text{ cm}^{-1}$ red and blue shifts were observed with each additional solvent molecule. These three initial observations likely indicate that the core structure

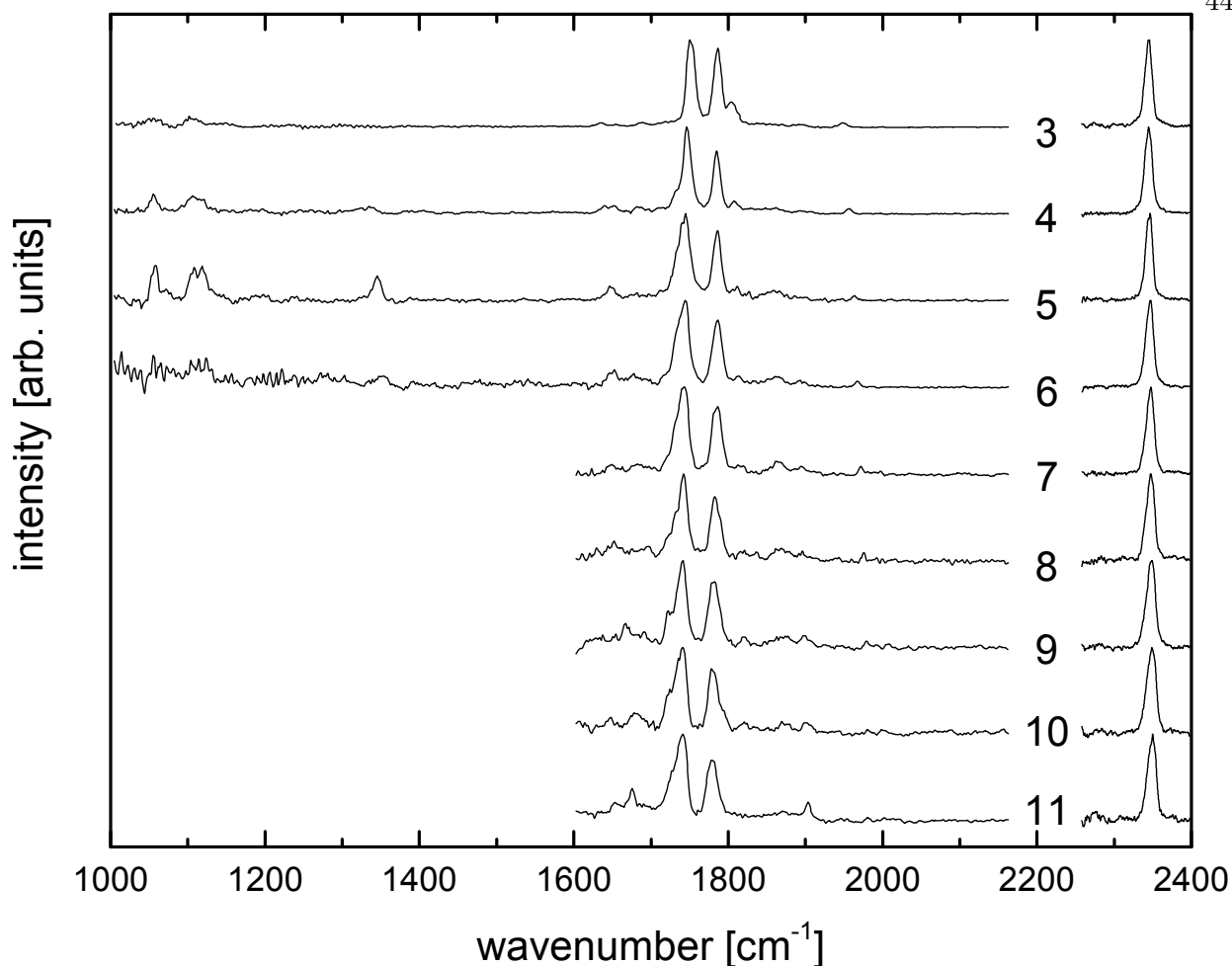


Figure 3.14: Experimental spectra of $[\text{Co}(\text{CO}_2)_n]^-$ clusters monitoring the loss of one CO_2 . The two regions (1000 cm^{-1} to 2150 cm^{-1} and 2270 cm^{-1} to 2400 cm^{-1}) are individually normalized and are therefore on different scales. Data was not acquired down to 1000 cm^{-1} for larger clusters due to low parent cluster intensity and correspondingly poor daughter anion signal intensity.

is significantly different from the formate motif observed in $[\text{Au}(\text{CO}_2)_n]^-$ and $[\text{Ag}(\text{CO}_2)_n]^-$ clusters (see Figure 3.15).

Complicating matters further is the possibility of both singlet and triplet electron configurations being present due to the $[\text{Ar}]4s^23d^8$ electron configuration of Co^- . As can be seen in Figure 3.16, calculations predict that different electron configurations result in unique core structures. For $[\text{Co}(\text{CO}_2)]^-$, the formate structure is predicted for a triplet configuration while a bidentate interaction of the CO_2 to the Co, where the CO_2 molecules make both a carbon-Co and an oxygen-Co

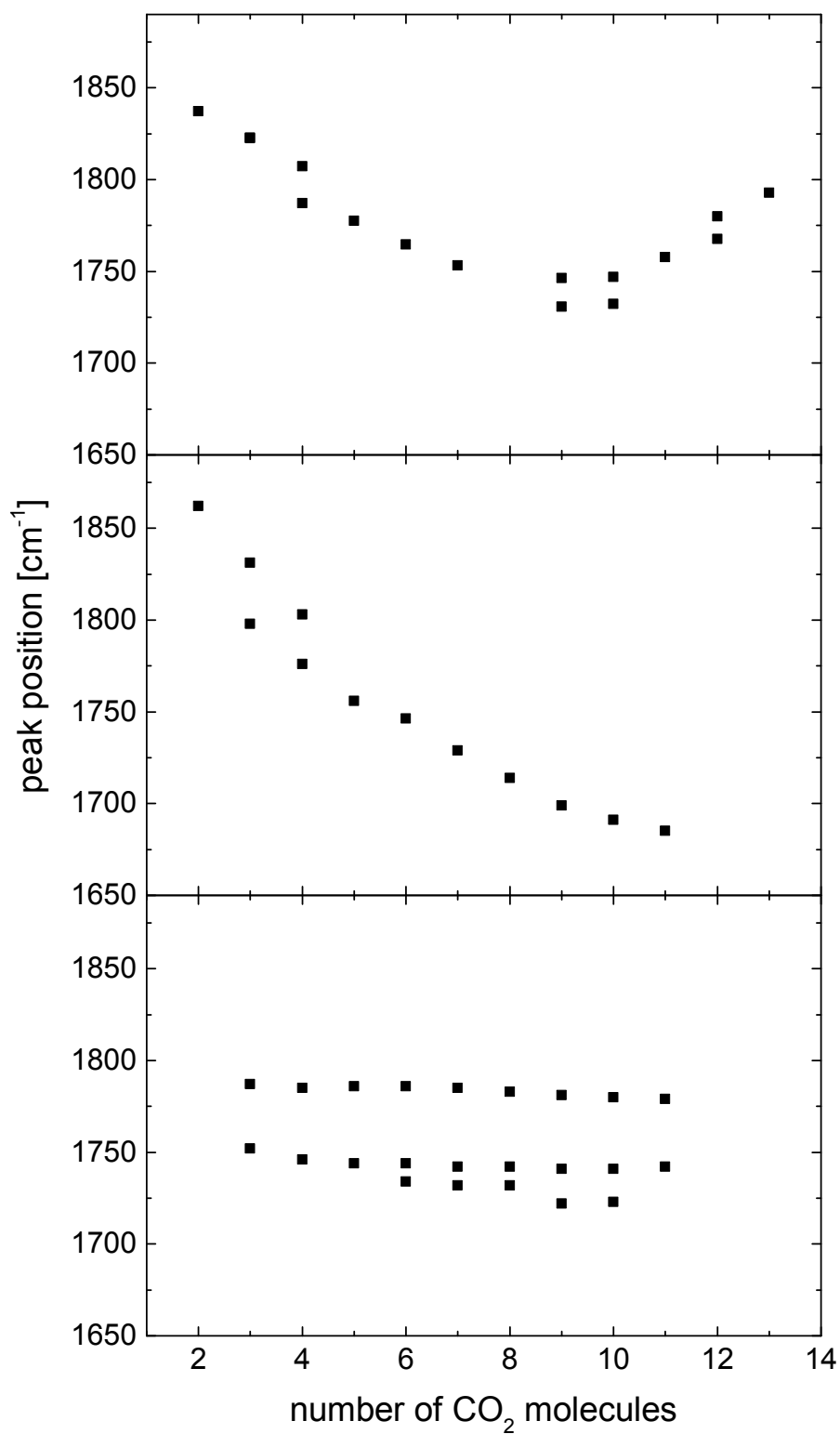


Figure 3.15: Comparison of the peak positions for $[\text{Au}(\text{CO}_2)_n]^-$ (top), $[\text{Ag}(\text{CO}_2)_n]^-$ (middle) and $[\text{Co}(\text{CO}_2)_n]^-$ (bottom) clusters. Note that fragmentation is first observed for Au and Ag at $n = 2$ while it not observed until $n = 3$ for Co. See text for discussion.

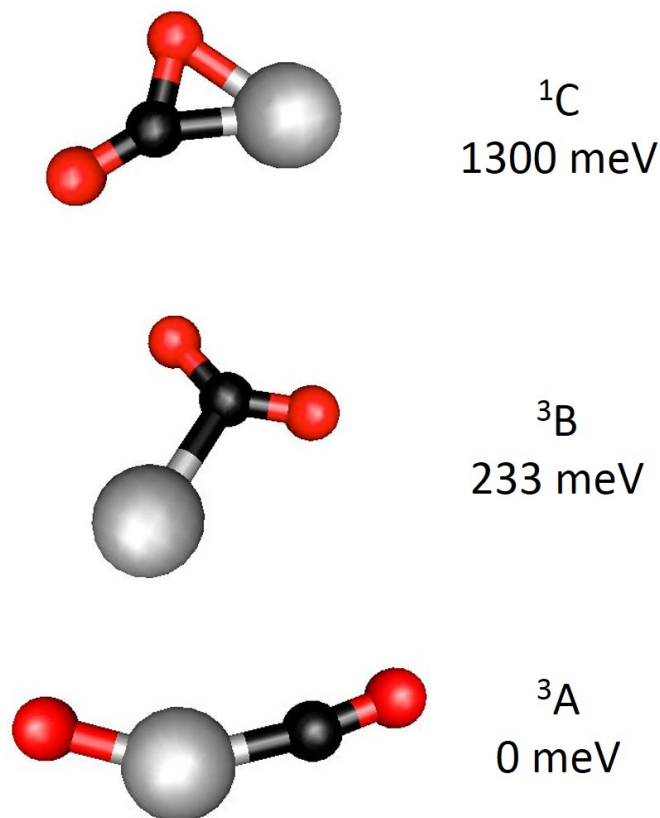


Figure 3.16: Structures of CoCO_2^- for singlet and triplet occupations. The capital letter denotes the core isomer while the subscript indicates a singlet or triplet conformation. Relative energies are given in units of meV.

bond, is predicted for a singlet configuration. The bidentate interaction shown in Figure 3.16 (${}^1\text{C}$) is referred to in the metal-organic literature as an η^2 interaction. [91] The lowest energy structure for $[\text{Co}(\text{CO}_2)]^-$ is isomer A where the Co atom is inserted across a C-O bond. It is already clear by looking at the predicted structures for $[\text{Co}(\text{CO}_2)]^-$ that there are a number of isomers different from the formate motif that will necessitate consideration to interpret the experimental spectra.

Since fragmentation is first observed at $n = 3$, it is likely that the core charge carrier is of the form $[\text{Co}(\text{CO}_2)_2]^-$ where the third CO_2 unit is the first solvent molecule and can be dissociated (this will be revisited below). Performing calculations on $[\text{Co}(\text{CO}_2)_2]^-$ species reveals a number of different structures (see Figure 3.17). The predicted global minimum structure is an insertion structure (see isomer D in Figure 3.17). In this family of structures the metal atom, here Co, is

inserted across a C-O double bond resulting in CO and O subunits bonded to the metal atom (similar to isomer A in Figure 3.16). The second CO₂ unit can then add to the lone O atom forming a CO₃ subunit. While the insertion structure is predicted to be the global minimum, we calculated a substantial barrier (1.5 eV) to formation of this family of structures. This barrier is largely a result of the breaking of the C-O double bond. Due to this barrier to formation, only a small population, if any, of this structure is expected to be found in the experiment.

The next higher energy family of structures are what we have termed butterfly structures. In this family of structures, two CO₂ molecules bind in a bidentate (η^2) fashion to the metal atom (here Co). There are a variety of orientations in which the two CO₂ molecules can be (see ¹E, ³E, and ³E* in Figure 3.17). Singlet and triplet occupations result in nearly perpendicular (¹E) and planar (³E) orientations of the two CO₂ molecules, respectively. Additionally, the CO₂ ligands can also be oriented such that the [CO₂CoCO₂]⁻ core exhibits C_{2h} symmetry (³E*). For all of these structures, the cobalt is predicted to be in a +1 oxidation state (Co(I)). The calculated binding energy of a CO₂ bound in a bidentate fashion to the Co atom is on the order of (8000 cm⁻¹ or 1 eV) which is well above the photon energy of our experiment. This explains why no fragmentation is observed until $n = 3$, i.e. when a solvent CO₂ exists.

The last family of structures that were calculated are those possessing a formate core similar to the core structure observed in [Au(CO₂)_{*n*}]⁻ and [Ag(CO₂)_{*n*}]⁻ clusters (see structure ³B(1) in Figure 3.17). The formate structure is only recovered for a triplet electron configuration and is predicted to be substantially higher in energy than any of the other structures calculated for [Co(CO₂)₂]⁻ (see Figure 3.17). It is also unlikely that the formate core exists in any detectable amount since no fragmentation was observed for $n = 2$ where one should be able to fragment isomer B(1).

At $n = 3$, the core structures presented in Figure 3.17 can be solvated. A comparison of the calculated spectra of these core structures with the [Co(CO₂)₃]⁻ experimental spectrum reveals that the butterfly family of structures most accurately recovers the experimental spectrum (see Figure 3.18). The insertion (³D), formate (³B(1)) and C_{2h} symmetric butterfly (³E*) structures do

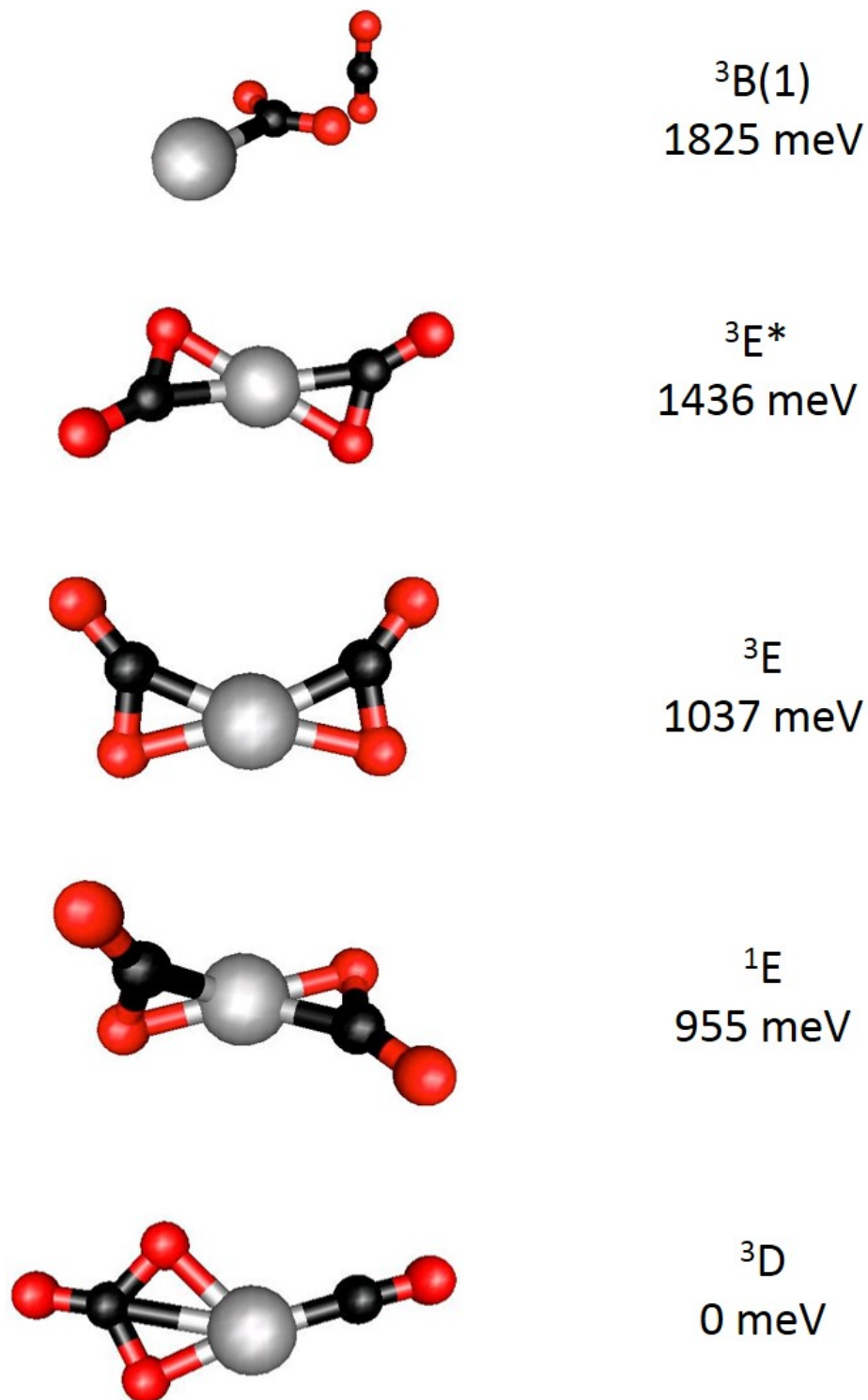


Figure 3.17: Lowest energy calculated structures for $[\text{Co}(\text{CO}_2)_2]^-$. The letter denotes the core structure while the number in parentheses indicates the number of solvent molecules and the superscript denotes singlet or triplet configuration. Relative energies are given in meV.

not recover the major features of the experimental spectrum. Unfortunately, there is not a clear difference between the singlet and triplet butterfly structures (^1E and ^3E) that would unambiguously distinguish the two from each other. At this stage, the dominant peaks in the experimental spectrum are tentatively assigned to the butterfly isomers ^1E and ^3E . It should be noted that the singlet butterfly isomer has slightly better agreement with the experimental spectrum both positionally and with respect to the predicted intensity ratio of the two dominant peaks. However, the possibility of a mixture of singlet and triplet butterfly structures cannot be discounted.

To further corroborate the assignment of the dominant features in the experimental spectra to those of the butterfly structures (^1E and ^3E), it is necessary to calculate the effect of solvation on the calculated frequencies. The experimental peak positions do not shift appreciably with increasing solvation. Figure 3.19 shows a comparison of the calculated spectra for different solvation positions around the butterfly core to the experimental spectrum of $[\text{Co}(\text{CO}_2)_4]^-$. Clearly, calculations predict little variation in the vibrational frequencies as a function of solvation position. This observation is also corroborated by the almost negligible differences in the calculated charge distributions on the butterfly core of the various solvation isomers (see Table 3.1) indicating that the butterfly cores are indeed robust core species. At this point the dominant peaks in the $[\text{Co}(\text{CO}_2)_n]^-$ spectra are assigned to both of the butterfly isomers (^1E and ^3E).

Table 3.1: Calculated partial charges for the solvation isomers of $[\text{Co}(\text{CO}_2)_4]^-$ presented in Figure 3.19. Isomers 1 - 4 refer to the top to bottom structures presented in Figure 3.19. The column labeled Solvent indicates the amount of partial charge delocalized into the solvent environment. The partial charges are reported in units of e .

Solvation Isomer	Co	CO ₂ (1)	CO ₂ (2)	Solvent
Isomer 1	+0.93	-1.0	-0.91	-0.02
Isomer 2	+0.92	-1.0	-0.91	-0.01
Isomer 3	+0.92	-1.0	-0.91	-0.01
Isomer 4	+0.94	-0.96	-0.97	-0.01

The last set of spectroscopic features to discuss are the minor peaks around 1635 cm^{-1} , 1685 cm^{-1} , and 1950 cm^{-1} (the 1950 cm^{-1} feature first appears at $n = 4$). All of these features can

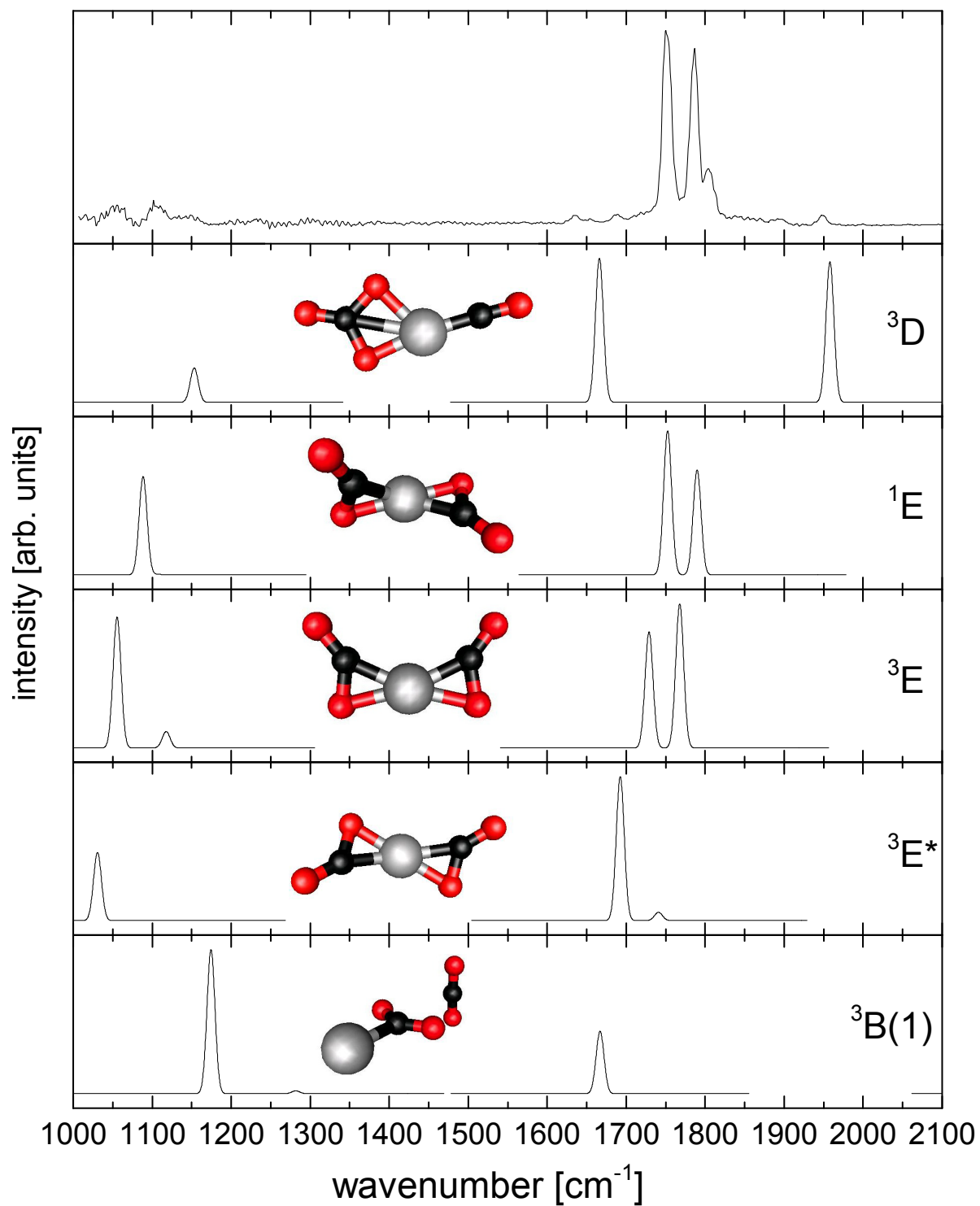


Figure 3.18: Comparison of the calculated lowest energy structures for $[\text{Co}(\text{CO}_2)_2]^-$ to the experimental spectrum. The letter denotes the core structure while the number in parentheses indicates the number of solvent molecules and the superscript denotes singlet or triplet configuration. Relative energies are given in meV.

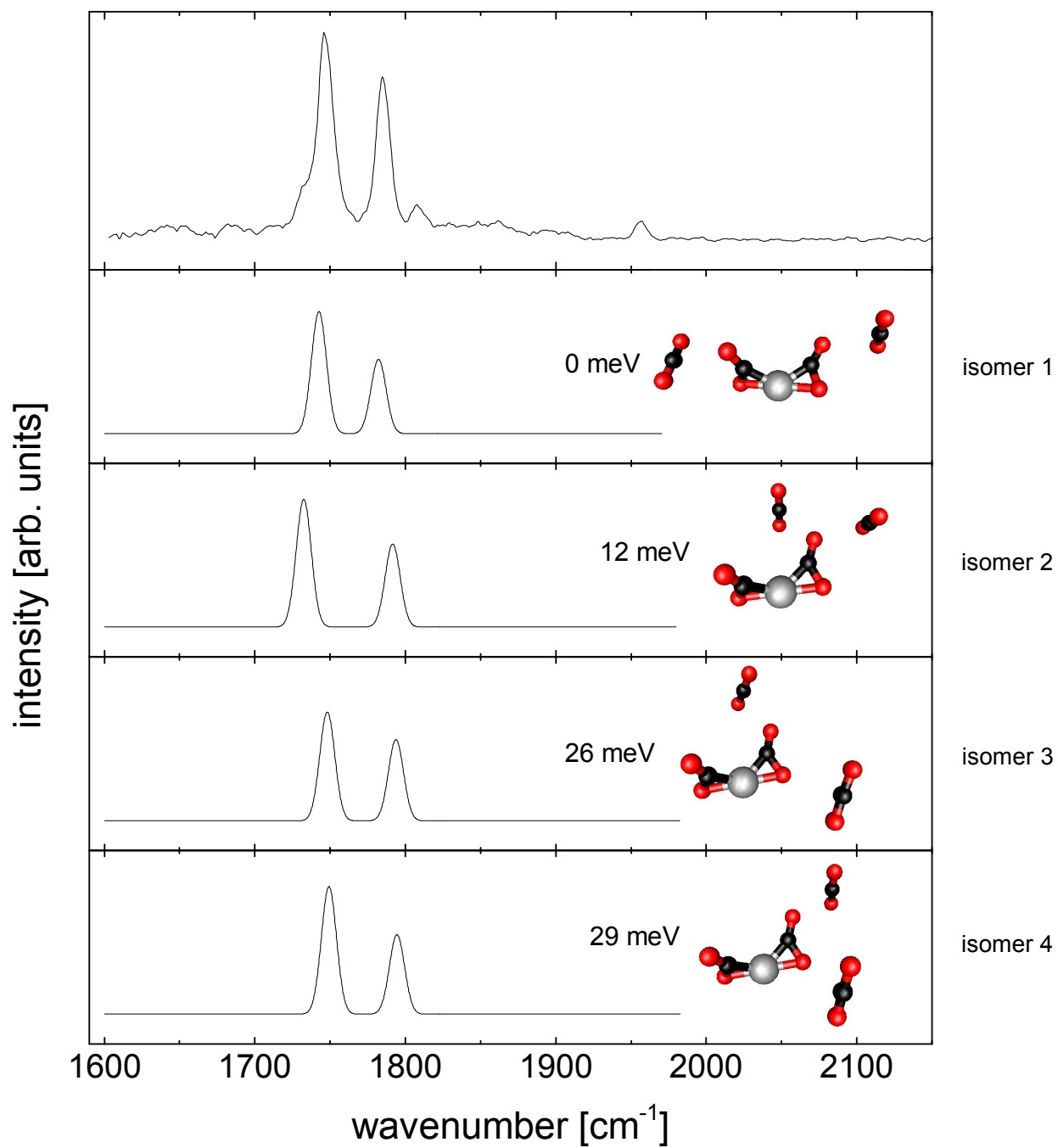


Figure 3.19: Comparison of calculated different solvation isomers around structure ^1E to the experimental spectrum for $[\text{Co}(\text{CO}_2)_4]^-$. Relative energies are given in meV.

be generally accounted for by the insertion structure (3D), the C_{2h} symmetry butterfly ($^3E^*$) and a species where the cluster consists of the cobalt atom, a CO_2 ligand and a C_2O_4 unit (G) (see Figure 3.20). Structure G will be discussed further in the next Section but for now it worth noting that G has a $[Co(CO_2)_3]^-$ core and would be first observable at $n = 4$. It is difficult to make a definite assignment of these weak features as their signal to noise ratio is poor compared to that of the dominant features. However, due to the position of the calculated and measured frequencies, it is likely that there is a small population of the insertion structure (3D) and possibly a mixture of structures $^3E^*$ and G being generated.

The structure of the butterfly core is reminiscent of many inorganic species. [91] It is informative to compare the calculated molecular orbitals of the singlet butterfly structure (1E) to those of general metal ligand complexes (ML_x). For an octahedral ML_6 complex, the five d -orbitals are split into the t_{2g} (lower energy) and the e_g (higher energy) orbitals. This is due to overlap of the ligands with the $d_{x^2-y^2}$ and d_{z^2} orbitals on the metal while there is little overlap with the d_{xy} , d_{xz} and d_{yz} orbitals. If two of the equatorial ligands are removed, a ML_4 complex is formed and the $d_{x^2-y^2}$ orbital is stabilized relative to the d_{z^2} orbital. This stabilization is a result of decreased overlap of ligands with the $d_{x^2-y^2}$ orbital (see left side of Figure 3.21). [92]

The ML_4 complex has a structural appearance close to that of the butterfly core, so one might assume the molecular orbitals are similar and that the $[CO_2CoCO_2]^-$ core could be described as such. However, the bidentate interaction creates a three membered ring which keeps the two metal-ligand bonds very close to each other. This interaction could also be thought of as pseudo-monodentate where even though two bonds are being formed, they are essentially bonding to the same d -orbital on the metal. If this were the case, one would not expect ML_4 behavior but rather ML_2 (see center column of Figure 3.21) where now the d_{z^2} orbital will be stabilized more than the $d_{x^2-y^2}$ orbital. [92]

The top five occupied molecular orbitals (HOMOs) were calculated in addition to the next two lowest lying unoccupied molecular orbitals (LUMOs) for the isomer 1E (see right side of Figure 3.21). The structure of the HOMO is similar to that of the d_{z^2} orbital while the LUMO bears

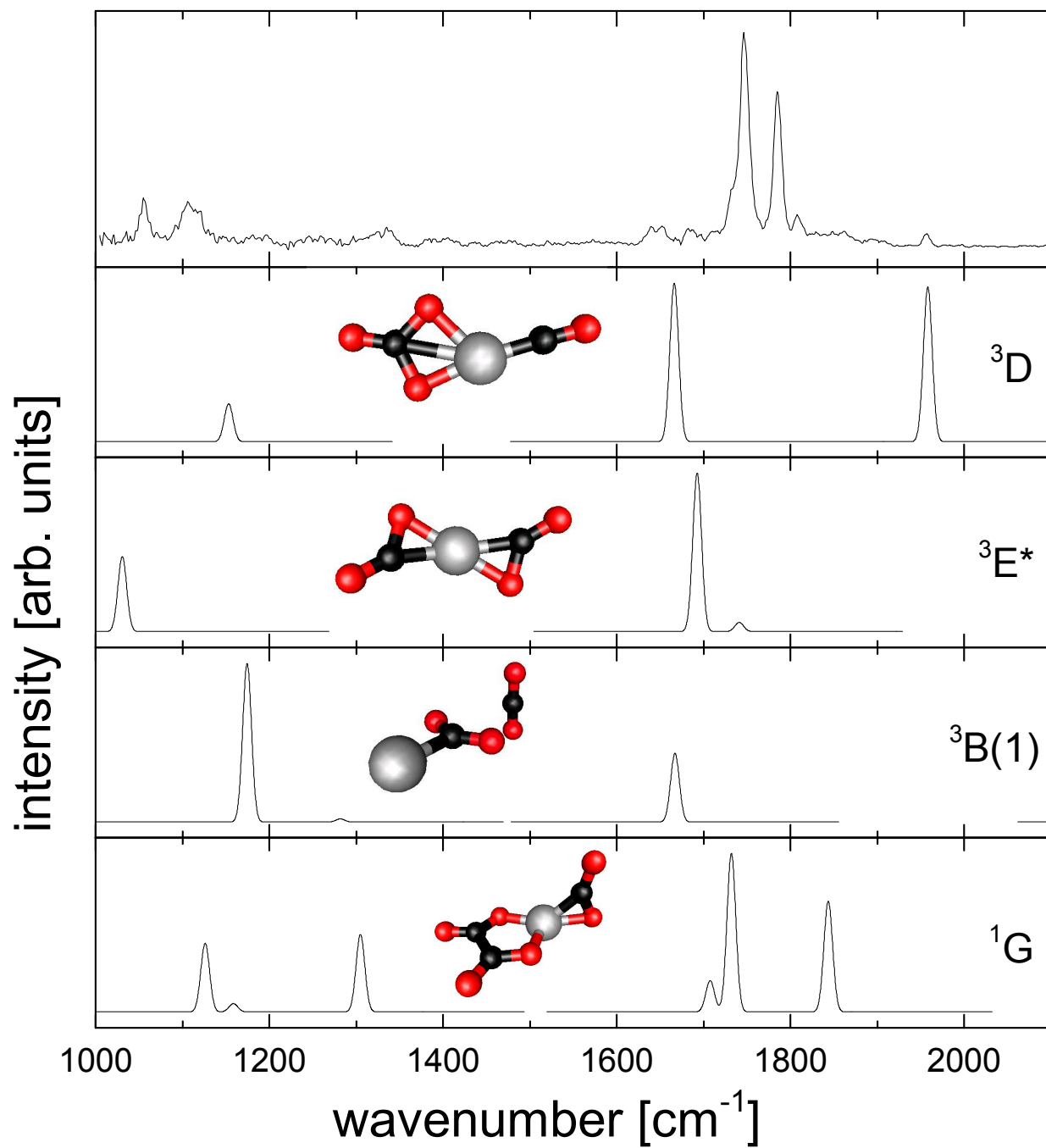


Figure 3.20: Comparison of calculated likely minor isomers to the experimental spectrum for $[\text{Co}(\text{CO}_2)_4]^-$. Relative energies are given in meV. See text for additional discussion of the isomers.

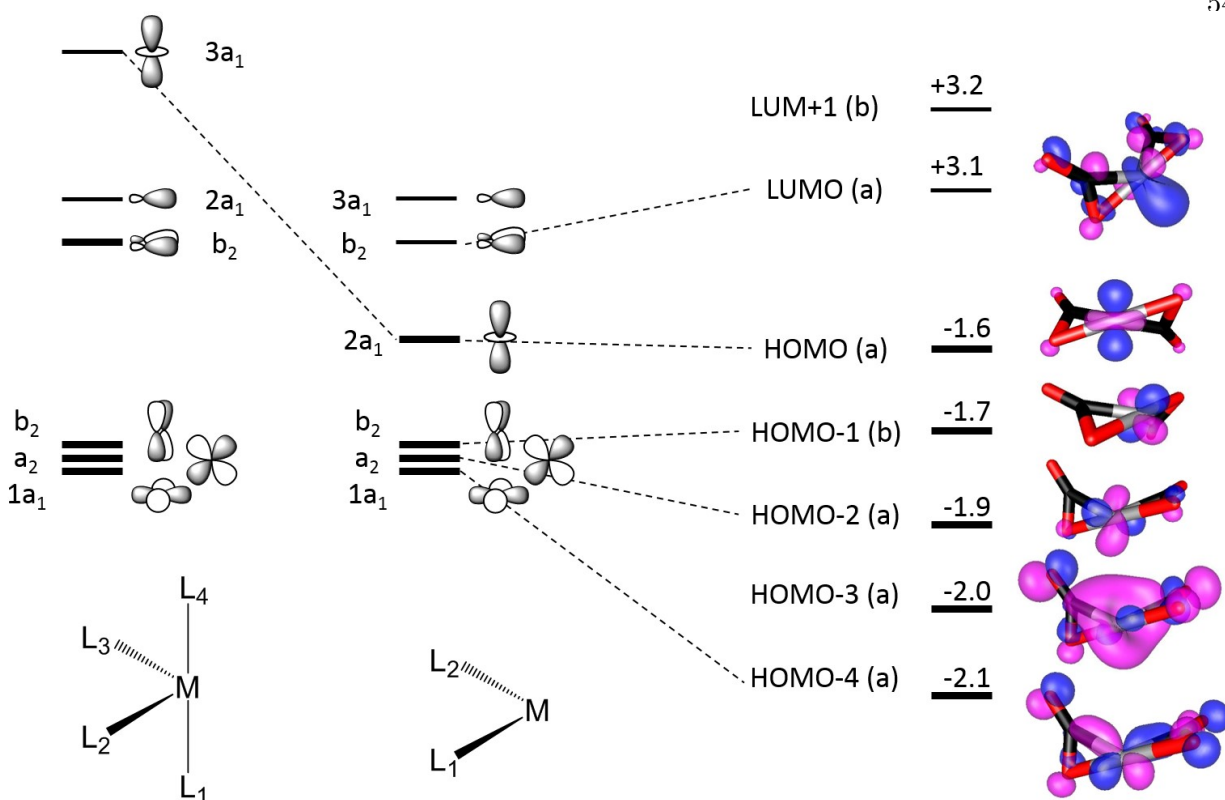


Figure 3.21: Orbitals in the d-block of the $[\text{CO}_2\text{CoCO}_2]$ core ion expected for a “butterfly” ML_4 configuration (left) and a bent ML_2 configuration (center), compared to the calculated molecular orbitals for the singlet core ion structure ^1E (right). Note that the HOMO-3 orbital is not part of the d-block but is shown for completeness. The occupied orbitals are shown as bold horizontal lines for each configuration. Calculated orbital energies are given in eV. The dotted lines show how the d_{z^2} orbital changes from ML_4 to ML_2 and correlation between calculations and ligand field theory. Note that the definition of the z -axis is not along the symmetry axis of the complex but rather is defined by the d_{z^2} character of the HOMO.

resemblance to the half interacting $d_{x^2-y^2}$ orbital in both ML_2 and ML_4 complexes. The energetic ordering of the HOMO and LUMO suggest that the butterfly complex bears more resemblance to a ML_2 complex than to a ML_4 complex suggesting that the core CO_2 ligands can be approximated as monodentate.

In the organometallic literature the bidentate CO_2 bonding is referred to as an η^2 complex, since there are two bonds from the ligand to the metal center. The butterfly structures are unique as most experiments have only observed one ligand η^2 complexes. [91] Here, there are two CO_2

ligands bonding to the metal atom creating a diligand η^2 complex. It is also interesting to note that while inorganic chemistry has characterized this bonding motif with two metal-ligand bonds, the MO picture appears to treat each CO_2 as a monodentate ligand. In addition to the unique number of ligands, the oxidation state of the Co in these clusters is also uncommon. Cobalt tends to form complexes where it is in an oxidation state +2. In these experiments, only Co(I) complexes were observed. Co(I) has been seen before in disproportionation reactions and in complexes with bipyridine used for water splitting and CO_2 reduction to CO but, again, is not a common species. [93,94] These two observations of the interaction of CO_2 with Co in the presence of an excess electron suggest that there are less explored synthetic routes and unknown novel chemistry involving Co^- and CO_2 .

3.3.3 Infrared Spectra of $[\text{Ni}(\text{CO}_2)_n]^-$ Clusters

Figure 3.22 shows the experimental spectra obtained by monitoring the loss of one CO_2 molecule from $[\text{Ni}(\text{CO}_2)_n]^-$ clusters ($n = 2 - 8$). The spectra, while clearly different from those of $[\text{Co}(\text{CO}_2)_n]^-$ clusters (see Figure 3.14), exhibit similar trends to those present in Co. The spectra tend to not shift as the number of CO_2 molecules increases and there are multiple dominant peaks present. These observations and the fact that the first solvent peak is observed at $n = 3$ likely indicates that, as is the case for Co, the dominant core species consists of two CO_2 units in addition to the Ni atom. There are, however, two primary differences. First, even though there is no signature of a solvent CO_2 molecule, photodissociation is observed for $n = 2$ where broad unresolved peaks are recovered. Second, rather than two dominant peaks as was observed in $[\text{Co}(\text{CO}_2)_n]^-$ clusters, three dominant features are present in $[\text{Ni}(\text{CO}_2)_n]^-$.

Since the experimental spectra bear some resemblance to those of $[\text{Co}(\text{CO}_2)_n]^-$, it is reasonable to compare a similar set of calculated structures. To be consistent with Section 3.3.2, the same designations for core structures and convention for indicating solvation will be used here. Figure 3.23 shows the energetically lowest lying calculated structures. Since there is only one unpaired electron for Ni^- , there is only one spin multiplicity to be concerned with here. The insertion

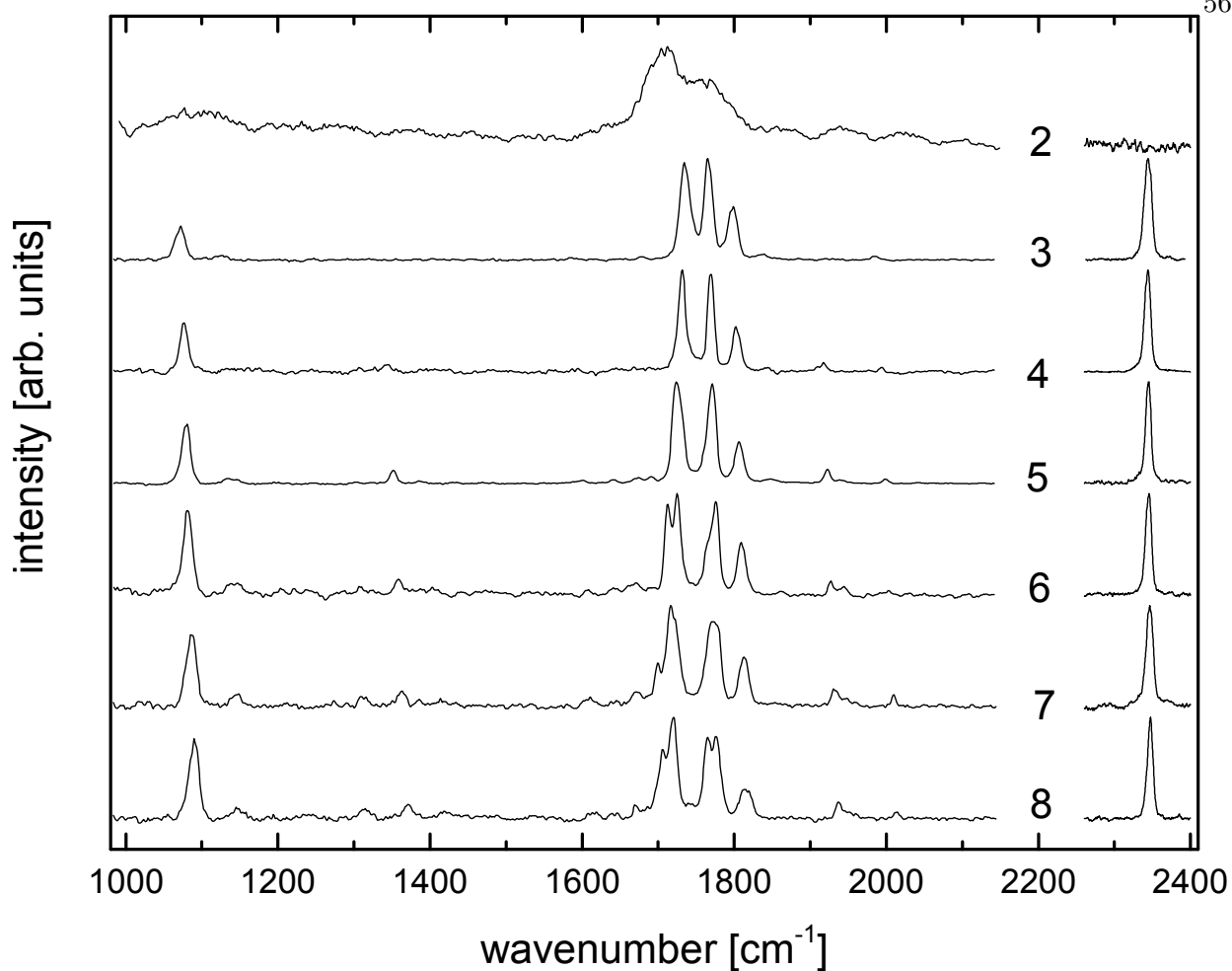


Figure 3.22: Experimental spectra of $[\text{Ni}(\text{CO}_2)_n]^-$ clusters. The numbers indicate the number of CO_2 molecules (n) present in each cluster. The traces on the left and right are individually normalized and are on different scales.

structure (D) is again predicted to be the global minimum and (like in $[\text{Co}(\text{CO}_2)_n]^-$ clusters) is predicted to have a roughly 1.5 eV barrier to formation (see Appendix B). The butterfly family of structures are also predicted to be low in energy. However, different from in $[\text{Co}(\text{CO}_2)_n]^-$ clusters, the C_{2h} butterfly (E^*) is calculated to be closer in energy to the asymmetric butterfly (E). The other major difference is that a structure containing a C_2O_4 subunit (F) is calculated to be energetically relevant for $[\text{Ni}(\text{CO}_2)_n]^-$ clusters.

A comparison of the core structures discussed above possessing one solvent CO_2 to the ex-

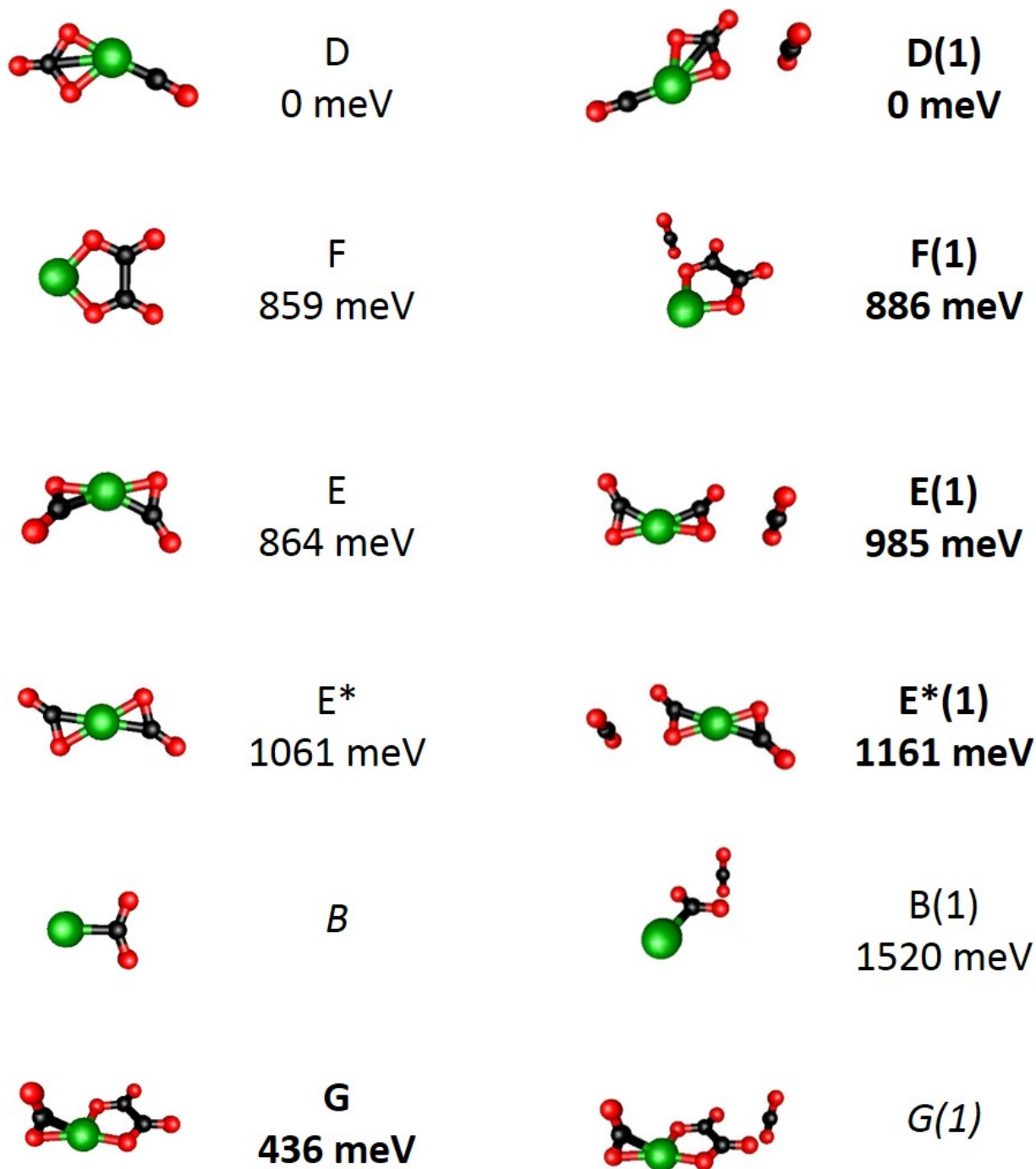


Figure 3.23: Calculated lowest energy structures for $[\text{Ni}(\text{CO}_2)_n]^-$ clusters. The capital letter indicates the core structure and the number denotes the number of solvent molecules present. Plain text indicates $n = 2$ structures while **bold** text denotes $n = 3$ structures. Relative energies are reported in meV and are given with respect to the lowest energy structure for a given cluster size. Relative energies for isomers B and G are not reported as there are no structures to compare them with and are shown in *italic* text.

perimental spectrum of $[\text{Ni}(\text{CO}_2)_3]^-$ is shown in Figure 3.24. It is clear that the insertion structure (D(1)), the formate motif (B(2)) and the isomer containing the C_2O_4 subunit (F(1)) do not recover the dominant peaks in the experimental spectrum. Only the two butterfly structures accurately recover the experimental spectrum. Because of the symmetry of isomer E^* the antisymmetric stretches of the two CO_2 moieties are coupled. This results in only the out of phase combination having an appreciable oscillator strength since the in-phase combination of the antisymmetric stretches results in a negligible change of the dipole moment of the core species. The single peak recovered from structure E^* is predicted to lie between the two frequencies calculated for isomer E. These two structures are close in energy and the combination of their calculated frequencies accounts for the three dominant peaks observed in the experimental spectrum. Two additional structures were predicted but are high in energy and do not recover the experimental spectra (see Appendix B).

It is necessary to check the effect of solvation on the calculated vibrational frequencies and core charge distributions for isomers E and E^* . The experimental spectra suggest that the effect of solvation is slightly more pronounced than it is in $[\text{Co}(\text{CO}_2)_n]^-$ clusters since the dominant peaks shift by 3 cm^{-1} to 5 cm^{-1} with increasing cluster size and bifurcate at large cluster size (i.e. $n \geq 6$). Figure 3.25 shows a comparison of various solvation positions around isomer E. There is a larger variation in the calculated vibrational frequencies as a function of solvation position in $[\text{Ni}(\text{CO}_2)_4]^-$ compared to $[\text{Co}(\text{CO}_2)_4]^-$ clusters (see Figure 3.19). However, the variations in peak position as a function of solvation are still not as large as they are in $[\text{Au}(\text{CO}_2)_n]^-$ and $[\text{Ag}(\text{CO}_2)_n]^-$. These calculations and comparisons suggest that the core charge distribution for $[\text{Ni}(\text{CO}_2)_n]^-$ clusters (specifically isomer E^*) is slightly more polarizable than comparable structures in $[\text{Co}(\text{CO}_2)_n]^-$ clusters.

Like in $[\text{Co}(\text{CO}_2)_n]^-$, there are a number of minor peaks observed in the $[\text{Ni}(\text{CO}_2)_n]^-$ spectra. In particular, there are peaks observed at 1350 cm^{-1} , 1920 cm^{-1} and 2000 cm^{-1} . Referring back to Figure 3.24, it appears as though the insertion structure could account for the peak observed near 2000 cm^{-1} . The predicted vibration at 1675 cm^{-1} for isomer D is likely present in the experimental

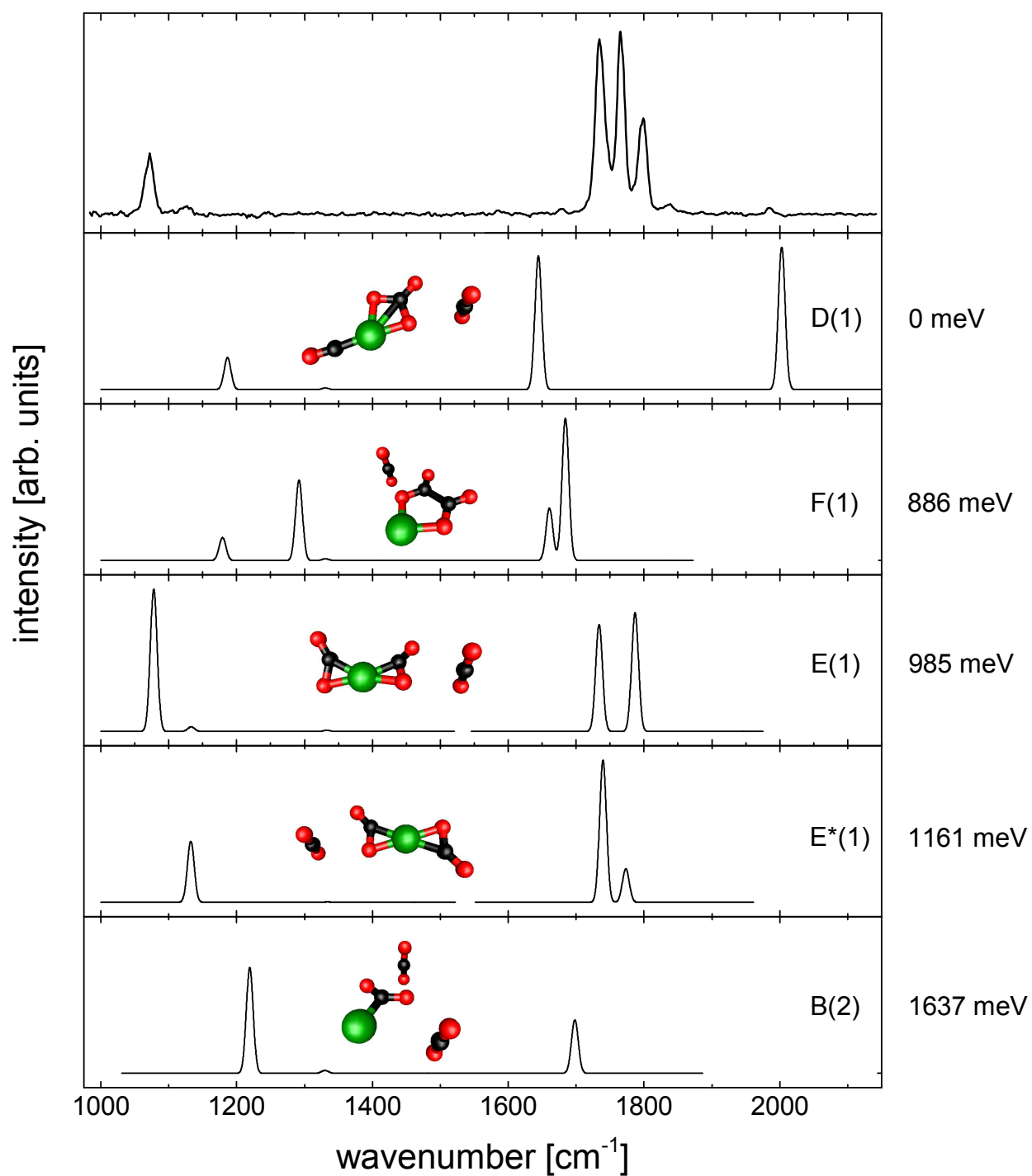


Figure 3.24: Comparison of calculated structures for $[\text{Ni}(\text{CO}_2)_3]^-$ to the experimental spectrum for $n = 3$. See Figure 3.23 and text for discussion on the structures. Relative energies are given in meV.

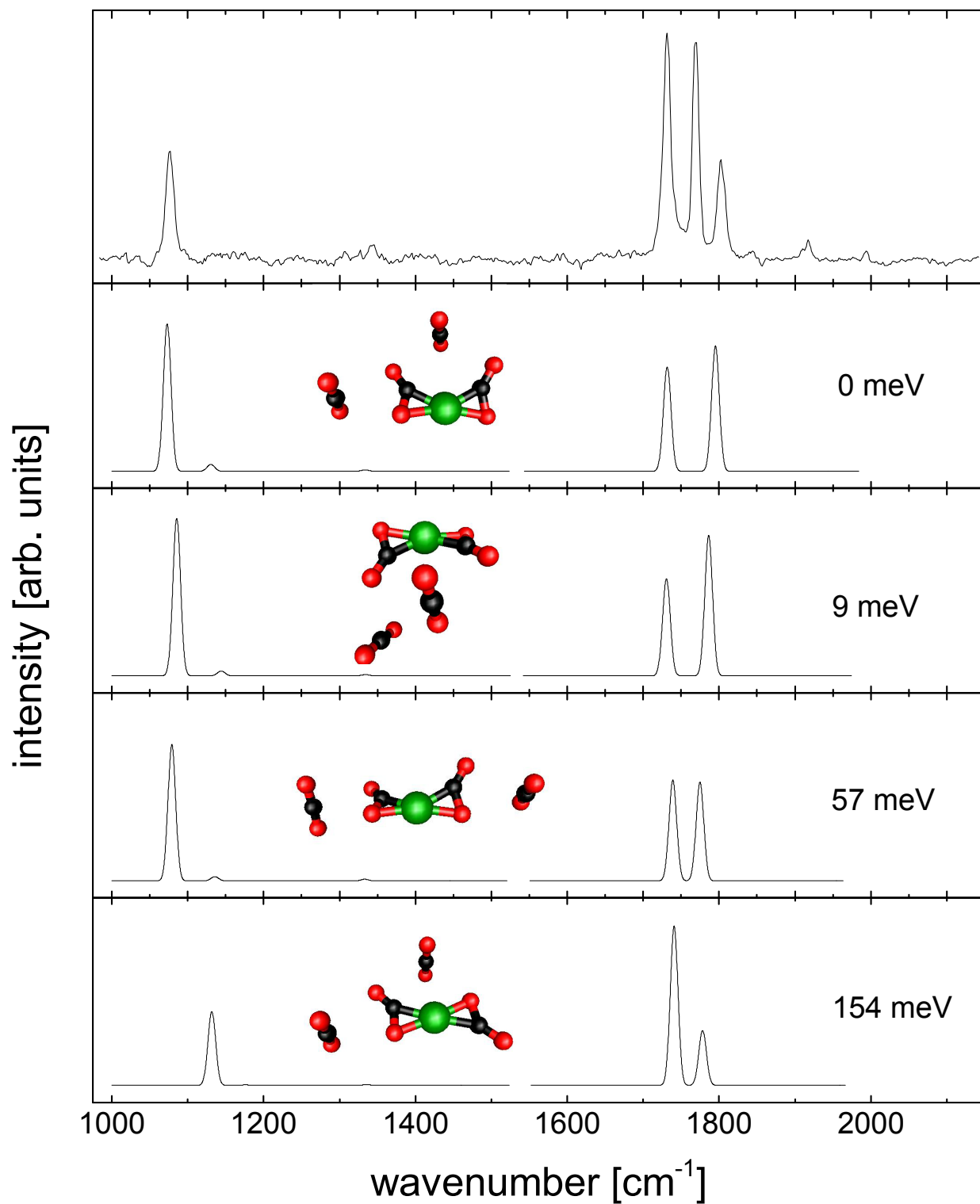


Figure 3.25: Comparison of various solvation positions around the core isomer E. Note that the predicted spectrum shifts only slightly with varying solvation position. The calculated spectrum of isomer E* is shown on the bottom for completeness.

spectra but is obscured by the low signal to noise ratio below the dominant features. The other two peaks are observed for the first time at $n = 4$, indicating that the core species responsible is likely of the form $[\text{Ni}(\text{CO}_2)_3]^-$ where the fourth CO_2 would be the first solvent molecule. Surveying the possible core species of the form $[\text{Ni}(\text{CO}_2)_3]^-$ reveals only one reasonable structure. That structure is shown in Figure 3.23 (isomer G) and consists of CO_2 and C_2O_4 subunits (a similar structure was also found in $[\text{Co}(\text{CO}_2)_n]^-$ clusters).

To definitively assign the experimental spectra, exploratory calculations on increased solvation of isomers D, E, E^* and G were performed to simulate the evolution of the experimental spectra. The results of these exploratory calculations is shown in Figure 3.26. It is clear that these four structures do account for the observed experimental peaks and recover the red and blue shifts occurring with increasing solvation. In particular, note that structure G does indeed clearly recover the two peaks at 1350 cm^{-1} and 1920 cm^{-1} and their solvation mediated blue shift. Based on the agreement of calculations with experiment, the three dominant peaks are assigned to the two butterfly structures (E and E^*), the peak at 2000 cm^{-1} to the insertion structure (D), and the two peaks at 1350 cm^{-1} and 1920 cm^{-1} to structure G.

It is worth noting that the calculated charge distribution on the dominant core species indicates two negatively charged CO_2 ligands and a positively charged Ni atom. However, isomer G is the only structure predicted to contain a Ni(I) atom. Instead, the charge on the Ni atom is $\sim +0.5 e$ for the butterfly structures and $\sim +0.7 e$ for the insertion isomer (see Table 3.2). This is in contrast to $[\text{Co}(\text{CO}_2)_n]^-$ clusters where the Co atom was exclusively in an oxidation state +1.

The last spectrum to discuss is that of $[\text{Ni}(\text{CO}_2)_2]^-$ (see Figure 3.22). The peaks observed at this cluster size are broad and unresolved. Since there is no solvent peak observed, the fragmented CO_2 must come from the core species. Since the binding energy of a core CO_2 is on the order of 10000 cm^{-1} , it is likely that this spectrum is due to multiphoton excitation of a hot bare core species (internal energy $\sim 5000\text{ cm}^{-1}$). The $n = 2$ cluster size was found in high abundance compared to the rest of the $[\text{Ni}(\text{CO}_2)_n]^-$ clusters. It is likely that due to the high abundance of parent ions at this cluster size and the lack of a one photon dissociation channel, multiphoton dissociation

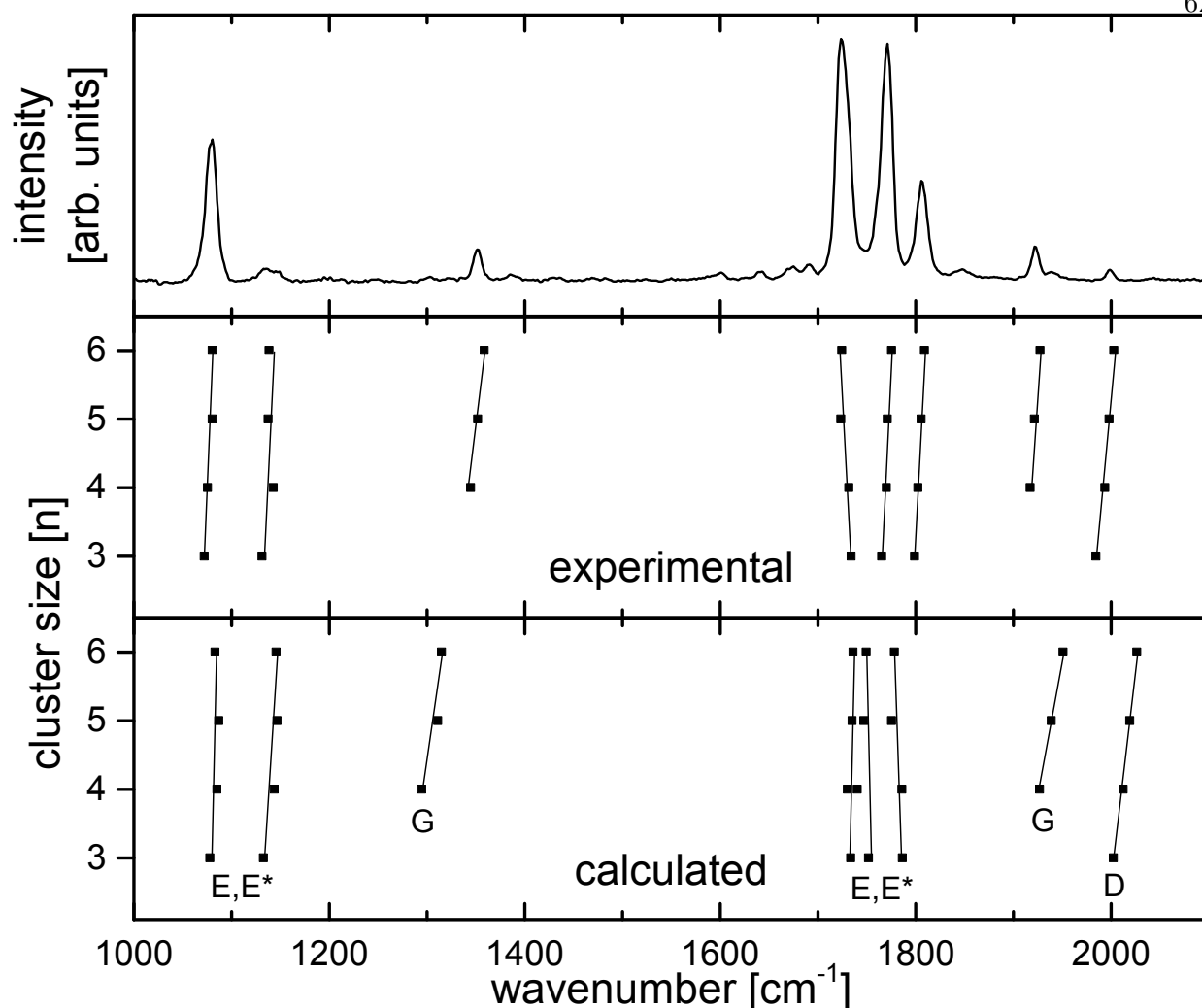


Figure 3.26: Calculated vibrational frequencies as a function of cluster size for assigned core structures compared to the experimental peak positions as a function of cluster size (see text for discussion). The letters indicate the core structure giving rise to each set of peaks (see Figures 3.23). The experimental spectrum for $[\text{Ni}(\text{CO}_2)_5]^-$ is shown on top for reference.

is observable for this cluster size. Figure 3.27 shows a comparison of the calculated spectra for structures E and F with the experimental spectrum for $n = 2$. The calculated peaks are in the same general frequency range as the broad experimental peaks and overlap with the envelope of the features in the experimental spectrum. Even though a combination of isomers E and F appears to reasonably recover the experimental spectrum, the fact that isomer F does not account for any of the dominant peaks at larger cluster sizes (i.e. $n \geq 3$) puts into question the likelihood that isomer

Table 3.2: Calculated partial charges of the core isomers for $[\text{Ni}(\text{CO}_2)_n]^-$. See Figure 3.23 and discussion in the text for additional information on the core structures. The column labeled Solvent indicates the amount of partial charge delocalized into the solvent environment. The partial charges are reported in units of e .

Core Structure	Ni	CO ₂	CO ₃	CO	C ₂ O ₄	Solvent
D	+0.67		-1.48	-0.19		0.00
F	+0.66				-1.66	0.00
E	+0.49	-0.75				+0.01
E*	+0.41	-0.71				+0.01
B	-0.35	-0.65				0.00
G	+0.99	-0.42			-1.57	0.00

F exists at $n = 2$. However, the assignment of the $n = 2$ spectrum is nearly impossible to confirm due to the low signal to noise ratio and the lack of a reference to discern multiphoton from single photon effects.

For both $[\text{Co}(\text{CO}_2)_n]^-$ and $[\text{Ni}(\text{CO}_2)_n]^-$ clusters, a “butterfly” core is the dominant structural motif. For Co, the two CO₂ ligands are nearly perpendicular to each other in isomer E while there is only a 42° angle between the two CO₂ moieties for the same isomer in Ni. For both Co and Ni there are signatures of the insertion structure and other minor isomers. The existence of these structures indicates that there are multiple ways in which CO₂ can bind to both Co and Ni atoms unlike what was observed in Au and Ag.

The calculated polarizability of the butterfly core increases from Co to Ni. At the same time, the electronegativity of the metal increases and the calculated charge on the metal becomes more negative. All three of these observations are connected. As the electronegativity of the metal increases, the metal will localize more of the excess charge onto itself. This results in the less positive partial charge on Ni compared to Co. Additionally, since Ni is now able to accommodate more of the excess charge, the polarizability of the core increases as electrons can now move more freely across the butterfly core.

Ni and Co form similar structures with CO₂ in the presence of an excess electron. Neither

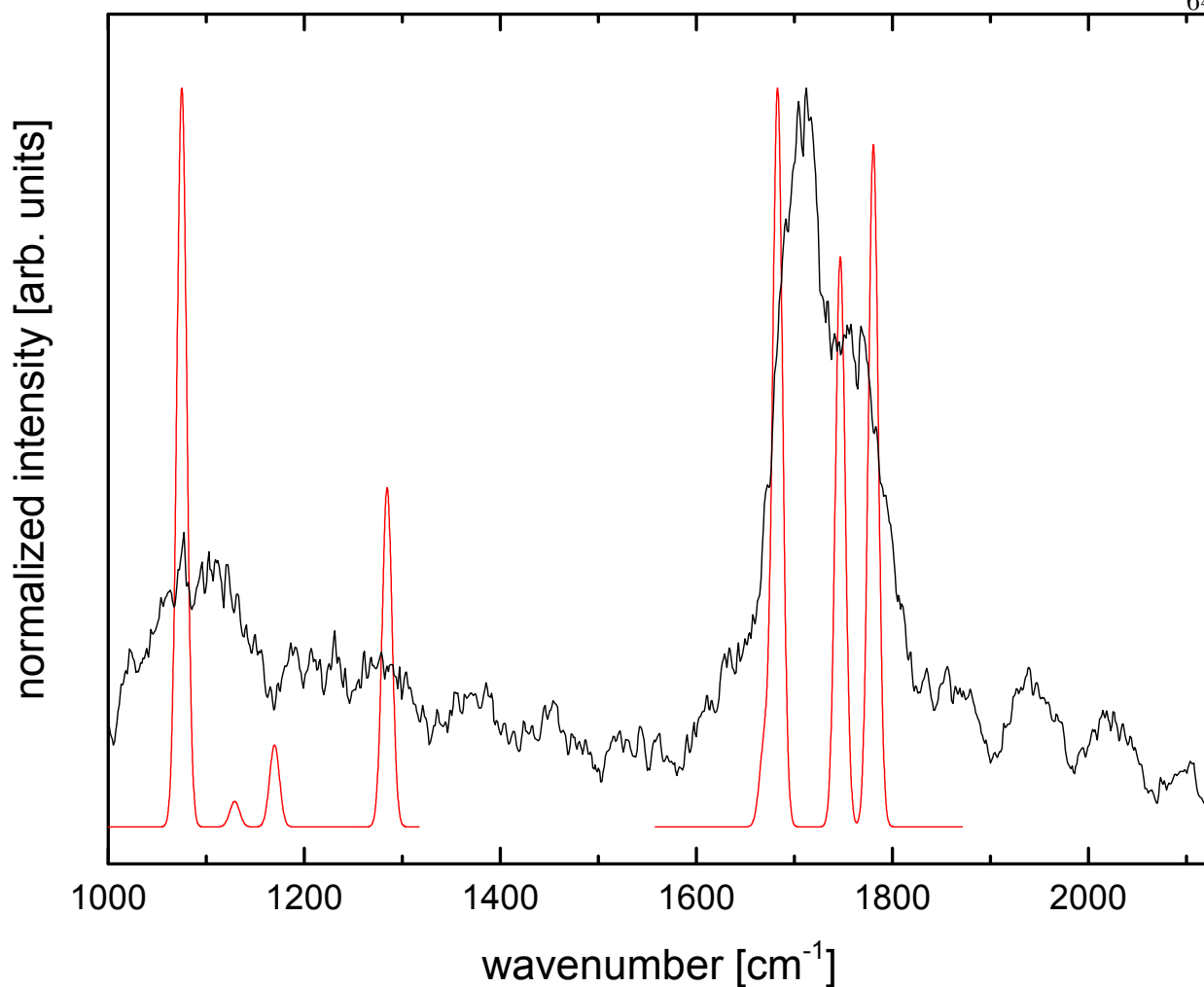


Figure 3.27: A comparison of the combined calculated spectra for isomers E and F to the experimental spectrum of $[\text{Ni}(\text{CO}_2)_2]^-$. Note that while the fit is not ideal, it is reasonable that a multiphoton process could recover the observed experimental spectrum. See text for discussion.

appear particularly suitable for applications as single atom catalysts in CO_2 reduction/conversion schemes since, in both cases, strong covalent bonds are formed with the reduced CO_2 ligands. However, the structures observed here suggest that there may be unique applications of CO_2 within inorganic and organometallic chemistry.

3.4 Infrared Studies of $[\text{Cu}(\text{CO}_2)_n]^-$ Clusters

There are a number of reasons why Cu carries a lot of interest in the context of these studies. First, there has been work showing the application of copper in catalytic systems and fuel cells where CO_2 has been converted to CO, [95–97] methane, [97–99], alcohols and other small organic species. [97, 100, 101] Unfortunately, there again has been little effort to study the active species and catalyst complexes spectroscopically to gain understanding of the molecular level functionality. Copper is also the final member of the coinage metals. For anionic complexes with CO_2 , one would expect that the structure of the charge carrier and the solvation behavior will be similar to that of Au and Ag. This would manifest itself in spectral signatures characteristic of the formate motif with solvation occurring around the CO_2 moiety, resulting in increased activation of the bonded CO_2 . Cu has a similar atomic radius and electronegativity to Ag, and one might expect more similarities to $[\text{Ag}(\text{CO}_2)_n]^-$ clusters than to $[\text{Au}(\text{CO}_2)_n]^-$ clusters. Cu is also immediately to the right of Ni continuing the study of first row transition metal anions interacting with CO_2 . The interactions of Co and Ni with CO_2 are markedly different than those of Au and Ag. Since Cu is also a first row transition metal, one may expect to see butterfly structures like those observed in Co and Ni. Studying $[\text{Cu}(\text{CO}_2)_n]^-$ clusters allows us to study two periodic groups simultaneously and discover if their behavior is interconnected and/or which bonding motifs are present.

3.4.1 Computational Methods

Density functional theory was performed using the TURBOMOLE v. 6.2 suite of programs. [58] For all calculations performed in this section, the B3-LYP functional [59, 60] with dispersion correction [90] was used. The def2-TZVPP basis sets were assigned to all atoms in these calculations. [61] Harmonic frequencies were calculated using the AOFORCE program. [66, 67] The calculated harmonic frequencies were scaled by 0.97537 to account for anharmonicity. This factor was obtained by comparing the antisymmetric stretch of CO_2 as reported by Shimanouchi [37] to the calculated value for the same molecular motion under this level of theory. Charge distributions were calculated

using a natural population analysis. [68]

3.4.2 Infrared Spectra of $[\text{Cu}(\text{CO}_2)_n]^-$ Clusters

Figure 3.28 shows the experimental spectra for $[\text{Cu}(\text{CO}_2)_n]^-$ for $n = 2 - 9$. These spectra are clearly far more complicated than any of the spectra observed previously for the other metals described in this chapter! Fragmentation is first observed at $n = 2$ where one dominant peak is observed in the region of the charge carrier at 1750 cm^{-1} with a shoulder at 1720 cm^{-1} . At $n = 3$, three dominant peaks are observed in the region of the charge carrier with a small peak at lower energies. As cluster size increases, the peaks begin to shift and split resulting in a large number of peaks for $n \geq 6$. While the prospect of assigning all of these peaks is at first glance daunting, identifying trends and using the information garnered from the other metal CO_2 studies will prove invaluable for interpreting these spectra.

Upon detailed inspection, there are three dominant trends within these spectra (shown in Figure 3.29). We will discuss these trends one at a time. First, the trend highlighted in red shows a red shifting peak that changes its role from the dominant feature in $n = 2$ to a minor feature at all larger cluster sizes. This set of peaks is similar to those observed in both $[\text{Au}(\text{CO}_2)_n]^-$ and $[\text{Ag}(\text{CO}_2)_n]^-$ clusters. These features were attributed to a formate like structure where solvation around the CO_2 results in polarization of the excess charge onto the bonding CO_2 moiety and a concomitant red shift of the CO_2 antisymmetric stretch for the bonded species. Since Cu, like Au and Ag, is a coinage metal, it is likely to exhibit the formate structural motif present in both $[\text{Au}(\text{CO}_2)_n]^-$ and $[\text{Ag}(\text{CO}_2)_n]^-$ clusters.

Performing calculations on a CuCO_2^- species yields only two possible core structures (see Figure 3.30). The formate structure (B) is predicted to be the lowest energy isomer. This is the same core structure assigned in $[\text{Au}(\text{CO}_2)_n]^-$ and $[\text{Ag}(\text{CO}_2)_n]^-$ clusters. The insertion structure (A) is higher in energy. Unlike for Co and Ni, the insertion structure is not predicted to be the lowest energy isomer for $n = 1$ in $[\text{Cu}(\text{CO}_2)_n]^-$ clusters. The monosolvated isomers are also shown in Figure 3.30. For isomer B these are the previously described side and terminal solvation isomers.

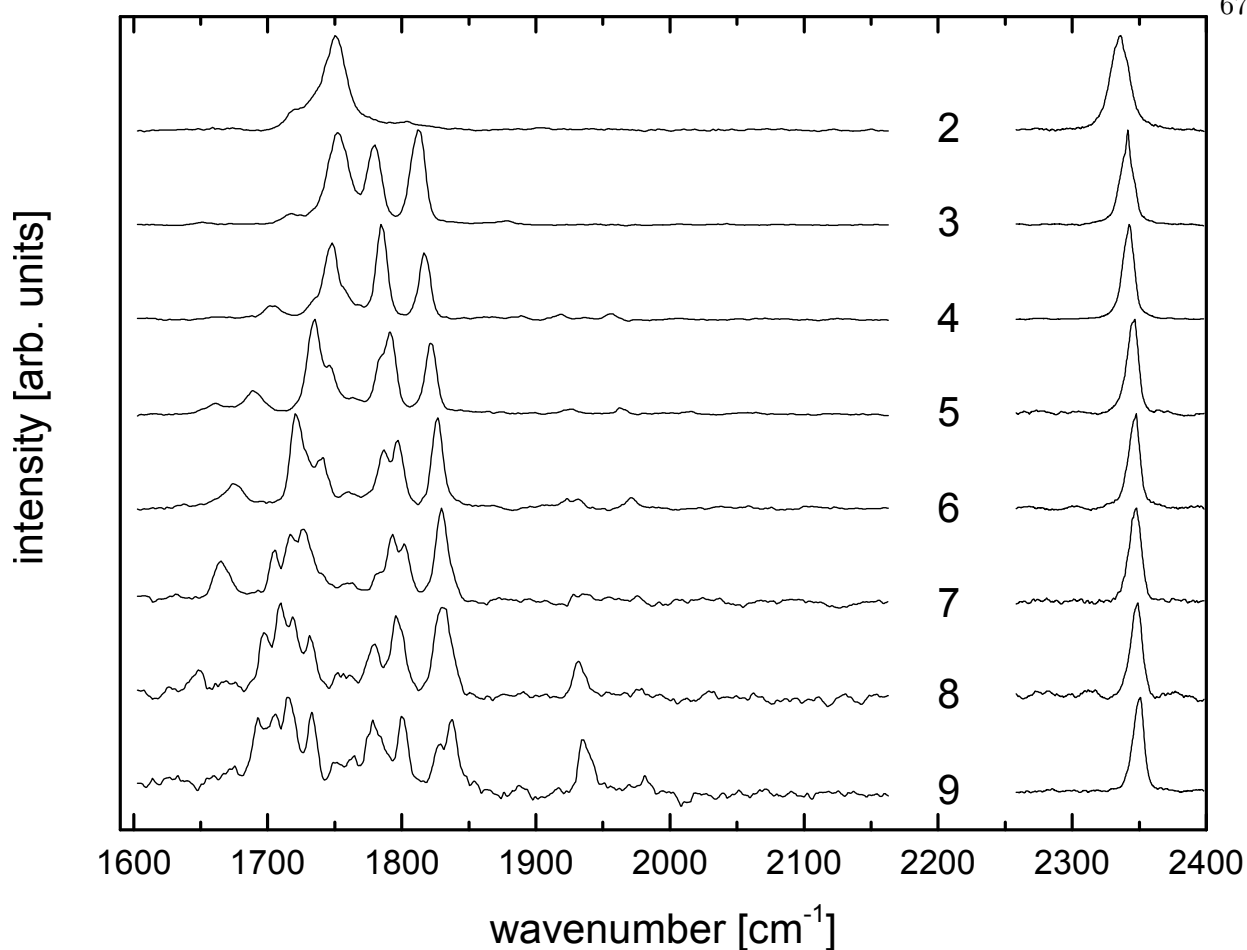


Figure 3.28: Experimental spectra of $[\text{Cu}(\text{CO}_2)_n]^-$. The numbers denote the number of CO_2 molecules in the cluster. All spectra are individually normalized so that the left and right traces are on different scales.

Isomer A can only be solvated around the CO moiety since solvation of the lone O atom would likely result in the formation of isomer D (discussed below).

Figure 3.31 shows a comparison of the formate core with side or terminal solvation positions occupied and the insertion structure to the experimental spectrum for $[\text{Cu}(\text{CO}_2)_2]^-$. It is clear that the insertion structure A(1) does not recover the experimental spectrum while the side solvated formate structure (B(1b)) does, and the terminal solvation isomer (B(1a)) recovers the small shoulder at 1720 cm^{-1} . This behavior has been observed before in $[\text{Au}(\text{CO}_2)_n]^-$ and $[\text{Ag}(\text{CO}_2)_n]^-$ clusters, where occupation of the terminal solvation position results in lower energy peaks compared

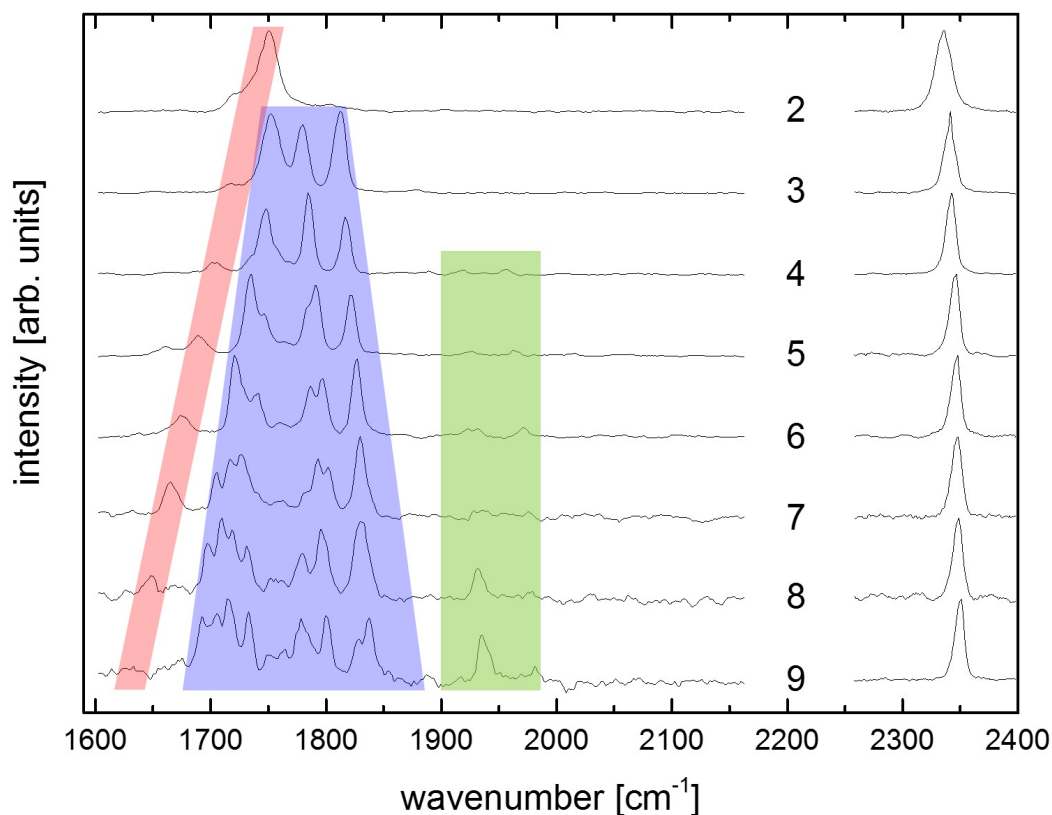


Figure 3.29: Experimental spectra of $[\text{Cu}(\text{CO}_2)_n]^-$ with the three groups of spectral features highlighted (see text for discussion). Numbers denote the number of CO_2 molecules in the cluster. All spectra are individually normalized so that the left and right traces are on different scales.

to when the terminal position is left vacant. Interestingly, while the formate motif is present, it is clearly not the dominant structural motif as cluster size increases but rather persists as a minor contributor to the experimental spectra.

We can compare the experimentally measured frequency of the red highlighted trend to the calculated charge on the bonded CO_2 ligand in the formate structures as was done for $[\text{Au}(\text{CO}_2)_n]^-$ and $[\text{Ag}(\text{CO}_2)_n]^-$ clusters (see Figure 3.13). Figure 3.32 shows the formate structure data for $[\text{Cu}(\text{CO}_2)_n]^-$ clusters together with the linear correlation generated from the Au and Ag data. All data sets are consistent with an empirical linear correlation. This further corroborates the

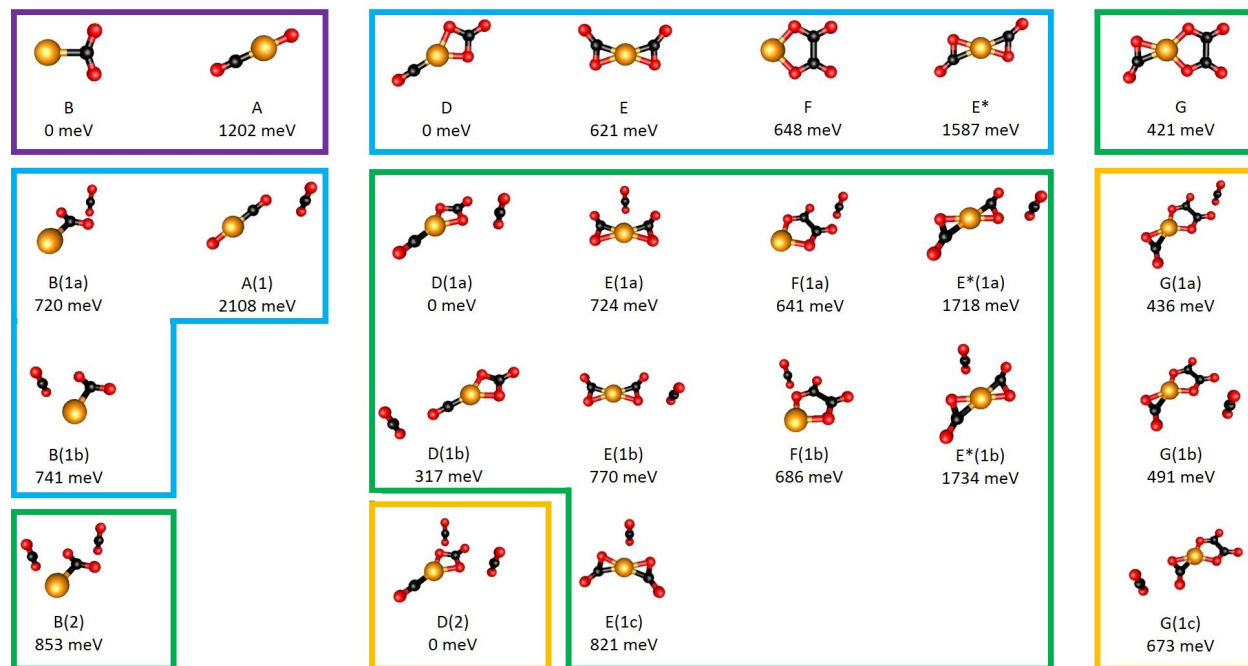


Figure 3.30: Calculated lowest energy structures for $[\text{Cu}(\text{CO}_2)_n]^-$ ($n = 1$ to 4). The notation is chosen to be consistent with that for $[\text{Co}(\text{CO}_2)_n]^-$ and $[\text{Ni}(\text{CO}_2)_n]^-$ clusters. The letter denotes the core structure and the number/letter combination in parentheses indicates the number of solvent molecules and their positions. The purple box indicates $n = 1$ species, the blue boxes indicate $n = 2$ species, the green boxes indicate $n = 3$ species and the orange box indicates $n = 4$ species. Bare core structures are shown on the top row while solvation isomers are shown in the descending columns. Relative energies are given in meV and are with respect to the lowest energy isomer for a given cluster size.

assignment of the formate structure and provides convincing evidence that the linear correlation in Figure 3.32 is a spectroscopic tool for assessing the degree of reduction of an η^1 bonded CO_2 to a metal.

The second set of features to consider is those highlighted in blue (see Figure 3.29). These peaks first appear at $n = 3$ indicating that the core species responsible is of the form $[\text{Cu}(\text{CO}_2)_2]^-$. The $[\text{M}(\text{CO}_2)_2]^-$ core composition was assigned primarily to butterfly structures in $[\text{Co}(\text{CO}_2)_n]^-$ and $[\text{Ni}(\text{CO}_2)_n]^-$ clusters. However, with the multitude of peaks present in the experimental spectra, all reasonable structural variations of the form $[\text{Cu}(\text{CO}_2)_2]^-$ should be considered. Figure 3.30 shows all of the calculated structures for $[\text{Cu}(\text{CO}_2)_2]^-$. As was predicted for Co and Ni, the

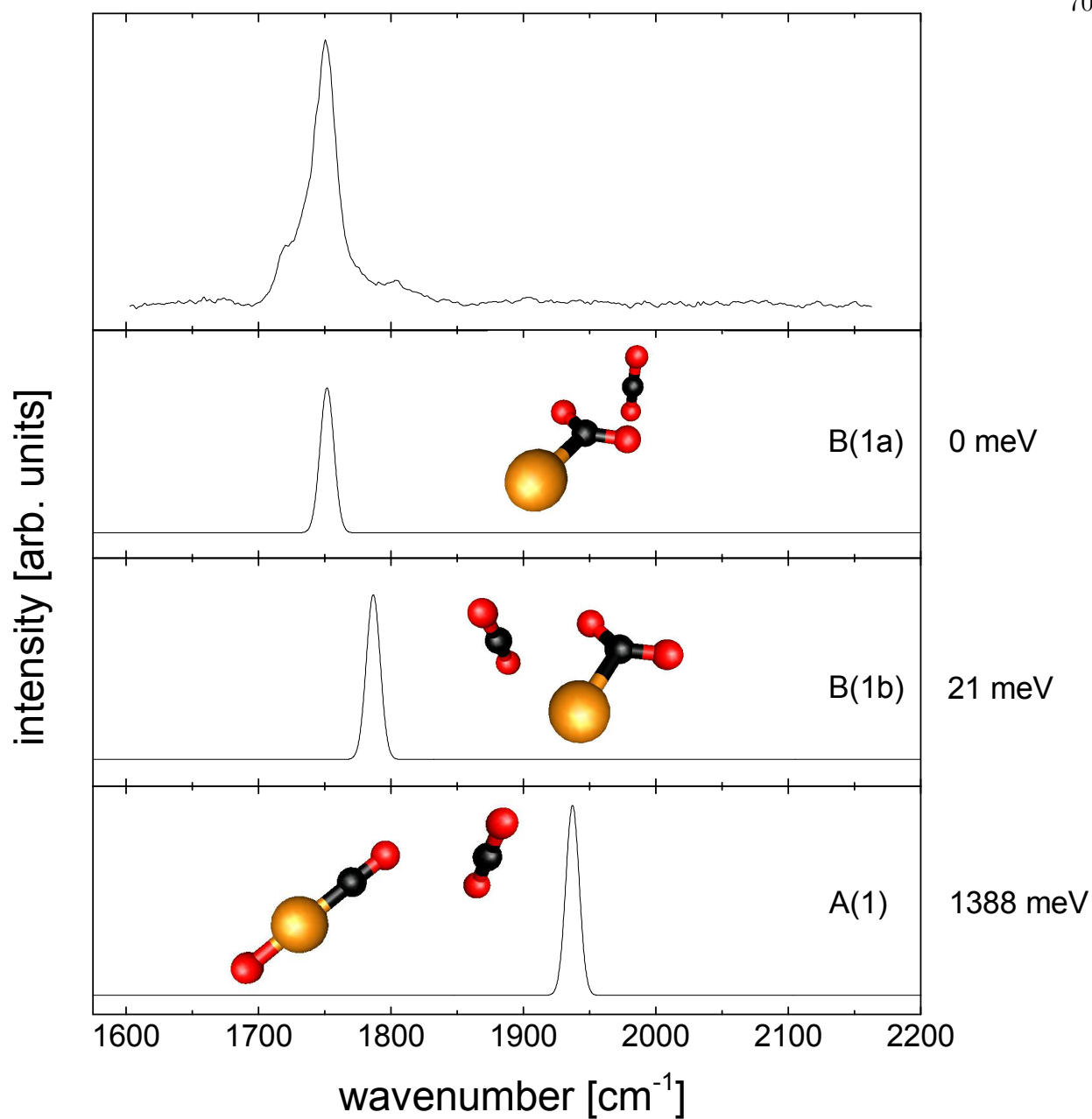


Figure 3.31: Comparison of calculated structures B(1a), B(1b) and A(1) to the experimental spectrum of $[\text{Cu}(\text{CO}_2)_2]^-$. See Figure 3.30 for relative energies and the text for discussion.

insertion structure (D) is the predicted lowest energy structure. The C_{2v} butterfly (E), C_2O_4 (F) and inversion butterfly (E*) are also predicted to be possible isomers. Figure 3.30 also shows a variety of different solvation positions possible for each of the core species in columns descending

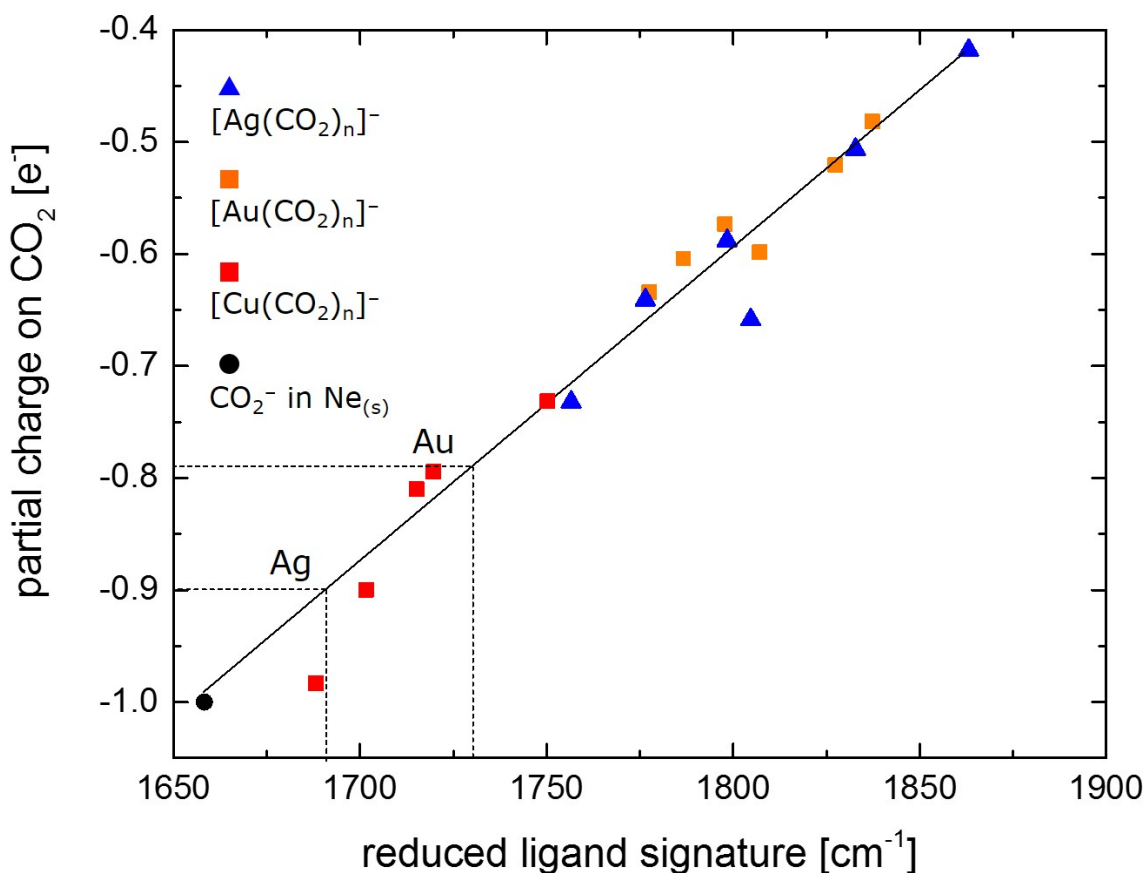


Figure 3.32: Plot of the antisymmetric CO stretching frequency in a formate core against the calculated partial charge localized on the activated CO₂ moiety for an assigned structure (see text). The blue triangles represent [Ag(CO₂)_n]⁻ clusters while the orange squares represent [Au(CO₂)₄]⁻ clusters and the red squares represent [Cu(CO₂)_n]⁻. The black circle is the antisymmetric stretching frequency of a CO₂⁻ in a Ne matrix. [38] The solid line is a linear fit of all the points in the plot. The dashed lines represent the maximum charge transfer observed based on the most red shifted frequency observed.

from the bare cores.

A comparison of the calculated spectra for the singly solvated [Cu(CO₂)₂]⁻ cores to the experimental spectrum for $n = 3$ is presented in Figure 3.33. The butterfly core, with two different solvation environments, most accurately recovers the experimental spectrum. These two motifs are termed symmetric (E(1a) and E(1c)) and asymmetric (E(1b)) solvation. In the case of symmetric

solvation, the two core CO₂ ligands are solvated equally. Stated another way, symmetric solvation is where the solvation positions behind each of the core CO₂ ligands are either both filled or vacant. This behavior results in an even distribution of the excess charge between the two CO₂ ligands. As a consequence, the vibrational modes of the CO₂ ligands are coupled, resulting in in-phase (higher energy) and out of phase (lower energy) combinations of the antisymmetric stretches (see third panel in Figure 3.33).

Asymmetric solvation occurs when one of the two core CO₂ ligands is preferentially solvated (see Figure 3.30 isomer E(1b)). In this case, the solvated CO₂ has additional charge density polarized onto it relative to the unsolvated CO₂ ligand. Since there is a difference between the two ligands, the C_{2v} symmetry is broken and the antisymmetric CO₂ stretching frequencies are no longer coupled like they are in symmetric solvation. The solvated CO₂ moiety, due to the increased partial charge being polarized onto it, exhibits a lower energy stretching mode compared to that of the unsolvated CO₂ moiety (see E(1b) in Figure 3.33). These two solvation behaviors account for the three peaks initially observed in [Cu(CO₂)₃]⁻ (see Figure 3.34).

As solvation increases, one can envision that these two solvation motifs, symmetric and asymmetric, will persist but become more convoluted. The solvation environment will likely be somewhere between these two extremes as more and more CO₂ molecules are added, resulting in the spectral congestion observed in the blue region. Since both solvation motifs recover the peak at approximately 1750 cm⁻¹, it is not surprising that this is the first feature to split and to have the most congestion associated with it. However, asymmetric solvation generally accounts for the peaks centered at 1810 cm⁻¹ while symmetric solvation will generally recover the features centered at 1770 cm⁻¹.

The final region of peaks to discuss is that highlighted in green in Figure 3.29. These peaks first appear at $n = 4$, indicating the presence of a [Cu(CO₂)₃]⁻ core species. Based on the calculated structures of a Cu atom and three CO₂ molecules with an excess electron, only one energetically relevant structure is predicted. This core consists of CO₂ and C₂O₄ subunits bonded to the Cu atom (see Figure 3.30, structure G) and is similar to the core structure assigned to analogous

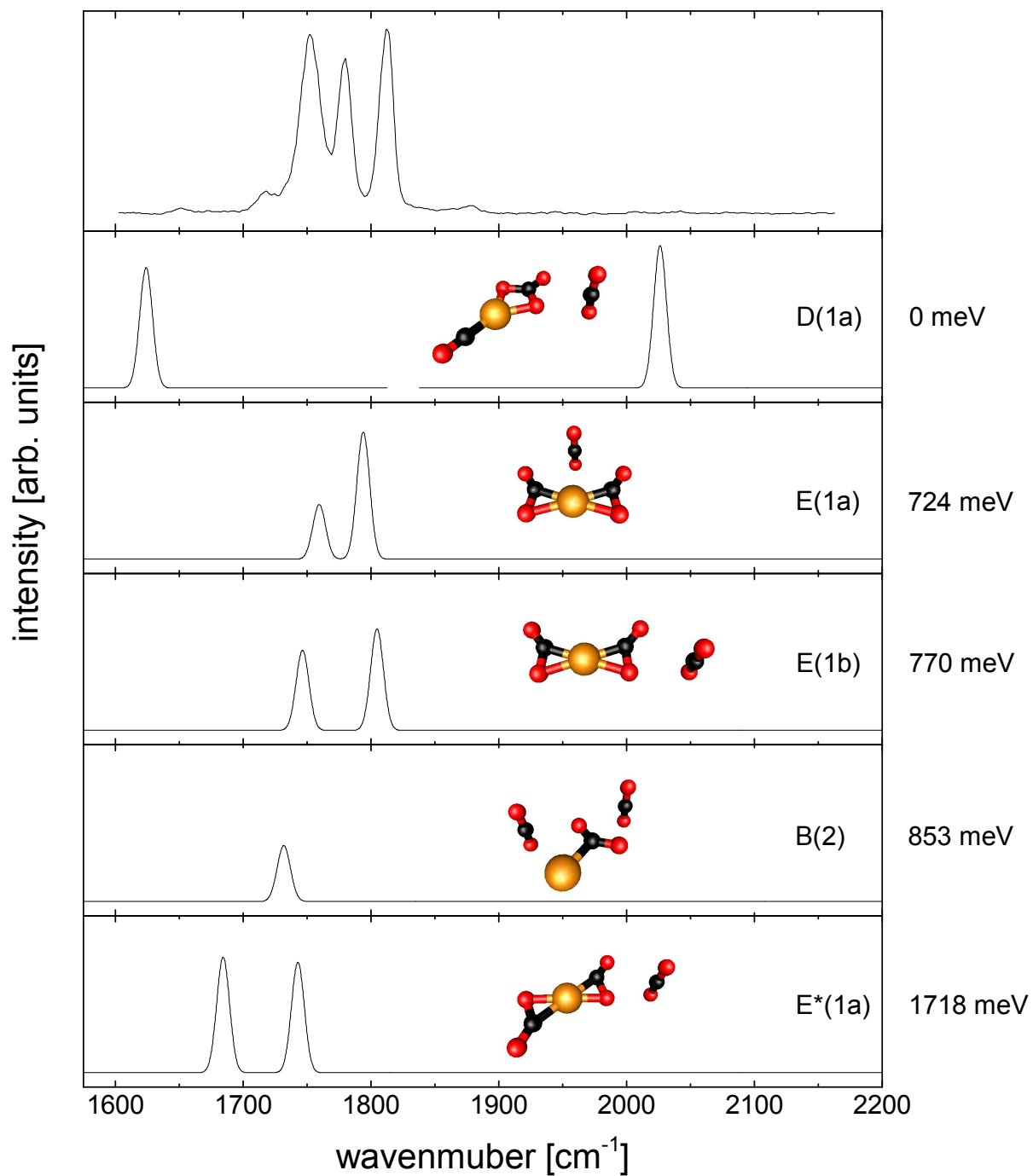


Figure 3.33: Comparison of calculated structures with a $[\text{Cu}(\text{CO}_2)_2]^-$ core to the experimental spectrum for $n = 3$. See Figure 3.30 for description and relative energies of the structures presented.

features observed in $[\text{Ni}(\text{CO}_2)_n]^-$ clusters.

While solvation position does not dramatically affect the charge distribution of structure G in $[\text{Ni}(\text{CO}_2)_n]^-$, different spectral features are predicted when different solvation positions are occupied in the Cu analog. Specifically, solvation around the CO_2 moiety results in increased localization of the excess charge onto that ligand, causing lengthening of the CO bonds and a predicted lower vibrational frequency compared to solvation around the C_2O_4 moiety. Interestingly, a comparison of these two different solvation motifs (CO_2 solvation position filled or vacant) to the experimental spectrum reveals that both are observed in the experiment. For the two peaks observed in the green region of the experimental spectra (see Figure 3.29), solvation around the CO_2 moiety recovers the lower energy feature while solvation around the C_2O_4 recovers the higher energy peak. It should be noted that while there is a signature predicted around 1700 cm^{-1} for structure G, it is likely obscured by the dominant features of the butterfly core. At $n = 8$, only the lower energy feature appears in the green region of the experimental spectra. This is expected since as the number of solvent molecules increases, there is a higher likelihood that the solvation position behind the CO_2 subunit will be filled. For $n \geq 8$, the solvation position behind the CO_2 subunit is always filled and results in only the lower energy feature being recovered.

As a final check of the assignment of the experimental spectra, we performed exploratory calculations on the three primary core structures up to $n = 6$ to verify that the structures and solvation motifs discussed above continue to recover the experimental spectra for larger cluster sizes. Figure 3.35 shows the results of these exploratory calculations compared to the experimental peak positions of $[\text{Cu}(\text{CO}_2)_n]^-$ ($n = 3 - 6$). As can be seen, the calculations recover the general shape and trends of the experimental spectra even though a definitive assignment is not possible.

3.5 Comparison of all Metal- $(\text{CO}_2)_n$ Anion Clusters

It is clear from the assignment of the experimental spectra that $[\text{Cu}(\text{CO}_2)_n]^-$ clusters exhibit structures and properties that have been observed in other metal- CO_2 clusters. Specifically, the butterfly structure observed as the dominant structural motif in $[\text{Co}(\text{CO}_2)_n]^-$ and $[\text{Ni}(\text{CO}_2)_n]^-$

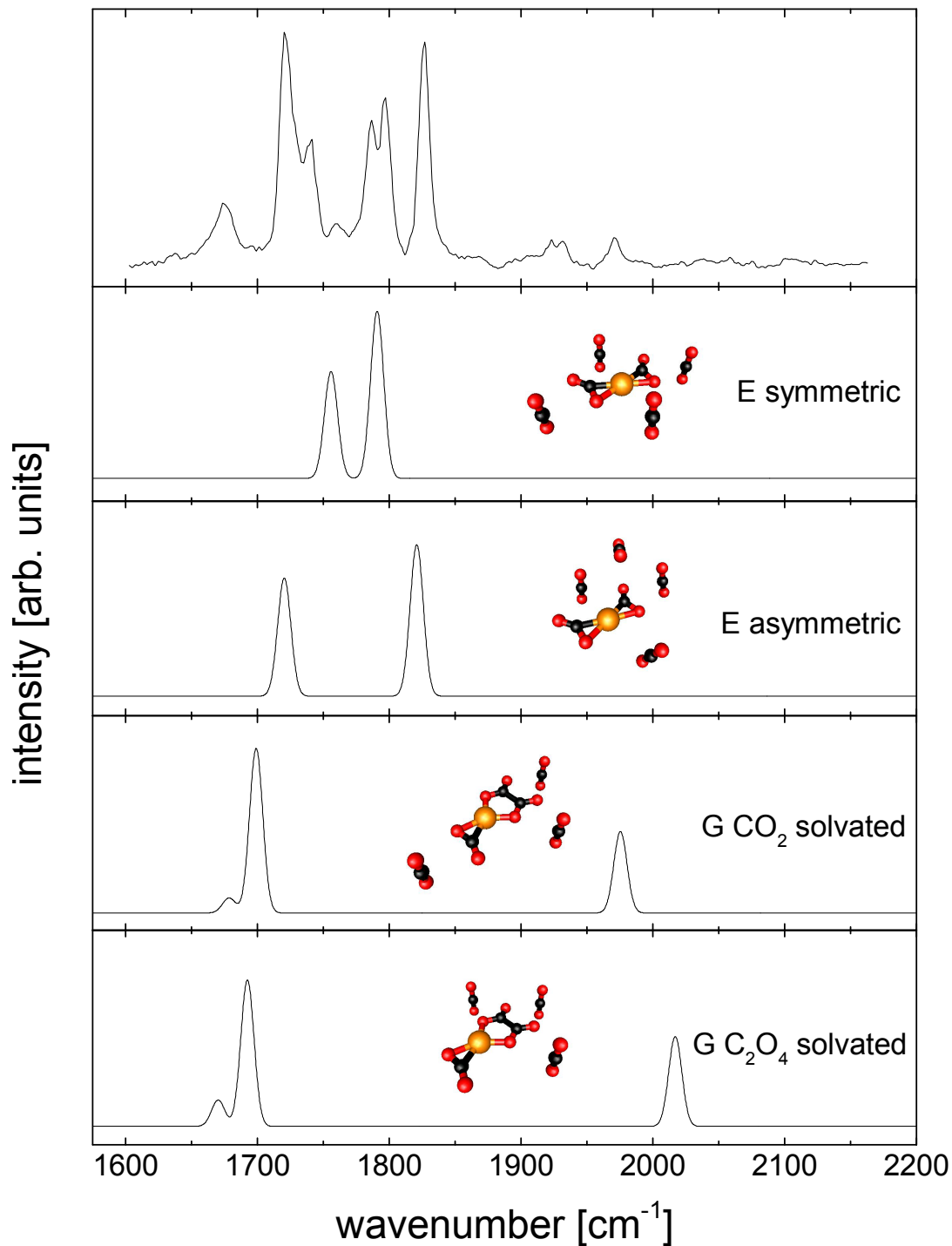


Figure 3.34: Comparison of the calculated spectra for different solvation positions around isomers E and G to the experimental spectrum for $[\text{Cu}(\text{CO}_2)_6]^-$. Note that since isomer G is a minor contributor to the experimental spectrum, the features around 1700 cm^{-1} will likely be obscured by the formate signature. See Figure 3.30 for additional information on the structures presented here and text for additional discussion on symmetric and antisymmetric solvation.

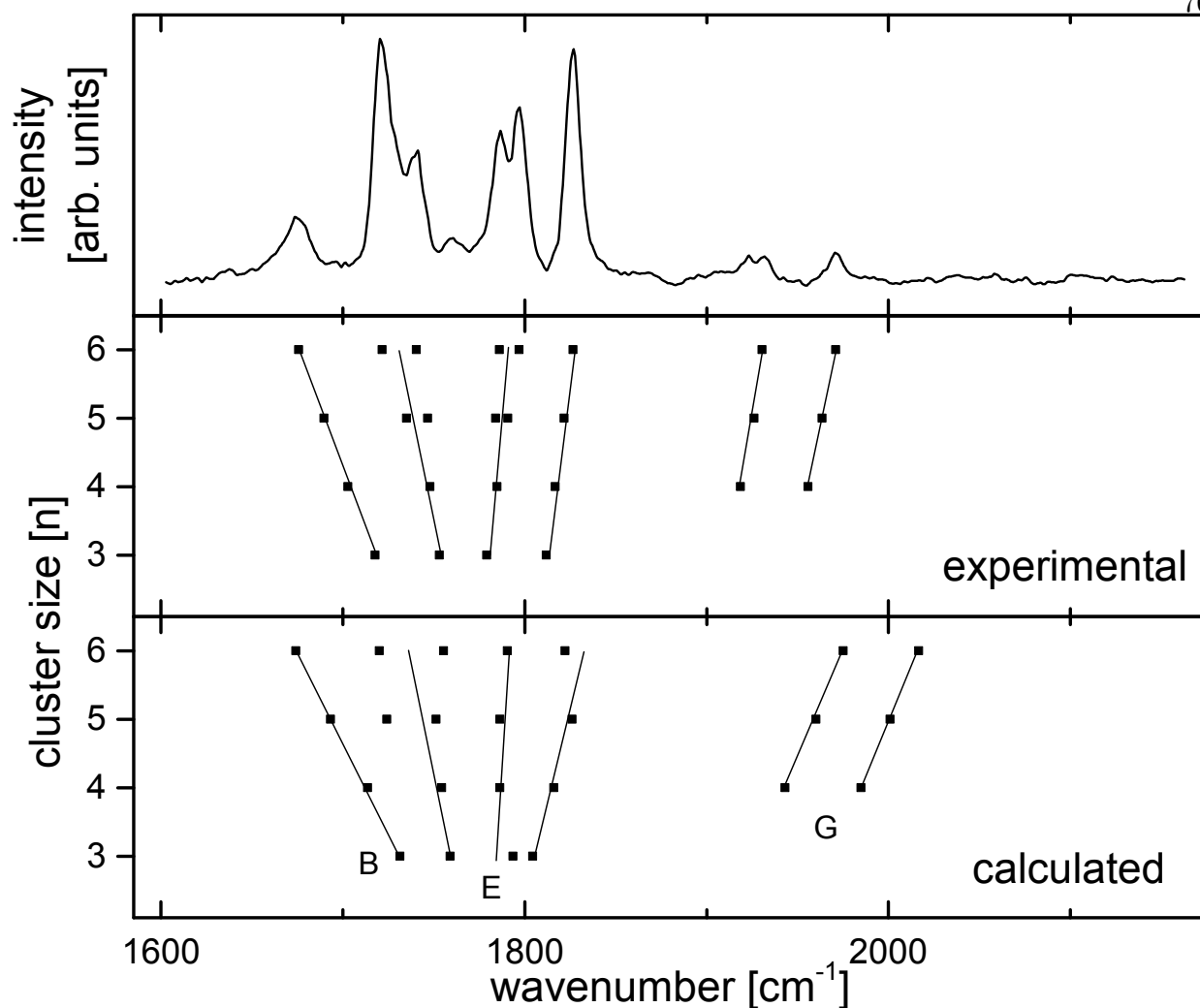


Figure 3.35: Spectral shifts of the experimental and simulated features for $[\text{Ni}(\text{CO}_2)_n]^-$ ($n = 3$ to 6). The top trace show the spectrum for $n = 6$ for comparison. The lines are meant to guide the eye and are not a fit of any of the data, the letters indicate the assignments of the core isomers as shown in Figure 3.30. See text for further discussion.

clusters is the primary core charged species in $[\text{Cu}(\text{CO}_2)_n]^-$ clusters. Additionally, the formate motif and the large polarizability of the charge carrier observed in $[\text{Au}(\text{CO}_2)_n]^-$ and $[\text{Ag}(\text{CO}_2)_n]^-$ clusters, are both present in $[\text{Cu}(\text{CO}_2)_n]^-$. These observations indicate that Cu is a switching point between the trends observed in the first row transition metals and in the coinage metals.

It is worth exploring these trends further. The electronegativity of the coinage metals increases moving down the periodic table (1.90 to 1.93 to 2.4 for Cu, Ag and Au, respectively). [49]

This trend is correlated with the maximum amount of excess charge localized on the CO₂ ligand of a formate structure for Au, Ag and Cu (see Figures 3.13 and 3.32). Au, being the most electronegative, allows for the least amount of charge transfer since Au will attract the excess electron more strongly than either Ag or Cu. This is manifested spectroscopically in the observation of the blue shifting antisymmetric stretching frequency in [Au(CO₂)_n]⁻ clusters for $n \geq 10$. For [Ag(CO₂)_n]⁻, there is spectroscopic evidence of Ag participating as a solvent species. This suggests that the electronegativity of a (CO₂)_n cluster is likely on the order of the electronegativity of Ag such that the two different cores ([AgCO₂]⁻ and CO₂ based charge carriers) can coexist. Since the electronegativity of Cu is lower than that of Ag, the increased localization of the excess charge to the bonded CO₂ is expected (see Figure 3.32). However, it is interesting to note that (CO₂)_n⁻ cluster signatures are not observed in the spectra of [Cu(CO₂)_n]⁻ clusters.

Like in both [Co(CO₂)_n]⁻ and [Ni(CO₂)_n]⁻ clusters, butterfly structures are the dominant core structure present in [Cu(CO₂)_n]⁻ clusters. However, the polarizability of the butterfly core is substantially higher than those of either Ni or Co complexes (the trace of the polarizability tensor is calculated to be 82.45, 76.04 and 69.71 Å³ for Cu, Ni and Co, respectively for assigned butterfly structures). This is manifested in the spectroscopic observations of only minor peak shifts and small splittings observed for Co and Ni versus the plethora of peaks in Cu. Interestingly, the noticeable effect of solvation on the charge distribution of the core species in Au and Ag is observed for all of the core species in Cu even though some of the core species are quite different. An additional explanation for the increased polarizability of the butterfly core in Cu versus Co and Ni concerns the geometry of the core. In Co, the primary core species has the two CO₂ ligands at roughly 90° to each other. In Ni, this angle has been reduced to roughly 45° and in Cu the two CO₂ moieties lie in the same plane. If one considers π conjugation like in an aromatic system, [102] it is reasonable to assume that there would likely be more conjugation of the p- and d-orbitals if the butterfly core is planar than in any other geometry. This would lead to a more polarizable distribution of the excess charge in the planar core (Cu) rather than a localized and robust distribution in a twisted butterfly core (Co and Ni). This hypothesis agrees with the experimental observations and the

calculations that were performed.

The data in this chapter show interesting trends in the bonding behavior of coinage metals and first row transition metals with CO_2 , which are in keeping with their positions in the periodic table. Additionally, the data indicate that Cu is indeed a switching point between the two sets of trends. The coinage metals appear to be more well suited to catalytic reductive activation of CO_2 than Co or Ni, with Ag being the most promising candidate based on these results. The first row transition metals present potentially novel chemistry of CO_2 and metal anions. It is our hope that these metal- CO_2 studies will illuminate molecular level details that can aid in rational catalyst design for the development of carbon neutral fuel cycles.

Chapter 4

Infrared Studies of $[\text{CoO}(\text{CO}_2)_n]^-$ and $[\text{NiO}(\text{CO}_2)_n]^-$ Clusters

This Chapter has been reproduced in part with permission from the following previously-published article:

Knurr, B. J., Weber, J. M., “Structures of $[\text{CoO}(\text{CO}_2)_n]^-$ and $[\text{NiO}(\text{CO}_2)_n]^-$ Clusters Studied by Infrared Spectroscopy.” *Journal of Physical Chemistry A*, 2015. DOI:10.1021/jp5108608 Copyright 2015 American Chemical Society.

4.1 Introduction

Metal-oxide species are a common occurrence in transition-metal chemistry with many catalytic reactions performed on metal-oxide surfaces with reactivity varying from oxide site to oxide vacancy. [103, 104] Understanding the chemical bonding and interactions at these types of active sites can aid catalyst design and understanding of surface chemistry. Studies of model metal-oxide species *in vacuo* provides detailed structural information by bypassing the difficulties of performing spectroscopy in the condensed phase environment. A number of groups have studied the structure and reactivities of various metal-oxide species in the gas phase. The experiments performed on these species range from reactivity studies [105–117] to photoelectron spectroscopy [111, 118, 119] and vibrational spectroscopy. [117, 120–128]

In Chapter 3, the structure and effects of solvation on $[\text{M}(\text{CO}_2)_n]^-$ clusters ($\text{M} = \text{Au}, \text{Ag}, \text{Co}, \text{Ni}, \text{and Cu}$) were reported. In this chapter, similar studies are reported for $[\text{CoO}(\text{CO}_2)_n]^-$ and $[\text{NiO}(\text{CO}_2)_n]^-$ clusters.

4.2 Computational Methods

Density functional theory calculations were performed on a number of $[\text{CoO}(\text{CO}_2)_n]^-$ and $[\text{NiO}(\text{CO}_2)_n]^-$ structures using the TURBOMOLE v. 6.2 suite of programs. [58] For all calculations performed in this chapter, the B3-LYP functional [59,60] with dispersion correction [90] was used. For all atoms in these calculations, the def2-TZVPP basis sets were assigned. [61] Harmonic frequencies were calculated using the AOFORCE program. [66,67] The calculated antisymmetric frequencies corresponding to a CO_2 bound in an η^1 motif (described in Chapter 3) were scaled by 0.9380 to account for anharmonicity. All other frequencies were scaled by 0.97537. The manner in which these factors were obtained is discussed in Section 3.2.1. Charge analyses were performed using a natural population analysis. [68]

4.3 Spectra and Analysis

Like in the previously discussed $[\text{M}(\text{CO}_2)_n]^-$ clusters, the spectra of $[\text{CoO}(\text{CO}_2)_n]^-$ and $[\text{NiO}(\text{CO}_2)_n]^-$ show spectral signatures in two distinct regions. Peaks in the higher energy region (2250 cm^{-1} to 2400 cm^{-1}) are attributed to solvent type CO_2 , which retain the structural nature of a free CO_2 molecule. The antisymmetric stretch of these CO_2 molecules deviates little from that of free CO_2 . The second region (1000 cm^{-1} to 2150 cm^{-1}) exhibits spectral features due to CO_2 molecules involved in the charge carrying species and are referred to as “core” CO_2 units. These CO_2 units are geometrically distorted from the geometry of a free CO_2 molecule and exhibit different CO stretching frequencies.

4.3.1 Infrared Spectra of $[\text{CoO}(\text{CO}_2)_n]^-$ Clusters

The spectra of $[\text{CoO}(\text{CO}_2)_n]^-$ show a single narrow peak in the solvent region and four pronounced features in the core ion region of the spectra (see Figure 4.1). Additionally, there are weaker peaks observed in the core ion region similar to what was seen in $[\text{Co}(\text{CO}_2)_n]^-$ clusters. As has been reported in the previously in Chapter 3, the binding energy of a core CO_2 is on the order of

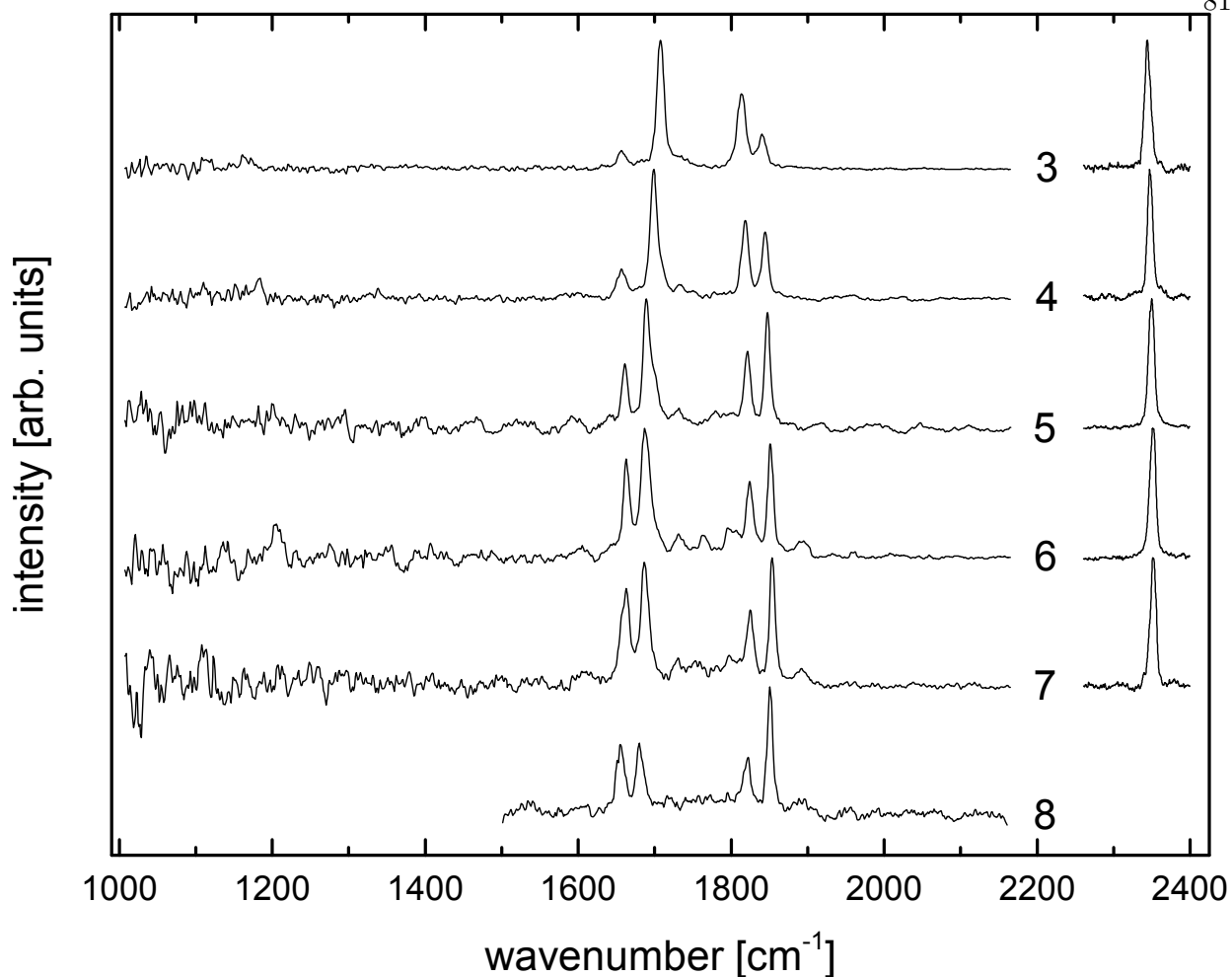


Figure 4.1: Experimental spectra of $[\text{CoO}(\text{CO}_2)_n]^-$ for ($n = 3 - 8$). The numbers denote the number of CO_2 molecules present in the cluster. The exploratory experimental data for $n = 8$ was truncated after determining that the spectrum was not appreciably evolving as a function of cluster size. The left and right traces are individually normalized and are not on the same scale.

10000 cm^{-1} , which is well above the photon energies used in this experiment. Since fragmentation is first observed at $n = 3$, the cluster is likely of the form $[\text{CoO}(\text{CO}_2)_2]^- \cdot \text{CO}_2$ so that a solvent molecule is present (binding energy of solvent $\text{CO}_2 \sim 1600 \text{ cm}^{-1}$) and the core species contains two CO_2 units.

Performing DFT calculations on a $[\text{CoO}(\text{CO}_2)_2]^-$ core yields a variety of possible structural configurations (see Figure 4.2). Both singlet and triplet states are possible for cobalt oxide- CO_2 anion complexes and give rise to different structural configurations. The predicted global minimum

contains a CO₃ and a CO₂ moiety, both bound in a bidentate fashion to the Co atom (see Figure 4.2 isomer ^{1,3}A). The bonding motif in isomer A can be likened to the η^2 structure of a CO₂ molecule bonding to a metal atom where both the CO₂ and CO₃ exhibit an η^2 bonding motif. [91] In the singlet configuration, the CO₃ and CO₂ moieties are nearly perpendicular while in the triplet configuration they are twisted by about 40° to each other. Additionally, the triplet structures tend to be predicted to be lower in energy than their singlet counterparts.

The next higher lying core isomer is B where the CO₂ unit is instead bound in an η^1 fashion (see Figure 4.2). In isomer B, the CO₂ and CO₃ moieties are nearly coplanar. Interestingly, while the bonding of the CO₂ unit is that of an η^1 configuration, the OCO bond angle is 10° larger than the OCO angle of similar structures in [Au(CO₂)_n]⁻ and [Ag(CO₂)_n]⁻ clusters (155° vs. 145°, respectively). The structure next higher in energy consists of a CO₃ and a CO₂ moiety where the CO₂ is bound by both of the oxygen atoms to the Co atom (isomer C) rather than by the carbon atom. Isomer D contains an η^2 CO₂ moiety and an η^1 bound CO₃ where there is only one O-Co bond. The CO₃ in this arrangement is structurally very similar to the formate structures discussed previously for [Au(CO₂)_n]⁻, [Ag(CO₂)_n]⁻ and [Cu(CO₂)_n]⁻ clusters. The OCO angle of the non-bonded portion of the CO₃ moiety is 136° which is nearly the same, for example, as the OCO angle calculated for [Ag(CO₂)₅]⁻ at 139°. Based on the Walsh digram for CO₂ (see Figure 3.1), this angle is predicted to decrease as additional charge is polarized onto the bound CO₂ moiety until it reaches approximately 135°. Without performing a charge analysis, the geometry of the CO₃ moiety in isomer D suggests that a full excess charge has been taken up by this subunit. Finally, isomer E shows a lone oxygen atom opposite a C₂O₄ moiety bonded to the Co atom.

Figure 4.3 shows a comparison of the calculated isomers in Figure 4.2 to the experimental spectrum of [CoO(CO₂)₃]⁻. Only isomers ^{1,3}A and ¹D recover the features in the experimental spectrum. Isomers ^{1,3}A predict the peaks at 1705 cm⁻¹ and 1815 cm⁻¹ with isomer ¹D recovering the 1655 cm⁻¹ and 1840 cm⁻¹ features. While isomer ³B does recover the feature at 1655 cm⁻¹, the second predicted feature around 1750 cm⁻¹ is not present in the experimental spectrum with an appropriate intensity compared to the 1655 cm⁻¹ peak. Based on this observation, isomer

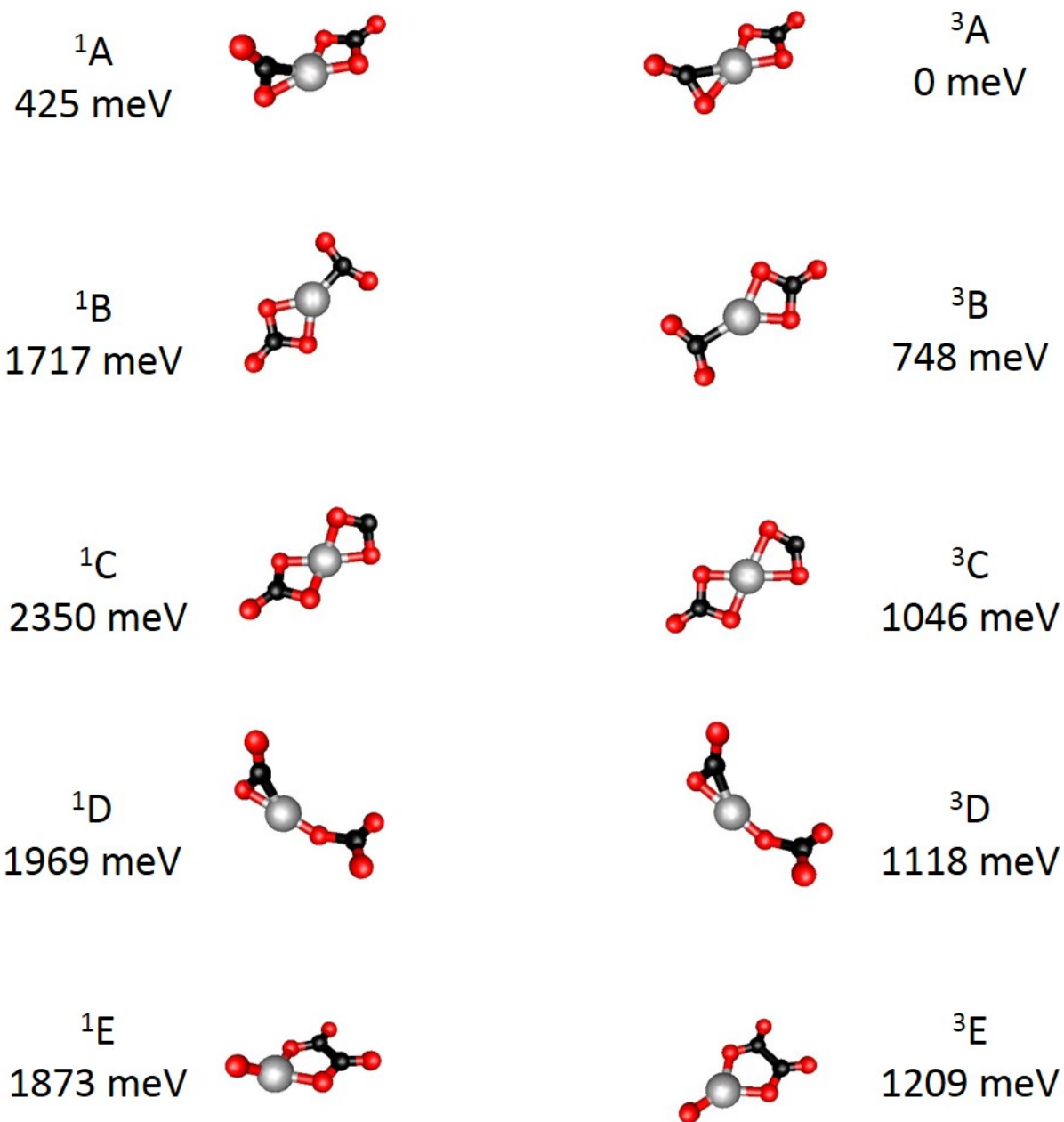


Figure 4.2: Calculated lowest energy structures for $[\text{CoO}(\text{CO}_2)_n]^-$. The capital letter denotes the core structure and superscripts 1 and 3 denote singlet and triplet, respectively. Relative energies are given in meV and are all with respect to isomer ${}^3\text{A}$.

B, if present in our experiment, only contributes to the experimental spectra as a minor isomer. Based on the observed relative peak intensities, it is clear that isomer A is the dominant core structure while there is less population of isomer D. At first glance, it is surprising that isomer D is a stable structure as it appears that the CO_3 could swing to either side making a second Co-O bond and forming isomer A. However, calculations on such a process revealed at least an 8000 cm^{-1} barrier to interconversion from isomer D to A. This is likely due to a substantially different orbital configuration of isomer A compared to isomer D resulting in the high predicted barrier to interconversion. Further calculations outside the scope of this work would be required to further understand this conversion process. None of the other calculated structures in Figure 4.2 recover the experimental spectrum.

As the degree of solvation increases, the experimentally observed peaks do not shift appreciably. Since isomers $^{1,3}\text{A}$ and ^1D are the only structures to recover the experimental features, it is necessary to investigate the effect of solvation on the predicted frequencies of these core structures. Figure 4.4 shows different solvation positions for isomers $^{1,3}\text{A}$ and ^1D . In addition to solvation of core structures A and D, a new energetically relevant core isomer is predicted (see isomer F in Figure 4.4). Isomer F results from the addition of the third CO_2 molecule to the lone oxygen atom in isomer E creating an $\eta^2\text{CO}_3$ moiety opposite the C_2O_4 subunit. In ^3F , the two subunits are planar while in the singlet structure (^1F) the CO_3 and C_2O_4 are perpendicular. If isomer F is populated in the experiment, it should not be observable until $[\text{CoO}(\text{CO}_2)_4]^-$ where the first solvent CO_2 molecule would be present. The core structure of isomer ^3D is predicted to be dependent on the solvation environment. If the CO_3 moiety is solvated, isomer ^3D is recovered, however if the CO_2 subunit is solvated the structure converts to ^3A . As solvation increases, it is unlikely that the CO_2 moiety will remain unsolvated, therefore we exclude isomer ^3D from consideration for assignment to the spectra. This same behavior is not observed for ^1D .

Singlet and triplet structures exhibit a $25 - 30\text{ cm}^{-1}$ difference in the predicted frequency of the lower energy feature of the dominant peaks and a $5 - 10\text{ cm}^{-1}$ difference for the higher energy dominant feature. This is on the same order as the predicted difference in signatures for solvation

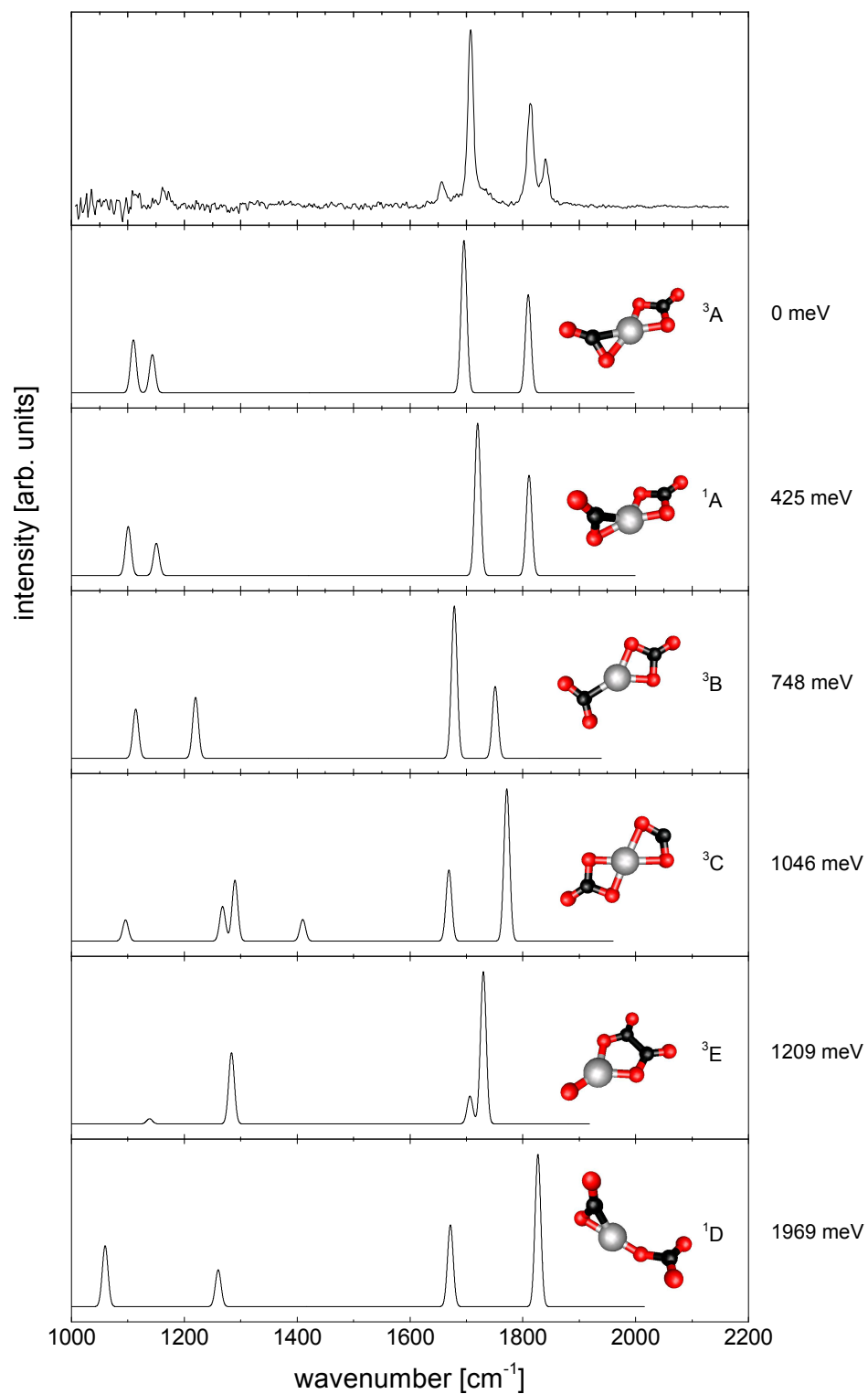


Figure 4.3: Comparison of calculated core isomers for $[\text{CoO}(\text{CO}_2)_2]^-$ to the experimental spectrum of $[\text{CoO}(\text{CO}_2)_3]^-$. Isomer labels and relative energies are given for each structure. See text for discussion.

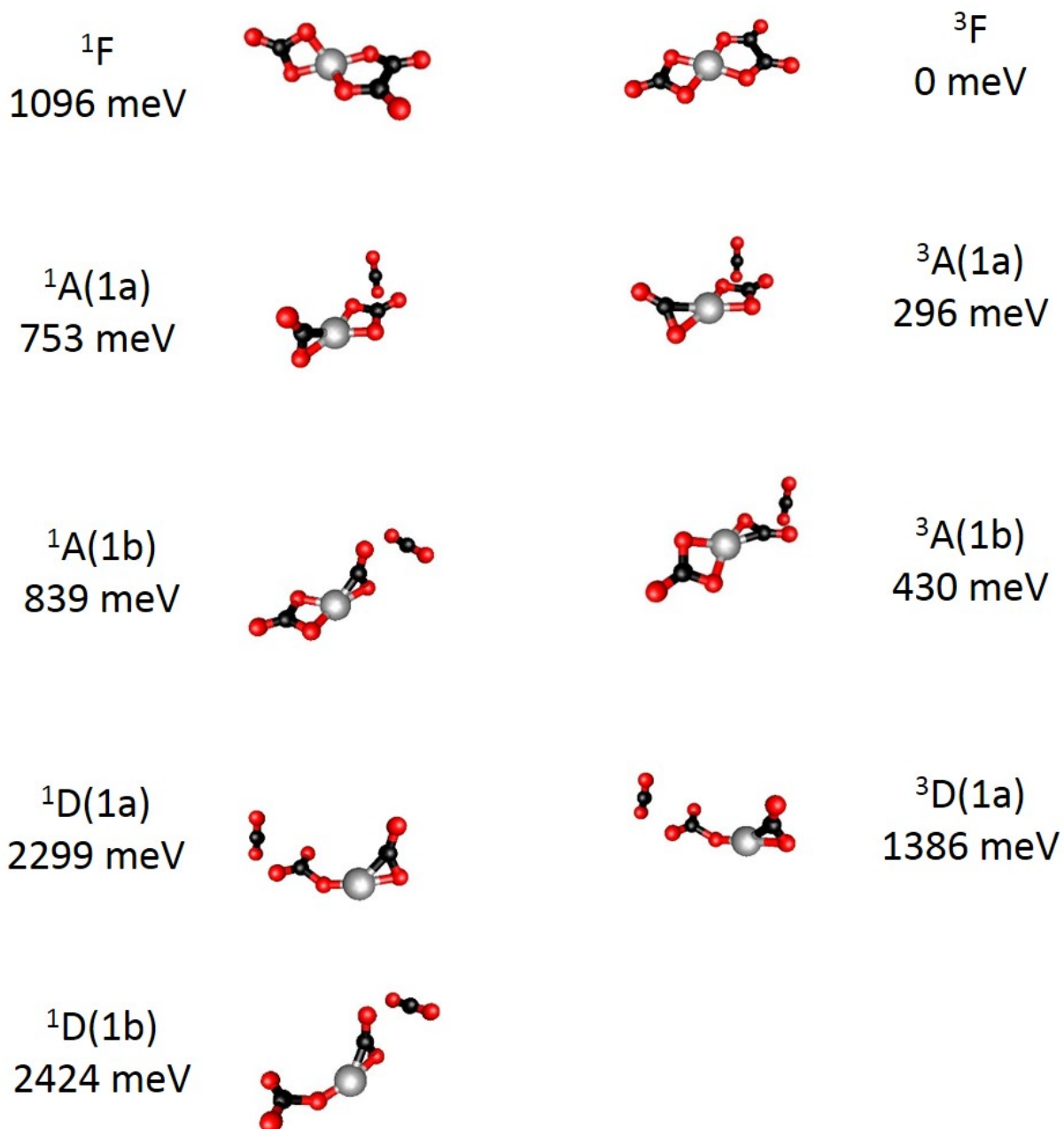


Figure 4.4: Calculated lowest energy structures for $[\text{CoO}(\text{CO}_2)_3]^-$. The capital letter denotes the core structure, the superscript 1 and 3 indicate singlet and triplet configurations, and the number/letter combination denote the number and configuration of the solvent molecules. Relative energies are reported in meV.

isomers of the same core structures. In contrast, the splittings between the experimental signatures are 50 cm^{-1} and 30 cm^{-1} for the lower and higher energy features, respectively. Based on the width of the experimental peaks and the stable peak position as cluster size increases suggests that there is likely only one multiplicity present and that theory overestimates solvation effects. While we cannot definitively assign one multiplicity to the spectra of $[\text{CoO}(\text{CO}_2)_n]^-$, we can distinguish structures with different cores. We also believe that theory over estimates the effect of solvation on the core structures. For simplicity, the rest of the discussion will look only at structures with a singlet configuration.

Figure 4.5 shows a comparison of the singlet structures presented in Figure 4.4 to the experimental spectrum of $[\text{CoO}(\text{CO}_2)_3]^-$. It is clear that isomer F does not recover any of the dominant features. However, it is possible that isomer F does contribute to the spectra of larger clusters ($n \geq 4$) in the region from 1750 cm^{-1} to 1800 cm^{-1} . The experimental spectrum is therefore assigned to isomer A in either a triplet or singlet configuration (1705 cm^{-1} and 1815 cm^{-1} features) and isomer ^1D (1655 cm^{-1} and 1840 cm^{-1} features). As the number of CO_2 molecules present increases, the peaks assigned to isomer ^1D grow in intensity relative to those assigned to isomers $^1,^3\text{A}$. This suggests that the population of isomer ^1D increases with increasing cluster size relative to the population of isomers $^1,^3\text{A}$.

Table 4.1: Calculated partial charges for the predicted core structures of $[\text{CoO}(\text{CO}_2)_n]^-$ presented in Figures 4.2 and 4.4. The partial charges are reported in units of e .

Core Structure	Co	CO_2	CO_3	C_2O_4
^3A	+1.10	-0.68	-1.42	
^1A	+0.79	-0.61	-1.18	
^3D	+0.88	-0.55	-1.33	
^1D	+0.68	-0.57	-1.11	
^3F	+1.42		-1.12	-1.30
^1F	+1.27		-1.06	-1.21

The final features to discuss are the minor peaks that appear between 1700 cm^{-1} and 1800 cm^{-1} in $[\text{CoO}(\text{CO}_2)_4]^-$ and larger clusters (see Figure 4.1). Since these features first appear in

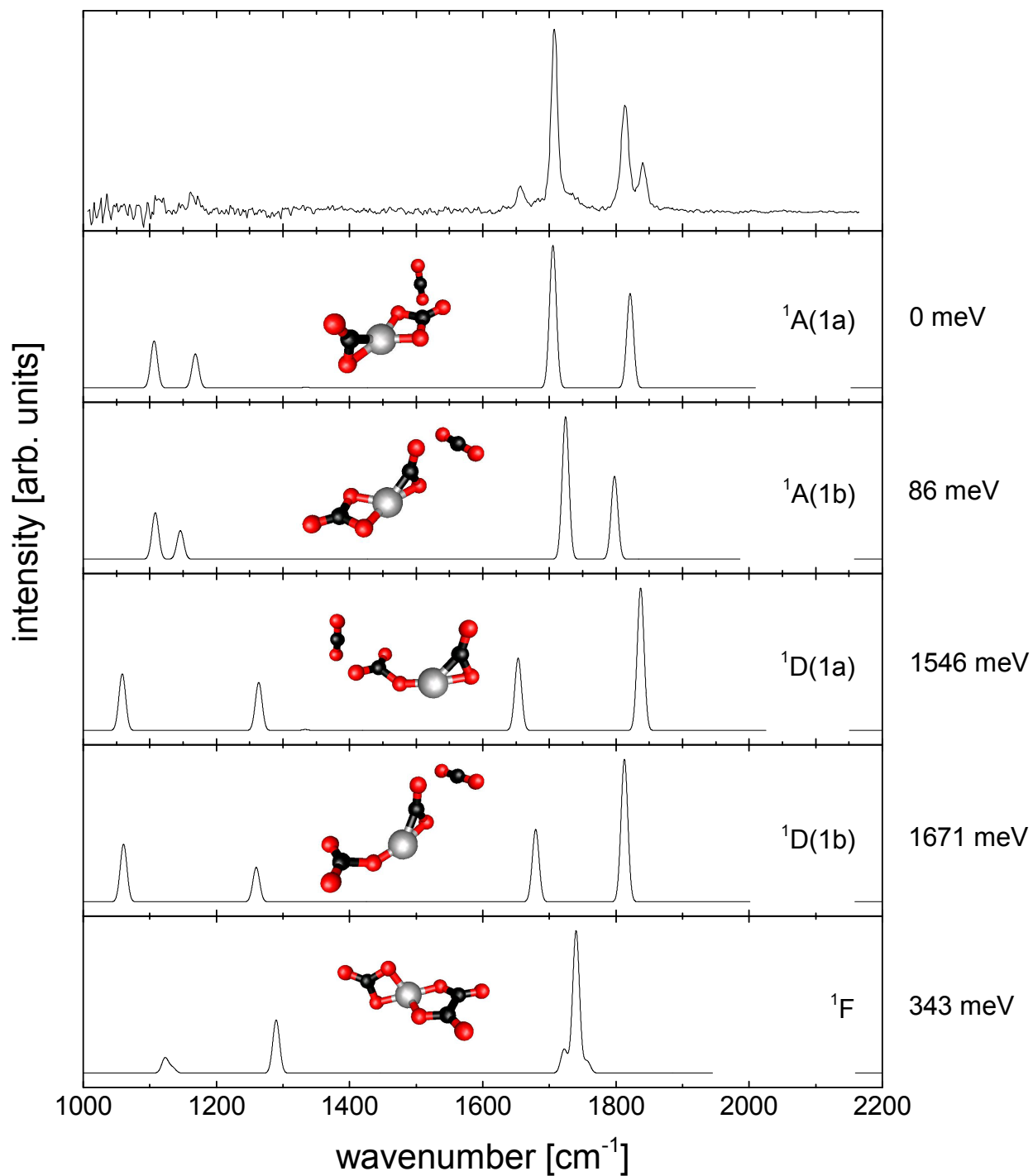


Figure 4.5: Comparison of the calculated singlet structures in Figure 4.4 to the experimental spectrum for $[\text{CoO}(\text{CO}_2)_3]^-$. Isomer labels and relative energies are given to the right. See text for discussion.

$[\text{CoO}(\text{CO}_2)_4]^-$ clusters, the cluster composition is likely of the form $[\text{CoO}(\text{CO}_2)_3]^- \cdot \text{CO}_2$. Isomer F is the most likely candidate and is predicted to exhibit vibrational frequencies within the 1700 cm^{-1} and 1800 cm^{-1} region. Exploratory calculations of various solvation positions around isomer F suggest that the charge distribution of isomer F is more polarizable than that of either A or D resulting in solvation around the C_2O_4 or CO_3 moieties giving rise to different predicted spectra. These shifts are to be expected since the combination of a C_2O_4 and a CO_3 subunit is large compared to all other calculated structures creating a more polarizable charge distribution. Isomer E also is predicted to exhibit vibrational features in this region and is a possible candidate for assignment of these features.

4.3.2 Infrared Spectra of $[\text{NiO}(\text{CO}_2)_n]^-$ Clusters

Figure 4.6 shows the experimental spectra of $[\text{NiO}(\text{CO}_2)_n]^-$ clusters ($n = 2 - 6$). As was mentioned at the beginning of this section, there are solvent (2260 cm^{-1} to 2400 cm^{-1}) and core (1000 cm^{-1} to 2150 cm^{-1}) spectral regions. Since the predicted structural motifs present in this study are similar to those predicted for $[\text{CoO}(\text{CO}_2)_n]^-$, the same labeling scheme will be used.

Unlike in $[\text{CoO}(\text{CO}_2)_n]^-$ clusters, fragmentation is first observed at $n = 2$ rather than at $n = 3$. Since a solvent peak is present for $[\text{NiO}(\text{CO}_2)_2]^-$ clusters, the form of the species giving rise to the observed features for $n = 2$ must be $[\text{NiO}(\text{CO}_2)]^- \cdot \text{CO}_2$. Calculations predict only two stable structures of this form; isomer G is a CO_3 moiety bound in an η^2 motif to the nickel atom and isomer H is a lone oxygen atom opposite an $\eta^2 \text{CO}_2$ unit (see Figure 4.7). These two structures are then solvated around the CO_3 and CO_2 moieties, respectively, by the second CO_2 molecule. Solvation around the open side of the Ni atom or the lone oxygen atom result in the formation of isomer A. While structures G and H are predicted to be stable, they are not predicted to be the lowest energy conformers calculated for $[\text{NiO}(\text{CO}_2)_2]^-$ (see isomer A in Figure 4.7).

The calculated spectra of isomers G and H are compared to the experimental spectrum of $[\text{NiO}(\text{CO}_2)_2]^-$ in Figure 4.8. The combination of isomers G and H recovers the two pronounced peaks at 1670 cm^{-1} and 1750 cm^{-1} in the experimental spectrum, respectively. The signal to noise

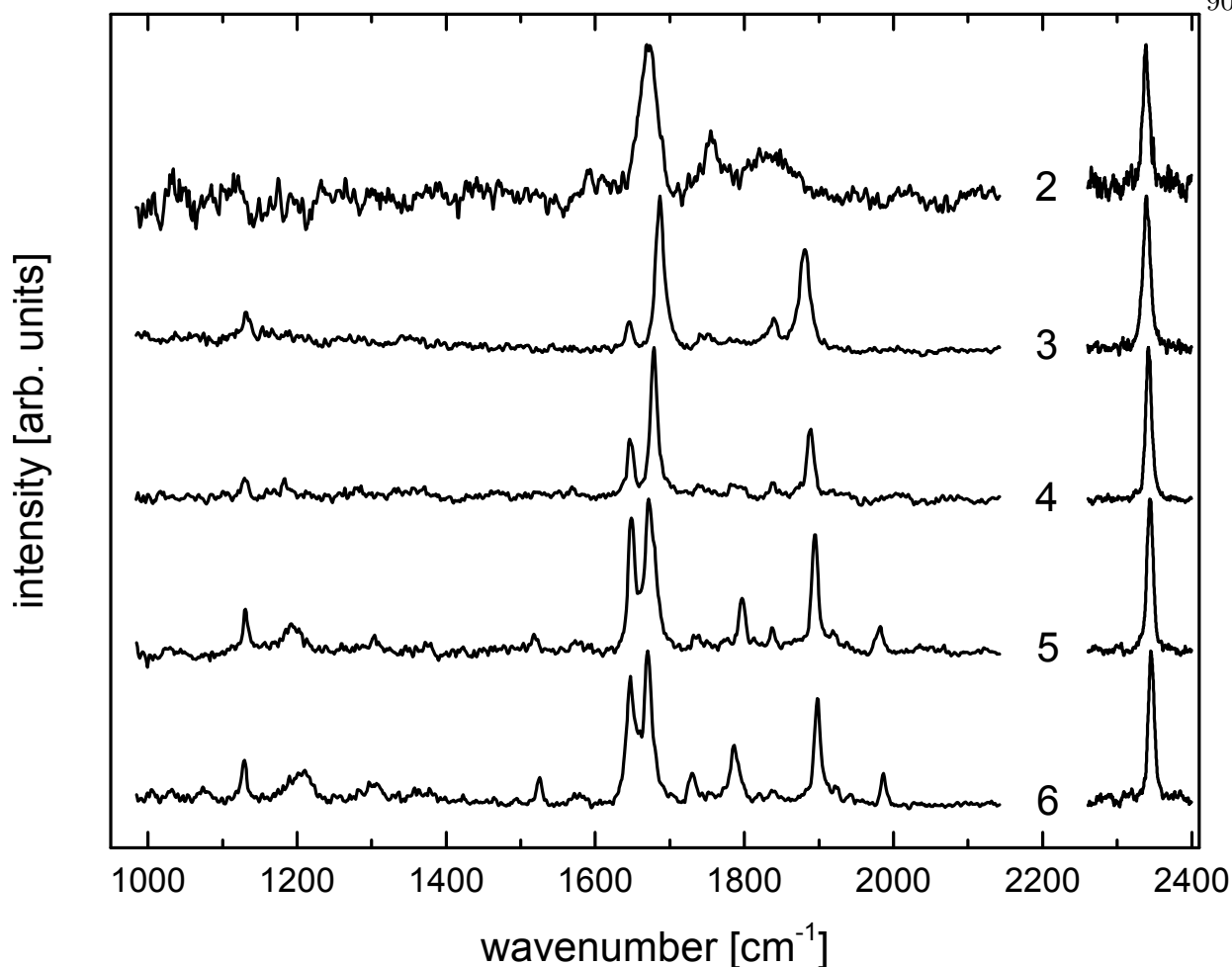


Figure 4.6: Experimental spectra of $[\text{NiO}(\text{CO}_2)_n]^-$. The numbers indicate the number of CO_2 molecules present. The left and right traces are individually normalized and are on different scales.

ratio of this spectrum is quite low compared to the spectra for $n \geq 3$. As was mentioned previously, isomers G and H are not the lowest energy structures at this cluster size but are the only calculated structures that are expected to be experimentally observable for $n = 2$. It is likely that isomer A has a much larger population in $[\text{NiO}(\text{CO}_2)_2]^-$ clusters leading to low populations of both G and H and, consequently, a relatively small number of parent ions containing a solvent CO_2 molecule. It should also be noted that similarly broad features observed in $[\text{Ni}(\text{CO}_2)_2]^-$ clusters were attributed to multiphoton effects since no solvent feature was observed (see Section 3.3). It is likely that the origin of the broad feature at 1825 cm^{-1} is multiphoton dissociation of isomer A (see Figure 4.8)

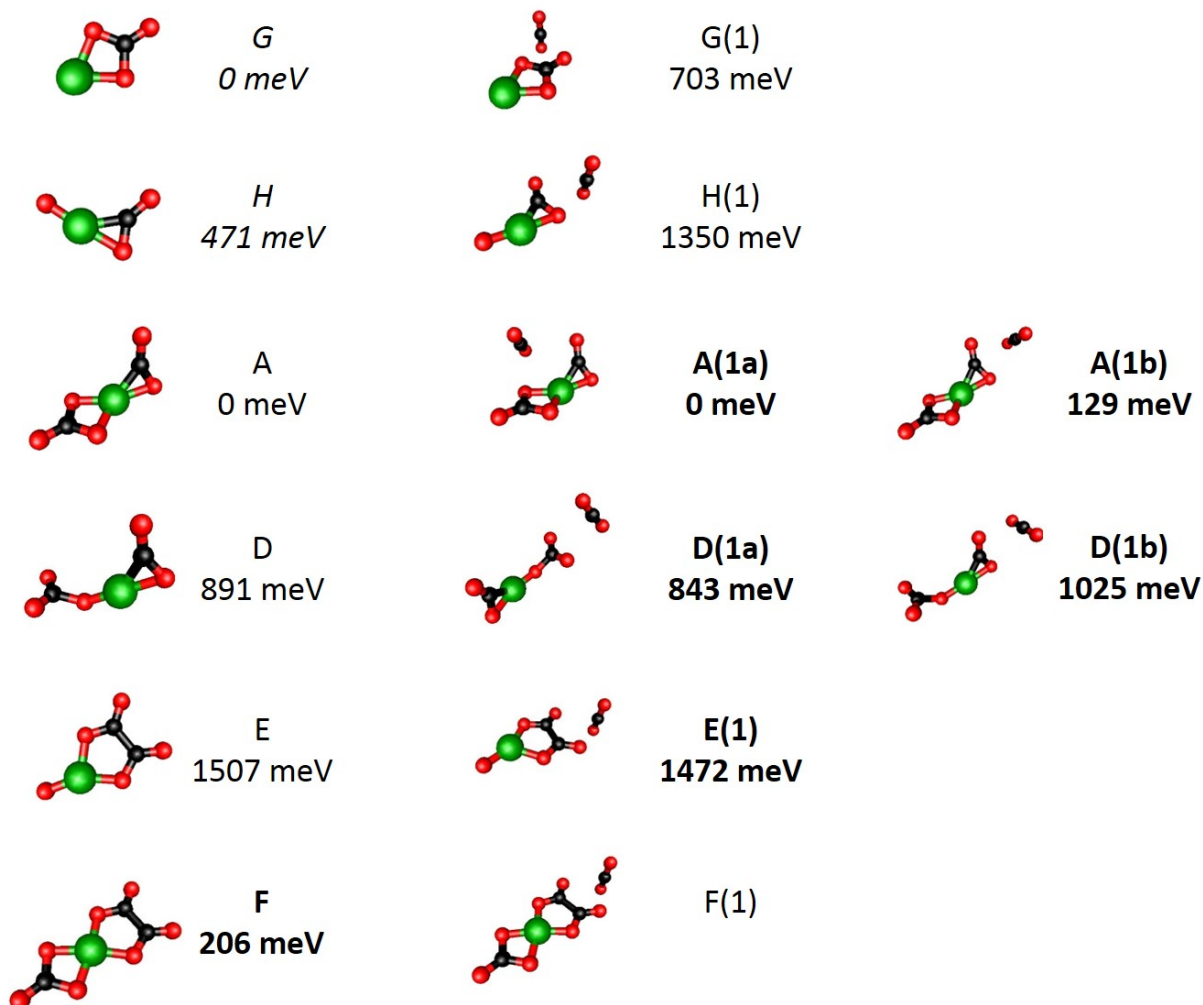


Figure 4.7: Calculated lowest energy structures for $[\text{NiO}(\text{CO}_2)_n]^-$. Structures in the leftmost column are bare core structures while the structures to the right are solvation isomer(s) of the core structures. The letters denote the core structure while the letter/number combination indicate the number of solvent molecules and their orientation around the core. Relative energies for $[\text{NiO}(\text{CO}_2)]^-$ structures are shown in *italics*, $[\text{NiO}(\text{CO}_2)_2]^-$ are shown in plain text and $[\text{NiO}(\text{CO}_2)_3]^-$ are shown in **bold**. No relative energy is presented for F(1) since there is no other structure of the form $[\text{NiO}(\text{CO}_2)_4]^-$ to compare it with. All relative energies are reported in meV.

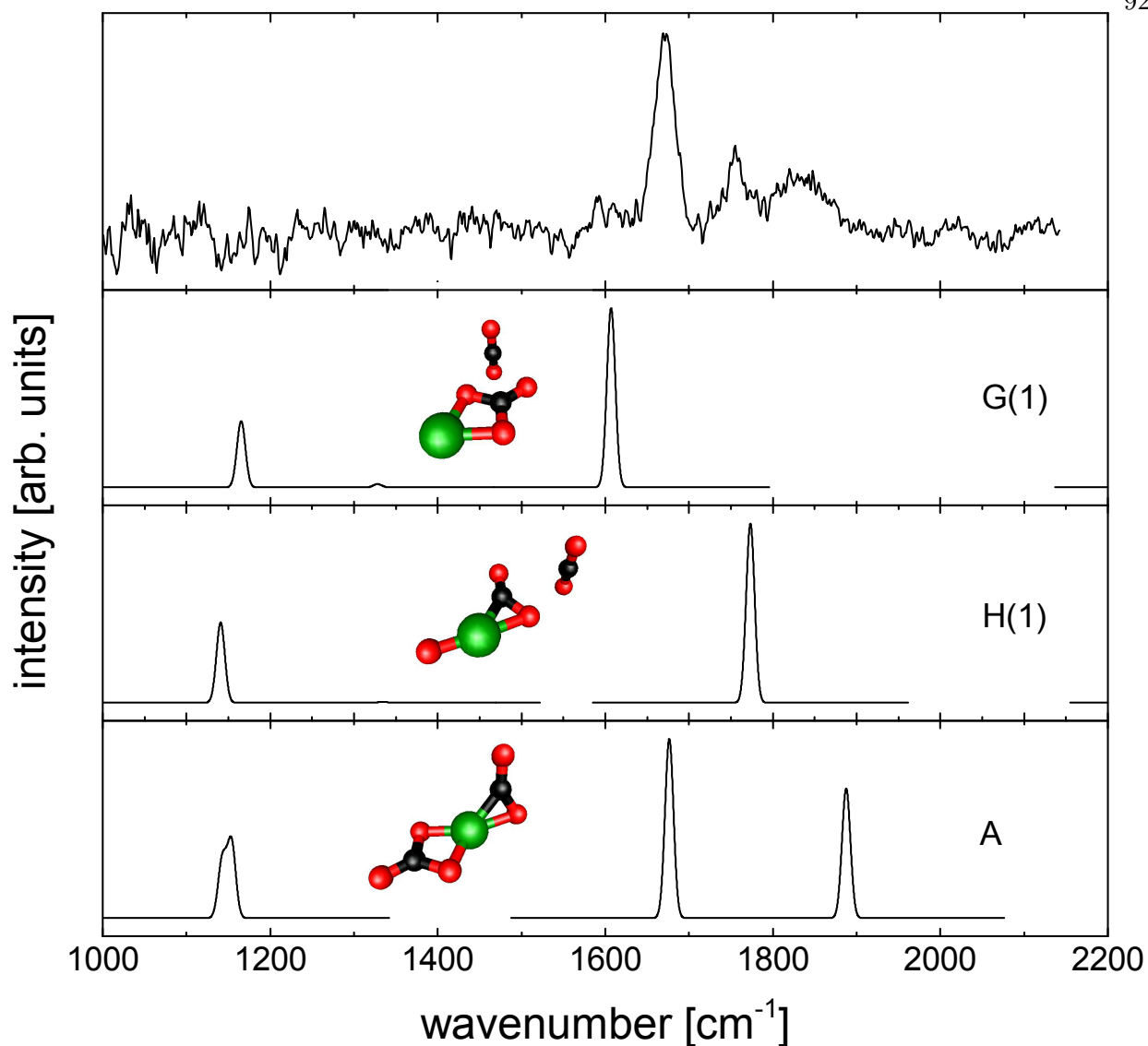


Figure 4.8: Comparison of calculated structures G(1), H(1) and A to the experimental spectrum of $[\text{NiO}(\text{CO}_2)_2]^-$. See Figure 4.7 for relative energies and text for discussion.

but, due to the low signal to noise ratio of the $n = 2$ spectrum, the presence of multiphoton effects is difficult to confirm.

For clusters $[\text{NiO}(\text{CO}_2)_3]^-$ and larger, not only does the signal to noise ratio improve drastically, but many new peaks are observed. This change in the spectrum suggests that multiple new structures contribute to the experimental spectrum. Figure 4.7 shows all of the relevant core structures calculated for $[\text{NiO}(\text{CO}_2)_n]^-$ clusters with the bare core structures shown in the left

column and various solvation isomers in the center and right columns. Like $[\text{CoO}(\text{CO}_2)_n]^-$, isomer A is predicted to be the global minimum structure. Structure D, also found and assigned in $[\text{CoO}(\text{CO}_2)_n]^-$ clusters, consists of an η^2 CO_2 moiety and an η^1 CO_3 subunit bound by only one of the oxygen atoms. Structures E and F are similar as they both contain a C_2O_4 moiety opposite either a lone oxygen atom or a CO_3 unit. Structures A, D, and E should all be observable at $[\text{NiO}(\text{CO}_2)_3]^-$ while isomer F should first be observable at $[\text{NiO}(\text{CO}_2)_4]^-$.

Figure 4.9 shows a comparison of select core isomers with formula $[\text{NiO}(\text{CO}_2)_3]^-$ to the experimental spectrum of $[\text{NiO}(\text{CO}_2)_3]^-$. Unlike in $[\text{CoO}(\text{CO}_2)_n]^-$, it is clear that solvation position makes a difference in the frequencies recovered. Structure A(1a) recovers the two major peaks at 1685 cm^{-1} and 1880 cm^{-1} while A(1b) recovers the major peaks at 1685 cm^{-1} and 1840 cm^{-1} . The difference between these two structures can be summarized by whether or not the CO_2 moiety is solvated. The two higher frequency modes represent molecular motion on the CO_2 moiety with the lower frequency of the two modes being recovered when the solvation position behind the CO_2 moiety is filled and the higher frequency when this position is vacant. This difference in predicted frequency as a function of solvation position shows that the charge distribution on the CO_2 moiety is noticeably affected by solvation. Conversely, the charge distribution of the CO_3 moiety, encoded in the 1685 cm^{-1} feature, is not strongly affected by solvation as both A(1a) and A(1b) recover the 1685 cm^{-1} peak. The peak at 1840 cm^{-1} is present for all clusters $n \geq 3$ indicating that if the solvation position behind the CO_2 moiety is filled, the peak at 1840 cm^{-1} is recovered.

The features at 1645 cm^{-1} and 1880 cm^{-1} are recovered by isomer D(1a) where the CO_3 moiety is solvated. The predicted charge distribution of isomers A and D differ only on the CO_3 moiety and the Ni atom leaving the CO_2 unit relatively unchanged. This similarity in partial charge on the CO_2 moiety results in spectral overlap of the 1880 cm^{-1} feature by isomers A(1a) and D(1a). This overlap is different from $[\text{CoO}(\text{CO}_2)_n]^-$ where the charge distributions of isomers A and D are completely different resulting in no overlap of their predicted spectra (see Table 4.1 and Figure 4.4). Another way to interpret the dominant spectral features is that the peaks from 1600 cm^{-1} to 1700 cm^{-1} encode the connectivity of the CO_3 moiety (ie. η^1 or η^2) while the features

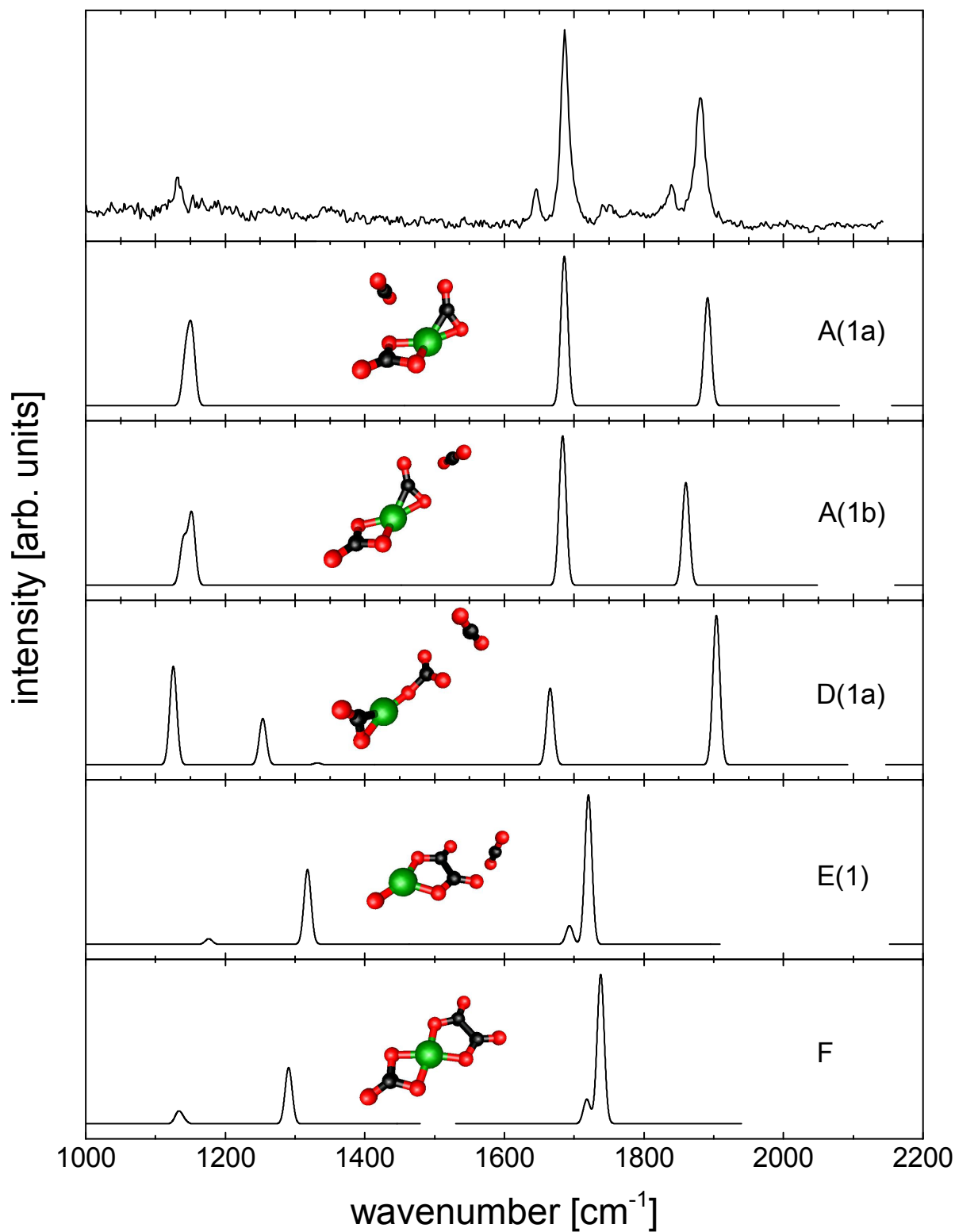


Figure 4.9: Comparison of calculated structures for $[\text{NiO}(\text{CO}_2)_3]^-$ to the experimental spectrum of $[\text{NiO}(\text{CO}_2)_3]^-$. See Figure 4.7 for relative energies and text for discussion.

between 1840 cm^{-1} and 1880 cm^{-1} indicate the occupation of the solvation positions around the CO_2 moiety. Table 4.2 shows the calculated charge distributions for the reported $[\text{NiO}(\text{CO}_2)_n]^-$ core structures.

Table 4.2: Calculated partial charges for the predicted core structures of $[\text{NiO}(\text{CO}_2)_n]^-$ presented in Figure 4.7. The partial charges are reported in units of e .

Core Structure	Ni	CO_3	CO_2	O	C_2O_4
^3G	+0.56	-1.56			
^1H	+0.65		-0.71	-0.94	
^3A	+0.93	-1.41	-0.52		
^1D	+0.72	-1.22	-0.50		
^3E	+1.17			-0.76	-1.41
^1F	+1.39	-1.10			-1.29

The last set of features to address are the weak peaks observed between 1730 cm^{-1} and 1830 cm^{-1} . These features can in part be attributed to isomer E(1) which is predicted to exhibit a peak around 1735 cm^{-1} (see Figure 4.9). At $n = 4$, a second feature appears at 1780 cm^{-1} . With the 1745 cm^{-1} feature being attributed to isomer E(1) and a cluster size of $n = 4$ at the onset of the 1780 cm^{-1} feature, it is logical to attribute the peak at 1780 cm^{-1} to isomer F. The comparison in Figure 4.9 shows that structure F does indeed predict a feature around 1780 cm^{-1} . Both isomer E and F persist as minor contributors to the experimental spectra as cluster size increases.

4.4 Conclusions

The structural motifs observed in both $[\text{CoO}(\text{CO}_2)_n]^-$ and $[\text{NiO}(\text{CO}_2)_n]^-$ clusters are similar. Structure A is the dominant structure in both sets of spectra with isomer D increasing in prevalence as the number of CO_2 molecules increases. Additionally, structures such as E and F are present as minor isomers for both CoO and NiO and persist with increasing cluster size.

While the structures and spectra for both clusters are similar, there are small differences. These differences can be attributed to the charge distributions of the core ions (See Tables 4.1 and 4.2). For $[\text{CoO}(\text{CO}_2)_n]^-$ clusters, the charge distribution is dependent on the connectivity of

the CO_3 moiety while in $[\text{NiO}(\text{CO}_2)_n]^-$ the charge distribution changes based on the connectivity of the CO_3 moiety and the occupation of specific solvation positions. The overall similarities and differences of these two cluster species are reminiscent of those between $[\text{Co}(\text{CO}_2)_n]^-$ and $[\text{Ni}(\text{CO}_2)_n]^-$ clusters.

Chapter 5

Observation of a Vibrationally Induced Electron Transfer Reaction in a Binary Molecular Complex

This Chapter has been reprinted with permission from Knurr, B. J., McCoy, A. B., Weber, J. M., “Vibrationally Induced Charge Transfer in a Bimolecular Model Complex in Vacuo.” *Journal of Chemical Physics*, 2013. 138: 224301. DOI: 10.1063/1.4808048. Copyright 2014, AIP Publishing LLC.

5.1 Introduction

Electron transfer is an elementary step in many chemical reactions and biological processes. [129] The means by which electrons can be transferred during a chemical reaction are many including detachment and recapture or simply by experiencing a potential difference causing the electron to move within the system. One unique class of reactions are those where the electron is excited such that a transfer event occurs by photodetachment of the electron. In this chapter, a vibrationally induced electron transfer reaction in a model system is observed and discussed.

In condensed phase chemistry, the potential energy surface tends to be characterized by relatively flat landscapes for reactants and products which are separated by a barrier. However, in gas phase reactions, pre-reaction complexes (entrance channel) and post-reaction complexes (exit channel) can be formed due to a lack of solvation effects that would otherwise destabilize the potential wells supporting these complexes. This is particularly true for reactions involving ionic species. [130–132] Experiments on mass selected ions in vacuo are well suited to study the

fundamental properties of entrance and exit channel complexes and the chemical reaction connecting them because the complexes can be prepared with well defined composition. One interesting class of reactions involves an ion-molecule complex which has an electron excited into the detachment-continuum is allowed to evolve. In these systems, the electron wave function is prepared at “half-collision” and the excited electron can either escape or be recaptured by the complex. [133–141]

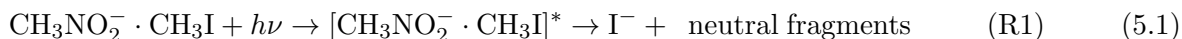
In certain systems vibrational excitation can lead to electron transfer on the electronic ground state potential energy surface. This has been observed, e.g., in CO₂ reduction mediated by excitation of a water network in CO₂·(H₂O)₆⁻ clusters, [142] an S_N2 like electron transfer reaction in Cl⁻·CH₃Br complexes initiated by the excitation of CH stretching modes, [143] and in hydrated nitromethane anion. [144]

An interesting prototype for this class of electron transfer reactions would be a vibrationally induced charge transfer between two molecular partners (rather than atom/molecule [143] or molecule/cluster [142, 144]). Here, the two molecules could be isolated as a binary complex or solvated by an inert solvent species (i.e. noble gas atoms). The question is whether or not mode specific behavior can be observed leading to increased efficiency of the electron transfer process. Observation of mode specific behavior would indicate that these “special” vibrational modes are connected efficiently to the transition state of the chemical reaction.

To carry out an experiment of this nature, there are certain requirements for the molecular partners. The donor must be able to detach an excess electron through vibrational excitation. In other words, the binding energy of the excess electron must be sufficiently low such that vibrational excitation can result in electron emission. Nitromethane (CH₃NO₂) has a well characterized valence anionic state where the excess electron is bound by ~ 1325 cm⁻¹. [145] Previous work has shown that vibrational excitation of CH stretching modes leads to efficient vibrational autodetachment in nitromethane as well as in other nitroalkanes. [146–148] These properties of nitromethane make it an ideal candidate as the electron donor species.

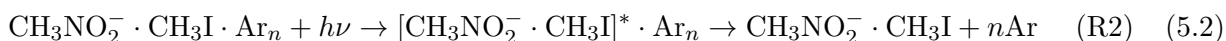
The acceptor must be able to exhibit a clearly detectable signature that electron transfer has occurred. Additionally, it would be ideal if recapture by the donor molecule is less favorable than

transfer to the acceptor. Considering these two criteria, iodomethane (methyl iodide or CH_3I) was chosen as an ideal acceptor molecule since it can only dissociatively attach an electron resulting in the irreversible formation of I^- and neutral fragments. The predicted outcome of vibrational excitation of a complex of nitromethane and iodomethane is shown in Equation 5.1.



Equation 5.1 (R1) is also shown graphically in Figure 5.1 (see top equation). The dissociative s-wave capture reaction for CH_3I is strongly exothermic [149] and has been extensively characterized before. [149, 150]

A second question with regard to these types of reactions is on what time scale the electron transfer process occurs. Depending on the time scale of the reaction, it may be possible to shut down the electron transfer reaction by employing a “bath” of solvent Ar atoms. The two competing processes would then be the electron transfer reaction resulting in the formation of I^- and relaxation of the vibrational energy to the solvent bath yielding Ar evaporation (see Equation 5.2 and bottom reaction in Figure 5.1).



In addition to information on the time scales of the competing reactions, insight can also be garnered on the barrier height of the electron transfer reaction based on the binding energy of Ar atoms and the number required to quench the reaction. [146, 151, 152]

In this chapter, we show that vibrationally mediated electron transfer does occur in this complex. We also answer questions concerning the structure of the entrance channel complex and give a lower limit estimate for the barrier height of the reaction. For experimental details please refer to Chapter 2.

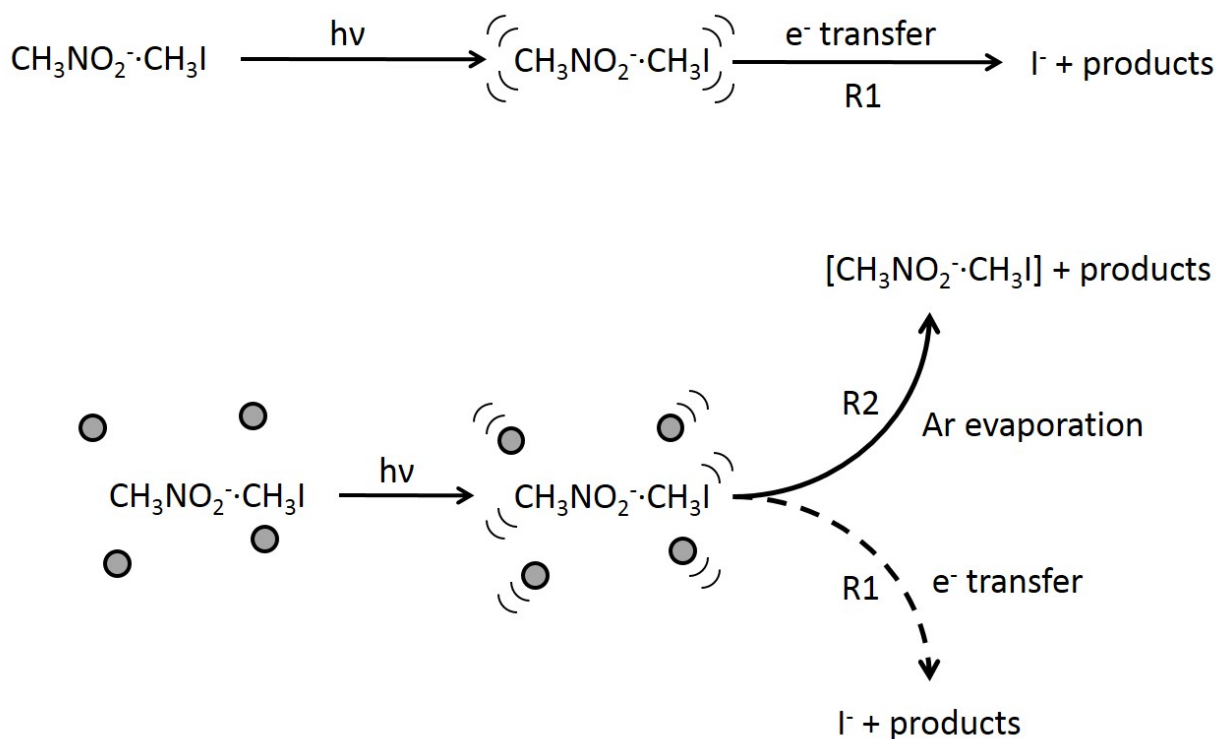


Figure 5.1: Schematic representations of the potential results of vibrational excitation of the bare binary complex (top) and the Ar solvated complex (bottom). R1 refers to Equation 5.1 while R2 refers to Equation 5.2. See text for additional discussion.

5.2 Computational Methods

Density functional theory calculations were used to determine the structures of reaction species and the energetics of the reaction. Calculations were performed employing the B3-LYP functional [59, 60] with dispersion correction [89] as implemented in the TURBOMOLE V. 5.9.1 suite of programs. [58] For all structure calculations the aug-cc-pVTZ-PP basis set [153] was used for iodine and aug-cc-pVTZ basis sets [65] were used for all other atoms. Potential energy scans of the C-I bond distance were performed using def2-TZVPP basis sets [61] for all atoms. Vibrational frequencies were calculated using the AOFORCE program. [66, 67] The calculated harmonic vibrational frequencies are scaled to account for the anharmonicities of the CH stretching modes. The scaling factors were obtained separately for each CH stretching mode in comparison with ex-

perimental values for neutral methyl iodide [37] and nitromethane anion. [147] The partial charges reported were calculated using a natural population analysis. [68]

5.3 Results and Discussion

The expected fragment ion to be generated in this reaction is I^- (see reaction R(1) at the top of Figure 5.1) by dissociative attachment of the transferred electron. [149] Previous studies on $I^- \cdot CH_3I$ have been observed to generate I^- upon electronic excitation in the equivalent of charge transfer to solvent. [133–135] Irradiation of $[CH_3NO_2 \cdot CH_3I]^-$ clusters results in the generation of I^- photo-products (see Figure 5.2 top trace). Five peaks are observed in the experimental spectrum when monitoring the formation of I^- and are all within the region corresponding to CH stretching frequencies. However, both nitromethane and iodomethane contain CH_3 groups complicating identification of the experimentally observed peaks.

To assign the observed peaks, we carried out experiments on $[CH_3NO_2 \cdot CD_3I]^-$ clusters. Here, all of the CH stretches belonging to iodomethane are replaced with CD stretches and therefore are shifted to lower frequencies. The spectrum of $[CH_3NO_2 \cdot CD_3I]^-$ monitoring the generation of I^- is shown in the bottom trace of Figure 5.2. As can be seen, the two peaks observed at 2950 cm^{-1} and 3056 cm^{-1} in the spectrum of the nondeuterated complex are absent in the spectrum of the deuterated complex indicating that those two peaks belong to CH stretches on iodomethane. The remaining peaks at 2804 cm^{-1} , 2937 cm^{-1} and 2977 cm^{-1} can then all be attributed to CH stretches on nitromethane (see Table 5.1).

There are a number of configurations in which the two molecules (CH_3NO_2 and CH_3I) can be arranged to form stable structures (see Figure 5.3). However, only two of the calculated structures have the starting molecular species intact (see structures I and II in Figure 5.3). In conformation I, the methyl group of CH_3I is pointing towards the nitro group in CH_3NO_2 , similar to the structure of a S_N2 entrance channel complex. The corresponding S_N2 exit channel is a structure where the methyl group binds to one of the oxygen atoms in the nitro group (see conformation IV in Figure 5.3), which is calculated to lie 1.16 eV lower in energy than conformation I. In conformation II, the

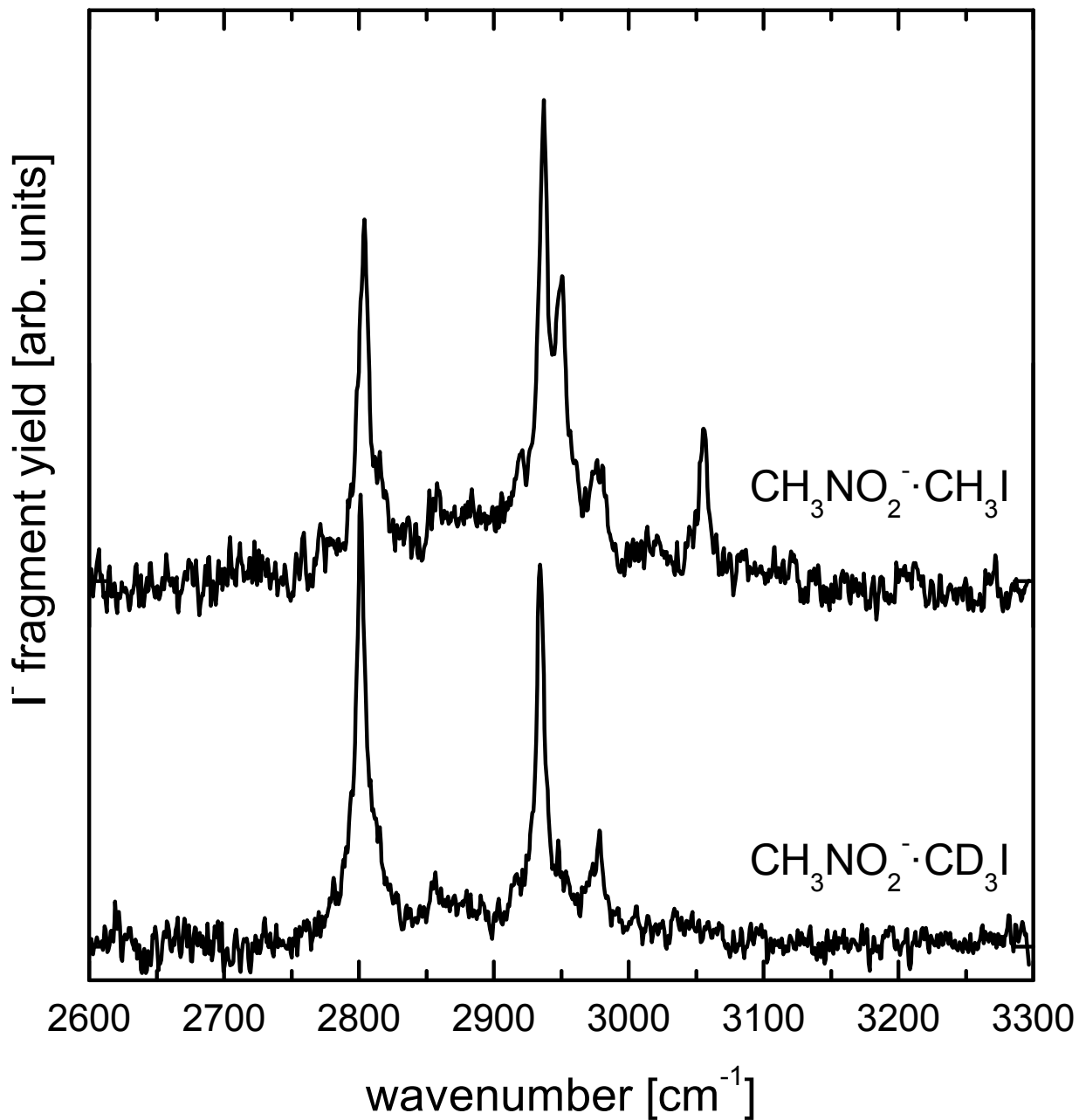


Figure 5.2: Photodissociation action spectra of $\text{CH}_3\text{NO}_2^-\cdot\text{CH}_3\text{I}$ (top trace) and $\text{CH}_3\text{NO}_2^-\cdot\text{CD}_3\text{I}$ (bottom trace) acquired by monitoring the formation of I^- photoproducts. The dashed lines indicate the CH stretching modes attributed to the CH_3I molecule within the complex. See text for further discussion.

Table 5.1: Experimentally determined and calculated peak positions in cm^{-1} for the dominant vibrational features observed in Figure 5.2. The experimental frequencies are reported for $\text{CH}_3\text{NO}_2^- \cdot \text{CH}_3\text{I}$ with values for $\text{CH}_3\text{NO}_2^- \cdot \text{CD}_3\text{I}$ given in parentheses where observed. Calculated frequencies (see above for discussion) are given for the non-deuterated complex only and are reported in $\text{km} \cdot \text{mol}^{-1}$. The vibrational assignments given are based on structure I in Figure 5.3.

Assignment	Experimental Wavenumber	Calculated Wavenumber	Calculated Intensity ($\text{km} \cdot \text{mol}^{-1}$)
Unique CH Stretch CH_3NO_2^-	2804 (2801)	2841	255
Symmetric CH_2 Stretch CH_3NO_2^-	2937 (2934)	2945	58
Antisymmetric CH_2 Stretch CH_3NO_2^-	2977 (2978)	2985	25
Symmetric CH_3 Stretch CH_3I	2950	2947	76
Antisymmetric CH_3 Stretch CH_3I	3056	3072	73
Antisymmetric CH_3 Stretch CH_3I	Not Observed	3097	0.02

iodine atom of CH_3I points towards the nitro group in CH_3NO_2^- , however this structure is ~ 100 meV higher in energy than conformation I. Other starting geometries either converged to conformation I or II or resulted in dissociation of the CH_3I molecule and the subsequent formation of I^- solvated by CH_3NO_2 and a methyl radical (this family of structures is represented by conformation III). In principle, conformation III is a possible exit channel complex as it lies ~ 500 meV lower in energy than the entrance channel complex conformation I.

The calculated IR spectra of conformers III and IV do not match the experimental spectra. In particular they both lack a dominant peak around 2800 cm^{-1} , a telltale signature of CH_3NO_2^- (the symmetric methyl stretch). This feature has been observed and well cataloged before in both $\text{CH}_3\text{NO}_2^- \cdot \text{Ar}_n$ and $\text{CH}_3\text{NO}_2^- \cdot (\text{H}_2\text{O})_n \cdot \text{Ar}_m$ clusters. [146,147] In order to confirm if conformation I or II is dominant or even present in the ion beam, we compare the calculated spectra for conformers I and II to the experimental spectrum (see Figure 5.4). It is clear in the comparison that conformation I recovers the experimental spectrum much better than does conformation II. Additionally, with the excess charge being localized on the nitro group, it is likely that the proximity of the nitro group to the iodine atom in conformation II will result in a substantially lower barrier to electron transfer than in conformation I. This lowering of the reaction barrier may be enough to allow

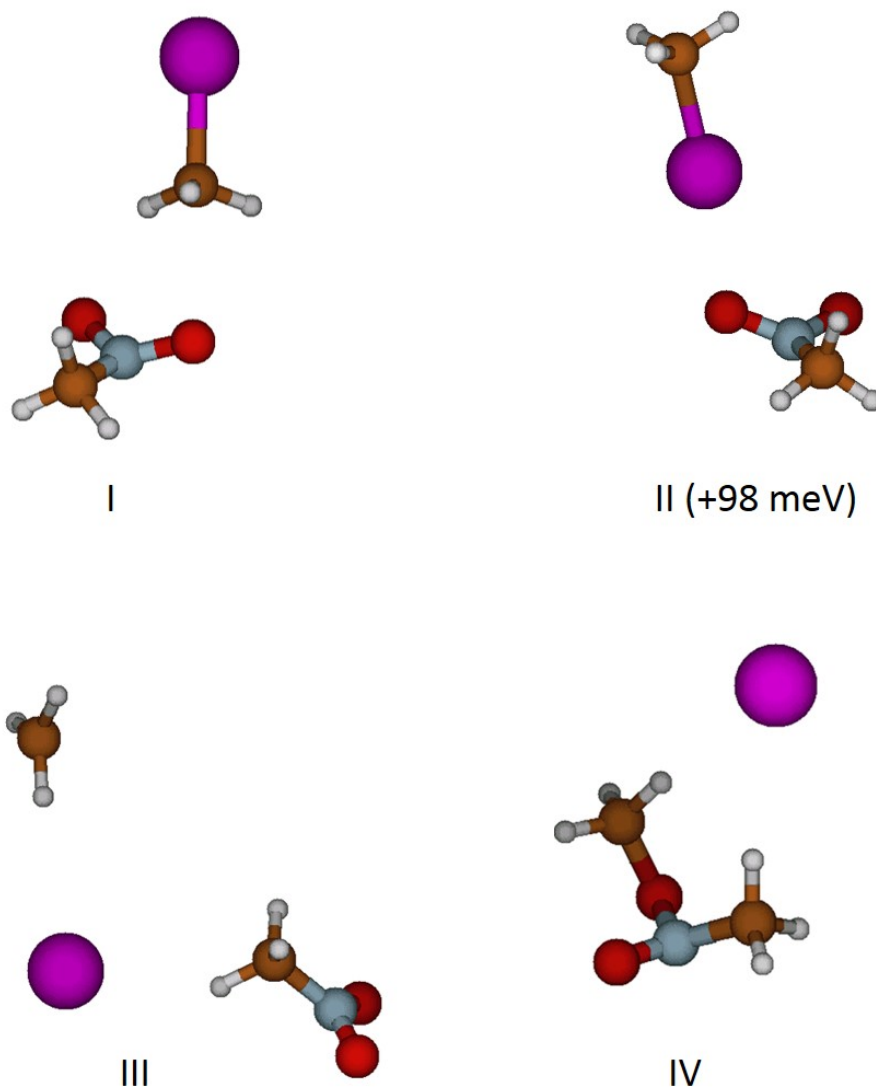


Figure 5.3: Calculated lowest energy structures for $[\text{CH}_3\text{NO}_2, \text{CH}_3, \text{I}]^-$ complexes. The relative energy for conformation II is with respect to conformation I. See text for discussion.

the electron transfer to proceed without vibrational excitation if the internal energy of the cluster is greater than the barrier height. We therefore, based on the predicted spectra and physical orientation considerations, assign our spectra to conformation I with negligible contribution from conformation II. Assignments of the vibrational features are given in Table 5.1.

As has been shown previously, Ar predissociation spectroscopy can give an estimate to the barrier height and information on the relative time scales of reaction to intra- and intermolecular

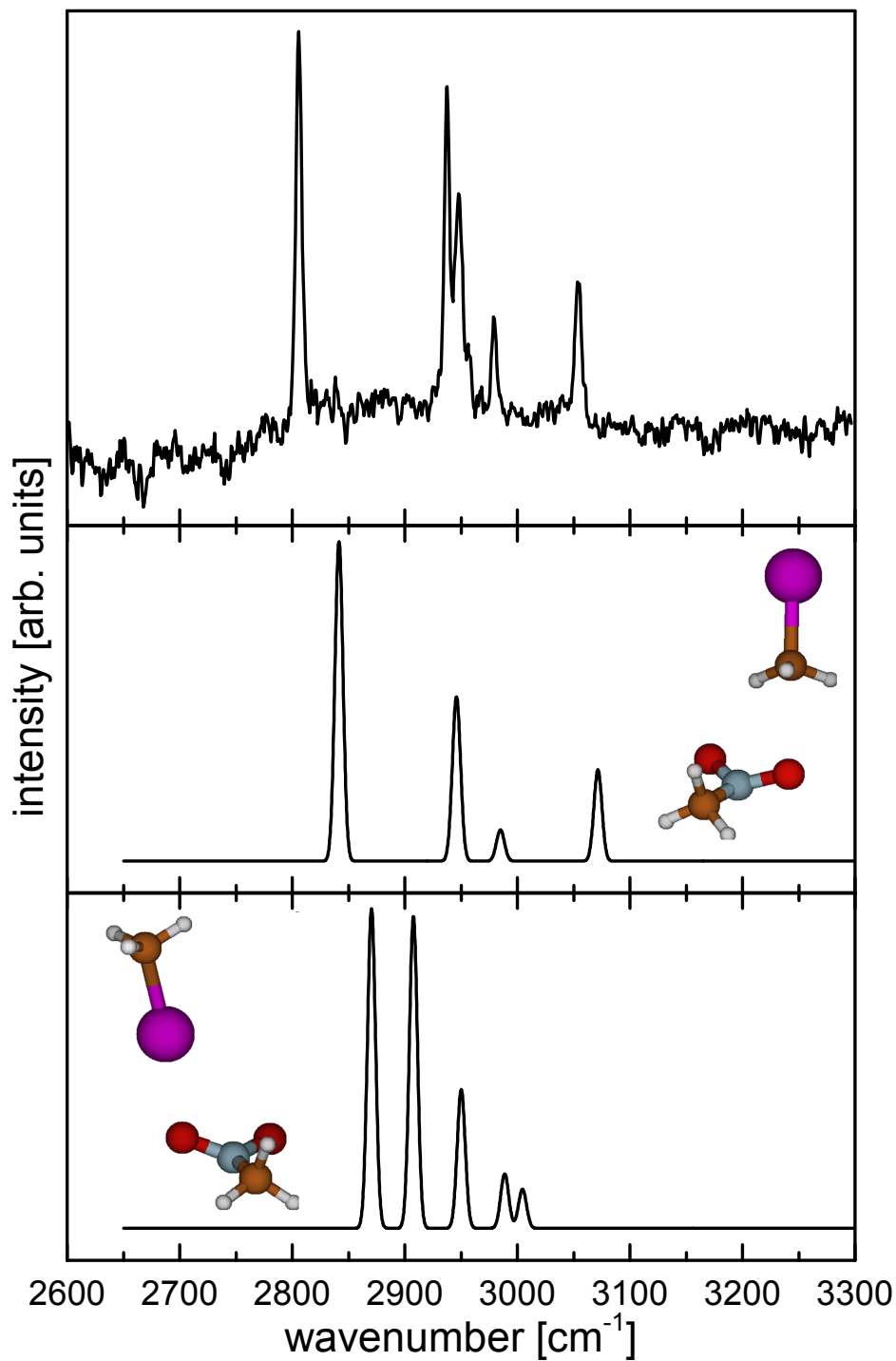


Figure 5.4: Comparison of the experimental spectrum of $\text{CH}_3\text{NO}_2 \cdot \text{CH}_3\text{I} \cdot \text{Ar}$ to the simulated spectra of calculated conformers I (middle panel) and II (bottom panel). The spectrum of the argon tagged ion is used because it is better resolved compared to the spectrum of the bare ion. Note that the peak at $\sim 2950 \text{ cm}^{-1}$ for conformer I contains two close lying transitions (see Table 5.1) which account for the splitting observed in the experimental spectrum.

molecular vibrational relaxation. [146, 151, 152] In the three studies cited, there is always a specific number of Ar atoms where the initially observed process (chemical reaction [151] or electron emission and vibrational autodetachment [146, 152]) is turned off. For $\text{CH}_3\text{NO}_2^- \cdot \text{CH}_3\text{I} \cdot \text{Ar}_n$, similar behavior is observed with a certain number of Ar atoms quenching the electron transfer reaction (see Figure 5.5). For $n = 1$, the only anionic fragment observed is I^- corresponding to R(1) in Figure 5.1. Spectra are sharper than they are for the bare cluster likely owing to the lower internal temperature of the cluster when Ar solvated. For $n = 2$, two different fragment channels are observed. While a small amount of I^- is still observed (red trace), the major pathway is a loss of Ar from the cluster without the formation of I^- but rather with the $\text{CH}_3\text{NO}_2^- \cdot \text{CH}_3\text{I}$ cluster intact (blue trace). The latter process corresponds to reaction R(2) as seen in Figure 5.1 and equation 5.2. At $n = 3$, no I^- formation is observed indicating that solvation by three Ar atoms is sufficient to deactivate the reaction. It should be noted that Ar solvation deactivated the electron transfer reaction for the deuterated cluster completely at $n = 2$ indicating that the barrier to reaction for CD_3I is slightly higher than for CH_3I .

The results of the Ar solvation experiments allow for an estimation of the barrier height. The binding energy of an Ar atom to nitromethane has been extensively measured by photoelectron spectroscopy and is reported to be ~ 60 meV or 480 cm^{-1} . [145] We assume that the binding energy of Ar to the $\text{CH}_3\text{NO}_2^- \cdot \text{CH}_3\text{I}$ complex is roughly the same. Since solvation by two Ar atoms is sufficient to mostly suppress the reaction channel, the height of the barrier should be on the order of the difference between the photon energy and the Ar binding energy. The lowest frequency peak observed is at $\sim 2800 \text{ cm}^{-1}$. Subtraction of the binding energy of the two Ar atoms gives an estimate of the barrier height at $\sim 1800 \text{ cm}^{-1}$ or 230 meV. The typical barrier for an $\text{S}_{\text{N}}2$ reaction is between $\sim 1000 \text{ cm}^{-1}$ and $\sim 3000 \text{ cm}^{-1}$ putting our estimate squarely in the typical range for an $\text{S}_{\text{N}}2$ reaction. [154–157] This estimate, within an error bar of 60 meV (the binding energy of one Ar atom), is in fact a lower limit of the barrier height as tunneling is possible at higher barrier energies. A schematic representation of the potential energy surface for the reaction coordinate is shown to scale in Figure 5.6.

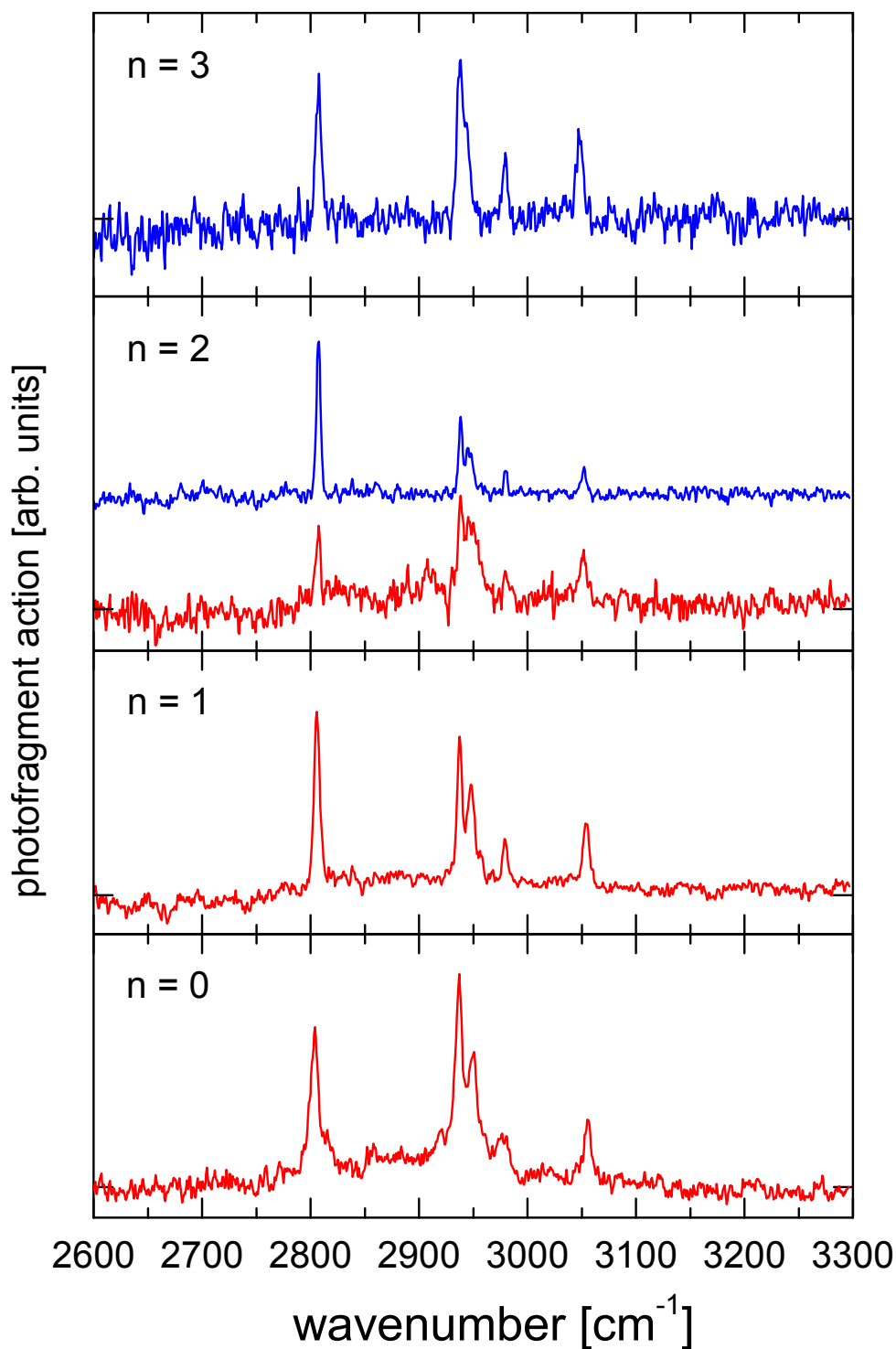


Figure 5.5: Experimental spectra of $\text{CH}_3\text{NO}_2 \cdot \text{CH}_3\text{I} \cdot \text{Ar}_n$ ($n = 0 - 3$). The different colors of the spectra indicate a change in the photofragmentation channel. The red curves are monitoring charge transfer and the subsequent formation of I^- photoproducts (see R1 in Figure 5.1) while the blue curves are monitoring Ar evaporation (see R2 in Figure 5.1). Note that both channels are observed for $n = 2$.

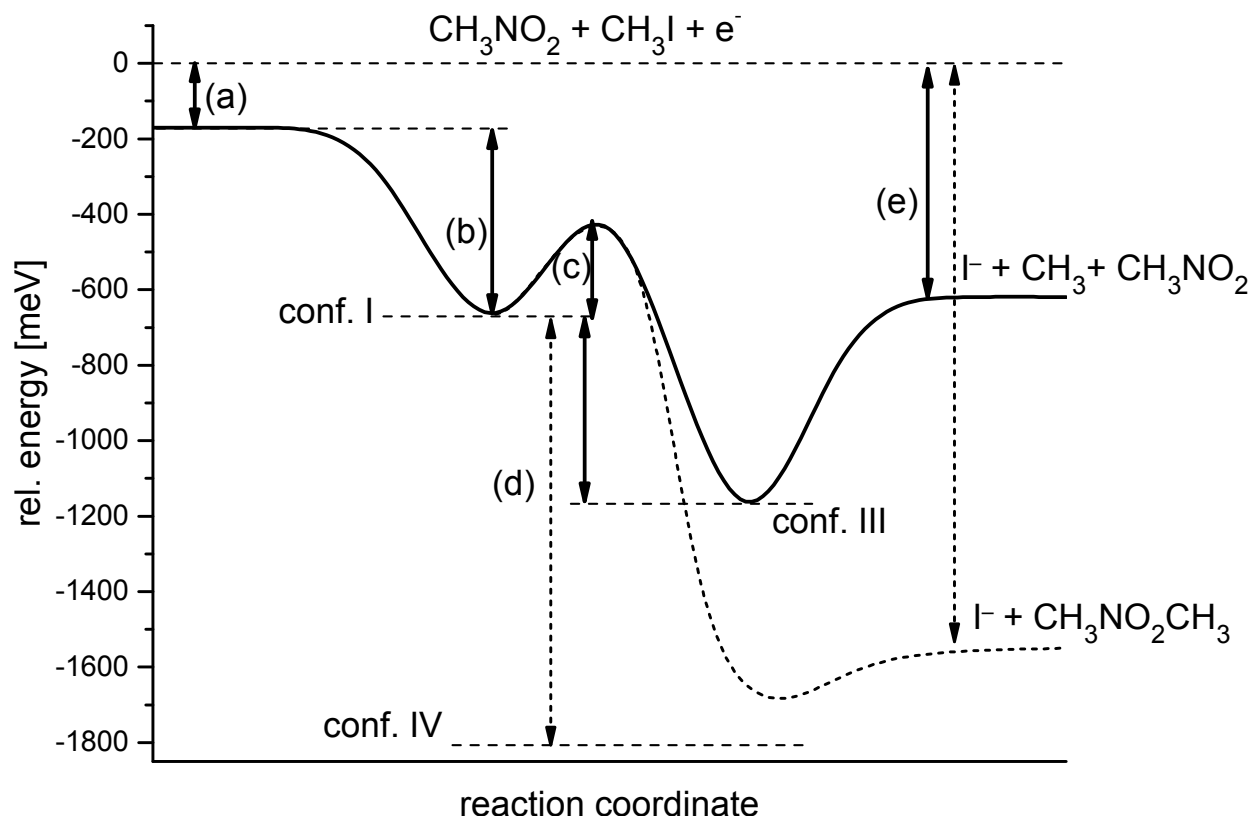


Figure 5.6: Schematic representation of the potential energy surface along the reaction coordinate of dissociative electron transfer from CH_3NO_2^- to CH_3I (energies are to scale). (a) Adiabatic electron affinity of CH_3NO_2^- (172 meV). [145] (b) Binding energy of the $\text{CH}_3\text{NO}_2^- \cdot \text{CH}_3\text{I}$ entrance channel complex (490 meV, calculated for conformation I). (c) Estimated lower limit of the barrier height for the electron transfer reaction (230 meV, experimentally determined from Ar solvation). (d) Relative energy of the exit channel complex for structure III (500 meV, solid curve) and structure IV (~ 1150 meV, dashed curve). The dashed line represents the $\text{S}_{\text{N}}2$ product. (e) Exit channel asymptote for the formation of I^- and neutral products based on the two possible exit channel complexes. The solid curve is based on the heat of reaction for dissociative electron attachment to CH_3I (620 meV). [149] The dashed curve represents the $\text{I}^- + \text{CH}_3\text{NO}_2\text{CH}_3$ asymptote (~ 1550 meV).

To further characterize the reaction and C-I bond cleavage, we calculated the potential energy of the cluster and the partial charge on the iodine atom as a function of C-I bond distance (see Figure 5.7). At a C-I bond distance of 2.6 \AA the calculated curves show a discontinuity indicating the likely presence of the transition state. The molecular coordinate showing the most change in this region is the out-of-plane angle of the CH_3 group of the iodomethane (θ_{OOP}). θ_{OOP} changes from

15.5° where the C atom is pointing towards the I atom to 5.5° where the C atom is pointing toward the nitro group with minute changes to a C-I bond distance of 2.6 Å. In addition to lengthening of the C-I bond, we regard this angle (θ_{OOP}) as a characteristic geometry parameter in this reaction. Additionally, the θ_{OOP} angle is characteristic of an S_N2 reaction giving credence to the idea that this reaction possesses S_N2 character even though the CH₃NO₂CH₃ radical is an unusual product.

In addition to geometry considerations, we can look at the amount of excess charge localized on the I atom as a function of C-I distance (bottom panel in Figure 5.7). The amount of charge changes abruptly from -0.5 e to -0.8 e at the transition state C-I distance of 2.6 Å. As the C-I bond distance continues to increase, the charge on the iodine approaches $-e$ indicating that the charge transfer reaction is complete.

The calculated potential energy curves discussed so far are an approximation for the adiabatic potential. If we fix θ_{oop} to the values of the entrance and exit geometries while varying the C-I bond length, we recover good approximations for the diabatic potential curves as well (shown in detail in the inset of the top panel of Figure 5.7). While it appears that we have recovered the potential energy surface, we caution that the reaction barrier height in this model is only predicted to be 54 meV. This is much lower than our experiments with Ar solvation suggest. While the qualitative picture of the S_N2 type of molecular motion leading to reaction appears to be correct, the calculated energetics of the potentials in Figure 5.7 would benefit from higher level calculations that are outside the scope of this study.

Finally, the question of whether or not mode-specific behavior is observed for this electron transfer reaction can be addressed. At best, mode specificity is weak for this reaction and several observations allow this conclusion. First, excitation of vibrational modes on either of the methyl groups results in electron transfer. This observation indicates that the mode into which energy is deposited is inconsequential for this reaction to proceed. Second, Ar evaporation must be faster than the electron transfer process since all observed vibrational frequencies were visible in the Ar loss spectra and the electron transfer reaction was shut down by addition of three Ar atoms. We expect intra- and intermolecular vibrational relaxation to prevent strong mode specific behavior

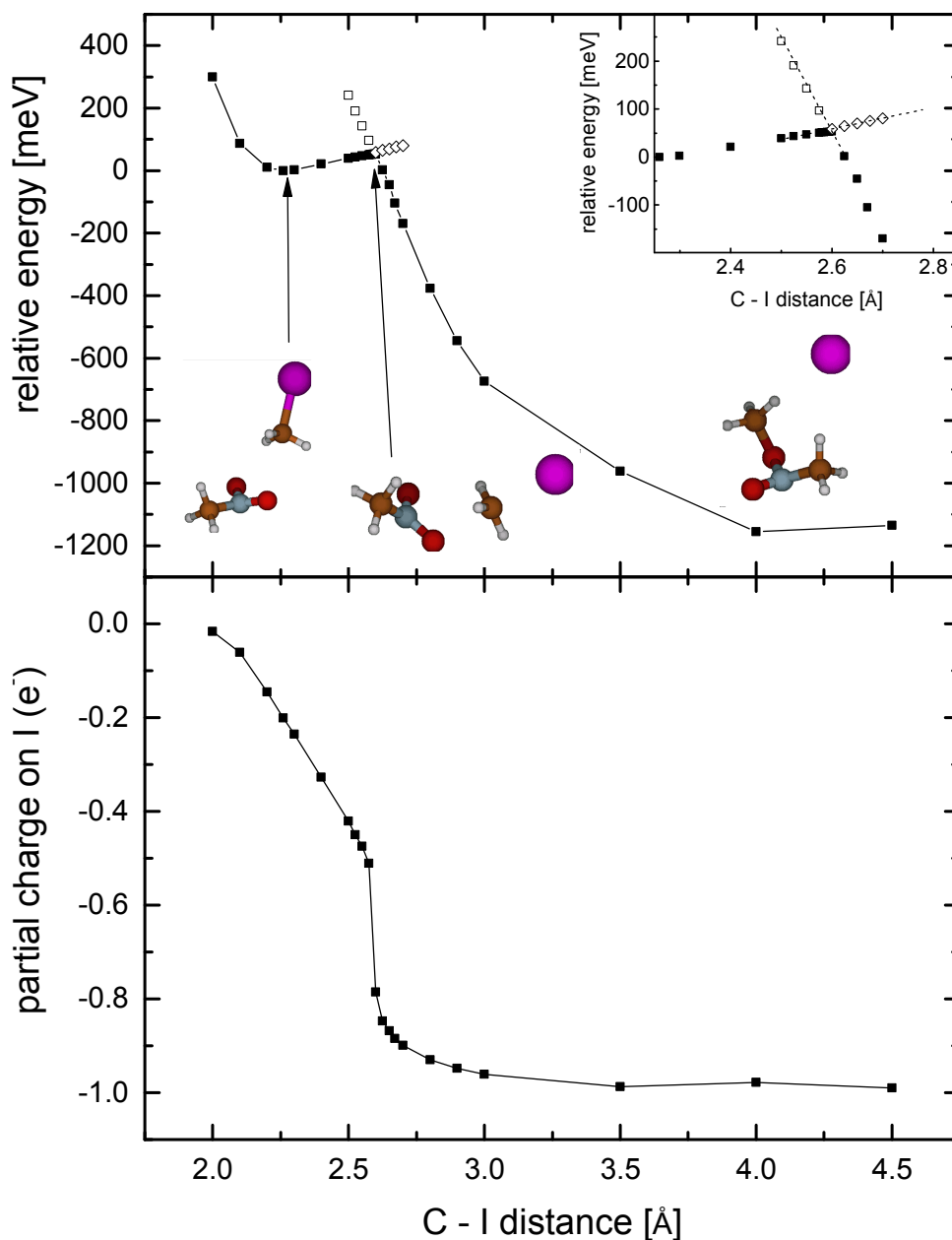


Figure 5.7: Calculated potential energy curve (top) and charge on the iodine atom (bottom) as a function of the CI bond distance. The full squares in the top trace are calculated with only the CI bond distance fixed, letting all other molecular coordinates relax. The open diamonds represent calculations where the out-of-plane angle of the methyl group of the CH_3I molecule (θ_{oop}) was fixed at 10.0° , corresponding to the geometry at a CI bond distance of ~ 2.575 Å in the unrestricted calculation. The open squares are data points calculated with the same angle (θ_{oop}) fixed at 5.5° , corresponding to the geometry at 2.625 Å CI bond distance in the unrestricted calculation. We note that θ_{oop} changes very rapidly as the transition state is approached. The resulting approximated diabatic potential energy curves are shown as dashed lines in the inset of the top panel; the structures shown as insets from left to right represent the entrance channel, transition state, and exit channel geometries, respectively.

as it appears that energy likely needs to localize in either the nitro wagging [148] or CI stretching modes for the reaction to proceed. Third, since it is unlikely that Ar evaporation is mode-specific, the close agreement of the relative intensities in the purely reactive ($n = 1$) and purely evaporative ($n = 3$) channels again likely indicates that there is no strong mode-specific behavior in the electron transfer reaction. This observation further suggests that the electron transfer reaction is quite slow compared to anharmonic coupling processes. Lastly, the CH bond lengths are calculated to change by only 0.02 \AA throughout the entire reaction. These calculations are for geometries corresponding to the data points in Figure 5.7 where a minimum C-H bond length of 1.07 \AA is observed at the transition state (2.6 \AA C-I distance in Figure 5.7). This calculation suggests that the CH stretching modes are barely participatory in the electron transfer reaction, consistent with the absence of mode specificity for the transitions probed.

5.4 Conclusion

In this study we looked at the binary complex of a nitromethane anion and a methyl iodide molecule as a model system for vibrationally mediated electron transfer. The electron transfer reaction can be triggered by excitation of any of the CH stretching vibrational modes in the complex, resulting in the formation of I^- product ions. The reaction was found to not exhibit mode-specific behavior. The electron transfer reaction can be partially deactivated by solvation of two Ar atoms and completely quenched by three Ar atoms. The barrier of the forward reaction is estimated to be on the order of 230 meV based on the partial quenching behavior of the reaction with two Ar atoms.

Chapter 6

Infrared Spectra of Naphthalene Water Clusters

This Chapter has been reprinted with permission from Knurr, B. J., Adams, C. L., Weber, J. M., “Structures and Charge Distributions of Cluster Anions Studied by Infrared Photodissociation Spectroscopy.” *Journal of Chemical Physics*, 2012. 137: 104303. DOI: 10.1063/1.4750371. Copyright 2014, AIP Publishing LLC.

6.1 Introduction

The solvation of ions is one of the most fundamental aspects of solution chemistry. In particular, the interaction of water molecules with negative charge has attracted a lot of attention. [158–165] While hydrated cluster anions are not direct analogs to bulk solutions, they do offer a unique opportunity to study ion solvation on a molecular level. Experiments on mass-selected cluster ions allow for precise control of ion composition and the number of water molecules in the microsolvation environment. Studies on microsolvated ions can be used to aid in modeling of solvation effects in addition to lending increased understanding to solution chemistry.

The interactions of water molecules within a cluster containing negatively charged species depends on the density and the shape of the charge distribution, among other factors. This can be particularly interesting when considering a diffuse charge distribution. In some cases, a molecular charge carrier is unstable but becomes stabilized through solvation. The most extreme case of a diffuse charge distribution is that of the solvated electron. The solvated electron is a case where there is no suitable molecular orbital to accommodate the electron but it can be stabilized through

interactions with a solvent species, e.g. by species that possess a dipole of sufficient magnitude ($\mu \geq 2.5$ D for a rotating dipole [166]). In the case of neat water, an excess electron can be solvated by two or more water molecules. [158]

A second interesting set of diffuse charge carriers are aromatic molecules. Here, the excess electron can be confined to the aromatic π -system where it will take the general shape of the π -system molecular orbital. The adiabatic electron affinities (AEA) of a number of small aromatic systems have been measured and the general trend is that as the π -system grows, the AEA also increases. The AEA of benzene (Bz) has been measured to be -1.1 eV [167] while the AEA of naphthalene (Np) is only -0.2 eV [168–170] and in the case of phenanthrene is thought to be -0.01 eV. [171] Anthracene appears to be the smallest (unsubstituted) aromatic hydrocarbon that can form a stable isolated anion in the gas phase (AEA = +0.53). [172]

Experiments by Mikami and co-workers have shown that for a sufficiently large cluster of the form $[\text{Bz} \cdot (\text{H}_2\text{O})_n]^-$, the anion is stable ($n \geq 6$). [159] However, it was unclear whether the excess charge was localized in the water network or if the π -system of the Bz molecule was involved in containing the excess electron, even though the data suggested that the valence orbitals of the Bz were involved.

Naphthalene anion (Np^-) has been found to be stable in a number of different organic solvents as early as the 1950's. [173–175] From one perspective, the interaction of water with Np^- is relevant for electrochemical applications of Np and other aromatic species. In many of these applications, the presence of water would be an impurity to the reaction and could result in protonation of the aromatic species thus inhibiting the performance of the reaction. [176] This is particularly important in regards to polycyclicaromatic hydrocarbons (PAH) becoming more common in organic electronics where exposure to water can be quite damaging to a device. [177–179] From a second perspective, Np can be viewed as a small model system for graphene or larger PAHs. Graphene and graphite systems are considered to be hydrophobic. However, the presence of a negative charge can change the nature of the interaction with water and water networks. In this sense Np can be used as a model system for studying the interaction of water with a charged carbon-based nanomaterial.

Photoelectron spectroscopy studies have shown that one water molecule is sufficient to stabilize an excess electron on the aromatic system of Np. [168–170] Unfortunately, little structural information could be obtained from these photoelectron studies. Infrared studies have been used to gain structural information on isolated gas phase clusters for years. [180–184] The hydrated Np^- has been investigated before by Mikami and co-workers where they studied vibrational autodetachment (VAD) after infrared absorption by $[\text{Np}\cdot(\text{H}_2\text{O})_2]^-$. Based on the infrared spectra, it was determined that all of the OH groups were involved in ionic π -H-bonds to the aromatic system of the Np or in water-water H-bonds. However, no structure was assigned that gave rise to the observed features. Additionally, no spectra existed on the monohydrate or on higher levels of hydration. One would expect either solvation of the entire π -system until no more water can be accommodated or the formation of water-water networks that reside on the surface of the Np^- anion with a competition of the two processes potentially being at play.

In this chapter, the spectra of $[\text{Np}\cdot(\text{H}_2\text{O})_n]^- \cdot \text{Ar}_m$ ($n = 1 - 6$) will be presented. Using density functional theory, the structural motifs of the water networks and the involvement of the π -system of the Np will be discussed.

6.2 Computational Methods

Density functional calculations were used to identify structural motifs for $[\text{Np}\cdot(\text{H}_2\text{O})_n]^-$ clusters. The B3-LYP functional [59,60] with dispersion correction [89] as implemented in the TURBO-MOLE v. 5.9.1 suite of programs was used for all calculations. [58] The def2-TZVP basis sets were used for all atoms. [64] Harmonic frequencies were calculated using the AOFORCE program. [66,67] To account for anharmonicity, the calculated harmonic frequencies were scaled by 0.96091. This scaling factor was obtained by comparing the calculated and experimentally measured OH stretching frequencies for a free H_2O molecule. For this study, calculated CH stretching frequencies are not reported as the CH stretching region of Np contains a plethora of Fermi resonances. [185–187] It is likely that the spectra of the anion also exhibit these resonances making harmonic approximation calculations generally meaningless.

It is worth noting that for all identified minimum energy structures, vibrational modes with very low frequencies ($\leq 50 \text{ cm}^{-1}$) were found. These modes can be attributed to the entire water network sliding, rocking or tilting on the surface of the Np π -system. This indicates that the potential energy surfaces of these clusters are quite flat and that low energy vibrational modes will be very anharmonic. As the number of water molecules increases, there are an increasing number of possible configurations of the water molecules. Additional structures and their relative energies and predicted spectra for all cluster sizes can be found in Appendix C.

6.3 Results and Discussion

6.3.1 OH Stretching Vibrations

6.3.1.1 $[\text{Np}\cdot(\text{H}_2\text{O})]^-$

Figure 6.1 shows the spectrum of $[\text{Np}\cdot(\text{H}_2\text{O})]^- \cdot \text{Ar}_8$ acquired by monitoring the loss of 6 Ar atoms. The region from 2900 cm^{-1} to 3100 cm^{-1} contains the CH stretching signatures of the Np molecule. The broad feature at 3540 cm^{-1} can be attributed to the water molecule. Interestingly, no feature is observed at 3700 cm^{-1} where the frequency of a free OH stretch would be expected. This observation indicates that both OH groups are interacting with the Np^- and that the one observed OH band is due to the symmetric water stretch. Features due to the antisymmetric water stretch (expected at higher energy) are predicted to be low in intensity and are likely below the detection limit of this experiment.

Calculated structures belonging to minima on the potential energy surface and their calculated infrared spectra are shown in Figure 6.1. Conformer 1-1 recovers the experimental spectrum the best. This structure is also consistent with the predictions of Schiedt *et al.* [168] and Kawamata *et al.* [188] In conformer 1-1, the water molecule is bridging the two carbon rings and binding the excess electron in the π -system of the Np molecule. Conformer 1-2 has the water molecule aligned roughly along the length of the Np molecule where the water molecule is only making one ionic hydrogen bond with the Np molecule. This results in a free OH group that is only weakly tethered

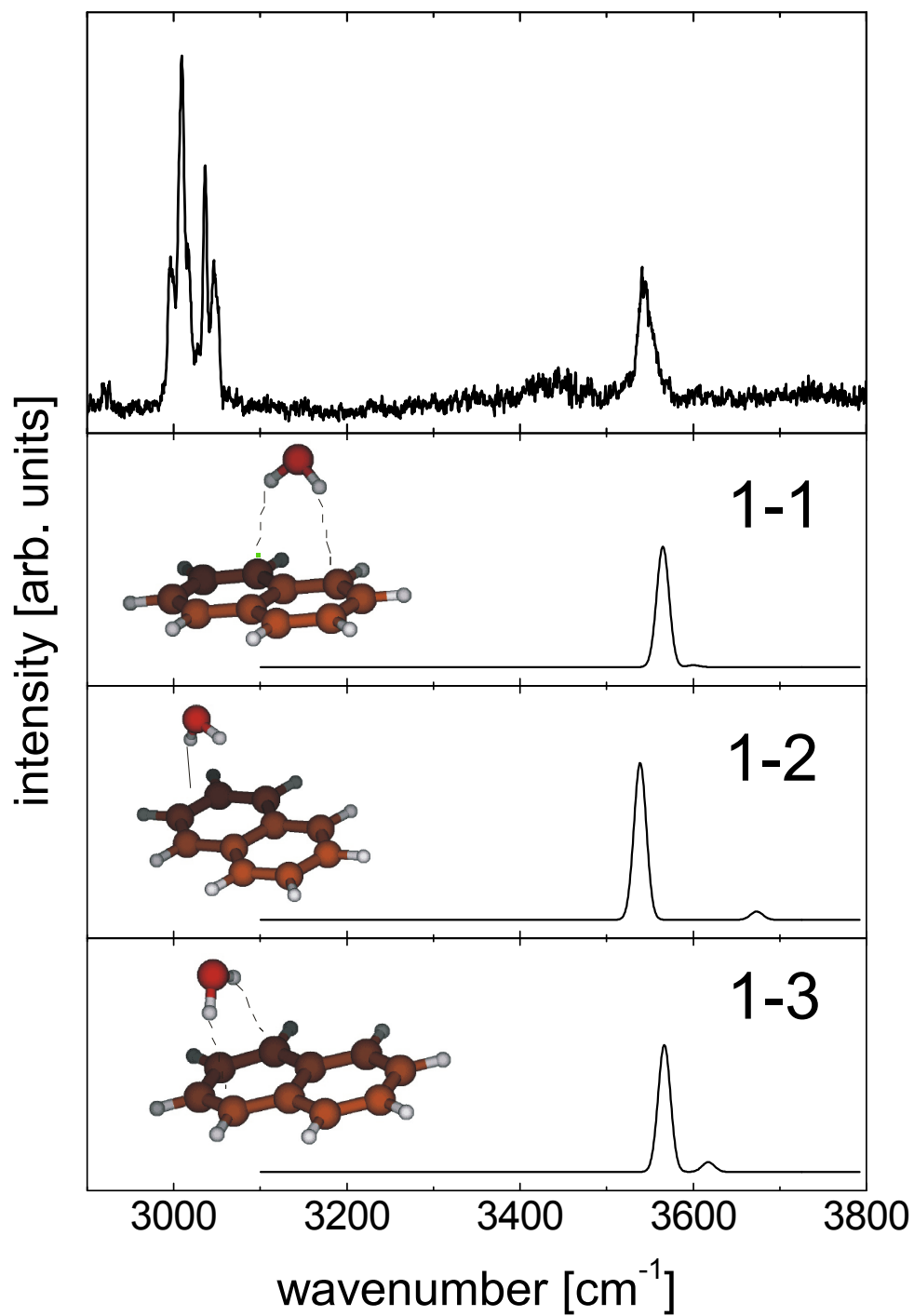


Figure 6.1: Experimental spectrum and calculated spectra of $[\text{Np}\cdot(\text{H}_2\text{O})]^-$. Top trace is the experimental spectrum of $[\text{Np}\cdot(\text{H}_2\text{O})]^- \cdot \text{Ar}_8$ acquired by monitoring the loss of 6 Ar atoms. Bottom traces are calculated conformers and their predicted infrared spectra. The dashed lines are meant to show ionic π -H-bonds. See text for discussion.

to the π -system. The signature of the free OH around 3700 cm^{-1} is not observed in the experimental spectrum. Conformer 1-3 is similar to conformer 1-1 in that it bridges two carbon atoms but rather than bridging the two carbon rings, conformer 1-3 bridges one carbon ring perpendicular to the length of the Np molecule. All of these calculated structures are within 25 meV of each other and we view them as isoenergetic.

Comparing the predicted harmonic frequencies of the calculated conformers shows that all conformers generally recover the experimental spectrum. However, as was mentioned above conformer 1-2 exhibits a feature of a free OH group which is not present in the experimental spectrum. Since the signatures due to the antisymmetric stretch are not recovered in the experimental spectrum we cannot unambiguously assign the experimental spectrum to one conformer. Additionally, it is likely that there are multiple isomers populated giving rise to the broad nature of the observed feature at 3540 cm^{-1} . Alternatively, conformers with the same position of the water molecule with different positions of the Ar atoms have been shown to lead to broadening of the observed vibrational features. It is most likely that there are multiple effects at play that are causing the broadening of the observed OH stretching feature. Regardless, we can definitively say that the water molecule is bound to the π -system with both OH groups and likely has a number of different positions it can bind to on the surface of the Np^- .

Aside from the structure of the cluster, the monohydrate offers an opportunity to consider the stabilization of the excess electron on the Np molecule. It has been firmly established that Np^- exists in organic solvents [173,189] but there has been no observation of Np^- in aqueous solution. Neither free Np or water bind an excess electron while water dimer anions can exist as dipole-bound states. However, since the AEA of Np is much lower than that of water combined with the evidence from photoelectron spectra by Bowen and co-workers, [170] it is very likely that the excess electron is localized primarily on the Np molecule.

If the electron binding energy is lower than the transition energies being studied, then excitation can result in VAD. VAD has been observed in a number of systems including $[\text{Np}\cdot(\text{H}_2\text{O})_2]^-$. [146–148,188,190] To observe VAD, the following condition must be met

$$h\nu - E(\text{Ar}) > AEA, \quad (6.1)$$

where AEA is the adiabatic electron affinity of the species and $E(\text{Ar})$ is the binding energy of the Ar atoms evaporated after photon absorption. By describing the system as an evaporative ensemble, [8] one can approximate

$$E(\text{Ar}) \approx m \cdot E_{avg}, \quad (6.2)$$

where E_{avg} is the average binding energy of one Ar atom.

Figure 6.2 shows a comparison of the action spectra taken for $[\text{Np} \cdot (\text{H}_2\text{O})]^- \cdot \text{Ar}_m$ ($m = 4, 5, 8$). Note that the OH stretch is strongly suppressed for $m = 4$ indicating that the energy remaining after evaporation of four Ar atoms is enough to undergo VAD. Stated another way, the remaining energy is greater than the AEA of $[\text{Np} \cdot (\text{H}_2\text{O})]^-$. However, the CH stretches are still observed indicating that $h\nu = 3055 \text{ cm}^{-1}$ is insufficient to observe VAD on the μs time scale of the experiment. Using the condition for VAD given in Equation 6.1 and an AEA of 0.11 eV, [168,170] the average binding energy of an Ar atom can be bracketed between 540 cm^{-1} and 660 cm^{-1} by comparing the spectra for $m = 4$ and 5. This range of calculated binding energies is consistent with a number of other studies that predict the binding energy of an Ar atom to be on the order of a few hundred cm^{-1} . [145,146] It is also worth noting that the peak position of the OH stretch is not sensitive to the number of Ar atoms.

6.3.1.2 $[\text{Np} \cdot (\text{H}_2\text{O})_2]^-$

The infrared spectrum of $[\text{Np} \cdot (\text{H}_2\text{O})_2]^-$ has been reported previously by Kawamata *et al.* [188] In their studies, VAD was used rather than Ar predissociation to acquire the spectra. They found multiple broad features that were attributed to a combination of higher energy water-water interactions and lower energy ionic π -H-bonds.

Figure 6.3 shows the infrared spectrum of $[\text{Np} \cdot (\text{H}_2\text{O})_2]^- \cdot \text{Ar}_2$ monitoring the loss of both Ar

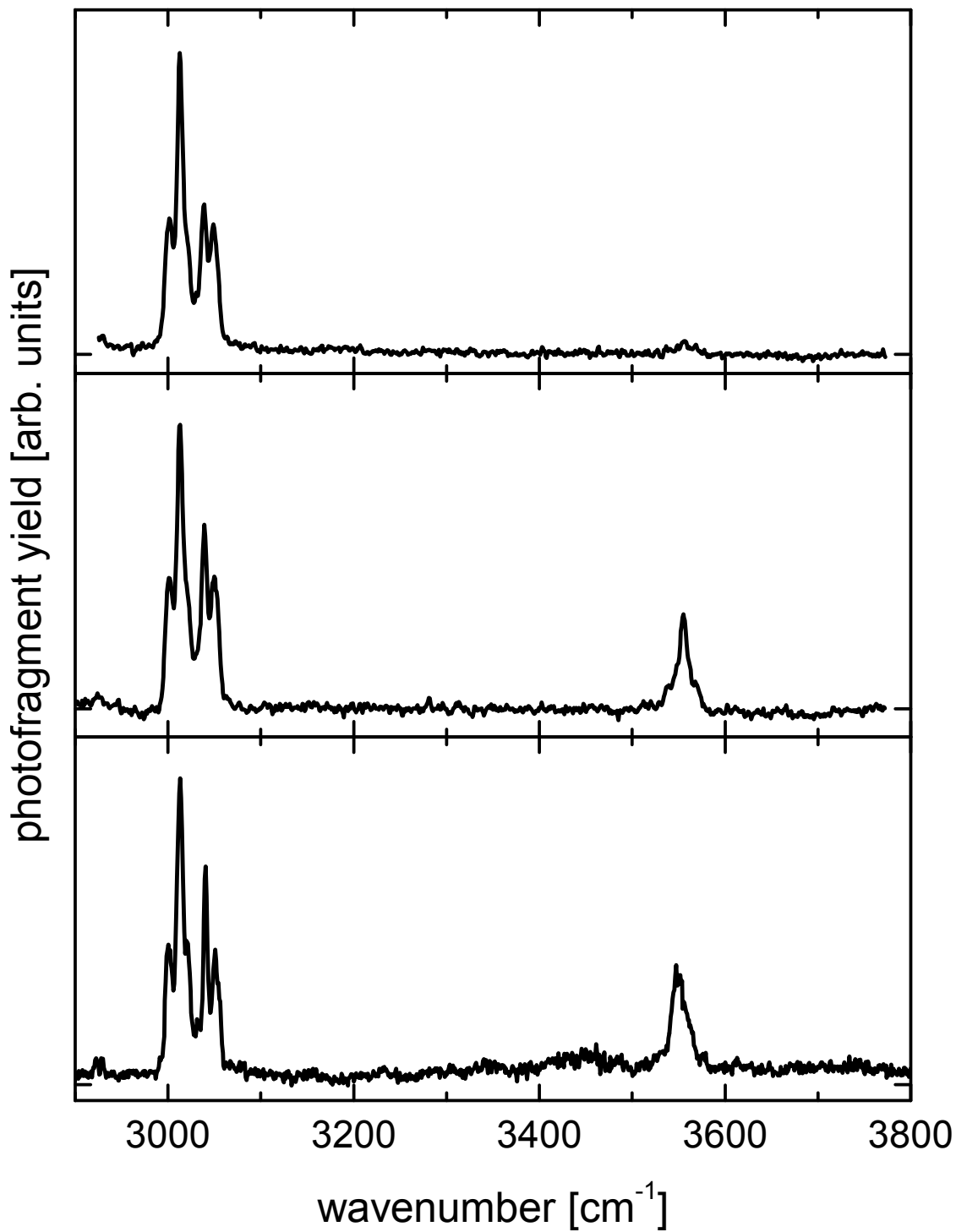


Figure 6.2: Observation of vibrational autodetachment in $[\text{Np} \cdot (\text{H}_2\text{O})]^- \cdot \text{Ar}_m$ clusters. Top trace: $m = 4$, monitoring the loss of all 4 Ar atoms. Center trace: $m = 5$, monitoring the loss of all 5 Ar atoms. Bottom trace: $m = 8$, monitoring the loss of 5 Ar atoms. Note that the loss of 6 Ar atoms (shown in Figure 6.1) yields the same spectrum as the loss of 5 Ar atoms.

atoms. The OH stretching region exhibits four well resolved and intense peaks, two around 3600 cm^{-1} and two around 3515 cm^{-1} . Again, there is no signature around 3700 cm^{-1} indicative of a free OH group. These spectra are consistent with those taken by Kawamata *et al.* [188] however, the spectra presented here exhibit sharper vibrational features allowing better structural assignment. This can be attributed to the lower cluster temperatures necessary to achieve Ar solvation.

Selected calculated conformers for $[\text{Np}\cdot(\text{H}_2\text{O})_2]^-$ are shown in Figure 6.3 beneath the experimental spectrum. In the lowest energy conformer (2-1), one water molecule forms two ionic π -H-bonds while the other forms one water-water H-bond and one π -ionic H-bond and the water subcluster is oriented roughly parallel to the long axis of the Np molecule. This structure is reminiscent of the $(\text{H}_2\text{O})_2^-$ anion where the excess electron is in a dipole bound state localized on one side of the two water molecules. Here, the water dimer is binding into the π -system of the Np molecule and is acting as a stabilizing presence for the excess electron localized in the π -system. Conformer 2-2 is isoenergetic with conformer 2-1 but structurally spans only one of the carbon rings rather than both. Additionally, one of the OH groups in conformer 2-2 is nearly free.

Conformers 2-3 and 2-4 are typical members of the family of structures where there are no water-water hydrogen bonds formed. Multiple structures were found in this family with both water molecules on the same side of the Np (2-3) or on different sides (2-4). This family of structures is rather high in energy compared to those where there are water-water H-bonds ($\sim 100\text{ meV}$ higher). This energetic difference indicates that there is a substantial energetic penalty for not forming water-water interactions and that water-water H-bonds are more energetically stabilizing compared to ionic π -H-bonds. The structure proposed by Kawamata *et al.* [188] was not found to be a stable structure in our calculations.

Comparison of the calculated spectra to the experimental spectrum reveals that only conformer 2-1 accurately recovers the experimental spectrum. Even though conformer 2-2 exhibits a nearly identical water subunit, the nature of its interaction with the Np^- results in a very different infrared spectrum specifically in the prediction of a nearly free OH group. Based on our structural assignment to conformer 2-1, the vibrational modes can also be assigned. The lowest frequency

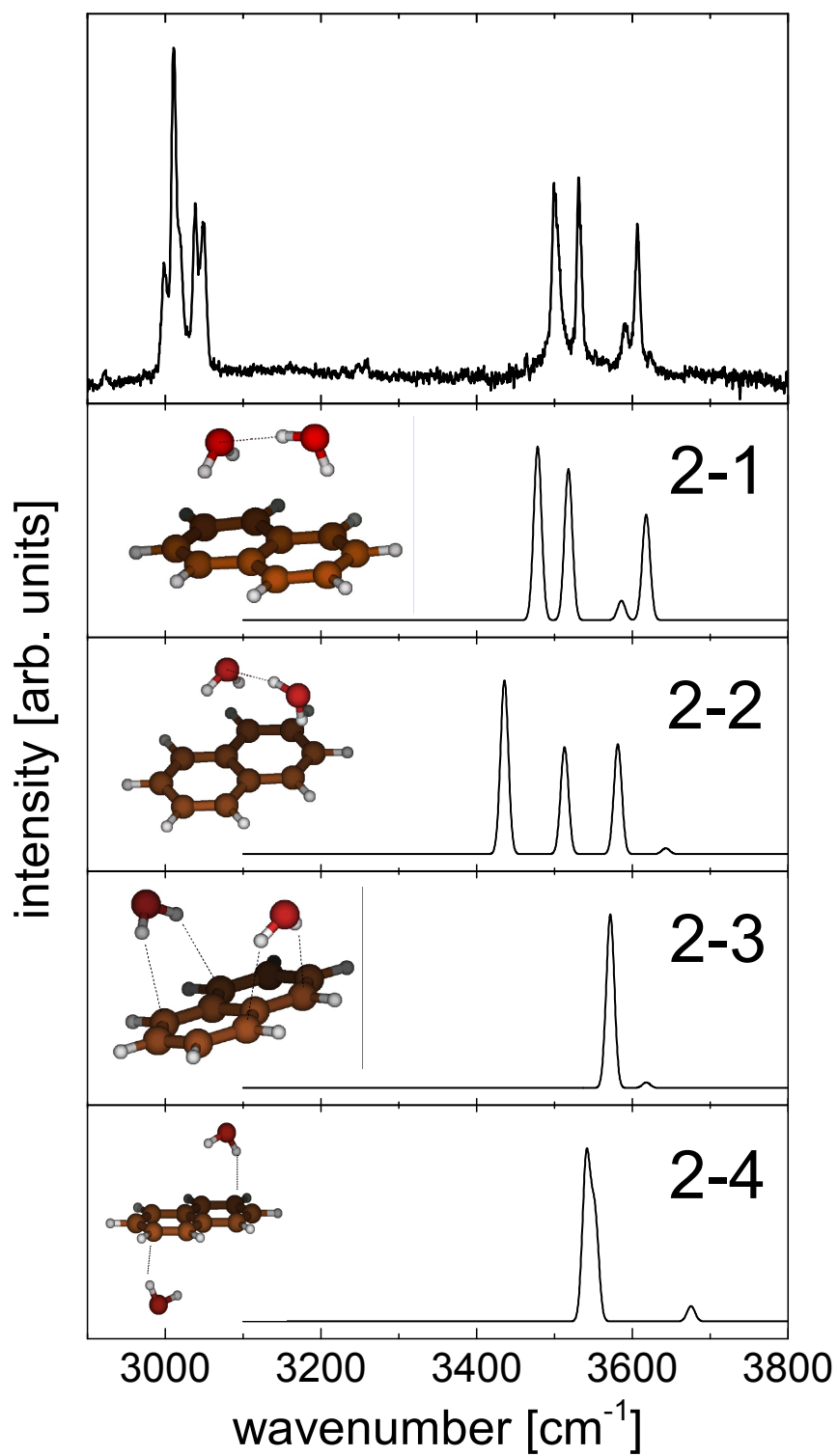


Figure 6.3: Experimental spectrum and calculated spectra of $[\text{Np}\cdot(\text{H}_2\text{O})_2]^-$. Top trace is the experimental spectrum of $[\text{Np}\cdot(\text{H}_2\text{O})_2]^- \cdot \text{Ar}_2$ acquired by monitoring the loss of 2 Ar atoms. Bottom traces are calculated conformers and their predicted infrared spectra. The dashed lines show the hydrogen bonds. See text for discussion.

peak corresponds to the symmetric stretching modes of the two water molecules coupled in phase while the next higher mode corresponds to their out-of-phase combination. These assignments are reminiscent of those of the water hexamer anion where the observed lowest frequency mode has been assigned to the symmetric stretch of a H-bond acceptor. [164,165] The next higher (and weakest) OH stretch is assigned to the antisymmetric stretch of the water with two hydrogen bonds to the π -system. The highest energy observed stretching frequency is assigned to the antisymmetric stretch of the H-bond donor water molecule. The weak shoulder feature around 3620 cm^{-1} is unassigned but could be due to an isomer where one water molecule is in a slightly different conformation with respect to the Np^- anion. Additionally, it should be noted that the small feature around 3260 cm^{-1} is likely due to the bend overtone of the water dimer. Since the symmetric stretching modes are lower in the dihydrate cluster compared to the monohydrate, there can be improved coupling to the bending overtones. This feature is absent in the monohydrate cluster.

6.3.1.3 $[\text{Np}\cdot(\text{H}_2\text{O})_3]^-$

Figure 6.4 show the experimental spectrum of $[\text{Np}\cdot(\text{H}_2\text{O})_3]^- \cdot \text{Ar}_8$. The broad feature centered at 3270 cm^{-1} can be attributed to the bend overtones of water molecules. The OH stretching region is quite complicated and exhibits far more bands than there are OH groups in the cluster. This indicates that there are at least two conformers populated to give rise to the number of observed peaks. The most stable calculated conformer is a homodromic ring (3-1) where the water molecules form a three membered ring with each water molecule donating and accepting a proton in the form of water-water H-bonds while also engaging in an ionic π -H-bond. A bent chain structure (3-2) is predicted 67 meV higher in energy. Here two of the water molecules each form a water-water H-bond and an ionic π -H-bond while the third water molecule has two ionic π -H-bonds. A second chain conformer (3-3) is predicted to lie 247 meV higher in energy than the ring structure. Both of the chain conformers are analogous to the water trimer anion but here, the dangling OH group on the end can bind to the π -system resulting in no free OH groups.

Other minimum energy structures were found that possessed a water dimer and a lone water

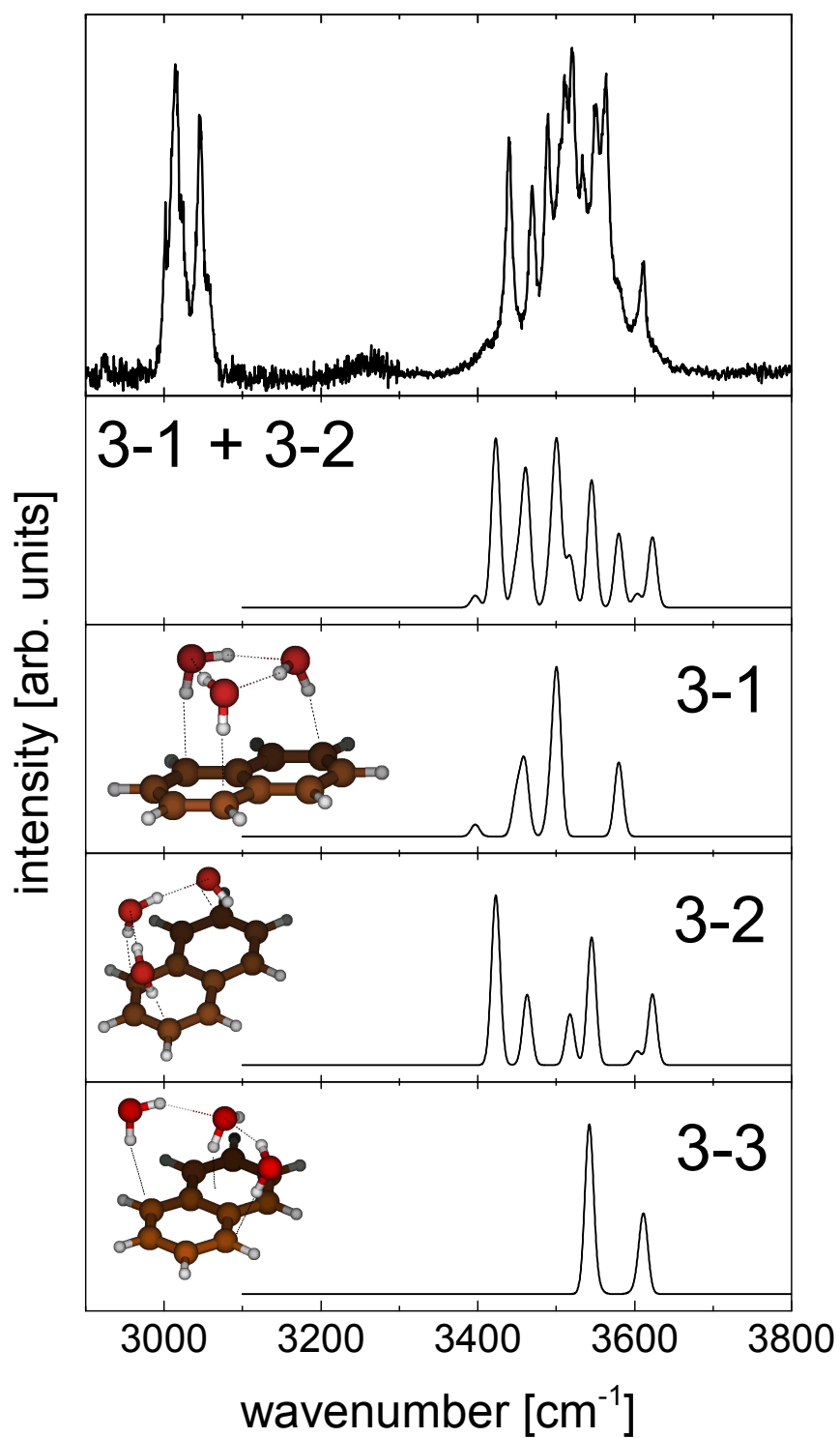


Figure 6.4: Experimental spectrum and calculated spectra of $[\text{Np} \cdot (\text{H}_2\text{O})_3]^-$. Top trace is the experimental spectrum of $[\text{Np} \cdot (\text{H}_2\text{O})_3]^- \cdot \text{Ar}_8$ acquired by monitoring the loss of 5 Ar atoms. Bottom traces are calculated conformers and their predicted infrared spectra. The second trace from the top is a combination of conformers 3-1 and 3-2. The dashed lines show the hydrogen bonds. See text for discussion.

as well as three lone water molecules. These structures were all found to be very high in energy relative to the ring and chain structures and to not recover the experimental spectrum. These calculations and the energetic difference between the ring (3-1) and the chain structures (3-2 and 3-3) further reinforce that it is energetically favorable to form water-water H-bonds rather than ionic π -H-bonds as was seen in the dihydrate case as well. Additionally, this pattern of bonding is consistent with the observation that the simulated normal modes of the lower frequency modes tend to correspond with π -H-bonds while the higher energy modes belong to water-water interactions. This behavior has also been observed before in $\text{Cl}_2^-(\text{H}_2\text{O})_3$ clusters. [161]

The complex nature of the experimental spectrum make a definitive assignment of the structures contributing to the spectrum difficult. However, as was mentioned above, it is clear that there are at least two conformers populated. Figure 6.4 shows a comparison of the two lowest energy isomers (3-1 and 3-2) which is consistent with the experimental spectrum. The higher energy and relatively simple nature of the spectrum of conformer 3-3 suggests that it does not contribute to the experimental spectrum. Because of the use of Ar solvation, it is likely that multiple isomers can be “frozen out”. [144,191–194] Alternatively, the large number of bands could be caused by combination bands of lower lying vibrational modes. However, the sharp nature of the experimental features and the large intensity relative to the other peaks suggests that a combination of different isomers is more likely. Experiments employing IR-IR hole burning would be useful in determining the identity of the contributing structures. [195]

6.3.1.4 $[\text{Np}\cdot(\text{H}_2\text{O})_4]^-$

Figure 6.5 shows the experimental spectrum of $[\text{Np}\cdot(\text{H}_2\text{O})_4]^- \cdot \text{Ar}_2$ monitoring the loss of both Ar atoms. The experimental spectrum exhibits a strong set of bands between 3450 cm^{-1} and 3600 cm^{-1} . Based on the discussion of $[\text{Np}\cdot(\text{H}_2\text{O})_3]^-$, these features can be attributed to the π -H-bonding OH groups in the water network. At lower frequencies, a broad unresolved peak is observed which can be assigned to the OH groups involved in water-water H-bonds. The pattern of the vibrational frequencies observed here is very similar to that observed in $\text{I}^-(\text{H}_2\text{O})_4$, [162] which

suggests that the same structural motif is present in both cases. Johnson and co-workers [162] tentatively assigned the structure of $\text{I}^{\cdot}(\text{H}_2\text{O})_4$ to a homodromic ring, similar to what was seen previously in other halide water cluster ions [163] in addition to $[\text{Np}\cdot(\text{H}_2\text{O})_3]^-$.

Of the calculated structures, the lowest energy structure (4-1) is a homodromic ring (see Figure 6.5). The next higher energy structure (4-2) is the homodromic ring from $[\text{Np}\cdot(\text{H}_2\text{O})_3]^-$ with the fourth water molecule H-bonding to the ring and the π -system of the Np^- . This conformer is predicted to be 201 meV higher in energy from conformer 4-1. In other higher energy conformers, the water network is fragmented (see 4-3 and 4-4 at 241 meV and 351 meV higher in energy than 4-1, respectively). Only conformers 4-1 and 4-2 are roughly consistent with the experimental spectrum where the spectrum of 4-1 is too simple while the spectrum of 4-2 exhibits too many peaks. While both structures recover a portion of the experimental spectrum, a definitive spectral assignment is not possible without additional high level anharmonic calculations. It is again possible that there are multiple isomers present for the same reasons as are stated above (evaporative cooling and barrier to formation of other structures). Additionally, the presence of higher energy isomers has precedence in similar experiments. [144,191–194] The spectrum of $[\text{Np}\cdot(\text{H}_2\text{O})_4]^-$ is tentatively assigned to conformer 4-1 with contributions from 4-2 and potentially other isomers.

6.3.1.5 $[\text{Np}\cdot(\text{H}_2\text{O})_5]^-$ and $[\text{Np}\cdot(\text{H}_2\text{O})_6]^-$

The infrared spectrum of $[\text{Np}\cdot(\text{H}_2\text{O})_5]^-$ (see Figure 6.6) is similar to that of $[\text{Np}\cdot(\text{H}_2\text{O})_4]^-$ possessing broad features below 3450 cm^{-1} and between 3450 cm^{-1} and 3600 cm^{-1} . It is likely that the broad features observed here are the result of multiple unresolved peaks of similar frequency. Again, the lower energy features are due to water-water interactions while the higher energy features are due to π -H-bonds. A number of different structures were calculated and, like in smaller clusters, the lowest energy conformer is a homodromic ring (see 5-1 in Figure 6.6). The calculated spectrum of conformer 5-1 is qualitatively consistent with the experimental spectrum however, similar to both the tri- and tetrahydrates, the water-water interactions are overestimated and the frequencies of the corresponding signatures are predicted to be too low. The other conformer shown (5-2) is

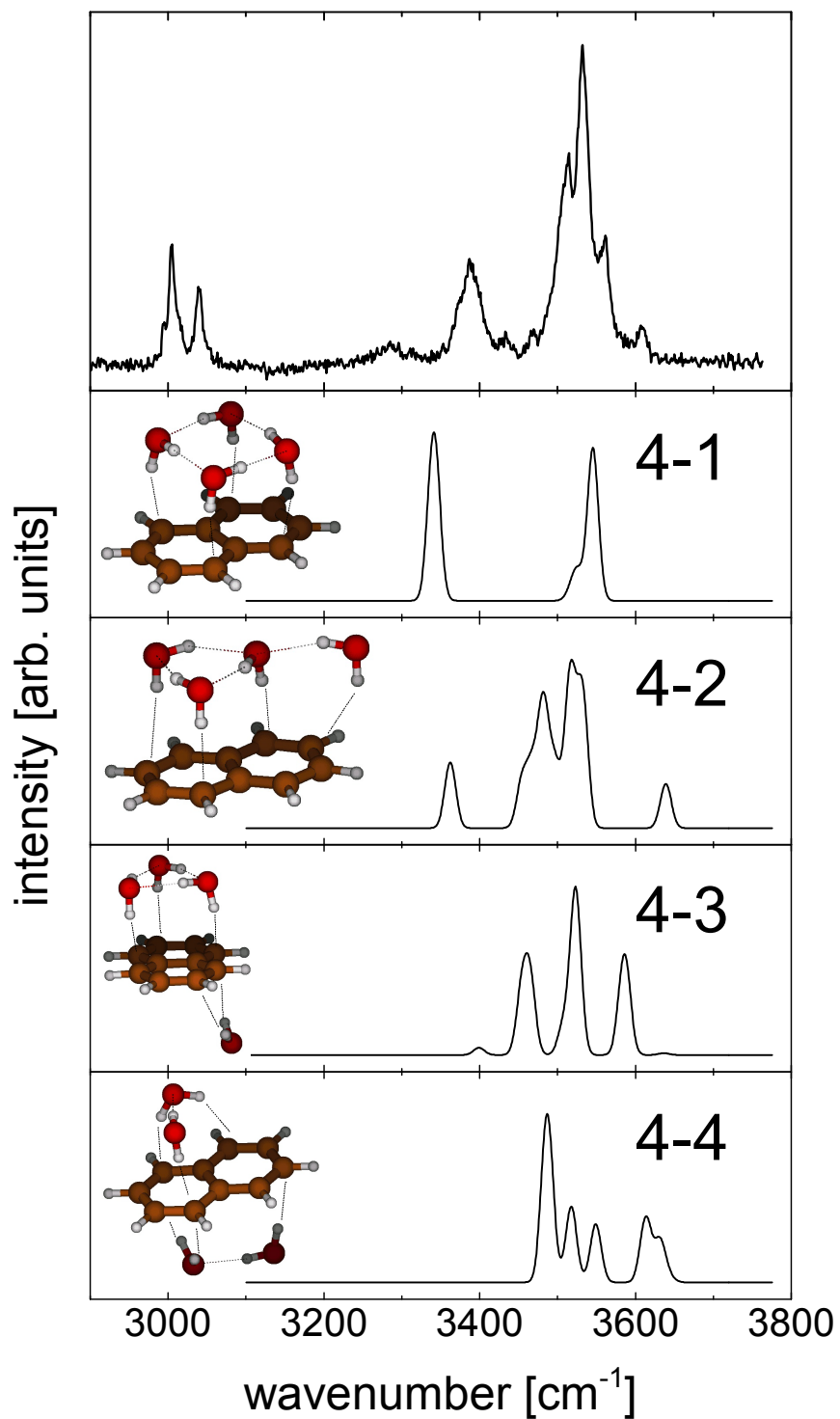


Figure 6.5: Experimental spectrum and calculated spectra of $[\text{Np}\cdot(\text{H}_2\text{O})_4]^-$. Top trace is the experimental spectrum of $[\text{Np}\cdot(\text{H}_2\text{O})_4]^- \cdot \text{Ar}_2$ acquired by monitoring the loss of 2 Ar atoms. Bottom traces are calculated conformers and their predicted infrared spectra. The dashed lines show the hydrogen bonds. See text for discussion.

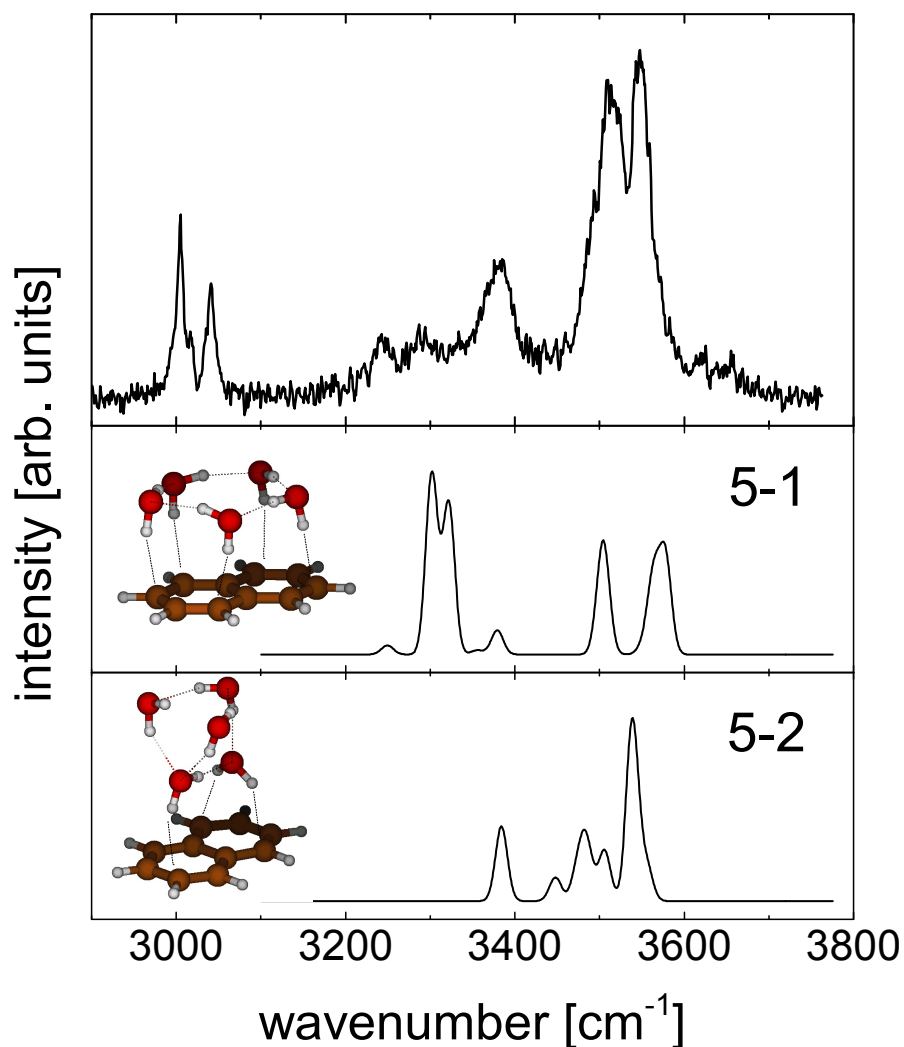


Figure 6.6: Experimental spectrum and calculated spectra of $[\text{Np}\cdot(\text{H}_2\text{O})_5]^-$. Top trace is the experimental spectrum of $[\text{Np}\cdot(\text{H}_2\text{O})_5]^- \cdot \text{Ar}_2$ acquired by monitoring the loss of 2 Ar atoms. Bottom traces are calculated conformers and their predicted infrared spectra. The dashed lines show the hydrogen bonds. See text for discussion.

also roughly consistent with the experimental spectrum and is calculated to be 184 meV above conformer 5-1. This structure is characteristic of the “cage” family of structures where the water network begins to favor water-water H-bonds over ionic π -H-bonds. Conformer 5-2 also bears resemblance to the water pentamer anion where the Np^- has taken the role of the diffuse electron. However, neither 5-1 or 5-2 can account for the small features observed above 3600 cm^{-1} .

The spectrum for $[\text{Np}\cdot(\text{H}_2\text{O})_6]^-$ (see Figure 6.7) is similar to that of $[\text{Np}\cdot(\text{H}_2\text{O})_5]^-$. There

are again intense broad peaks around 3550 cm^{-1} , water-water features trailing down to 3150 cm^{-1} and some weak features above 3600 cm^{-1} . The water hexamer has been studied extensively and has been shown to exhibit a number of different structures. [164,165] While it is unlikely that a definitive structural assignment can be made, a comparison with a number of different structures is warranted.

Conformer 6-1 is similar to the “book” structure that has been observed before in both neutral and anionic water clusters and recovers the general envelope of the experimental spectrum. [164,165] Conformation 6-2 is another variation on the “book” structure that is in the vein of a four membered homodromic ring with a water dimer attached on the side and is isoenergetic with conformer 6-1. Conformer 6-2 is more consistent with the features above 3600 cm^{-1} but overestimates the lower energy features. Conformer 6-3 is a cage structure where two three-membered rings are stacked on top of each other and is calculated to be only 62 meV above 6-1. The spectrum for conformer 6-3 recovers the general shape of the experimental spectrum but does not predict the features above or below the bulk of the spectrum from 3350 cm^{-1} to 3600 cm^{-1} . The final reported structure is the six membered homodromic ring (6-4) which is calculated to be 68 meV above 6-1. The calculated spectrum for 6-4 does not recover the experimental spectrum well but it is possible that the low energy ring modes could be broadened by ring deformation modes. In summary, none of the calculated spectra recover the experimental spectrum individually but a combination may. Higher level anharmonic calculations would be necessary to truly assign the experimental spectrum of $[\text{Np}\cdot(\text{H}_2\text{O})_6]^-$.

For both the penta- and hexahydrate of Np^- the experimental spectrum is too congested to allow for a definitive structural assignment. This is likely due to the presence of multiple conformers and the coupling of various frequencies resulting in broad unresolved features. However, a unique insight for these larger clusters is that it appears as though the water network may be partially detached from the Np^- π -system. In particular, the hexahydrate is the first cluster where the lowest energy structure is not the homodromic ring but rather two different “book” conformations. This observation again shows that the water-water interaction appears to be favorable compared

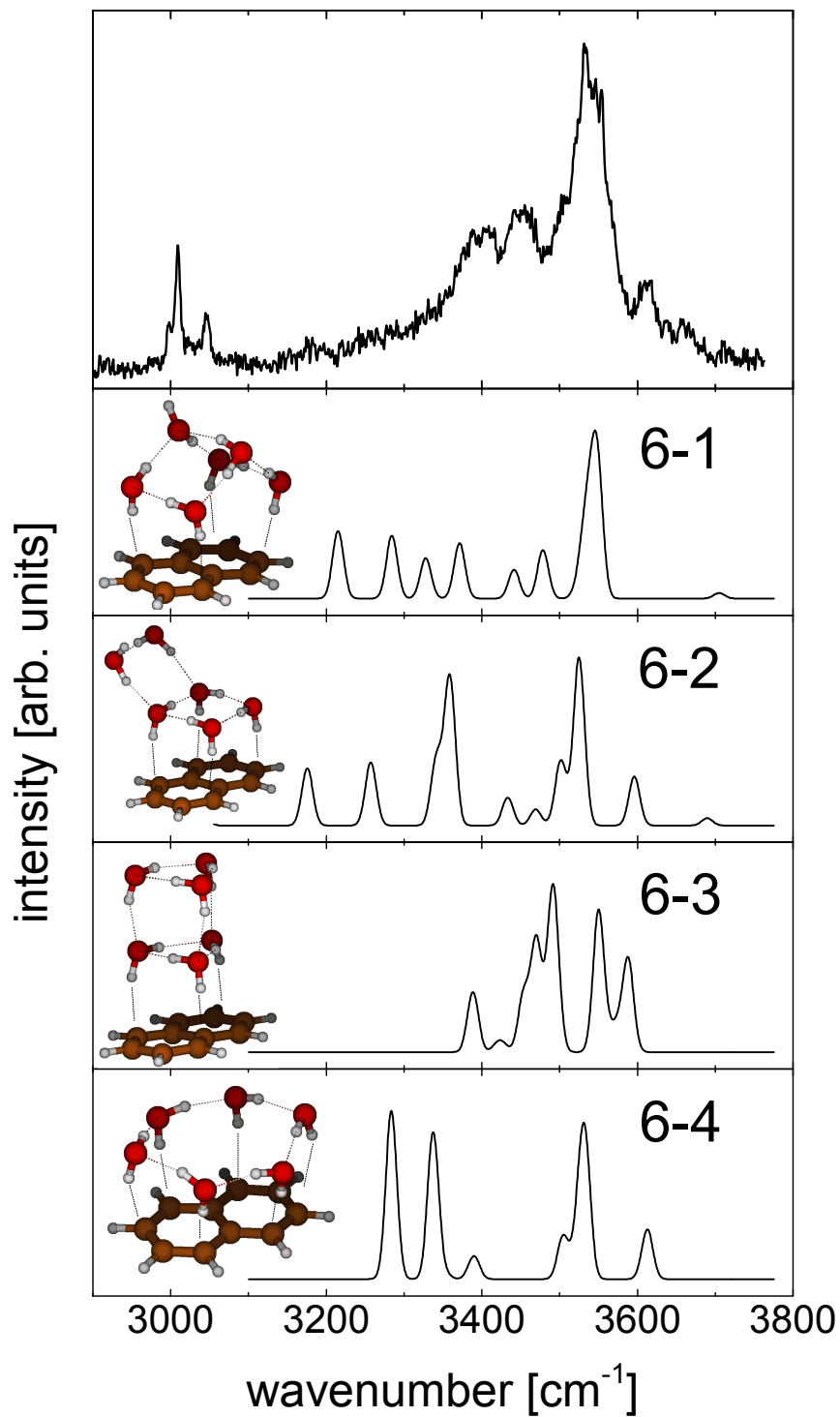


Figure 6.7: Experimental spectrum and calculated spectra of $[\text{Np}\cdot(\text{H}_2\text{O})_6]^-$. Top trace is the experimental spectrum of $[\text{Np}\cdot(\text{H}_2\text{O})_6]^- \cdot \text{Ar}_2$ acquired by monitoring the loss of 2 Ar atoms. Bottom traces are calculated conformers and their predicted infrared spectra. The dashed lines show the hydrogen bonds. See text for discussion.

to ionic π -H-bonds.

6.3.2 CH Stretching Vibrations

The CH stretches of Np are severely affected by Fermi resonances. [185–187] Similar effects are expected here making harmonic calculations in this region useless. It is therefore not worth presenting an depth analysis of calculations in this region, however some useful qualitative insight can be gained by comparisons of calculated frequencies and trends from one cluster size to another. It is worth noting that the CH stretching region of $[\text{Np}\cdot(\text{H}_2\text{O})]^-$ does not show significant variation with different structural orientation of the water molecule indicating that the CH stretches are not strongly affected by position of the water network and consequently the CH stretches are not a useful aid in structural assignment (all structures showed an invariance within 2 cm^{-1}).

The overall structure of the CH stretching region does not change appreciably with increasing level of hydration. However, the CH stretching frequencies shift to the blue by $2 - 10\text{ cm}^{-1}$ for each additional water molecule. This can be rationalized by stabilization of the excess electron into the π -system. At low levels of hydration, the excess electron can be partially localized in σ^* orbitals of C-H bonds resulting in a weakening of the C-H bonds and subsequent red shift of the CH stretching frequencies. As the level of hydration increases, the excess charge is more concentrated in the π -system and even the water network itself. This strengthens the C-H bonds resulting in the observed blue shift of the CH stretching region with increasing solvation. Similar behavior has been observed before in $\text{CH}_3\text{NO}_2^-\cdot(\text{H}_2\text{O})_n$ cluster anions. [192, 196] One remaining question is whether the excess electron will remain localized in the π -system in the limit of bulk solution or if there is a critical water network size where the excess electron will instead reside in the water network exclusively. Np^- has been observed in bulk acetonitrile solution [189] where a solvated electron has also been detected [197] which lends credence to the idea that the excess electron can stay bound to the π -system even in the limit of bulk solution. However, thus far there has been no detection of Np^- in bulk water.

6.4 Conclusion

The infrared Ar predissociation spectra of $[\text{Np} \cdot (\text{H}_2\text{O})_n]^- \cdot \text{Ar}_m$ ($n = 1 - 6$) were presented in this chapter. Analysis of the spectra indicated that the excess electron is mostly localized in the π -system of the Np molecule with some spill-out into the σ^* CH orbitals. This results in a weakening of the CH bonds of the Np molecule. However, due to the low AEA of Np, the excess charge is also partially accommodated in the water network. This effect increases with increasing hydration. The excess charge is stabilized in the π -system through ionic π -H-bonds made by the water molecules.

The water molecules form networks on the surface of the Np^- . As hydration increases, the more favorable water-water interactions dictate polycyclic and cage like structures between the water molecules. Many of the structures predicated have been observed before in a number of different hydrated anion or hydrated electron clusters. It is clear that when three or more water molecules are present, multiple structures are being populated leading to massive spectral congestion and an inability to definitively assign structures to the spectra while still allowing for qualitative understanding of the water network behavior.

Bibliography

- [1] D. A. McQuarrie and J. D. Simon. Physical Chemistry: A Molecular Approach. University Science Books, Sausalito, California, 1997.
- [2] E. Herbst. “The Chemistry of Interstellar Space”. Angewandte Chemie-International Edition, 29(6):595–608, 1990.
- [3] J. I. Steinfeld, J. S. Francisco, and W. L. Hase. Chemical Kinetics and Dynamics 2nd Edition. Prentice Hall, Upper Saddle River, New Jersey, 1998.
- [4] H. Schneider and J. M. Weber. “Infrared spectra of $\text{SF}_6^-(\text{H}_2\text{O})_n$ ($n = 1-3$): Incipient Reaction and Delayed Onset of Water Network Formation”. Journal of Chemical Physics, 127:244310, 2007.
- [5] C. G. Zhan, F. Zheng, and D. A. Dixon. “Theoretical Studies of Photoelectron Spectra of $\text{SO}_4^{2-}(\text{H}_2\text{O})_n$ Clusters and the Extrapolation to Bulk Solution”. Journal of Chemical Physics, 119(2):781–793, 2003.
- [6] J. V. Coe. “Connecting Cluster Anion Properties to Bulk: Ion Solvation Free Energy Trends with Cluster Size and the Surface vs Internal Nature of Iodide in Water Clusters”. Journal of Physical Chemistry A, 101(11):2055–2063, 1997.
- [7] M. A. Johnson and W. C. Lineberger. Techniques for the Study of Gas-Phase Ion Molecule Reactions, page 591. Wiley, New York, 1988.
- [8] C. E. Klots. “Evaporative Cooling”. Journal of Chemical Physics, 83(11):5854–5860, 1985.
- [9] J. M. Weber. “A Pulsed Ion Source for the Preparation of Metal Containing Cluster Ions Using Supersonic Entrainment of Laser Vaporized Metal”. Review of Scientific Instruments, 76:043301, 2005.
- [10] U. Even, J. Jortner, D. Noy, N. Lavie, and C. Cossart-Magos. “Cooling of Large Molecules Below 1 K and He Clusters Formation”. Journal of Chemical Physics, 112(18):8068–8071, 2000.
- [11] R. Campargue. “Aerodynamic Separation Effect on Gas and Isotope Mixtures Induced by Invasion of Free Jet Shock Wave Structure”. Journal of Chemical Physics, 52(4):1795, 1970.
- [12] J. Riedel, S. Yan, H. Kawamata, and K. Liu. “A Simple Yet Effective Multipass Reflector for Vibrational Excitation in Molecular Beams”. Review of Scientific Instruments, 79, 2008.

- [13] J. R. Petit, J. Jouzel, D. Raynaud, N. I. Barkov, J. M. Barnola, I. Basile, M. Bender, J. Chappellaz, M. Davis, G. Delaygue, M. Delmotte, V. M. Kotlyakov, M. Legrand, V. Y. Lipenkov, C. Lorius, L. Pepin, C. Ritz, E. Saltzman, and M. Stievenard. "Climate and Atmospheric History of the Past 420,000 Years from the Vostok Ice Core, Antarctica". *Nature*, 399:429–436, 1999.
- [14] C. D. Thomas, A. Cameron, R. E. Green, M. Bakkenes, L. J. Beaumont, Y. C. Collingham, B. F. N. Erasmus, M. F. de Siqueira, A. Grainger, L. Hannah, L. Hughes, B. Huntley, A. S. van Jaarsveld, G. F. Midgley, L. Miles, M. A. Ortega-Huerta, A. T. Peterson, O. L. Phillips, and S. E. Williams. "Extinction Risk from Climate Change". *Nature*, 427:145–148, 2004.
- [15] J. Fargione, J. Hill, D. Tilman, S. Polasky, and P. Hawthorne. "Land Clearing and the Biofuel Carbon Debt". *Science*, 319:1235–1238, 2008.
- [16] Y. Hori. *Modern Aspects of Electrochemistry, No 42*, pages 89–189. *Modern Aspects of Electrochemistry*. Springer, 2008.
- [17] E. B. Cole, P. S. Lakkaraju, D. M. Rampulla, A. J. Morris, E. Abelev, and A. B. Bocarsly. "Using a One-Electron Shuttle for the Multielectron Reduction of CO₂ to Methanol: Kinetic, Mechanistic, and Structural Insights". *Journal of the American Chemical Society*, 132:1153911551, 2010.
- [18] A. J. Morris, R. T. McGibbon, and A. B. Bocarsly. "Electrocatalytic Carbon Dioxide Activation: The Rate-Determining Step of Pyridinium-Catalyzed CO₂ Reduction". *ChemSuschem*, 4(2):191–196, 2011.
- [19] K. Tanaka and D. Ooyama. "Multi-Electron Reduction of CO₂ via Ru-CO₂, -C(O)OH, -CO, -CHO, and -CH₂OH Species". *Coordination Chemistry Reviews*, 226(1-2):211–218, 2002.
- [20] Z. Y. Bian, K. Sumi, M. Furue, S. Sato, K. Koike, and O. Ishitani. "A Novel Tripodal Ligand, Tris (4'-methyl-2,2'-bipyridyl-4-yl)-methyl carbinol and its Trinuclear Ru-II/Re-I Mixed-Metal Complexes: Synthesis, Emission Properties, and Photocatalytic CO₂ Reduction". *Inorganic Chemistry*, 47(23):10801–10803, 2008.
- [21] A. Inagaki and M. Akita. "Visible-Light Promoted Bimetallic Catalysis". *Coordination Chemistry Reviews*, 254(11-12):1220–1239, 2010.
- [22] A. M. Khenkin, I. Efremenko, L. Weiner, J. M. L. Martin, and R. Neumann. "Photochemical Reduction of Carbon Dioxide Catalyzed by a Ruthenium-Substituted Polyoxometalate". *Chemistry-a European Journal*, 16(4):1356–1364, 2010.
- [23] M. D. Doherty, D. C. Grills, J. T. Muckerman, D. E. Polyansky, and E. Fujita. "Toward more Efficient Photochemical CO₂ Reduction: Use of ScCO₂ or Photogenerated Hydrides". *Coordination Chemistry Reviews*, 254(21-22):2472–2482, 2010.
- [24] Y. H. Chen, C. W. Li, and M. W. Kanan. "Aqueous CO₂ Reduction at Very Low Overpotential on Oxide-Derived Au Nanoparticles". *Journal of the American Chemical Society*, 134(49):19969–19972, 2012.
- [25] Y. H. Chen and M. W. Kanan. "Tin Oxide Dependence of the CO₂ Reduction Efficiency on Tin Electrodes and Enhanced Activity for Tin/Tin Oxide Thin-Film Catalysts". *Journal of the American Chemical Society*, 134(4):1986–1989, 2012.

- [26] C. W. Li and M. W. Kanan. “CO₂ Reduction at Low Overpotential on Cu Electrodes Resulting from the Reduction of Thick Cu₂O Films”. Journal of the American Chemical Society, 134(17):7231–7234, 2012.
- [27] U. Heiz and E. L. Bullock. “Fundamental Aspects of Catalysis on Supported Metal Clusters”. Journal of Materials Chemistry, 14(4):564–577, 2004.
- [28] P. L. Richardson, Marisa L. N. Perdigoto, W. Wang, and Rodrigo J. G. Lopes. “Manganese- and Copper-Doped Titania Nanocomposites for the Photocatalytic Reduction of Carbon Dioxide into Methanol”. Applied Catalysis B-Environmental, 126:200–207, 2012.
- [29] J. Janlamool, P. Praserttham, and B. Jongsomjit. “Ti-Si Composite Oxide-Supported Cobalt Catalysts for CO₂ Hydrogenation”. Journal of Natural Gas Chemistry, 20(5):558–564, 2011.
- [30] Q. Zhang, W. Han, Y. Hong, and J. Yu. “Photocatalytic Reduction of CO₂ with H₂O on Pt-loaded TiO₂ Catalyst”. Catalysis Today, 148(3-4):335–340, 2009.
- [31] N. Sasirekha, S. J. S. Basha, and K. Shanthy. “Photocatalytic Performance of Ru doped Anatase mounted on Silica for Reduction of Carbon Dioxide”. Applied Catalysis B-Environmental, 62(1-2):169–180, 2006.
- [32] G. E. Oosterom, J. N. H. Reek, P. C. J. Kamer, and Pwnm van Leeuwen. “Transition Metal Catalysis using Functionalized Dendrimers”. Angewandte Chemie-International Edition, 40(10):1828–1849, 2001.
- [33] D. R. Kauffman, D. Alfonso, C. Matranga, H. F. Qian, and R. C. Jin. “Experimental and Computational Investigation of Au-25 Clusters and CO₂: A Unique Interaction and Enhanced Electrocatalytic Activity”. Journal of the American Chemical Society, 134(24):10237–10243, 2012.
- [34] M. Knapp, O. Echt, D. Kreisler, T. D. Mark, and E. Recknagel. “Formation of Long-Lived CO₂⁻, N₂O⁻, and their Dimer Anions, by Electron-Attachment to Vanderwaals Clusters”. Chemical Physics Letters, 126(3-4):225–231, 1986.
- [35] A. D. Walsh. “The Electronic Orbitals, Shpaes, and Spectra of Polyatomic Molecules. Part II.* Non-hydride AB₂ and BAC Molecules”. Journal of the Chemical Society (Resumed), 467:2266–2288, 1953.
- [36] G Herzberg. Molecular Spectra and Molecular Structure, volume III. Krieger Publishing Co., Malabar, Florida, 1991.
- [37] T. Shimanouchi. “Tables of Molecular Vibrational Frequencies Consolidated Volume I”, 1972.
- [38] W. E. Thompson and M. E. Jacox. “The Vibrational Spectra of CO₂⁺, (CO₂)₂⁺, CO₂⁻, and (CO₂)₂⁻ Trapped in Solid Neon”. Journal of Chemical Physics, 111(10):4487–4496, 1999.
- [39] H. J. Freund and M. W. Roberts. “Surface Chemistry of Carbon Dioxide”. Surface Science Reports, 25:225–273, 1996.
- [40] M. B. Ansari and S. Park. “Carbon Dioxide Utilization as a Soft Oxidant and Promoter in Catalysis”. Energy and Environmental Science, 5:9419–9437, 2012.

- [41] M. Haruta and M. Date. “Advances in the Catalysis of Au Nanoparticles”. Applied Catalysis A-General, 222(1-2):427–437, 2001.
- [42] H. Häkkinen, W. Abbet, A. Sanchez, U. Heiz, and U. Landman. “Structural, Electronic, and Impurity-Doping Effects in Nanoscale Chemistry: Supported Gold Nanoclusters”. Angew. Chem.-Int. Edit., 42(11):1297–1300, 2003.
- [43] A. Sanchez, S. Abbet, U. Heiz, W. D. Schneider, H. Häkkinen, R. N. Barnett, and U. Landman. “When Gold is Not Noble: Nanoscale Gold Catalysts”. Journal of Physical Chemistry A, 103(48):9573–9578, 1999.
- [44] L. D. Socaciu, J. Hagen, T. M. Bernhardt, L. Woste, U. Heiz, H. Häkkinen, and U. Landman. “Catalytic CO Oxidation by Free Au_2^- : Experiment and Theory”. Journal of the American Chemical Society, 125(34):10437–10445, 2003.
- [45] M. L. Kimble, A. W. Castleman, R. Mitric, C. Burgel, and V. Bonacic-Koutecky. “Reactivity of Atomic Gold Anions toward Oxygen and the Oxidation of CO: Experiment and Theory”. Journal of the American Chemical Society, 126(8):2526–2535, 2004.
- [46] A. D. Boese, H. Schneider, A. N. Gloess, and J. M. Weber. “The Infrared Spectrum of $\text{Au}^- \cdot \text{CO}_2$ ”. Journal of Chemical Physics, 122:154301, 2005.
- [47] D. W. Arnold, S. E. Bradforth, E. H. Kim, and D. M. Neumark. “Study of Halogen Carbon-Dioxide Clusters and the Fluoroformyloxyl Radical by Photodetachment of $\text{X}^- \cdot (\text{CO}_2)$ ($\text{X}=\text{I}, \text{Cl}, \text{Br}$) and FCO_2 ”. Journal of Chemical Physics, 102(9):3493–3509, 1995.
- [48] J. M. Weber and H. Schneider. “Infrared Spectra of $\text{X}^- \text{CO}_2 \cdot \text{Ar}$ Cluster Anions ($\text{X}=\text{Cl}, \text{Br}, \text{I}$)”. Journal of Chemical Physics, 120:10056, 2004.
- [49] L. Pauling. The Nature of the Chemical Bond. Cornell University Press, Ithaca, United States, 3 edition, 1960.
- [50] C. H. An, J. Z. Wang, W. Jiang, M. Y. Zhang, X. J. Ming, S. T. Wang, and Q. H. Zhang. “Strongly Visible-Light Responsive Plasmonic Shaped $\text{AgX}:\text{Ag}$ ($\text{X}=\text{Cl}, \text{Br}$) Nanoparticles for Reduction of CO_2 to Methanol”. Nanoscale, 4(18):5646–5650, 2012.
- [51] R. Grabowski, J. Sloczynski, M. Sliwa, D. Mucha, R. P. Socha, M. Lachowska, and J. Skrzypek. “Influence of Polymorphic ZrO_2 Phases and the Silver Electronic State on the Activity of Ag/ZrO_2 Catalysts in the Hydrogenation of CO_2 to Methanol”. ACS Catalysis, 1(4):266–278, 2011.
- [52] Y. Hori, H. Ito, K. Okano, K. Nagasu, and S. Sato. “Silver-Coated ion Exchange Membrane Electrode Applied to Electrochemical Reduction of Carbon Dioxide”. Electrochimica Acta, 48(18):2651–2657, 2003.
- [53] K. Kneipp, Y. Wang, A. J. Berger, R. R. Dasari, and M. S. Feld. “Surface-Enhanced Raman-Scattering of CO_2 Dissolved in Aqueous Colloidal Solutions of Silver and Gold”. Journal of Raman Spectroscopy, 26(10):959–962, 1995.
- [54] K. Koci, K. Mateju, L. Obalova, S. Krejcikova, Z. Lacny, D. Placha, L. Capek, A. Hospodkova, and O. Solcova. “Effect of Silver Doping on the TiO_2 for Photocatalytic Reduction of CO_2 ”. Applied Catalysis B-Environmental, 96(3-4):239–244, 2010.

- [55] G. W. Coates and D. R. Moore. “Discrete Metal-Based Catalysts for the Copolymerization CO₂ and Epoxides: Discovery, Reactivity, Optimization, and Mechanism”. Angewandte Chemie-International Edition, 43(48):6618–6639, 2004.
- [56] H. Hotop and W. C. Lineberger. “Dye-Laser Photodetachment Studies of Au⁻, Pt⁻, Pt_n⁻, and Ag⁻”. Journal of Chemical Physics, 58(6):2379–2387, 1973.
- [57] H. Hotop, R. A. Bennett, and W. C. Lineberger. “Electron Affinities of Cu and Ag”. Journal of Chemical Physics, 58(6):2373–2378, 1973.
- [58] R. Ahlrichs, M. Br, M. Hser, H. Horn, and C. Klmeel. “Electronic-Structure Calculations on Workstation Computers - The Program System Turbomole”. Chemical Physics Letters, 162(3):165–169, 1989.
- [59] C. T. Lee, W. T. Yang, and R. G. Parr. “Development of the Colle-Salvetti Correlation-Energy Formula into a Functional of the Electron-Density”. Physical Review B, 37(2):785–789, 1988.
- [60] R. G. Parr and W. Yang. Density-Functional Theory of Atoms and Molecules. Oxford University Press, New York, 1989.
- [61] F. Weigend and R. Ahlrichs. “Balanced Basis Sets of Split Valence, Triple Zeta Valence and Quadruple Zeta Valence Quality for H to Rn: Design and Assessment of Accuracy”. Physical Chemistry Chemical Physics, 7(18):3297–3305, 2005.
- [62] C. Adamo and V. Barone. “Toward Reliable Density Functional Methods without Adjustable Parameters: The PBE0 Model”. Journal of Chemical Physics, 110(13):6158–6170, 1999.
- [63] F. Weigend and M. Hser. “RI-MP2: First Derivatives and Global Consistency”. Theoretical Chemistry Accounts, 97(1-4):331–340, 1997.
- [64] F. Weigend, M. Hser, H. Patzelt, and R. Ahlrichs. “RI-MP2: Optimized Auxiliary Basis Sets and Demonstration of Efficiency”. Chemical Physics Letters, 294(1-3):143–152, 1998.
- [65] T. H. Dunning, Jr. “Gaussian-Basis Sets for use in Correlated Molecular Calculations .1. The Atoms Boron through Neon and Hydrogen”. Journal of Chemical Physics, 90(2):1007, 1989.
- [66] P. Deglmann, F. Furche, and R. Ahlrichs. “An Efficient Implementation of Second Analytical Derivatives for Density Functional Methods”. Chemical Physics Letters, 362(5-6):511–518, 2002.
- [67] P. Deglmann and F. Furche. “Efficient Characterization of Stationary Points on Potential Energy Surfaces”. Journal of Chemical Physics, 117(21):9535–9538, 2002.
- [68] A. E. Reed, R. B. Weinstock, and F. Weinhold. “Natural-Population Analysis”. Journal of Chemical Physics, 83(2):735–746, 1985.
- [69] A. Klamt, V. Jonas, T. Burger, and J. C. W. Lohrenz. “Refinement and Parametrization of COSMO-RS”. Journal of Physical Chemistry A, 102(26):5074–5085, 1998.
- [70] A. Klamt and G. Schuurmann. “COSMO - A New Approach to Dielectric Screening in Solvents with Explicit Expressions for the Screening Energy and its Gradient”. Journal of the Chemical Society-Perkin Transactions 2, (5):799–805, 1993.

- [71] F. Eckert and A. Klamt. “Fast Solvent Screening via Quantum Chemistry: COSMO-RS Approach”. *Aiche Journal*, 48(2):369–385, 2002.
- [72] S. Sinnecker, A. Rajendran, A. Klamt, M. Diedenhofen, and F. Neese. “Calculation of Solvent Shifts on Electronic g -Tensors with the Conductor-Like Screening Model (COSMO) and its Self-Consistent Generalization to Real Solvents (Direct COSMO-RS)”. *Journal of Physical Chemistry A*, 110(6):2235–2245, 2006.
- [73] E. F. May, M. R. Moldover, and J. W. Schmidt. “The Dielectric Permittivity of Saturated Liquid Carbon Dioxide and Propane Measured using Cross Capacitors”. *International Journal of Thermophysics*, 26(3):563–576, 2005.
- [74] H. Schneider, A. D. Boese, and J. M. Weber. “Infrared Spectra of $O_2^-(CO_2)_n$ Clusters ($n = 1 - 6$): Asymmetric Docking at the π^* Orbital”. *Journal of Chemical Physics*, 123(7), 2005.
- [75] J. W. Shin, N. I. Hammer, M. A. Johnson, H. Schneider, A. Glss, and J. M. Weber. “An Infrared Investigation of the $(CO_2)_n^-$ Clusters: Core Ion Switching from Both the Ion and Solvent Perspectives”. *Journal of Physical Chemistry A*, 109(14):3146–3152, 2005.
- [76] R. M. Badger. “A Relation Between Internuclear Distances and Bond Force Constants”. *Journal of Chemical Physics*, 2(3), 1934.
- [77] R. M. Badger. “Between the Internuclear Distances and Force Constants of Molecules and Its Application to Polyatomic Molecules”. *Journal of Chemical Physics*, 3(11):710–714, 1935.
- [78] P. M. Bialach, M. Braun, A. Luchow, and M. Gerhards. “Structures of Isolated $Co_2(\text{alcohol})_1$ Cluster Anions”. *Physical Chemistry Chemical Physics*, 11(44):10403–10408, 2009.
- [79] P. M. Bialach, A. Funk, M. Weiler, and M. Gerhards. “IR Spectroscopy on Isolated $Co_n(\text{alcohol})_m$ Cluster Anions ($n = 1 - 4$, $m = 1 - 3$): Structures and Spin States”. *Journal of Chemical Physics*, 133(19), 2010.
- [80] G. W. Huber, S. Iborra, and A. Corma. “Synthesis of Transportation Fuels from Biomass: Chemistry, Catalysts, and Engineering”. *Chemical Reviews*, 106(9):4044–4098, 2006.
- [81] T. Abe, F. Taguchi, T. Yoshida, S. Tokita, G. Schnurpfeil, D. Wohrle, and M. Kaneko. “Electrocatalytic CO_2 Reduction by Cobalt Octabutoxyphthalocyanine Coated on Graphite Electrode”. *Journal of Molecular Catalysis A-Chemical*, 112(1):55–61, 1996.
- [82] Z. Q. He, L. Y. Zhan, Q. Wang, S. Song, J. M. Chen, K. R. Zhu, X. H. Xu, and W. P. Liu. “Increasing the Activity and Stability of Chemi-Deposited Palladium Catalysts on Nickel Foam Substrate by Electrochemical Deposition of a Middle Coating of Silver”. *Separation and Purification Technology*, 80(3):526–532, 2011.
- [83] L. P. Yang, Z. Y. Liu, H. W. Shi, H. Hu, and W. F. Shangguan. “Design Consideration of Photocatalytic Oxidation Reactors using TiO_2 -Coated Foam Nickels for Degrading Indoor Gaseous Formaldehyde”. *Catalysis Today*, 126(3-4):359–368, 2007.
- [84] N. Jeong, K. S. Hwang, and S. C. Yang. “High-Yield Growth of Carbon Nanofilaments on Nickel Foam Using Nickel-Tin Intermetallic Catalysts”. *Journal of Nanoscience and Nanotechnology*, 14(10):7734–7739, 2014.

- [85] W. Donphai, K. Faungnawakij, M. Chareonpanich, and J. Limtrakul. “Effect of Ni-CNTs/Mesocellular Silica Composite Catalysts on Carbon Dioxide Reforming of Methane”. *Applied Catalysis A-General*, 475:16–26, 2014.
- [86] T. F. M. Chang, M. Sone, A. Shibata, C. Ishiyama, and Y. Higo. “Bright Nickel Film Deposited by Supercritical Carbon Dioxide Emulsion using Additive-Free Watts Bath”. *Electrochimica Acta*, 55(22):6469–6475, 2010.
- [87] S. T. Chung, H. C. Huang, S. J. Pan, W. T. Tsai, P. Y. Lee, C. H. Yang, and M. B. Wu. “Material Characterization and Corrosion Performance of Nickel Electroplated in Supercritical CO₂ Fluid”. *Corrosion Science*, 50(9):2614–2619, 2008.
- [88] E. Simon-Manso and C. P. Kubiak. “Dinuclear Nickel Complexes as Catalysts for Electrochemical Reduction of Carbon Dioxide”. *Organometallics*, 24(1):96–102, 2005.
- [89] S. Grimme. “Accurate Description of Van der Waals Complexes by Density Functional Theory including Empirical Corrections”. *Journal of Computational Chemistry*, 25(12):1463–1473, 2004.
- [90] S. Grimme. “Semiempirical GGA-Type Density Functional Constructed with a Long-Range Dispersion Correction”. *Journal of Computational Chemistry*, 27(15):1787–1799, 2006.
- [91] D. H. Gibson. “The Organometallic Chemistry of Carbon Dioxide”. *Chemical Review*, 96(6):2063–2096, 1996.
- [92] Y. Jean. *Molecular Orbitals of Transition Metal Complexes*, pages 37–84. Oxford University Press Inc, New York, 2005.
- [93] D. Zhao and L. Brammer. “Allogons .1. Low-Temperature X-Ray Crystal-Structures of the Trigonal Bipyramidal and Square-Pyramidal Forms of HCo(CO)₂(PPh₃)₂”. *Inorganic Chemistry*, 33(25):5897–5902, 1994.
- [94] D. A. Reitsma and F. R. Keene. “Reduction of Terminal Alkynes Mediated by Tris(2,2'-Bipyridine)Cobalt(I)”. *Organometallics*, 13(4):1351–1354, 1994.
- [95] Y. Hori, A. Murata, and R. Takahashi. “Formation of Hydrocarbons in the Electrochemical Reduction of Carbon-Dioxide at a Copper Electrode in Aqueous-Solution”. *Journal of the Chemical Society-Faraday Transactions I*, 85:2309–2326, 1989.
- [96] G. Kyriacou and A. Anagnostopoulos. “Electrochemical Reduction of CO₂ at Cu + Au Electrodes”. *Journal of Electroanalytical Chemistry*, 328(1-2):233–243, 1992.
- [97] K. Hara, A. Tsuneto, A. Kudo, and T. Sakata. “Electrochemical Reduction of CO₂ on a Cu Electrode Under High-Pressure - Factors that Determine the Product Selectivity”. *Journal of the Electrochemical Society*, 141(8):2097–2103, 1994.
- [98] Y. Hori, K. Kikuchi, A. Murata, and S. Suzuki. “Production of Methane and Ethylene in Electrochemical Reduction of Carbon-Dioxide at Copper Electrode in Aqueous Hydrogencarbonate Solution”. *Chemistry Letters*, 6:897–898, 1986.
- [99] Y. Hori, K. Kikuchi, and S. Suzuki. “Production of CO and CH₄ in Electrochemical Reduction of CO₂ at Metal-Electrodes in Aqueous Hydrogencarbonate Solution”. *Chemistry Letters*, 11:1695–1698, 1985.

- [100] R. L. Cook, R. C. Macduff, and A. F. Sammells. "Evidence for Formaldehyde, Formic-Acid, and Acetaldehyde as Possible Intermediates during Electrochemical Carbon-Dioxide Reduction at Copper". Journal of the Electrochemical Society, 136(7):1982–1984, 1989.
- [101] R. J. Lim, M. S. Xie, M. A. Sk, J. M. Lee, A. Fisher, X. Wang, and K. H. Lim. "A Review on the Electrochemical Reduction of CO₂ in Fuel Cells, Metal Electrodes and Molecular Catalysts". Catalysis Today, 233:169–180, 2014.
- [102] J. March. Advanced Organic Chemistry Reactions, Mechanisms and Structure (6th ed.), pages 54–95. John Wiley and Sons, Inc., Hoboken, New Jersey, 2007.
- [103] I. E. Wachs. "Raman and IR Studies of Surface Metal Oxide Species on Oxide Supports: Supported Metal Oxide Catalysts". Catalysis Today, 27(3-4):437–455, 1996.
- [104] R. D. L. Smith, M. S. Prevot, R. D. Fagan, S. Trudel, and C. P. Berlinguette. "Water Oxidation Catalysis: Electrocatalytic Response to Metal Stoichiometry in Amorphous Metal Oxide Films Containing Iron, Cobalt, and Nickel". Journal of the American Chemical Society, 135(31):11580–11586, 2013.
- [105] K. A. Zemski, D. R. Justes, and A. W. Castleman. "Studies of Metal Oxide Clusters: Elucidating Reactive Sites Responsible for the Activity of Transition Metal Oxide Catalysts". Journal of Physical Chemistry B, 106(24):6136–6148, 2002.
- [106] J. U. Reveles, G. E. Johnson, S. N. Khanna, and A. W. Castleman. "Reactivity Trends in the Oxidation of CO by Anionic Transition Metal Oxide Clusters". Journal of Physical Chemistry C, 114(12):5438–5446, 2010.
- [107] G. E. Johnson, J. U. Reveles, N. M. Reilly, E. C. Tyo, S. N. Khanna, and A. W. Castleman. "Influence of Stoichiometry and Charge State on the Structure and Reactivity of Cobalt Oxide Clusters with CO". Journal of Physical Chemistry A, 112(45):11330–11340, 2008.
- [108] G. E. Johnson, N. M. Reilly, and A. W. Castleman. "Effect of Charge State and Stoichiometry on the Structure and Reactivity of Nickel Oxide Clusters with CO". International Journal of Mass Spectrometry, 280(1-3):93–100, 2009.
- [109] N. M. Reilly, J. U. Reveles, G. E. Johnson, S. N. Khanna, and A. W. Castleman. "Experimental and Theoretical Study of the Structure and Reactivity of Fe₁₋₂O_{≥6}⁻ Clusters with CO". Journal of Physical Chemistry A, 111(20):4158–4166, 2007.
- [110] D. Schröder, J. Roithova, and H. Schwarz. "Electrospray Ionization as a Convenient New Method for the Generation of Catalytically Active Iron-Oxide Ions in the Gas Phase". International Journal of Mass Spectrometry, 254(3):197–201, 2006.
- [111] J. E. Mann, S. E. Waller, D. W. Rothgeb, and C. C. Jarrold. "Study of Nb₂O_y (y = 2 - 5) Anion and Neutral Clusters Using Anion Photoelectron Spectroscopy and Density Functional Theory Calculations". Journal of Chemical Physics, 135(10), 2011.
- [112] D. E. Clemmer, N. Aristov, and P. B. Armentrout. "Reactions of ScO⁺, TiO⁺, and VO⁺ with D₂: M⁺-OH Bond-Energies and Effects of Spin Conservation". Journal of Physical Chemistry, 97(3):544–552, 1993.

- [113] D. E. Clemmer, N. F. Dalleska, and P. B. Armentrout. "Gas-Phase Thermochemistry of the Group-3 Dioxides - ScO_2 , YO_2 and LaO_2 ". Chemical Physics Letters, 190(3-4):259–265, 1992.
- [114] F. Y. Liu, F. X. Li, and P. B. Armentrout. "Guided Ion-Beam Studies of the Reactions of Co_n^+ ($n = 2 - 20$) with O_2 : Cobalt Cluster-Oxide and -Dioxide Bond Energies". Journal of Chemical Physics, 123(6), 2005.
- [115] M. Li, S. R. Liu, and P. B. Armentrout. "Collision-Induced Dissociation Studies of Fe_mO_n^+ : Bond Energies in Small Iron Oxide Cluster Cations, Fe_mO_n^+ , ($m = 1 - 3$, $n = 1 - 6$)". Journal of Chemical Physics, 131(14), 2009.
- [116] M. R. Sievers and P. B. Armentrout. "Gas Phase Activation of Carbon Dioxide by Niobium and Niobium Monoxide Cations". International Journal of Mass Spectrometry, 180:103–115, 1998.
- [117] D. Schröder and H. Schwarz. "Intrinsic Mechanisms of Oxidation Reactions as Revealed by Gas-Phase Experiments". Organometallic Oxidation Catalysis, 22:1–15, 2007.
- [118] E. Hossain, D. W. Rothgeb, and C. C. Jarrold. "CO₂ Reduction by Group 6 Transition Metal Suboxide Cluster Anions". Journal of Chemical Physics, 133(2), 2010.
- [119] D. W. Rothgeb, J. E. Mann, S. E. Waller, and C. C. Jarrold. "Structures of Trimetallic Molybdenum and Tungsten Suboxide Cluster Anions". Journal of Chemical Physics, 135(10), 2011.
- [120] K. R. Asmis. "Structure Characterization of Metal Oxide Clusters by Vibrational Spectroscopy: Possibilities and Prospects". Physical Chemistry Chemical Physics, 14(26):9270–9281, 2012.
- [121] A. M. Burow, T. Wende, M. Sierka, R. Wlodarczyk, J. Sauer, P. Claes, L. Jiang, G. Meijer, P. Lievens, and K. R. Asmis. "Structures and Vibrational Spectroscopy of Partially Reduced Gas-Phase Cerium Oxide Clusters". Physical Chemistry Chemical Physics, 13(43):19393–19400, 2011.
- [122] T. M. Maier, A. D. Boese, J. Sauer, T. Wende, M. Fagiani, and K. R. Asmis. "The Vibrational Spectrum of FeO_2^+ Isomers-Theoretical Benchmark and Experiment". Journal of Chemical Physics, 140(20), 2014.
- [123] A. Fielicke, P. Gruene, M. Haertelt, D. J. Harding, and G. Meijer. "Infrared Spectroscopy and Binding Geometries of Oxygen Atoms Bound to Cationic Tantalum Clusters". Journal of Physical Chemistry A, 114(36):9755–9761, 2010.
- [124] A. Kirilyuk, A. Fielicke, K. Demyk, G. von Helden, G. Meijer, and Th Rasing. "Ferrimagnetic Cage-like Fe_4O_6 Cluster: Structure Determination from Infrared Dissociation Spectroscopy". Physical Review B, 82(2), 2010.
- [125] A. Fielicke, G. Meijer, and G. von Helden. "Infrared Multiple Photon Dissociation Spectroscopy of Transition Metal Oxide Cluster Cations - Comparison of Group Vb (V, Nb, Ta) Metal Oxide Clusters". European Physical Journal D, 24(1-3):69–72, 2003.

- [126] A. Fielicke, G. Meijer, and G. von Helden. “Infrared Spectroscopy of Niobium Oxide Cluster Cations in a Molecular Beam: Identifying the Cluster Structures”. Journal of the American Chemical Society, 125(12):3659–3667, 2003.
- [127] A. Fielicke and K. Rademann. “Molybdenum Doped Bismuth Oxide Clusters and Their Reactivity Towards Ethene: Comparison with Pure Bismuth Oxide Clusters”. Chemical Physics Letters, 359(5-6):360–366, 2002.
- [128] J. Opitz-Coutureau, A. Fielicke, B. Kaiser, and K. Rademann. “Antimony and Bismuth Oxide Cluster Ions”. Physical Chemistry Chemical Physics, 3(15):3034–3041, 2001.
- [129] R. A. Marcus and N. Sutin. “Electron Transfers in Chemistry and Biology”, 1985.
- [130] S. S. Shaik, H. B. Schlegel, and S. Wolfe. Theoretical Aspects of Physical Organic Chemistry. John Wiley and Sons, Inc., New York, 1992.
- [131] John I. Brauman. “Chemistry - Not So Simple”. Science, 319(5860):168–168, 2008.
- [132] C. H. Depuy and V. M. Bierbaum. “Gas-Phase Reactions of Organic-Anions as Studied by the Flowing Afterglow Technique”. Accounts of Chemical Research, 14(5):146–153, 1981.
- [133] C. E. H. Dessent, C. G. Bailey, and M. A. Johnson. “On the Vibrational Fine Structure in the Near-Threshold Photofragmentation Spectrum of the $I^- \cdot CH_3I$ Complex: Spectroscopic Observation of Nonadiabatic Effects in Electron-Molecule Scattering”. Journal of Chemical Physics, 105(23):10416–10423, 1996.
- [134] C. E. H. Dessent, J. Kim, and M. A. Johnson. “Photochemistry of Halide Ion-Molecule Clusters: Dipole Bound Excited States and the Case for Asymmetric Solvation”. Accounts of Chemical Research, 31(9):527–534, 1998.
- [135] C. E. H. Dessent, J. Kim, and M. A. Johnson. “Spectroscopic Observation of Vibrational Feshbach Resonances in Near-Threshold Photoexcitation of $X^- \cdot CH_3NO_2$ ($X^- = I^-$ and Br^-)”. Faraday Discussion, 115:395–406, 2000.
- [136] R. Mabbs, E. Surber, and A. Sanov. “Photoelectron Imaging of Negative Ions: Atomic Anions to Molecular Clusters”. Analyst, 128(6):765–772, 2003.
- [137] R. Mabbs, K. Pichugin, and A. Sanov. “Dynamic Molecular Interferometer: Probe of Inversion Symmetry in I_2^- Photodissociation”. Journal of Chemical Physics, 123(5), 2005.
- [138] R. Mabbs, E. R. Grumbling, K. Pichugin, and A. Sanov. “Photoelectron Imaging: An Experimental Window into Electronic Structure”. Chemical Society Reviews, 38:2169–2177, 2009.
- [139] E. Surber and A. Sanov. “Imaging of Direct Photodetachment and Autodetachment of $(OCS)_2^-$: Excited-State Dynamics of the Covalent Dimer Anion”. Physical Review Letters, 90(9), 2003.
- [140] D. J. Goebbert, K. Pichugin, and A. Sanov. “Low-Lying Electronic States of CH_3NO_2 via Photoelectron Imaging of the Nitromethane Anion”. Journal of Chemical Physics, 131(16):164308, 2009.

- [141] A. Sanov and R. Mabbs. “Photoelectron Imaging of Negative Ions”. International Reviews in Physical Chemistry, 27(1):53–85, 2008.
- [142] K. J. Breen, A. F. DeBlase, T. L. Guasco, V. K. Voora, K. D. Jordan, T. Nagata, and M. A. Johnson. “Bottom-Up View of Water Network-Mediated CO₂ Reduction Using Cryogenic Cluster Ion Spectroscopy and Direct Dynamics Simulations”. Journal of Physical Chemistry A, 116(3):903–912, 2012.
- [143] P. Ayotte, J. Kim, J. A. Kelley, S. B. Nielsen, and M. A. Johnson. “Photoactivation of the Cl⁻+CH₃Br S_N2 Reaction via Rotationally Resolved C-H Stretch Excitation of the Cl⁻·CH₃Br Entrance Channel Complex”. Journal of the American Chemical Society, 121(29):6950–6951, 1999.
- [144] R. Nakanishi and T. Nagata. “Formation and Photodestruction of Dual Dipole-Bound Anion (H₂O)₆(e⁻)CH₃NO₂⁻”. Journal of Chemical Physics, 130(22), 2009.
- [145] C. L. Adams, H. Schneider, K. M. Ervin, and J. M. Weber. “Low-Energy Photoelectron Imaging Spectroscopy of Nitromethane Anions: Electron Affinity, Vibrational Features, Anisotropies and the Dipole-Bound State”. Journal of Chemical Physics, 130:074307–1 – 10, 2009.
- [146] J. M. Weber, W. H. Robertson, and M. A. Johnson. “Argon Predissociation and Electron Autodetachment Spectroscopy of Size-Selected CH₃NO₂⁻·Ar_n Clusters”. Journal of Chemical Physics, 115(23):10718–10723, 2001.
- [147] H. Schneider, K. M. Vogellhuber, F. Schinle, J. F. Stanton, and J. M. Weber. “Vibrational Spectroscopy of Nitroalkane Chains using Electron Detachment and Ar Predissociation”. J. Phys. Chem. A, 112:7498–7506, 2008.
- [148] C. L. Adams, H. Schneider, and J. M. Weber. “Vibrational Autodetachment Intramolecular Vibrational Relaxation Translated Into Electronic Motion”. Journal of Physical Chemistry A, 114:4017–4030, 2010.
- [149] A. Schramm, II Fabrikant, J. M. Weber, E. Leber, M. W. Ruf, and H. Hotop. “Vibrational Resonance and Threshold Effects in Inelastic Electron Collisions with Methyl Iodide Molecules”. Journal of Physics B-Atomic, Molecular and Optical Physics, 32(9):2153–2171, 1999.
- [150] D. Hanstorp and M. Gustafsson. “Determination of the Electron-Affinity of Iodine”. Journal of Physics B-Atomic Molecular and Optical Physics, 25(8):1773–1783, 1992.
- [151] H. Schneider, K. Takahashi, R. T. Skodje, and J. M. Weber. “Infrared Spectra of SF₆⁻·HCOOH·Ar_n (n = 0 - 2): Infrared Triggered Reaction and Ar-Induced Reactive Inhibition”. Journal of Chemical Physics, 130(17), 2009.
- [152] B. J. Knurr, C. L. Adams, and J. M. Weber. “Infrared Spectroscopy of Hydrated Naphthalene Cluster Anions”. Journal of Chemical Physics, 137(10), 2012.
- [153] K. A. Peterson, B. C. Shepler, D. Figgen, and H. Stoll. “On the Spectroscopic and Thermochemical Properties of ClO, BrO, IO, and their Anions”. Journal of Physical Chemistry A, 110(51):13877–13883, 2006.

- [154] J. V. Seeley, R. A. Morris, A. A. Viggiano, H. B. Wang, and W. L. Hase. "Temperature Dependence of the Rate Constants and Branching Ratios for the Reactions of $\text{Cl}^- (\text{D}_2\text{O})_{1-3}$ with CH_3Br and Thermal Dissociation Rates for $\text{Cl}^- (\text{CH}_3\text{Br})$ ". Journal of the American Chemical Society, 119(3):577–584, 1997.
- [155] P. Botschwina, C. Hennig, and S. Schmatz. "Quantum Dynamics of the Complex-Forming $\text{S}_\text{N}2$ Reaction $\text{Cl}^- + \text{CD}_3\text{Cl} \rightarrow \text{ClCD}_3 + \text{Cl}^-$ on a Four-Dimensional Coupled-Cluster Potential Surface". Physical Chemistry Chemical Physics, 6(19):4630–4635, 2004.
- [156] S. Schmatz, P. Botschwina, J. Hauschildt, and R. Schinke. "Resonances in $\text{S}_\text{N}2$ Reactions: Two-Mode Quantum Calculations for $\text{Cl}^- + \text{CH}_3\text{Br}$ on a Coupled-Cluster Potential Energy Surface". Journal of Chemical Physics, 117(21):9710–9718, 2002.
- [157] S. Schmatz, P. Botschwina, and H. Stoll. "Coupled Cluster Calculations for the $\text{S}_\text{N}2$ Reaction $\text{Cl}^- + \text{CH}_3\text{Br} \rightarrow \text{ClCH}_3 + \text{Br}^-$ ". International Journal of Mass Spectrometry, 201(1-3):277–282, 2000.
- [158] H. Haberland, H. Langosch, H. G. Schindler, and D. R. Worsnop. "Negatively Charged Water Clusters - Mass-Spectra of $(\text{H}_2\text{O})_N^-$ and $(\text{D}_2\text{O})_N^-$ ". Journal of Physical Chemistry, 88(17):3903–3904, 1984.
- [159] T. Maeyama, T. Oikawa, K. Seguchi, and W. Mikami. "Considerable Stability and Visible Absorption of the Benzene-Water Hexamer Cluster Anion". Journal of Physical Chemistry A, 101(45):8371–8373, 1997.
- [160] N. I. Hammer, J. R. Roscioli, M. A. Johnson, E. M. Myshakin, and K. D. Jordan. "Infrared Spectrum and Structural Assignment of the Water Trimer Anion". Journal of Physical Chemistry A, 109(50):11526–11530, 2005.
- [161] E. A. Price, N. I. Hammer, and M. A. Johnson. "A Cluster Study of Cl_2^- Microhydration: Size-Dependent Competition Between Symmetrical H-Bonding to the Anion and the Formation of Cyclic Water Networks in the $\text{Cl}_2^- \cdot 1-5(\text{H}_2\text{O})$ Series". Journal of Physical Chemistry A, 108(18):3910–3915, 2004.
- [162] J. M. Weber, J. A. Kelley, W. H. Robertson, and M. A. Johnson. "Hydration of a Structured Excess Charge Distribution: Infrared Spectroscopy of the $\text{O}_2^- \cdot (\text{H}_2\text{O})_n$, ($1 \leq n \leq 5$) Clusters". Journal of Chemical Physics, 114(6):2698–2706, 2001.
- [163] S. S. Xantheas. "Quantitative Description of Hydrogen Bonding in Chloride-Water Clusters". Journal of Physical Chemistry, 100(23):9703–9713, 1996.
- [164] J. Kim and K. S. Kim. "Structures, Binding Energies, and Spectra of Isoenergetic Water Hexamer Clusters: Extensive Ab Initio Studies". Journal of Chemical Physics, 109(14):5886–5895, 1998.
- [165] E. G. Diken, W. H. Robertson, and M. A. Johnson. "The Vibrational Spectrum of the Neutral $(\text{H}_2\text{O})_6$ Precursor to the "Magic" $(\text{H}_2\text{O})_6^-$ Cluster Anion by Argon-Mediated, Population-Modulated Electron Attachment Spectroscopy". Journal of Physical Chemistry A, 108(1):64–68, 2004.

- [166] C. Desfrancois, H. Abdoul-Carime, N. Khelifa, and J. P. Schermann. "From $1/R$ to $1/R^2$ Potentials - Electron-Exchange between Rydberg Atoms and Polar-Molecules". Physical Review Letters, 73(18):2436–2439, 1994.
- [167] P. D. Burrow, J. A. Michejda, and K. D. Jordan. "Electron Transmission Study of the Temporary Negative-Ion States of Selected Benzenoid and Conjugated Aromatic-Hydrocarbons". Journal of Chemical Physics, 86(1):9–24, 1987.
- [168] J. Schiedt, W. J. Knott, K. Le Barbu, E. W. Schlag, and R. Weinkauff. "Microsolvation of Similar-Sized Aromatic Molecules: Photoelectron Spectroscopy of Bithiophene-, Azulene-, and Naphthalene-Water Anion Clusters". Journal of Chemical Physics, 113(21):9470–9478, 2000.
- [169] K. Le Barbu, J. Schiedt, R. Weinkauff, E. W. Schlag, J. M. Nilles, S. J. Xu, O. C. Thomas, and K. H. Bowen. "Microsolvation of Small Anions by Aromatic Molecules: An Exploratory Study". Journal of Chemical Physics, 116(22):9663–9671, 2002.
- [170] S. A. Lyapustina, S. K. Xu, J. M. Nilles, and K. H. Bowen. "Solvent-Induced Stabilization of the Naphthalene Anion by Water Molecules: A Negative Cluster Ion Photoelectron Spectroscopic Study". Journal of Chemical Physics, 112(15):6643–6648, 2000.
- [171] M. Tschurl, U. Boesl, and S. Gilb. "The Electron Affinity of Phenanthrene". Journal of Chemical Physics, 125(19), 2006.
- [172] J. Schiedt and R. Weinkauff. "Photodetachment Photoelectron Spectroscopy of Mass Selected Anions: Anthracene and the Anthracene- H_2O Cluster". Chemical Physics Letters, 266(1-2):201–205, 1997.
- [173] A. Carrington, F. Dravnieks, and M. C. R. Symons. "Unstable Intermediates .4. Electron Spin Resonance Studies of Univalent Aromatic Hydrocarbon Ions". Journal of the Chemical Society, pages 947–952, 1959.
- [174] D. E. Paul, D. Lipkin, and S. I. Weissman. "Reactions of Sodium Metal with Aromatic Hydrocarbons". Journal of the American Chemical Society, 78(1):116–120, 1956.
- [175] D. Lipkin, D. E. Paul, J. Townsend, and S. I. Weissman. "Observations on a Class of Free Radicals Derived from Aromatic Compounds". Science, 117(3046):534–535, 1953.
- [176] J. R. Jezorek and H. B. Mark. "Effect of Water as a Proton Donor on Decay of Anthracene and Naphthalene Anion Radicals in Aqueous Mixtures of Acetonitrile, Dimethylformamide, and Dimethyl Sulfoxide". Journal of Physical Chemistry, 74(7):1627, 1970.
- [177] B. Fraboni, P. Cosseddu, Y. Q. Wang, R. K. Schulze, Z. F. Di, A. Cavallini, M. Nastasi, and A. Bonfiglio. "Aging Control of Organic Thin Film Transistors via Ion-Implantation". Organic Electronics, 12(9):1552–1559, 2011.
- [178] D. Simeone, M. Rapisarda, G. Fortunato, A. Valletta, and L. Mariucci. "Influence of Structural Properties on Environmental Stability of Pentacene Thin Film Transistors". Organic Electronics, 12(3):447–452, 2011.
- [179] O. D. Jurchescu, J. Baas, and T. T. M. Palstra. "Electronic Transport Properties of Pentacene Single Crystals Upon Exposure to Air". Applied Physics Letters, 87(5), 2005.

- [180] M. A. Duncan. “Infrared Spectroscopy to Probe Structure and Dynamics in Metal Ion-Molecule Complexes”. *International Reviews in Physical Chemistry*, 22(2):407–435, 2003.
- [181] W. H. Robertson and M. A. Johnson. “Molecular Aspects of Halide Ion Hydration: The Cluster Approach”. *Annual Review of Physical Chemistry*, 54:173–213, 2003.
- [182] E. J. Bieske and O. Dopfer. “High-Resolution Spectroscopy of Cluster Ions”. *Chemical Reviews*, 100(11):3963–3998, 2000.
- [183] O. Dopfer. “Spectroscopic and Theoretical Studies of CH_3^+ - Rg_n Clusters ($\text{Rg} = \text{He}, \text{Ne}, \text{Ar}$): From Weak Intermolecular Forces to Chemical Reaction Mechanisms”. *International Reviews in Physical Chemistry*, 22(3):437–495, 2003.
- [184] T. Ebata, A. Fujii, and N. Mikami. “Vibrational Spectroscopy of Small-Sized Hydrogen-Bonded Clusters and Their Ions”. *International Reviews in Physical Chemistry*, 17(3):331–361, 1998.
- [185] E. Cane, P. Palmieri, R. Tarroni, A. Trombetti, and N. C. Handy. “The High-Resolution Infrared Spectra of Naphthalene-H(8) and Naphthalene-D(8): Comparison of Scaled SCF and Density Functional Force Fields”. *Gazzetta Chimica Italiana*, 126(5):289–296, 1996.
- [186] D. M. Hanson and A. R. Gee. “Raman Scattering Tensors for Single Crystals of Naphthalene”. *Journal of Chemical Physics*, 51(11):5052, 1969.
- [187] E. Cane, A. Miani, and A. Trombetti. “Anharmonic Force Fields of Naphthalene-h₈ and Naphthalene-d₈”. *Journal of Physical Chemistry A*, 111(33):8218–8222, 2007.
- [188] H. Kawamata, T. Maeyama, and N. Mikami. “First Observation of Ionic π -Hydrogen Bonds; Vibrational Spectroscopy of Dihydrated Naphthalene Anion ($\text{Nph}-(\text{H}_2\text{O})_2$)”. *Chemical Physics Letters*, 370(3-4):535–541, 2003.
- [189] J. C. M. Henning. “ ^{14}n Hyperfine Structure in ESR Spectra of Heterocyclic Anions”. *Journal of Chemical Physics*, 44(5):2139, 1966.
- [190] B. M. Elliott, L. R. McCunn, and M. A. Johnson. “Photoelectron Imaging Study of Vibrationally Mediated Electron Autodetachment in the Type I Isomer of the Water Hexamer Anion”. *Chemical Physics Letters*, 467(1-3):32–36, 2008.
- [191] A. L. Nicely, D. J. Miller, and J. M. Lisy. “Charge and Temperature Dependence of Biomolecule Conformations: K^+ Tryptamine $(\text{H}_2\text{O})_{n=0-1} \cdot \text{Ar}_{m=0-1}$ Cluster Ions”. *Journal of the American Chemical Society*, 131(18):6314, 2009.
- [192] H. Motegi, T. Takayanagi, T. Tsuneda, K. Yagi, R. Nakanishi, and T. Nagata. “Theoretical Study on the Excess Electron Binding Mechanism in the $[\text{CH}_3\text{NO}_2 \cdot (\text{H}_2\text{O})_n]^-$ ($n = 1 - 6$) Anion Clusters”. *Journal of Physical Chemistry A*, 114(34):8939–8947, 2010.
- [193] Jr. Rodriguez, O. and J. M. Lisy. “Revisiting $\text{Li}^+(\text{H}_2\text{O})_{3-4}\text{Ar}_1$ Clusters: Evidence of High-Energy Conformers from Infrared Spectra”. *Journal of Physical Chemistry Letters*, 2(12):1444–1448, 2011.
- [194] J. D. Rodriguez and J. M. Lisy. “Infrared Spectroscopy of Gas-Phase Hydrated K^+ :18-Crown-6 Complexes: Evidence for High Energy Conformer Trapping Using the Argon Tagging Method”. *International Journal of Mass Spectrometry*, 283(1-3):135–139, 2009.

- [195] T. L. Guasco, B. M. Elliott, M. A. Johnson, J. Ding, and K. D. Jordan. “Isolating the Spectral Signatures of Individual Sites in Water Networks Using Vibrational Double-Resonance Spectroscopy of Cluster Isotopomers”. Journal of Physical Chemistry Letters, 1(15):2396–2401, 2010.
- [196] J. C. Marcum and J. M. Weber. “Microhydration of Nitromethane Anions from Both a Solute and Solvent Perspective”. Journal of Physical Chemistry A, 114(34):8933–8938, 2010.
- [197] A. Singh, H. D. Gesser, and A. R. Scott. “Solvated Electron in Acetonitrile”. Chemical Physics Letters, 2(5):271–273, 1968.

Appendix A

Supplementary Material for Chapter 3.2.2

This appendix contains additional calculated structures for $[\text{Au}(\text{CO}_2)_n]^-$ clusters ($n = 4, 5$). The number of conformers that can be calculated at larger cluster sizes and the flatness of the potential energy surface makes identifying larger clusters computationally prohibitive.

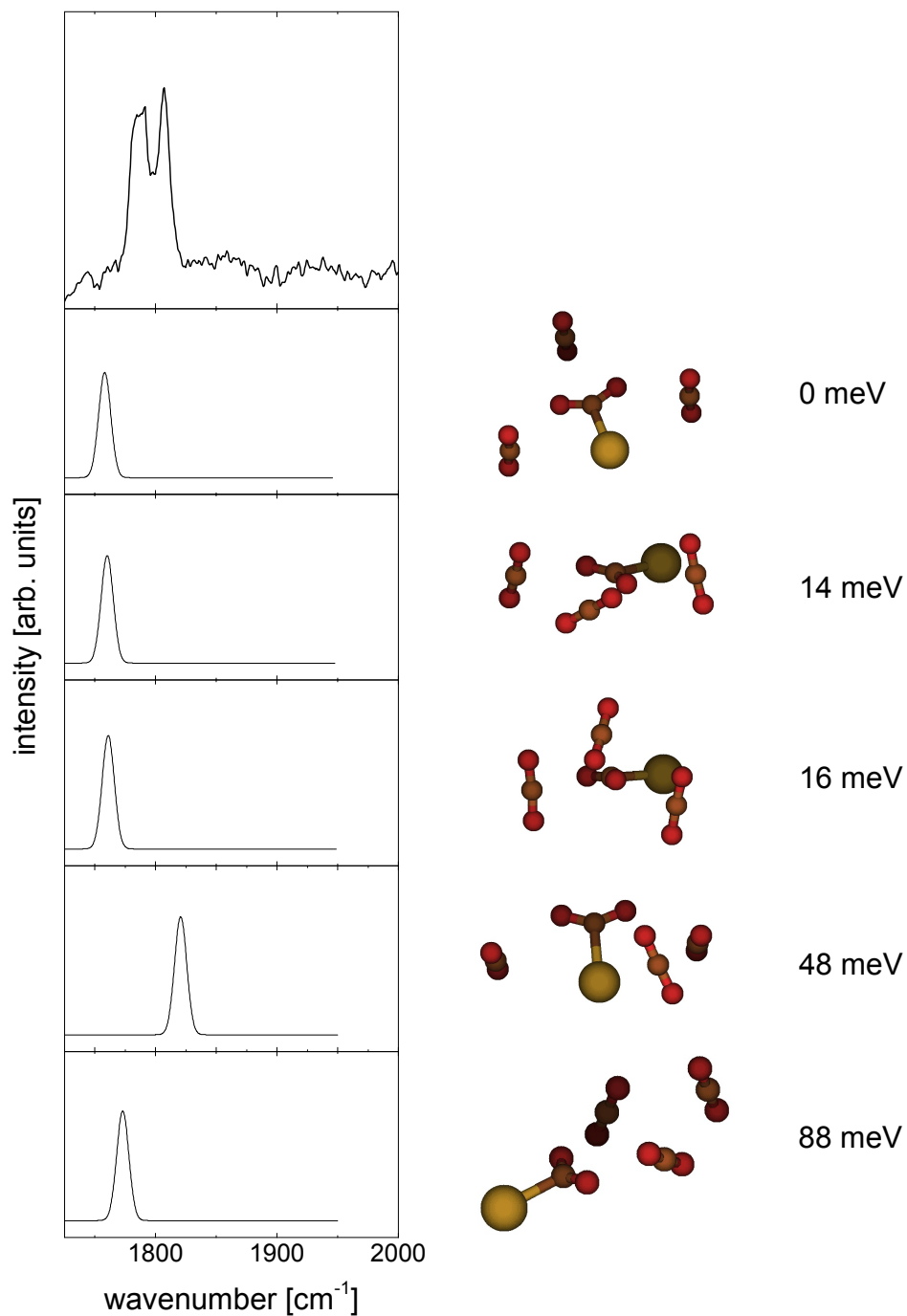


Figure A.1: Calculated infrared spectra in the region of the partially reduced antisymmetric CO stretch of the formate core for $[\text{Au}(\text{CO}_2)_4]^-$ clusters. The experimental spectrum for $[\text{Au}(\text{CO}_2)_4]^-$ is shown in the top panel. The calculated spectra are shown in the lower panels with their corresponding structures and relative energies given to the right. Calculated OCO bond angles range from 139.3° to 142.6° for the bonded CO_2 moiety and 175.2° to 178.0° for the solvent CO_2 molecules.

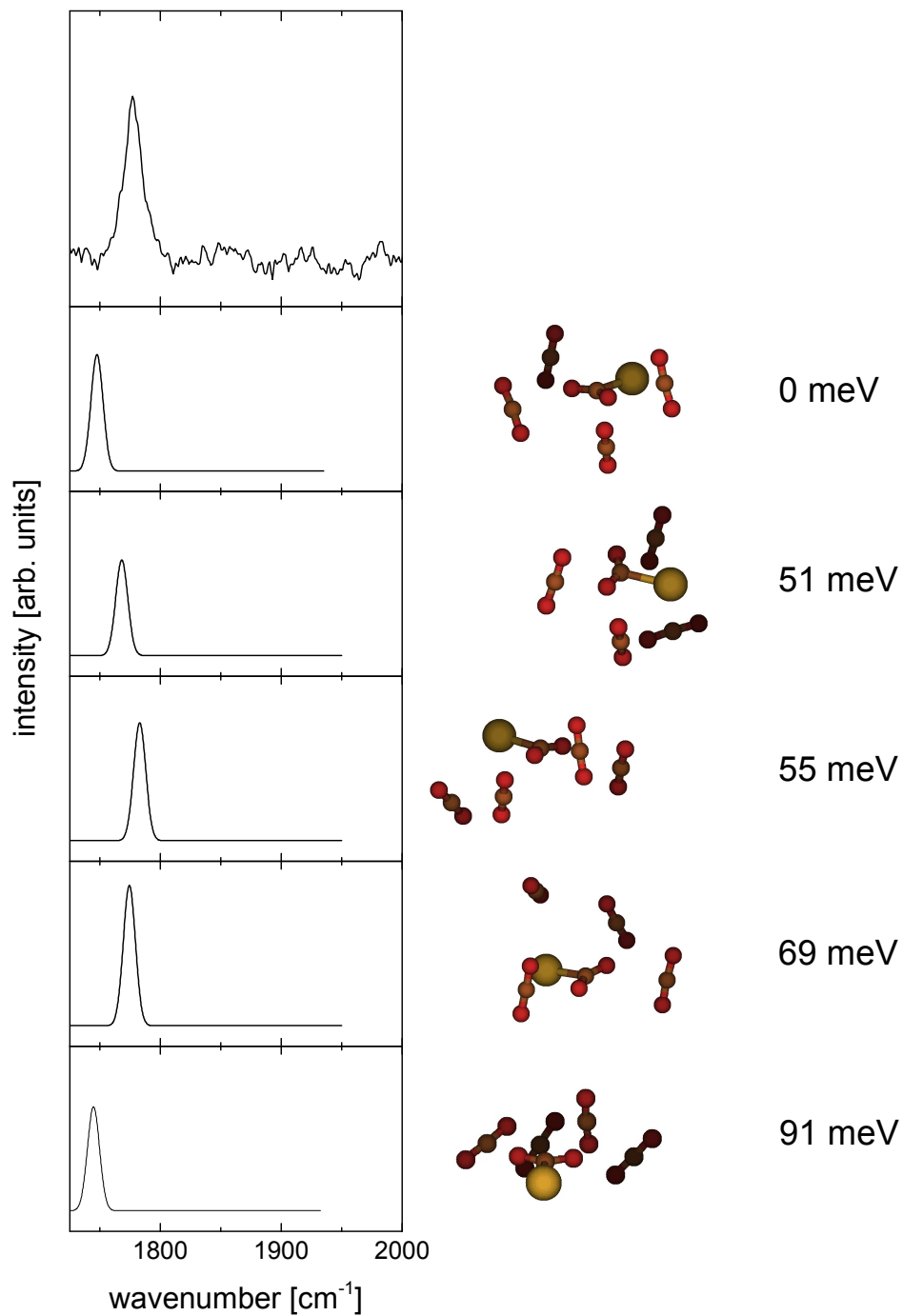


Figure A.2: Calculated infrared spectra in the region of the partially reduced antisymmetric CO stretch of the formate core for $[\text{Au}(\text{CO}_2)_5]^-$ clusters. The experimental spectrum for $[\text{Au}(\text{CO}_2)_5]^-$ is shown in the top panel. The calculated spectra are shown in the lower panels with their corresponding structures and relative energies given to the right. Calculated OCO bond angles range from 139.0° to 140.2° for the bonded CO_2 moiety and 175.3° to 178.0° for the solvent CO_2 molecules.

Appendix B

Supplementary Material for Chapter 3.3.3

This appendix contains additional calculated structures for $[\text{Ni}(\text{CO}_2)_n]^-$ clusters and an estimation for the barrier height for conversion of isomer E* to isomer D. See Chapter 3.3.3 for discussion.

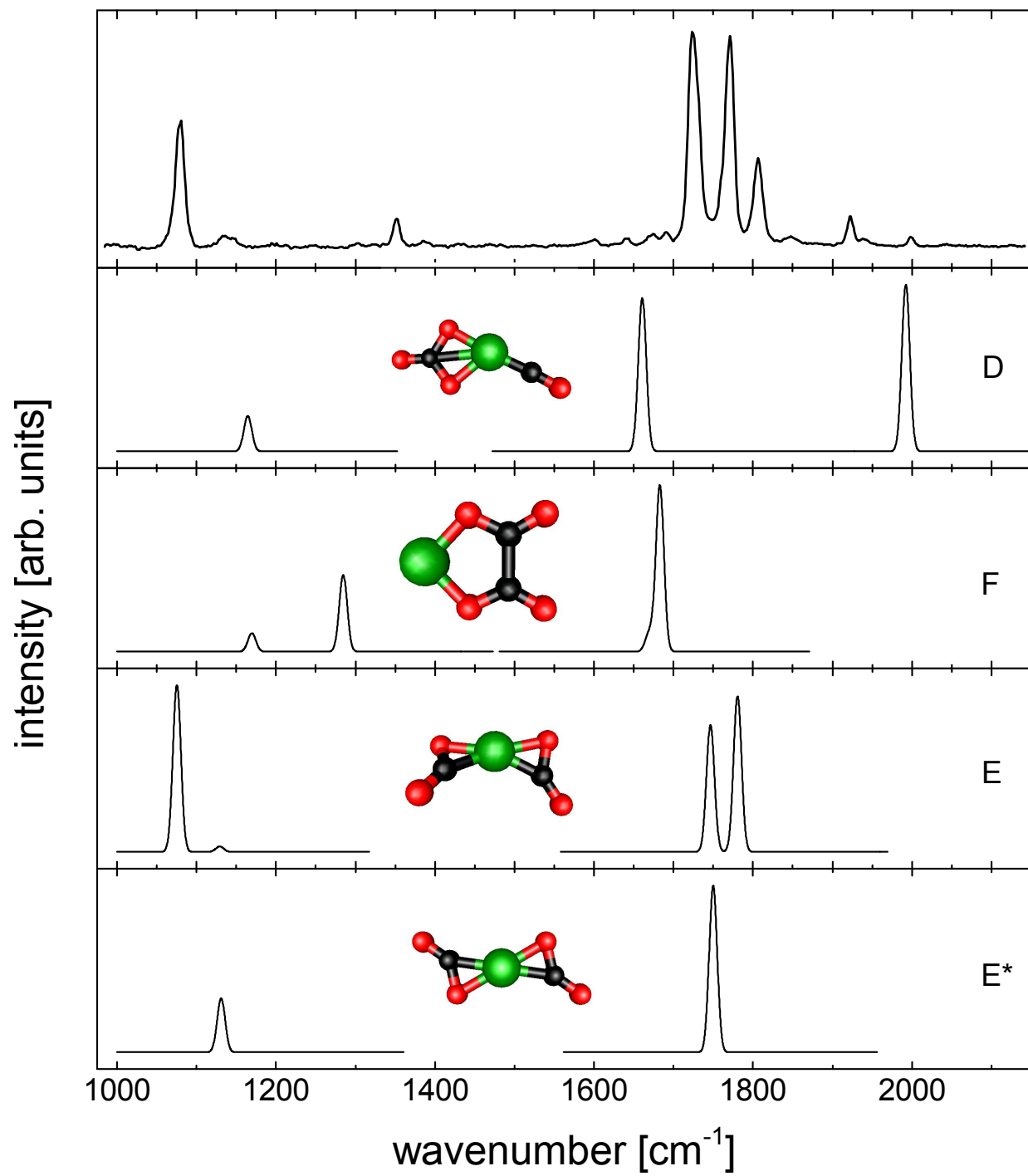


Figure B.1: Calculated spectra of bare core isomers for $[\text{Ni}(\text{CO}_2)_2]^-$ clusters. All of the isomers presented here are discussed in Chapter 3.3.3.

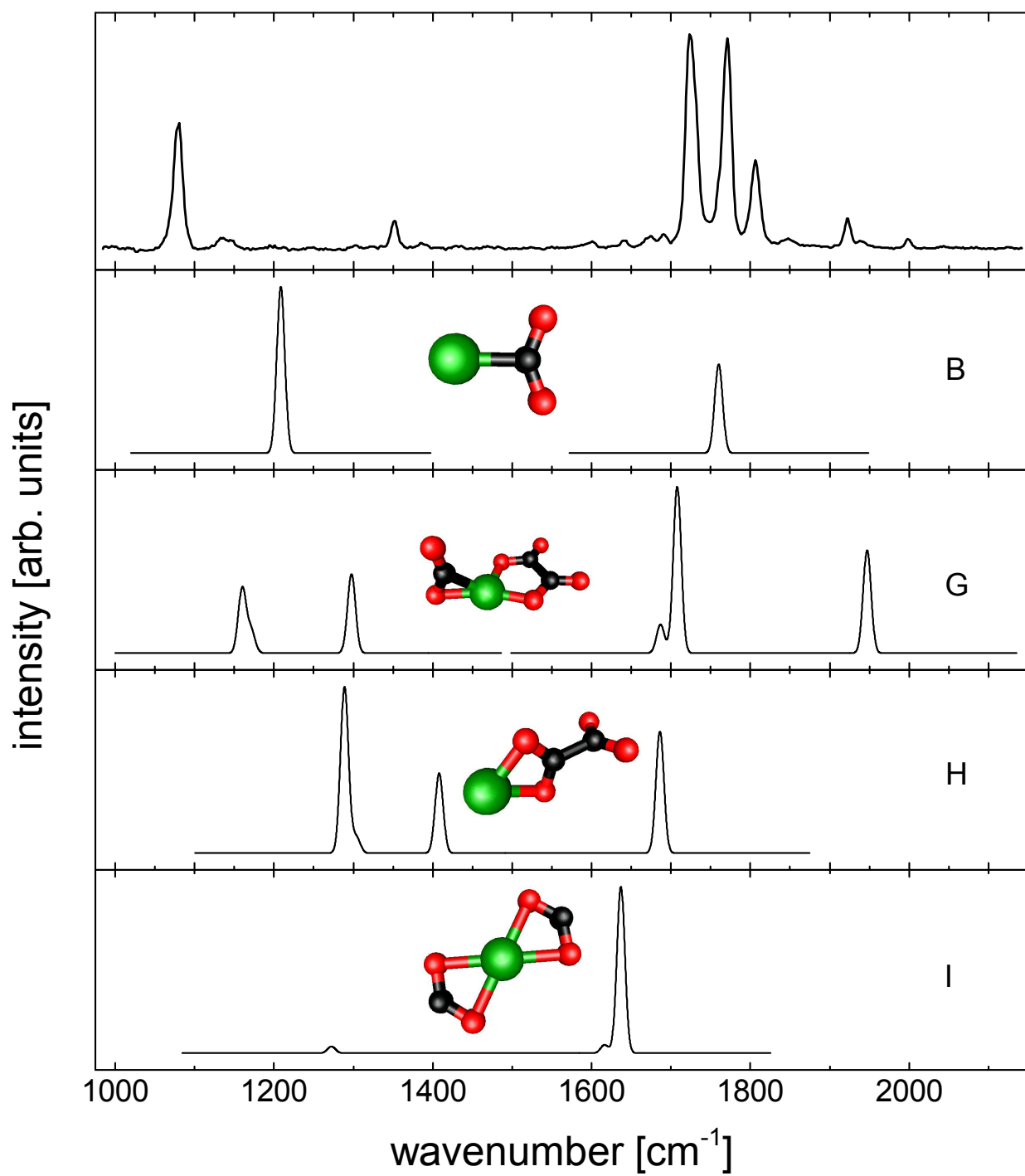


Figure B.2: Additional calculated spectra of bare core isomers for $[\text{Ni}(\text{CO}_2)_n]^-$ clusters. Isomers B and G are discussed in Chapter 3.3.3. Isomers H and I were determined not to contribute to the experimental spectra and were not included in the discussion.

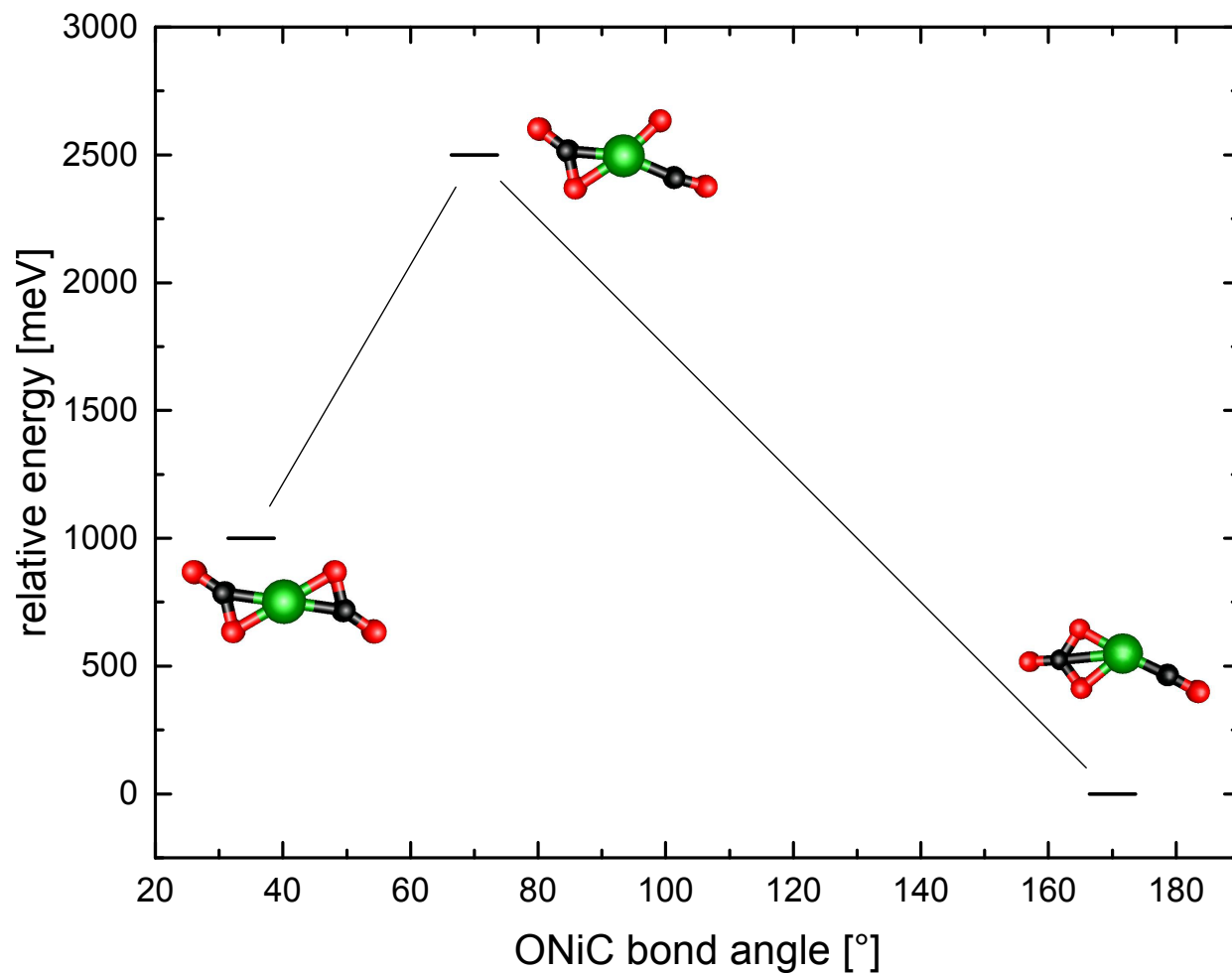


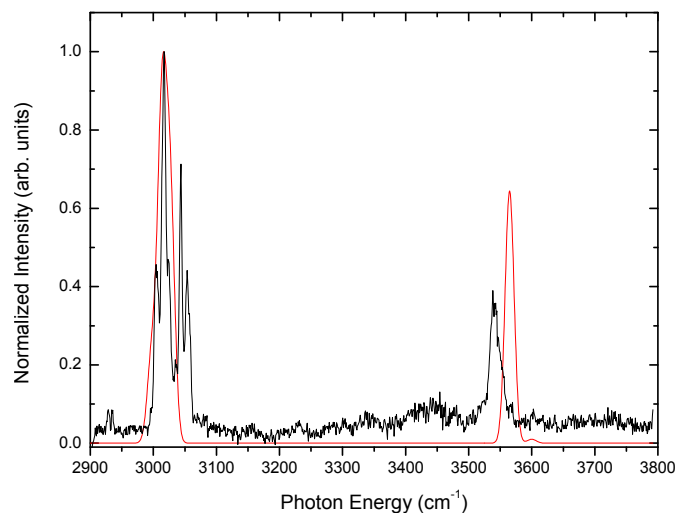
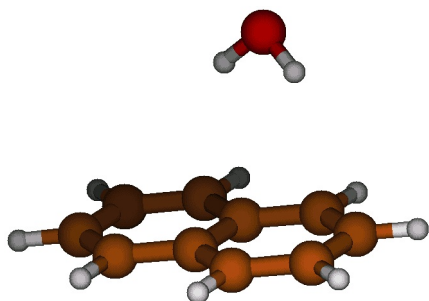
Figure B.3: Estimated barrier height for the conversion of isomer E* to D. Due to the barrier height, we do not expect this isomer conversion process to occur in our experiment.

Appendix C

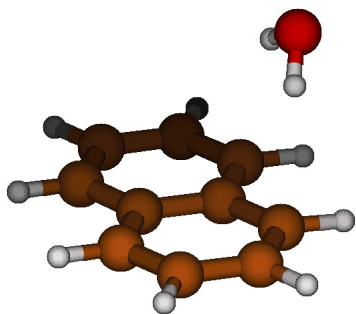
Supplementary Material for Chapter 6

This appendix contains additional structures calculated for $[\text{Np}\cdot(\text{H}_2\text{O})_n]^-$ clusters. The structure is given on the left with the spectrum on the right and the relative energy for that cluster size below. See Chapter 6 for discussion.

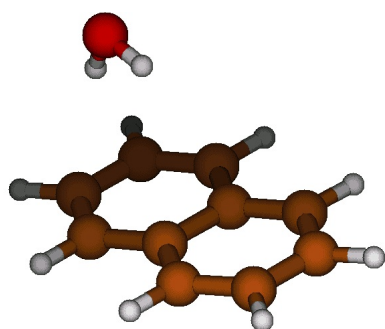
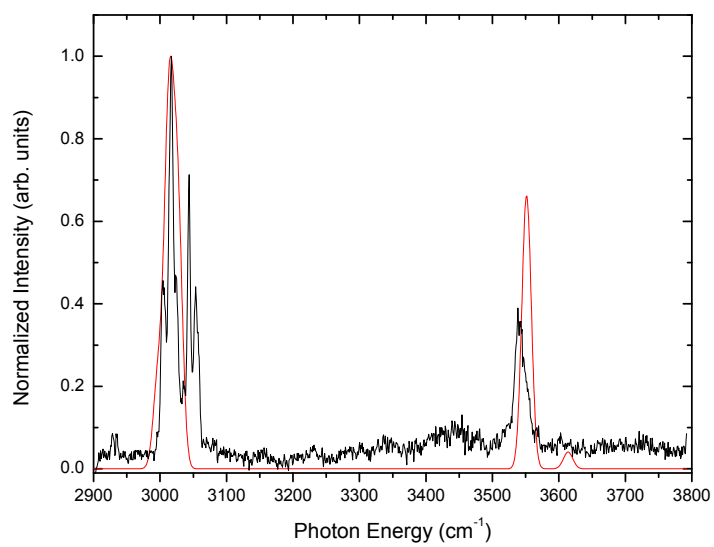
C.1 $[\text{C}_{10}\text{H}_8\cdot\text{H}_2\text{O}]^-$



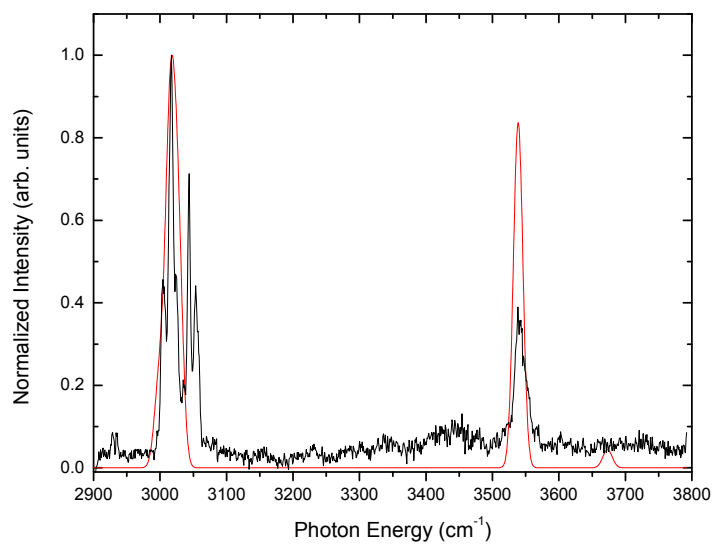
Relative Energy: 0 meV

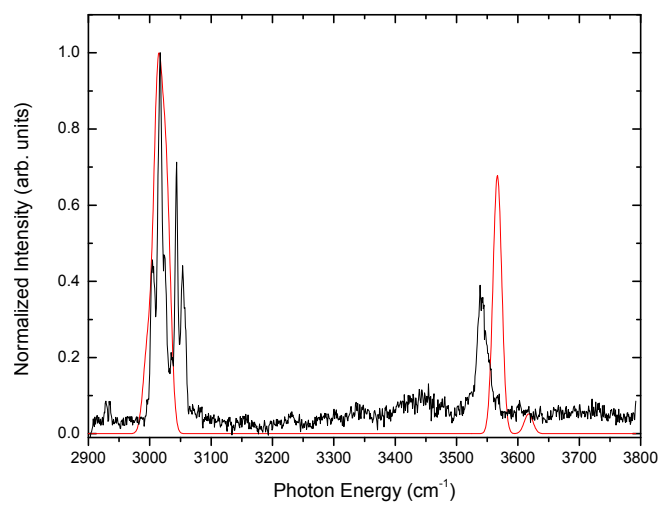
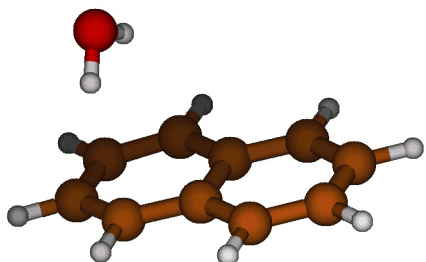


Relative Energy: 4 meV

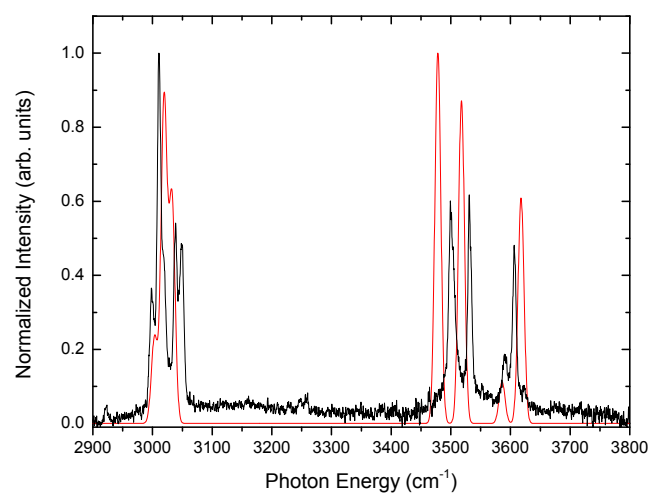
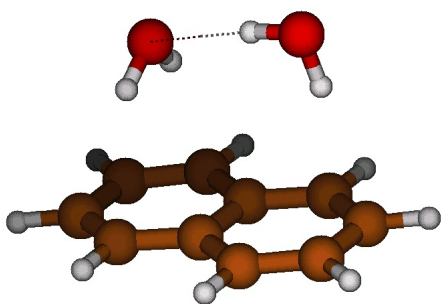


Relative Energy: 18 meV

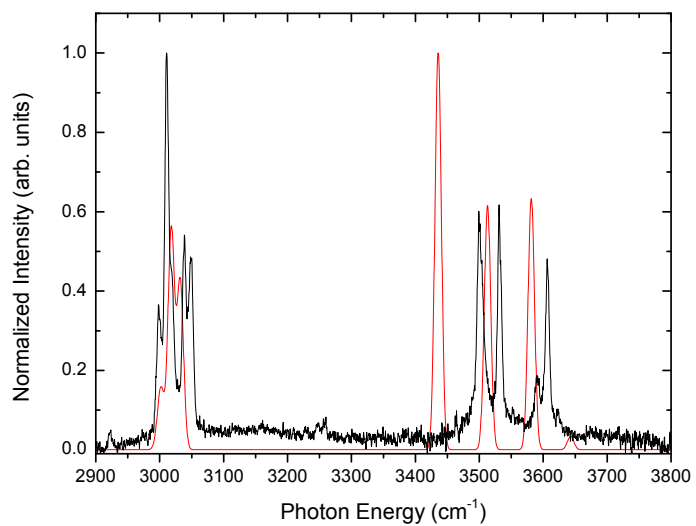
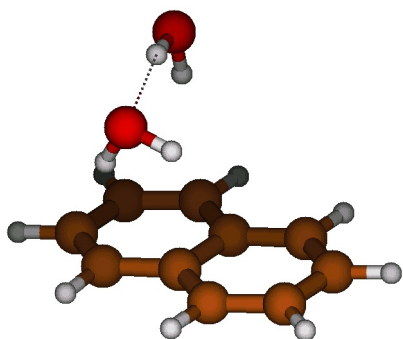




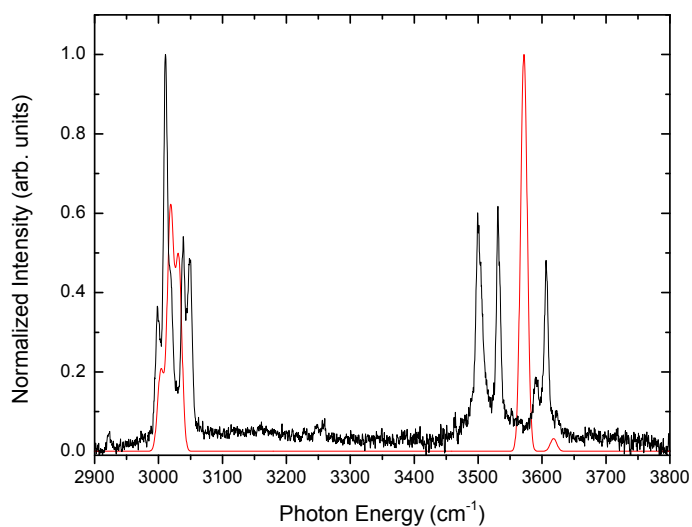
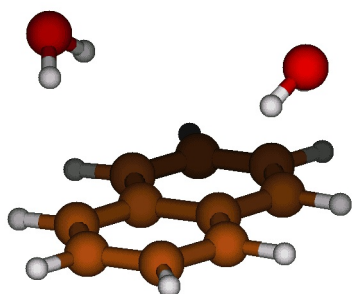
Relative Energy: 25 meV

C.2 $[\text{C}_{10}\text{H}_8 \cdot (\text{H}_2\text{O})_2]^-$ 

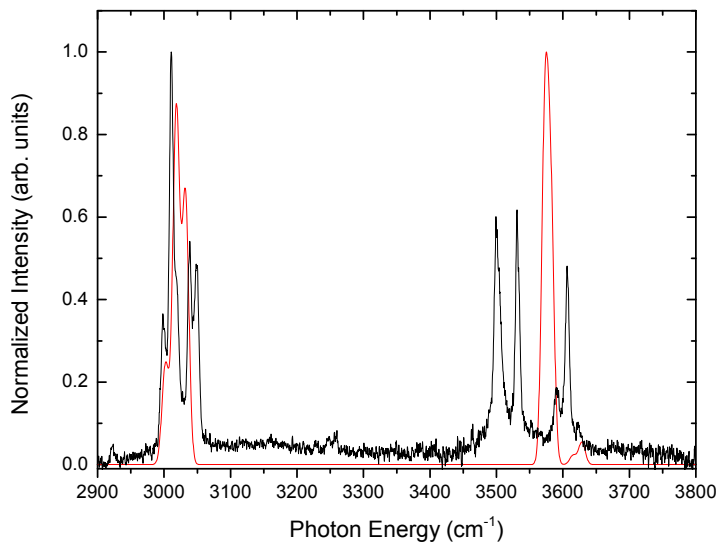
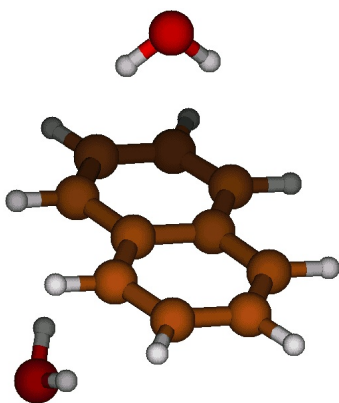
Relative Energy: 0 meV



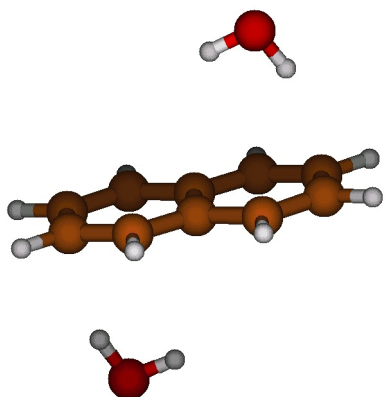
Relative Energy: 9 meV



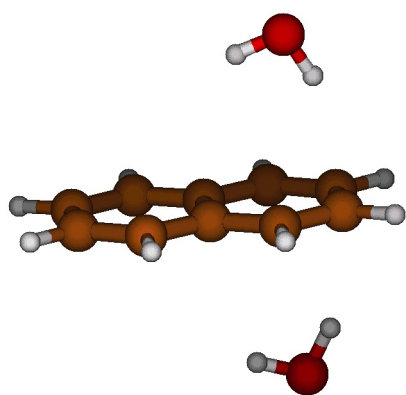
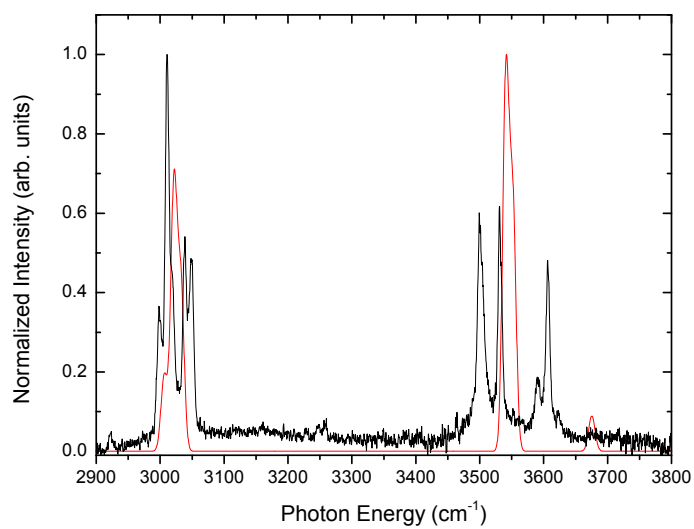
Relative Energy: 92 meV



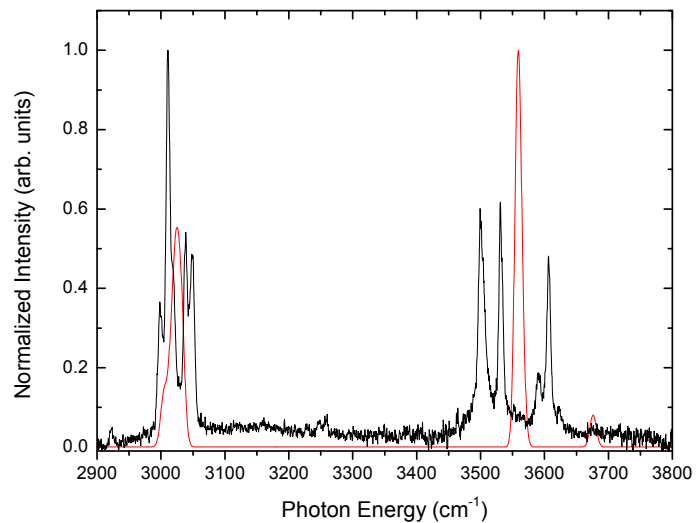
Relative Energy: 95 meV

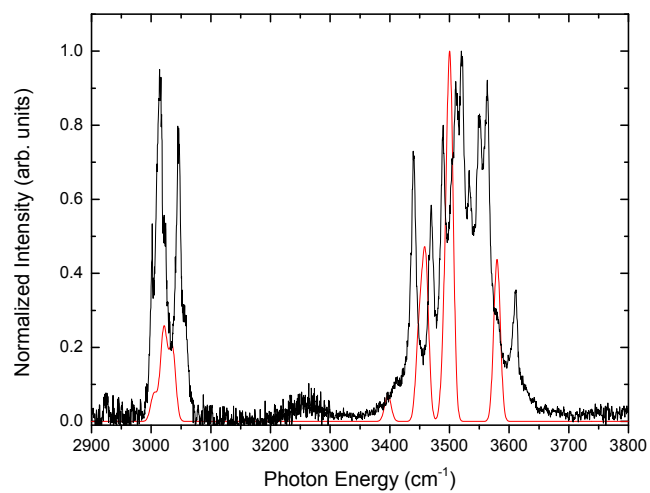
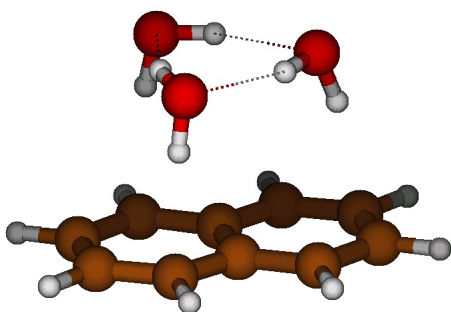


Relative Energy: 98 meV

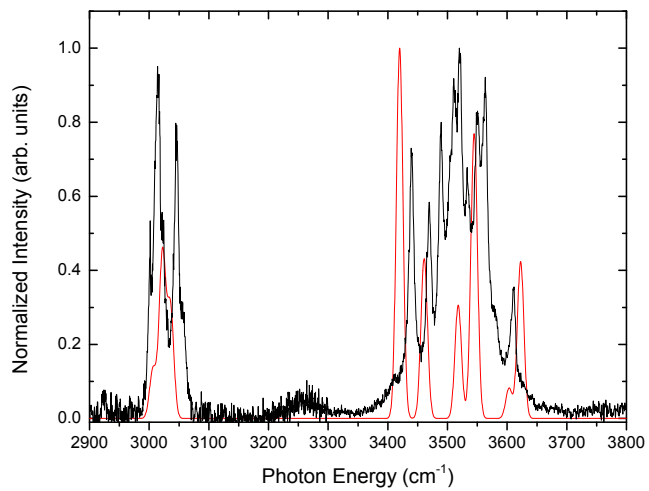
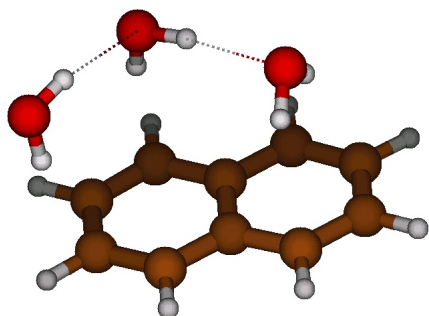


Relative Energy: 102 meV

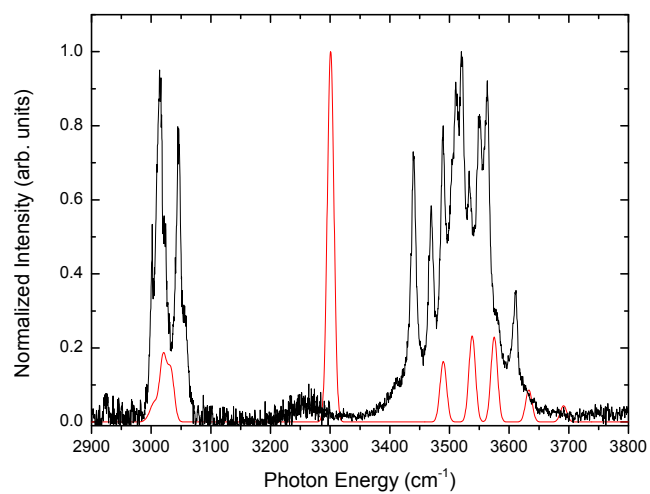
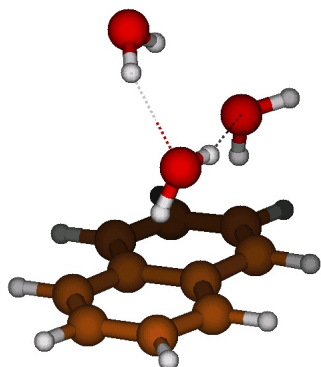


C.3 $[\text{C}_{10}\text{H}_8 \cdot (\text{H}_2\text{O})_3]^-$ 

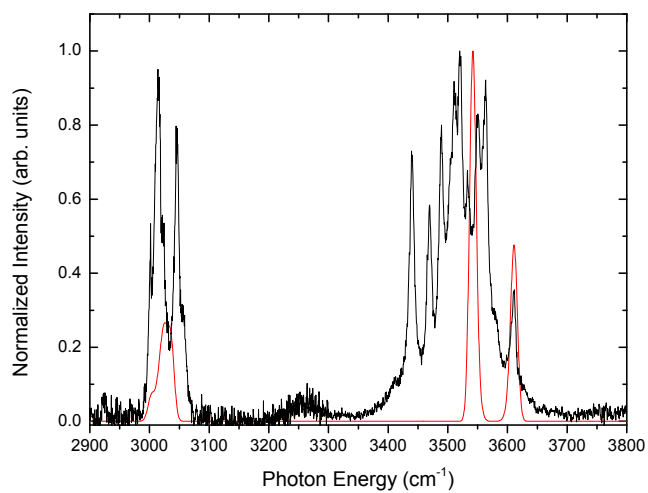
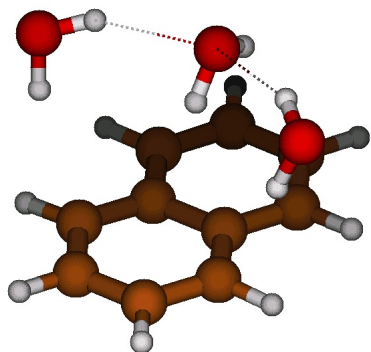
Relative Energy: 0 meV



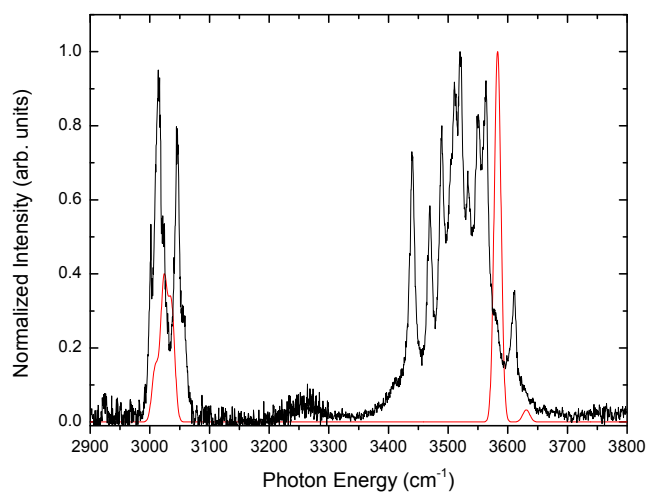
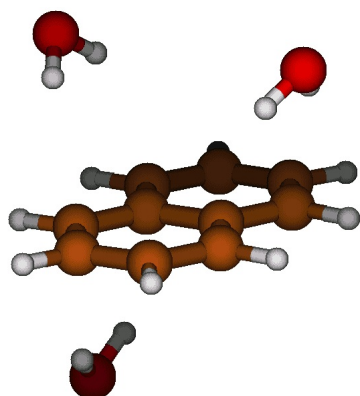
Relative Energy: 67 meV



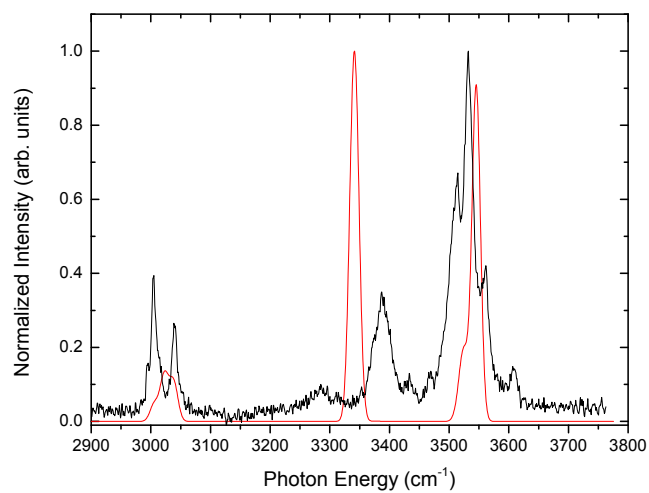
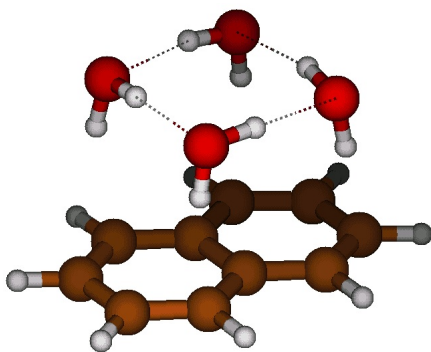
Relative Energy: 218 meV



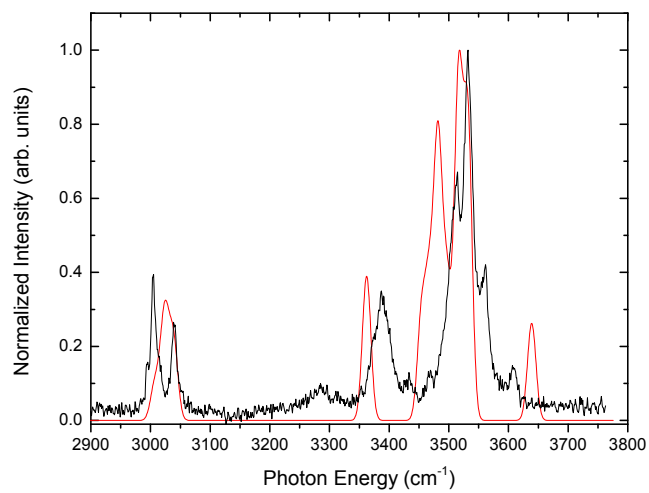
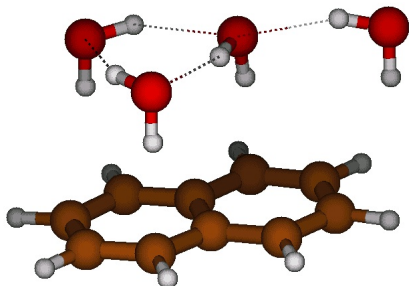
Relative Energy: 248 meV



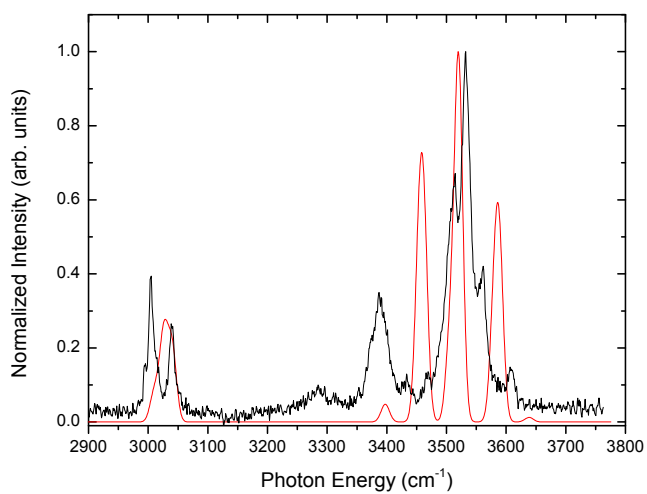
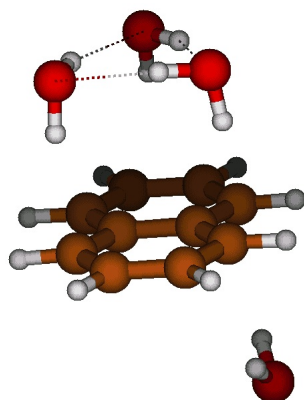
Relative Energy: 274 meV

C.4 $[\text{C}_{10}\text{H}_8 \cdot (\text{H}_2\text{O})_4]^-$ 

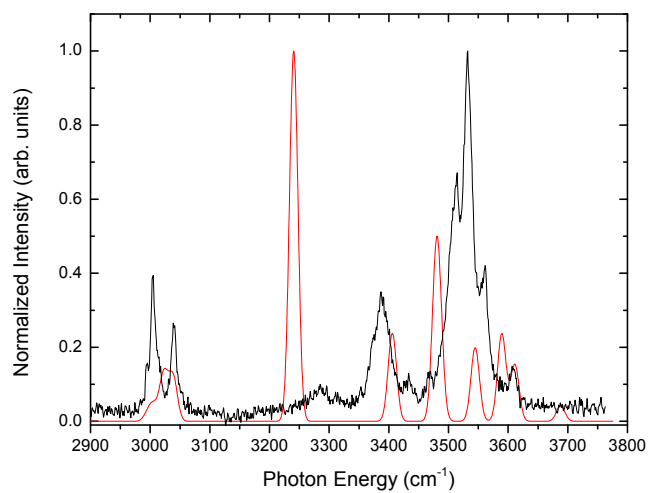
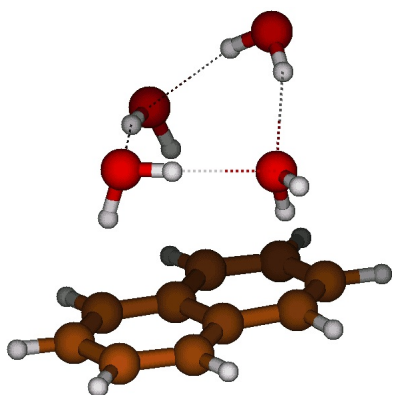
Relative Energy: 0 meV



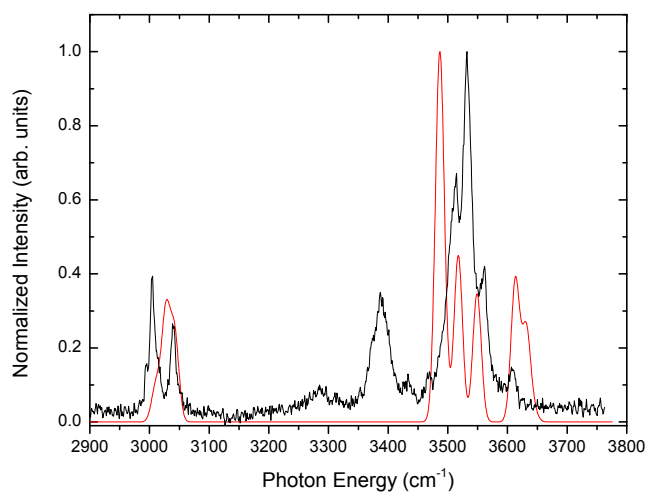
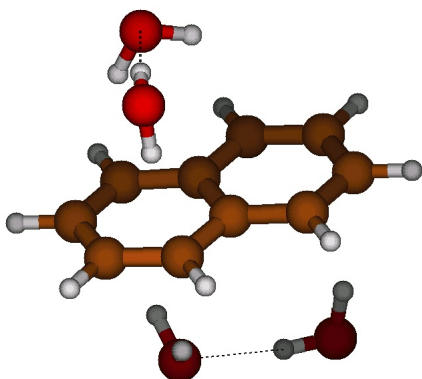
Relative Energy: 201 meV



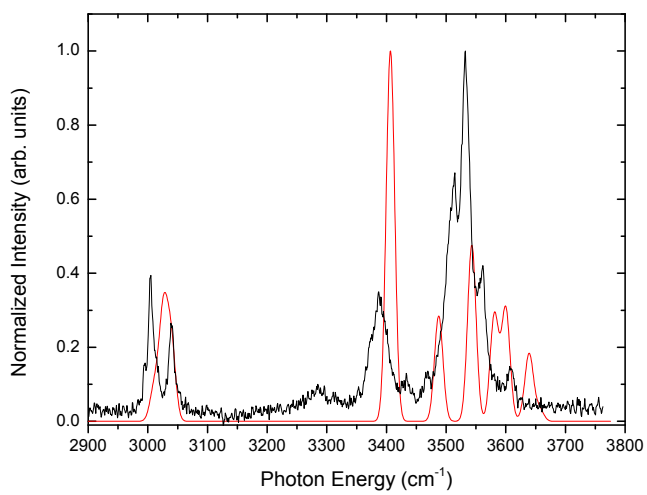
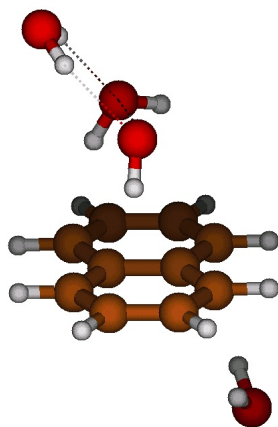
Relative Energy: 241 meV



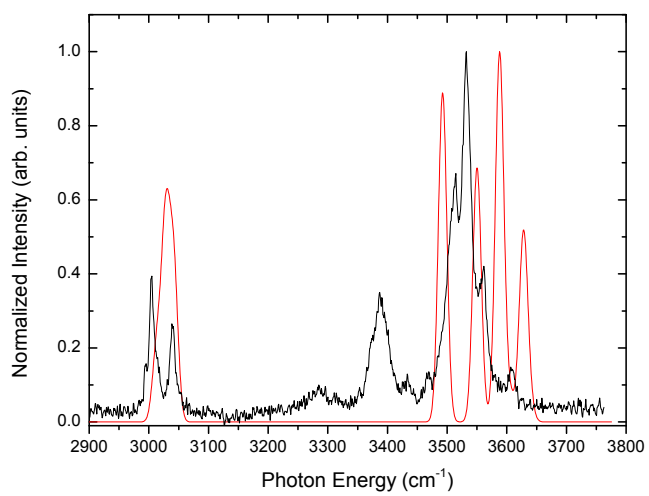
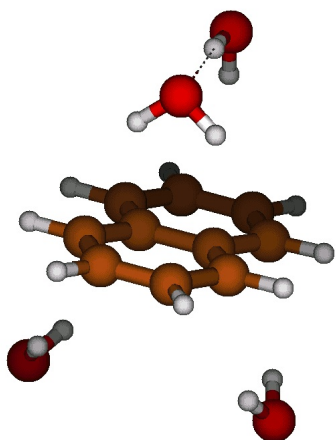
Relative Energy: 270 meV



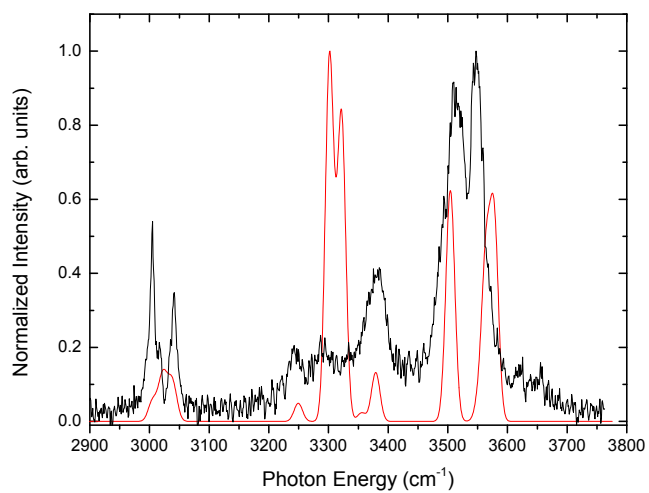
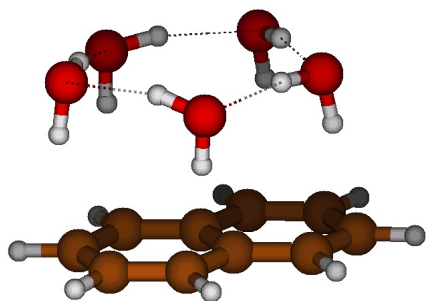
Relative Energy: 351 meV



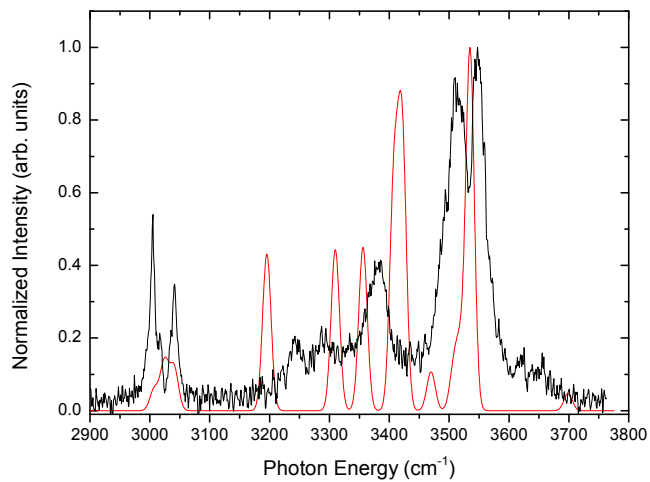
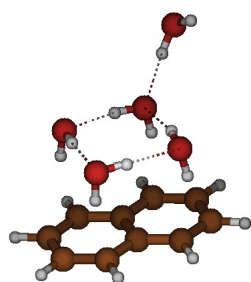
Relative Energy: 370 meV



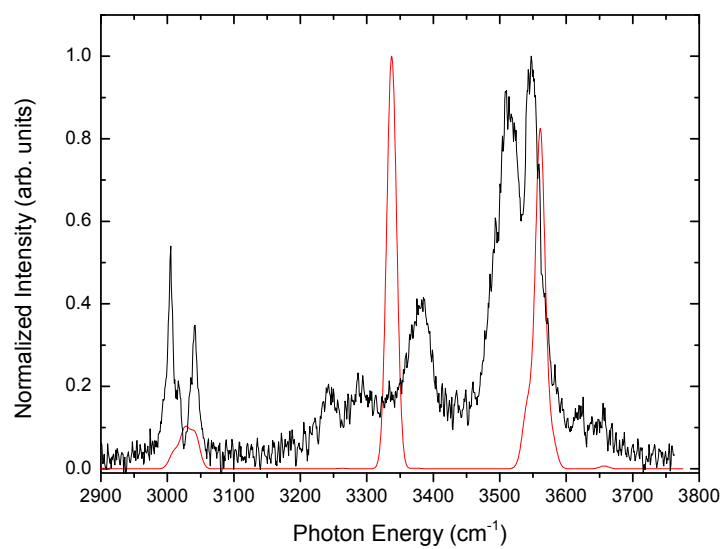
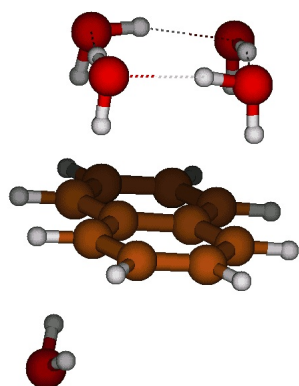
Relative Energy: 433 meV

C.5 $[\text{C}_{10}\text{H}_8 \cdot (\text{H}_2\text{O})_5]^-$ 

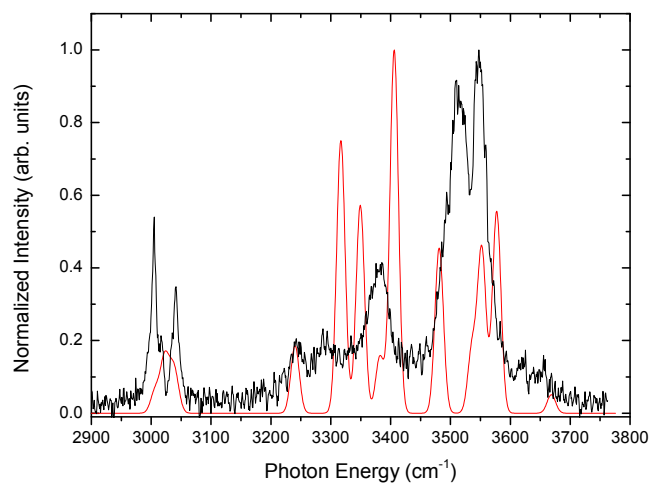
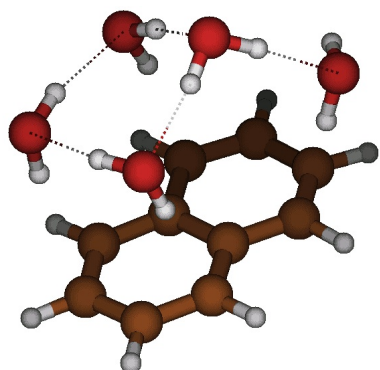
Relative Energy: 0 meV



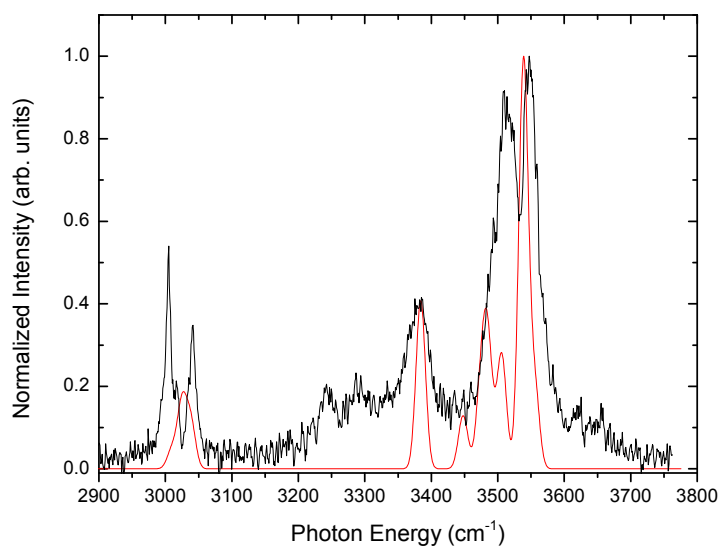
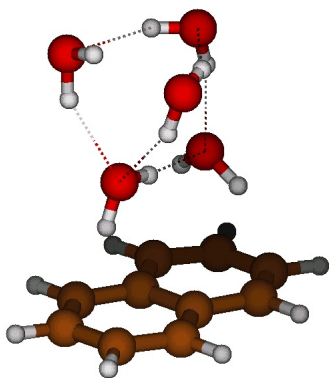
Relative Energy: 25 meV



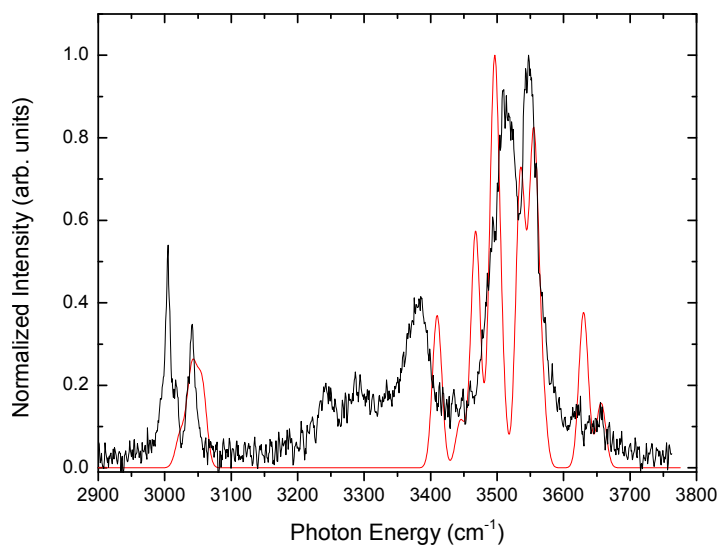
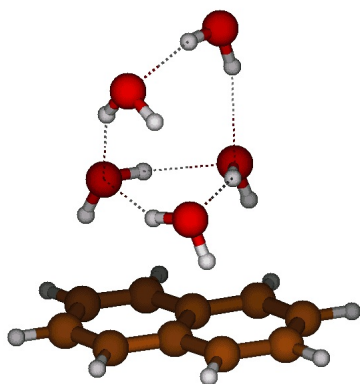
Relative Energy: 81 meV



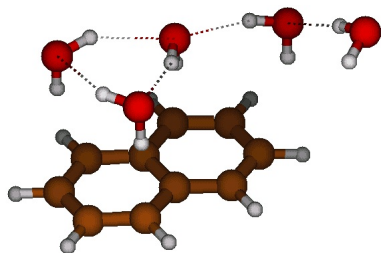
Relative Energy: 102 meV



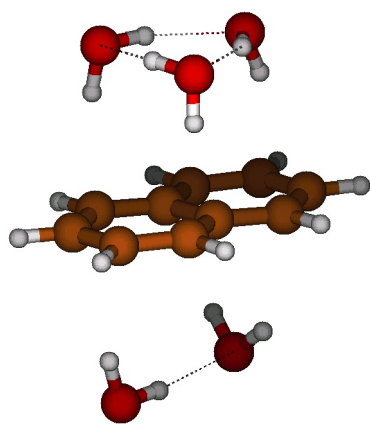
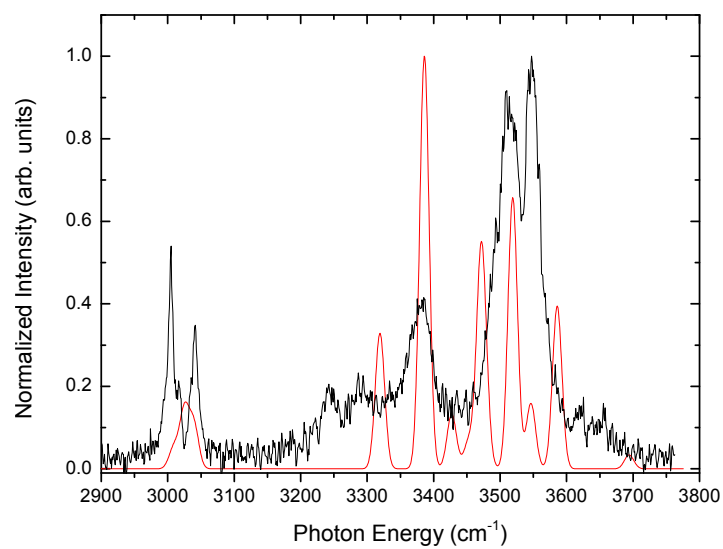
Relative Energy: 163 meV



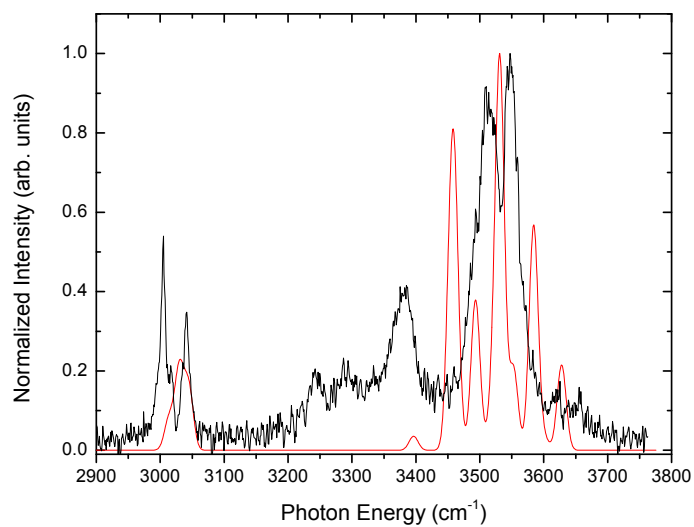
Relative Energy: 184 meV

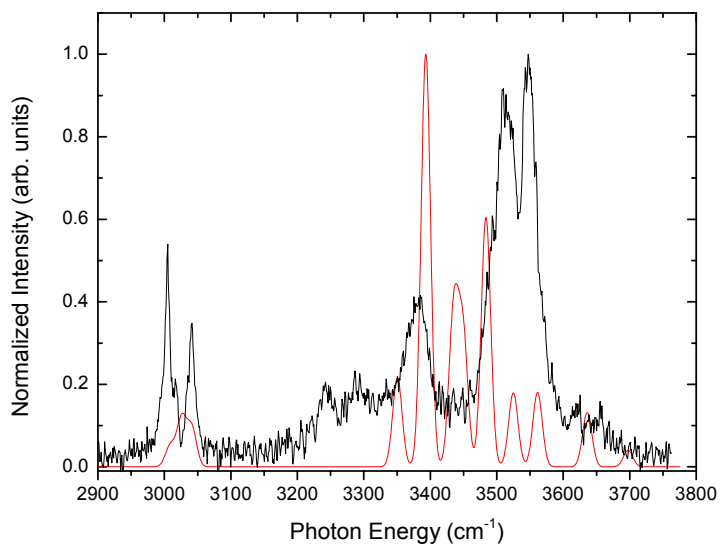
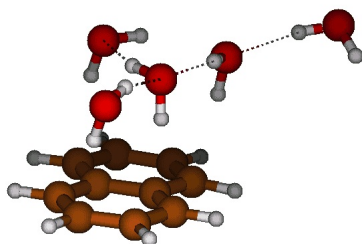


Relative Energy: 208 meV

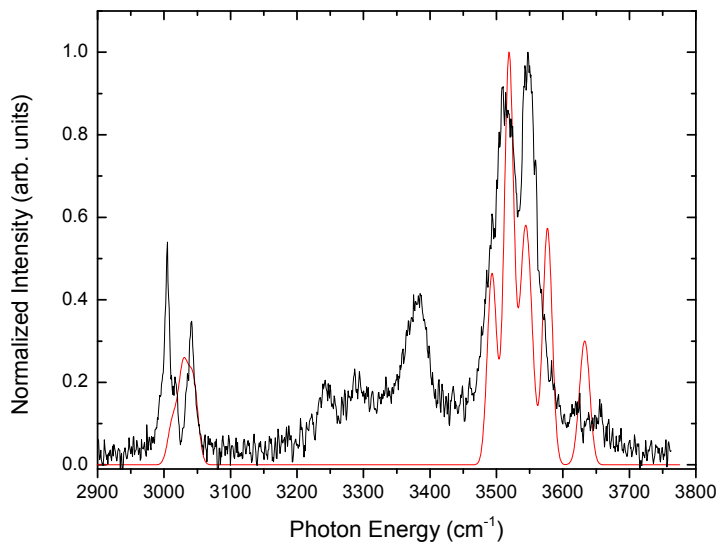
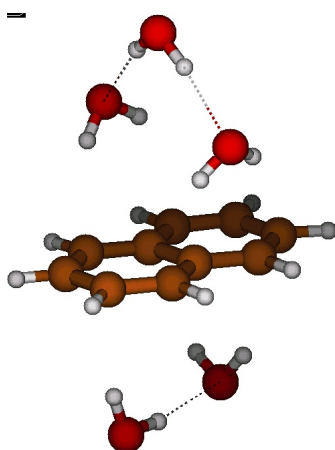


Relative Energy: 225 meV

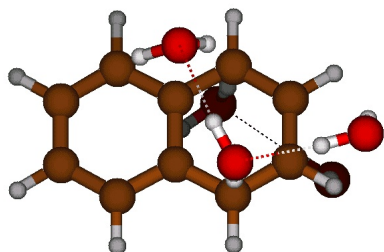




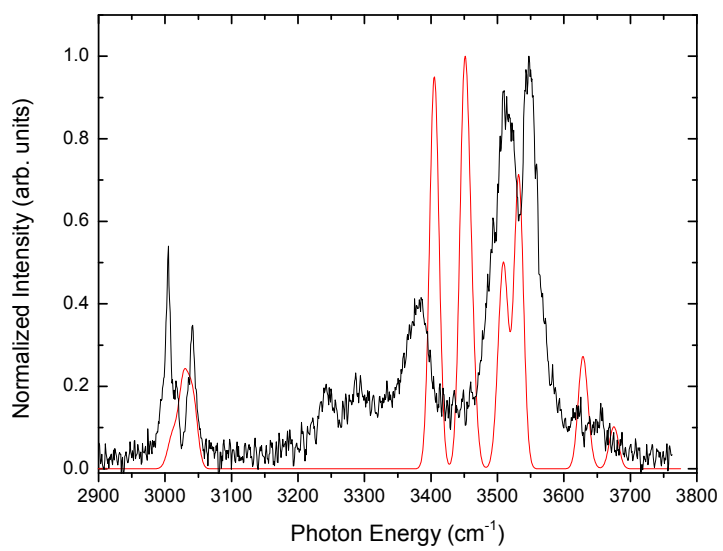
Relative Energy: 243 meV

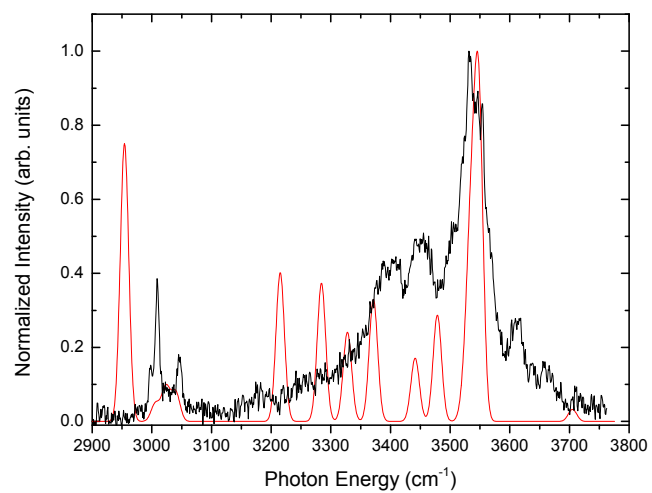
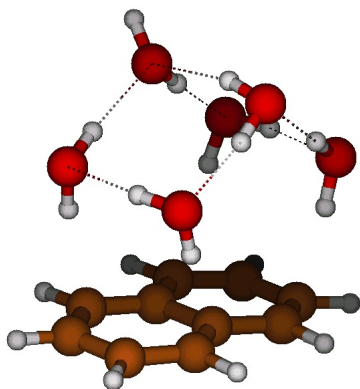


Relative Energy: 356 meV

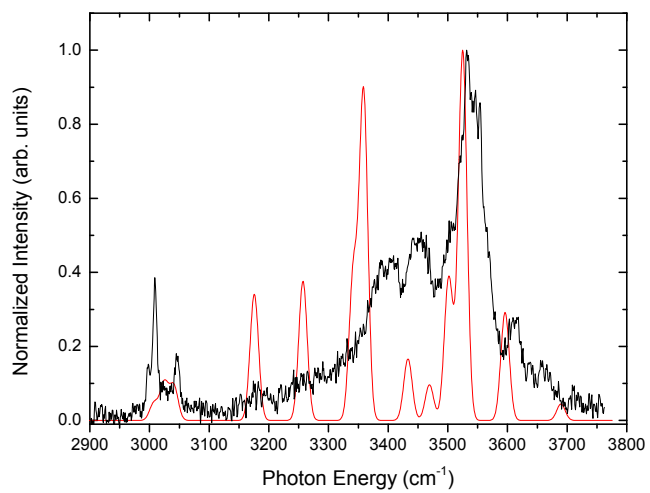
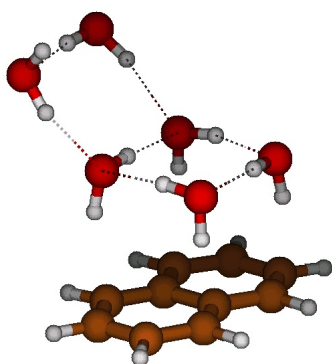


Relative Energy: 371 meV

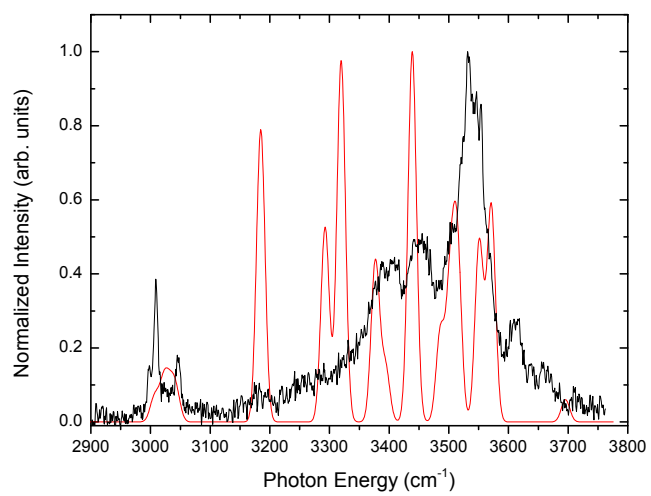
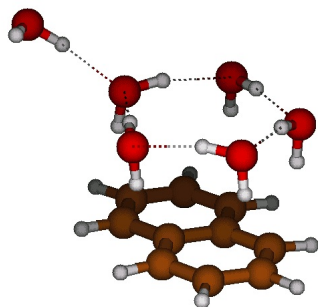


C.6 $[\text{C}_{10}\text{H}_8 \cdot (\text{H}_2\text{O})_6]^-$ 

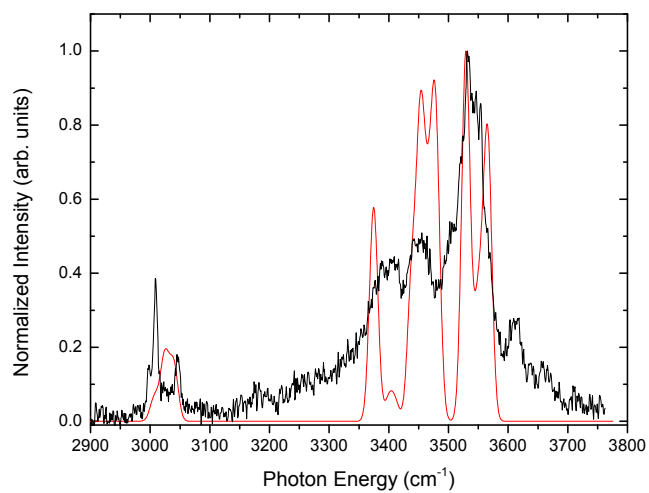
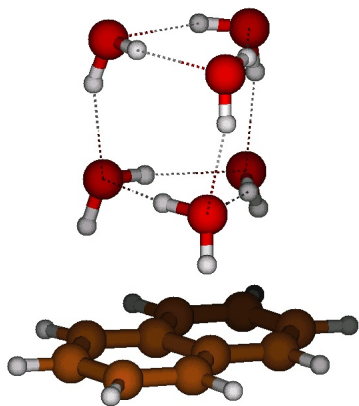
Relative Energy: 0 meV



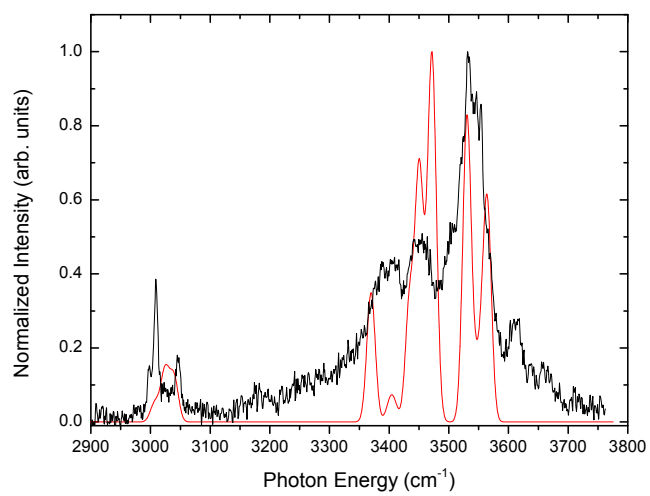
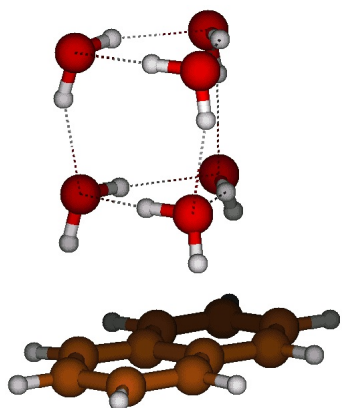
Relative Energy: 19 meV



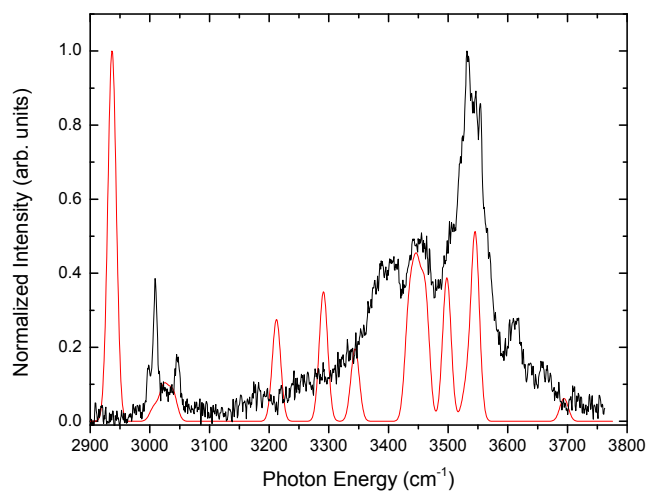
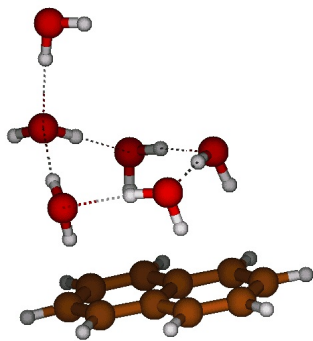
Relative Energy: 52 meV



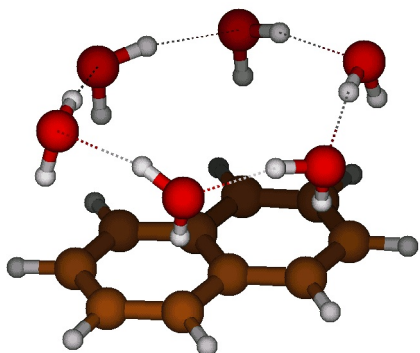
Relative Energy: 57 meV



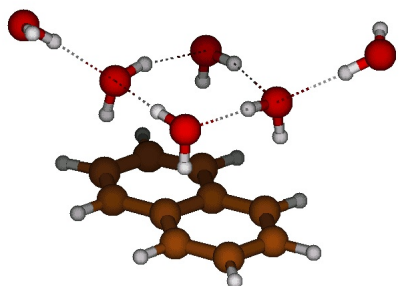
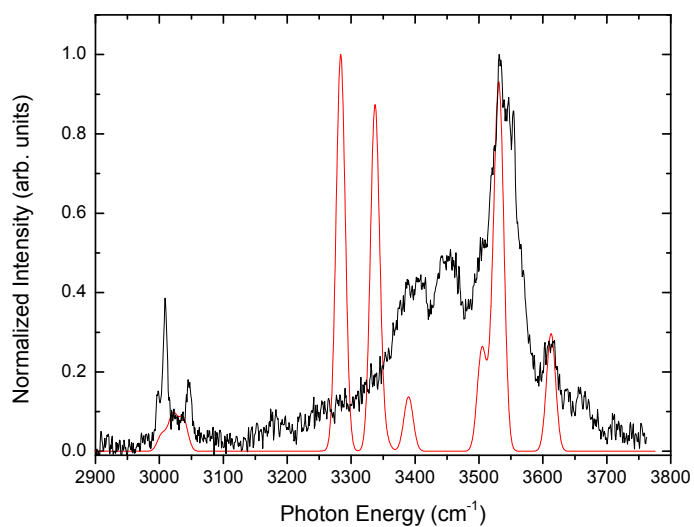
Relative Energy: 62 meV



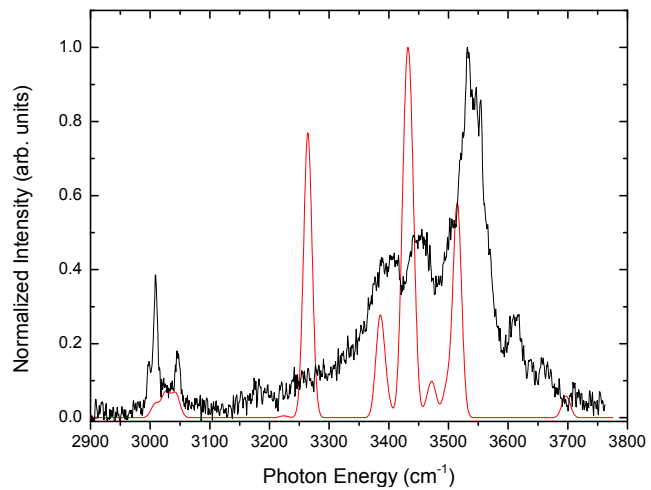
Relative Energy: 66 meV

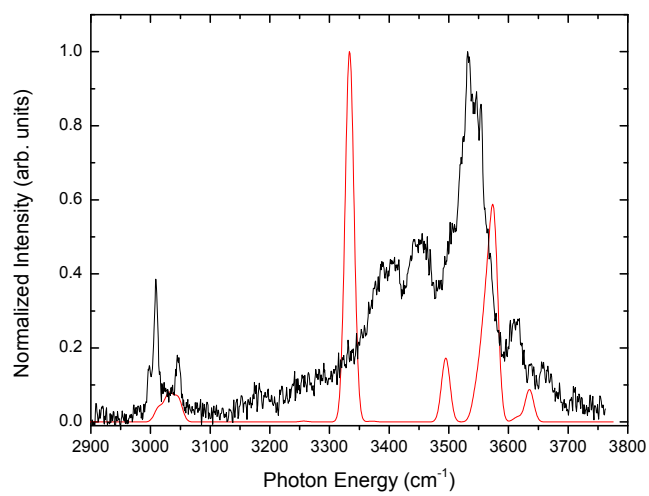
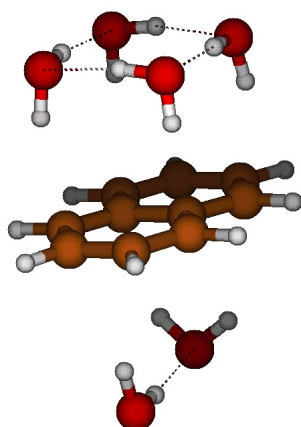


Relative Energy: 68 meV

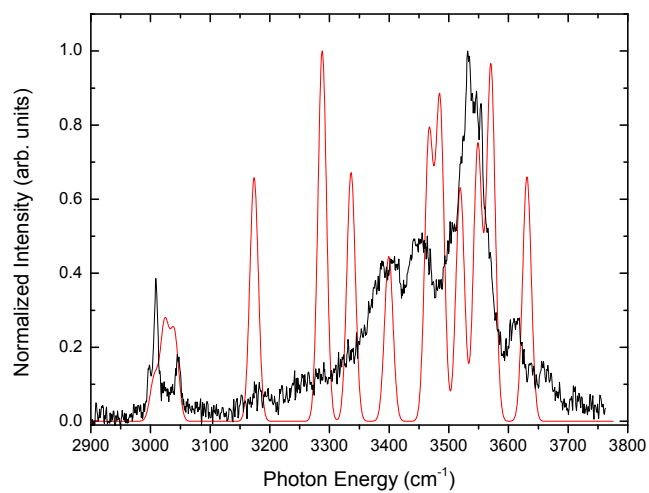
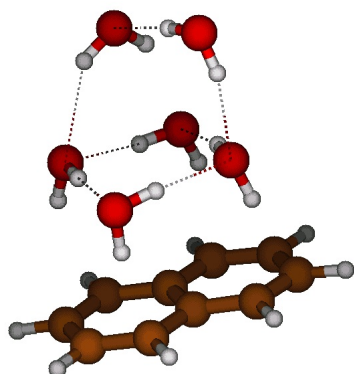


Relative Energy: 89 meV

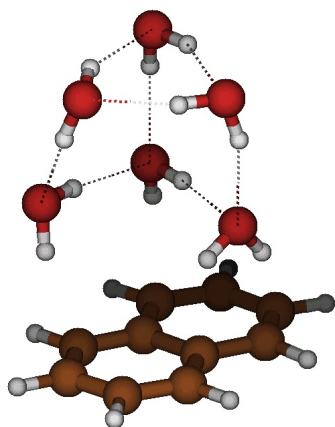




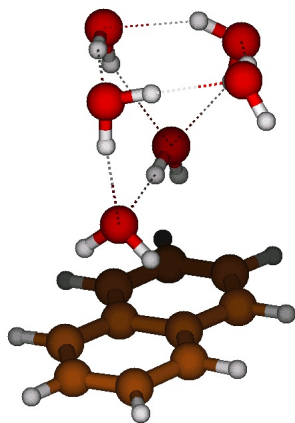
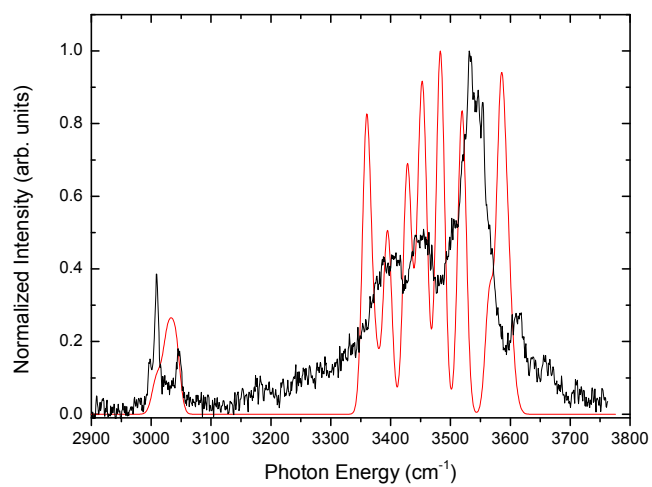
Relative Energy: 92 meV



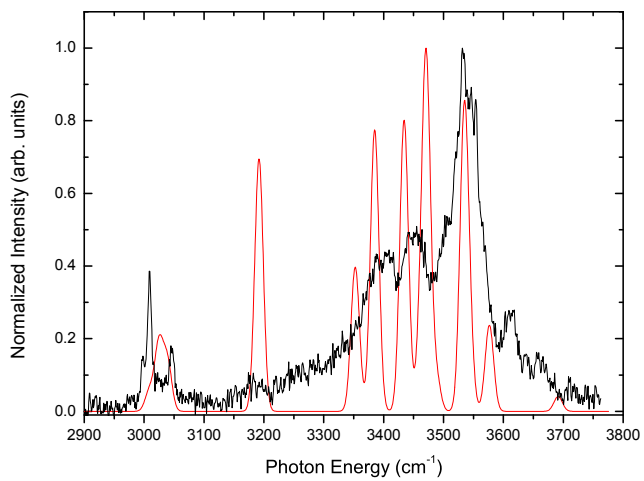
Relative Energy: 95 meV

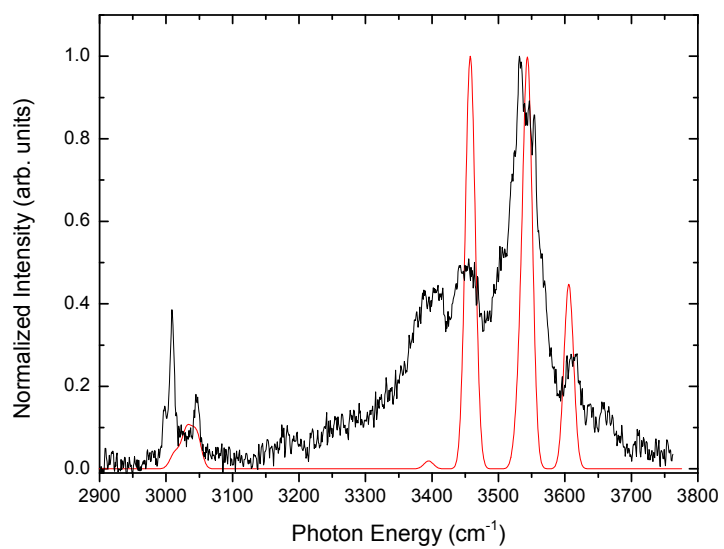
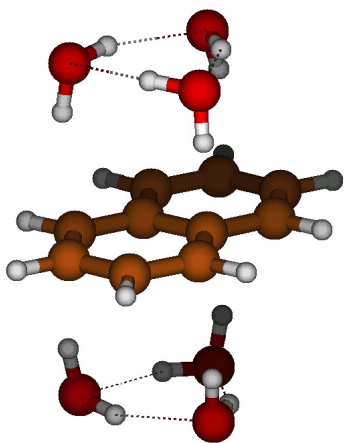


Relative Energy: 111 meV

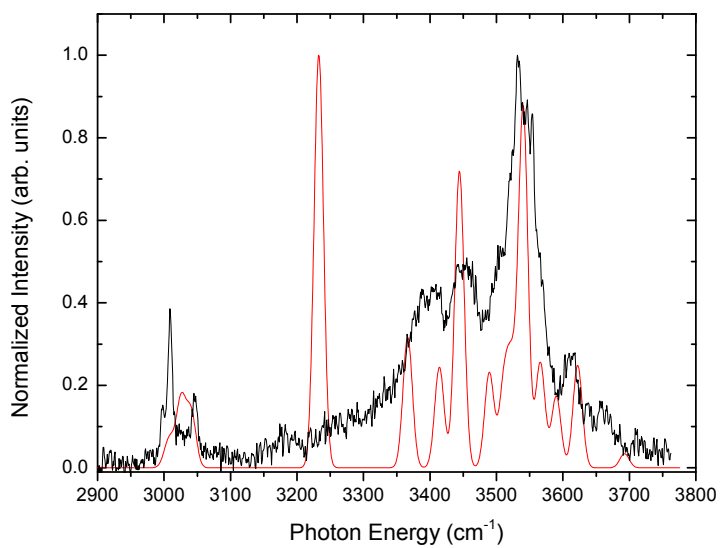
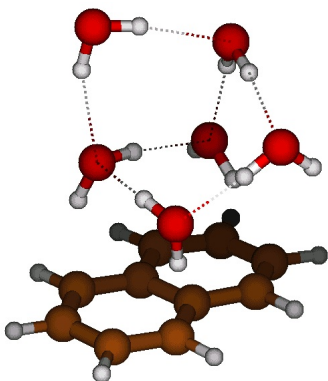


Relative Energy: 113 meV

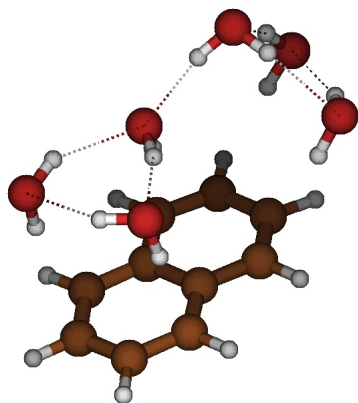




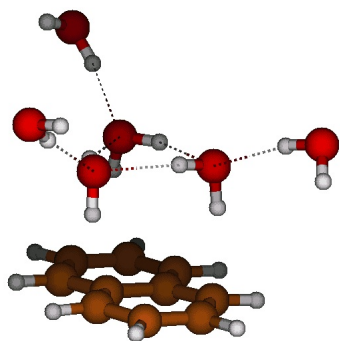
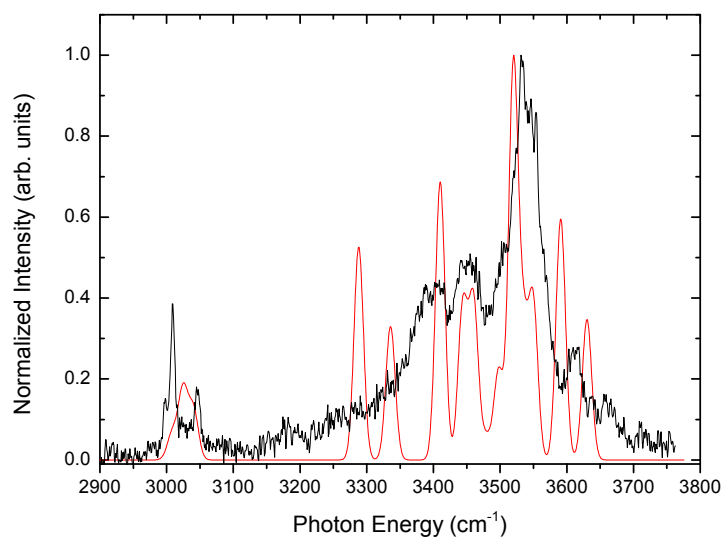
Relative Energy: 161 meV



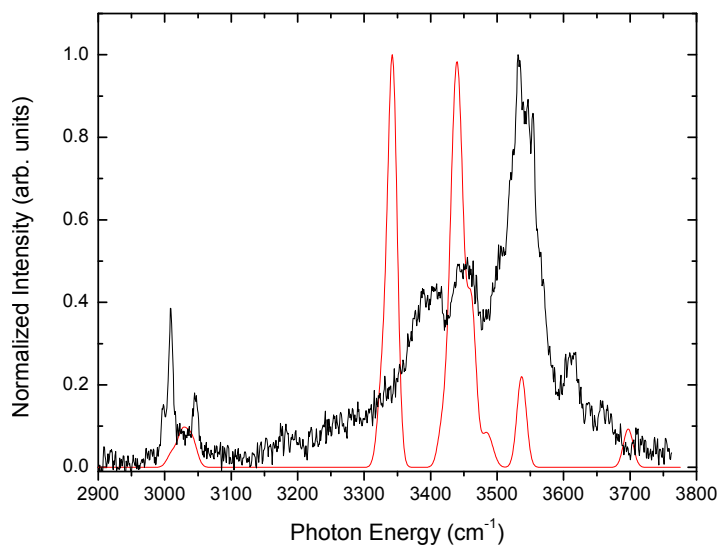
Relative Energy: 190 meV

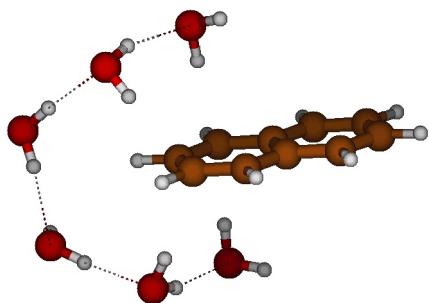


Relative Energy: 220 meV



Relative Energy: 325 meV





Relative Energy: 459 meV

